polymers

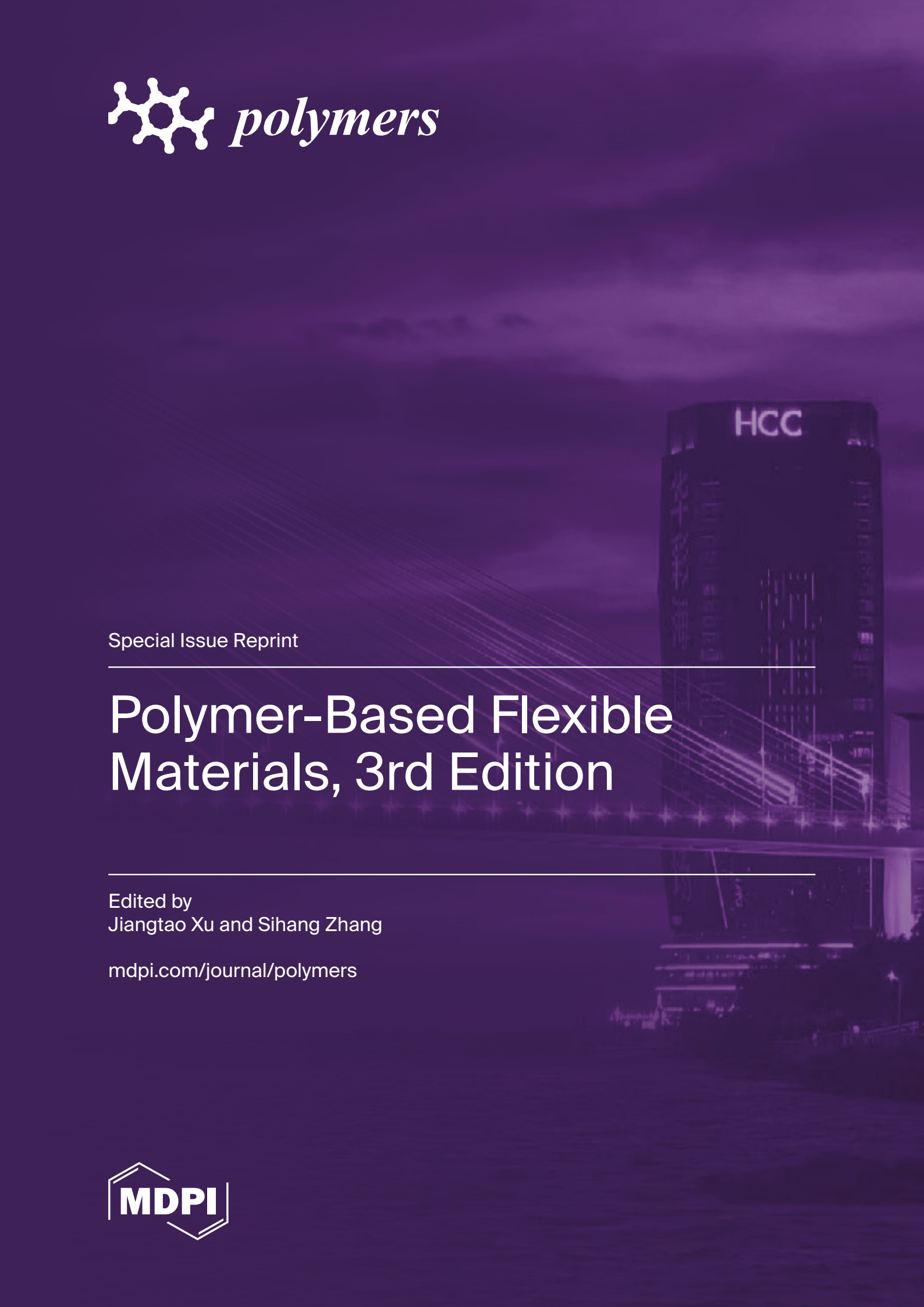

Special Issue Reprint

Polymer-Based Flexible Materials, 3rd Edition

Edited by
Jiangtao Xu and Sihang Zhang

mdpi.com/journal/polymers

MDPI

Polymer-Based Flexible Materials, 3rd Edition

Polymer-Based Flexible Materials, 3rd Edition

Guest Editors

Jiangtao Xu
Sihang Zhang

MDPI

Basel • Beijing • Wuhan • Barcelona • Belgrade • Novi Sad • Cluj • Manchester

Guest Editors

Jiangtao Xu
College of Materials
and Energy
South China Agricultural
University
Guangzhou
China

Sihang Zhang
School of Food Science
and Engineering
Hainan University
Haikou
China

Editorial Office

MDPI AG
Grosspeteranlage 5
4052 Basel, Switzerland

This is a reprint of the Special Issue, published open access by the journal *Polymers* (ISSN 2073-4360), freely accessible at: https://www.mdpi.com/journal/polymers/special_issues/389GE71WJI.

For citation purposes, cite each article independently as indicated on the article page online and as indicated below:

Lastname, A.A.; Lastname, B.B. Article Title. *Journal Name* **Year**, *Volume Number*, Page Range.

ISBN 978-3-7258-7677-8 (Hbk)
ISBN 978-3-7258-7678-5 (PDF)
https://doi.org/10.3390/books978-3-7258-7678-5

Cover image courtesy of Sihang Zhang

Contents

About the Editors

Jiangtao Xu

Jiangtao Xu obtained his Ph.D. from Hong Kong Polytechnic University in 2021 and subsequently worked as a Postdoctoral Researcher there from 2021 to 2023. He is currently an Associate Professor and Master's Supervisor at South China Agricultural University. His research primarily focuses on biomass composite materials, the functional modification of biomass materials, and the comprehensive utilization of biomass resources. Specifically, he works with nanocellulose, wood, and other biomass-derived materials to develop high-performance SERS substrates, flexible stress sensors, and electromagnetic shielding materials. Dr. Xu is committed to innovating and developing high-value-added biomass materials for applications in food safety, environmental security, and healthcare. As a first author or corresponding author, he has published multiple SCI papers in prestigious journals such as *Materials Today*, *Nano Research*, *Composites Part B*, and *ACS Applied Materials & Interfaces*. He has also secured several competitive research grants, including projects funded by the National Natural Science Foundation of China (NSFC) and the Natural Science Foundation of Guangdong Province.

Sihang Zhang

Sihang Zhang is an Associate Professor at Hainan University. In June 2018, he obtained a master's degree in engineering from Sichuan University, and in June 2021, he earned a PhD in materials science from the State Key Laboratory of Polymer Materials Engineering at Sichuan University. Subsequently, from September 2021 to November 2023, he conducted postdoctoral research in the field of food safety detection at Hong Kong Polytechnic University. In 2023, he joined Hainan University as a Distinguished Associate Professor and a supervisor for master's and PhD students. His research areas include food quality and safety detection, the preparation of flexible SERS substrates, and the design of organic and inorganic nanomaterials. He has published over 30 SCI papers in journals such as *J. Energy Chem.*, *Chem. Eng. J.*, *ACS Appl. Mater. Interfaces*, *ACS Sustain. Chem. Eng.*, *Anal. Chem.*, *J. Hazard. Mater.*, and *Food Chem.* He serves as a Guest Editor for the SCI journal *Polymers*. He has been the principal investigator for projects such as the National Natural Science Foundation of China (Youth Program), Hainan Province Natural Science Foundation General Program, Hainan University High-level Talent Startup Fund, Hong Kong Special Administrative Region Government Research Talent Pool Postdoctoral Project (RTH-ITF), and the Sichuan Provincial Science and Technology Department Miaozi Project.

Preface

The field of polymer-based flexible materials has continued to evolve rapidly since the publication of the previous editions of this Reprint. The third edition arrives at a moment when the boundaries between materials science, engineering, and applied device physics are becoming increasingly blurred, driven by the growing demand for lightweight, conformable, and mechanically robust systems.

This Reprint brings together a collection of recent contributions that reflect both the maturation of established concepts and the emergence of new directions within this interdisciplinary domain. In this volume, particular attention is given to the rational design of polymer matrices and the incorporation of functional nanofillers to achieve tailored mechanical, electrical, and optical properties. Several contributions explore the relationship between polymer network architecture—such as crosslinking density, chain mobility, and phase separation—and macroscopic performance metrics, including stretchability, toughness, and self-healing capability. Advances in fabrication strategies, ranging from solution processing and electrospinning to three-dimensional printing and surface patterning, are also highlighted, demonstrating the increasing capability to construct hierarchical structures with precise spatial control. The application-oriented chapters of this Reprint cover a broad spectrum of emerging uses for polymer-based flexible systems. Wearable and implantable devices for health monitoring, flexible energy storage and conversion systems, soft actuators and sensors for robotics, and conformable optoelectronic interfaces are among the key areas addressed. Collectively, these contributions illustrate how fundamental insights into polymer physics and chemistry are being translated into practical devices that can withstand repeated deformation while maintaining stable performance. A notable feature of this third edition is the emphasis on the durability and long-term reliability of flexible materials under real-world operating conditions. Several studies systematically examine the effects of cyclic mechanical loading, environmental exposure, and interfacial stability on device performance, providing valuable guidance for the transition from laboratory prototypes to field-deployable systems.

The editors wish to express their sincere gratitude to all authors who have contributed their original research and comprehensive reviews to this Reprint. We also thank the dedicated reviewers whose constructive feedback ensured the scientific rigor and clarity of each manuscript. Finally, we acknowledge the editorial team for their professional support throughout the publication process. It is our hope that this Reprint will serve as a valuable resource for researchers, engineers, and students working at the intersection of polymer science and flexible device engineering. By compiling the current state of knowledge and identifying remaining challenges, we aim to inspire further innovation that will shape the next generation of polymer-based flexible materials.

Jiangtao Xu and Sihang Zhang
Guest Editors

polymers

MDPI

Article

Preparation of Low-Surface-Energy SSBR@FA Hybrid Fillers via Solution Mechanochemical Approach and Its Enhancement in Mechanical Strength on the Modified FA/SBR Composites

Wei Gao [1,2,*], Jiangshan Zhao [1,2], Wei Qi [2], Zhaohui Huang [1,2,*], Guofeng Liu [2], Chuanqi Feng [1,2], Chao Sang [1,2], Xiujuan Wang [3] and Xiaolei Zhang [1,2]

[1] Shandong Provincial Key Laboratory of Monocrystalline Silicon Semiconductor Materials and Technology, Dezhou University, Dezhou 253023, China; zhaojshtxy@163.com (J.Z.); chq_feng@dzu.edu.cn (C.F.); 18810988921@163.com (C.S.); zhangxl@dzu.edu.cn (X.Z.)

[2] College of Chemistry and Chemical Engineering, Experimental Management Center, Institute of Biophysics, Dezhou University, Dezhou 253023, China; 13305345667@189.cn (W.Q.); gfliu26@163.com (G.L.)

[3] State Key Laboratory of Advanced Optical Polymer and Manufacturing Technology/Key Laboratory of Advanced Rubber Material, Ministry of Education, Qingdao University of Science and Technology, Qingdao 266042, China; wangxj@qust.edu.cn

* Correspondence: wgao567@126.com (W.G.); huangzhaohui_2021@163.com (Z.H.)

Abstract

Owing to the substantial polarity difference and weak interfacial interaction, the large-scale application of fly ash (FA) in rubber materials still faces substantial challenges. To solve this issue, this study prepared a modified hybrid SSBR@FA filler through a solution mechanochemical reaction between solution-polymerized styrene-butadiene rubber (SSBR) and FA in a lab planetary ball mill. Fourier transform infrared spectroscopy (FTIR) and energy-dispersive spectroscopy (EDS) analyses demonstrated the in situ grafting-neutralization between the carboxyl in the SSBR chains and metal oxides in FA. Transmission electron microscopy (TEM) showed that surface-grafted SSBR formed a rubber-constrained layer on FA particle surfaces, which can reduce their surface energy and improve the wettability between FA and SBR matrix. Compared with the SBR vulcanizate, the mechanical properties, thermal conductivity, and flame-retardant properties of the SBR/SSBR@FA vulcanizates were obviously improved. This was because of the uniform distribution of FA and the improved interfacial interaction between FA and the rubber matrix. For example, the tensile strength, tear strength, and elongation at break increased by 66.3%, 52.9%, and 17.7%, respectively. This easy, efficient, and environmentally modified method for FA was expected offer a practical and creative solution for its application in rubber manufacturing.

Keywords: fly ash; ball milling-surface modification; rubber; mechanical properties

1. Introduction

Although wind, solar, and biogas power generation are practicable alternative energy sources at present, coal-fired power factory still play a vital role in the production of electricity. It accounts for nearly 41% of global power output, and the figure is expected to rise to 44% by 2030 [1–3]. The coal-fired power factory will produce about one ton of fly ash (FA) as a byproduct [1] when every four tons of coal is burned. In China, the annual production of FA reaches hundreds of millions of tons, yet its utilization rate remains at only about 45% [4,5], leading to serious environmental problems. In order to promote the

recycling use of FA, researchers have put it into use in the construction industry [6], oil extraction [7], agriculture, and so on [8]. In addition, FA has the advantages of low cost, low density, strong filling capability, smooth surface, and good processability [9–11]. It can serve as a filler in polymer materials, especially rubber-based composites, which is a sustainable development strategy.

In the micromorphology, FA's spherical structure is similar to carbon black [12], which is made from silica and metal oxides. At the same time, FA shows a low agglomeration tendency [10]. As a non-synthetic filler, the low cost and zero carbon emissions [2] of FA make it an ideal substitute for reducing both the production cost and environmental influence of rubber-based composites [12]. The incorporation of raw FA into rubber matrices reduced curing time but damaged mechanical properties compared to silica-filled rubber composites [13–16]. This is mainly attributed to the low structural dimensionality, low specific surface area, and surface inertness of unmodified FA, which decreases the interfacial contact between polymer chains and FA and impairs surface wettability, thereby weakening their interfacial interaction [13]. To overcome this issue, surface treatment is an indispensable step. Garde et al. used acid-base modification to alter the surface morphology of FA, but the modified FA-filled polyisoprene still exhibited low bound rubber content and poor mechanical strength, even with the addition of Si69 [17]. This is due to the large particle size of FA and the absence of surface-reactive groups [10,18,19]. Based on the above analysis, the key factors such as particle size, morphology, and interfacial activity make a big difference in the reinforcing efficiency of FA.

In terms of the chemical composition, in addition to silica, FA also contains substantial amounts of metallic oxides such as CaO, Al_2O_3, and Fe_2O_3. Because of this compositional feature, Yang's group proposed the concept of in situ grafting-neutralization, aiming to enhance the performance of FA-filled rubber composites [1,7,10,19]. Under heating conditions, an in situ carboxylate reaction facilitated the immobilization of a carboxylated nitrile butadiene rubber (XNBR) layer on FA surfaces, which enhanced the interaction of the interface. Therefore, compared to pure XNBR, the mechanical properties of the XNBR composite, which was filled with FA, were improved significantly [10]. The research team also fabricated composite materials by incorporating sorbic acid (SA) or tannic acid (TA) into non-carboxylated rubbers along with FA. One end of SA or TA reacted with metallic oxides in FA filler, and the other reacted with rubber chains, which strengthened interfacial attachment in composite materials [1,7,19]. Following the same principle, FA was subjected to carbonation through CO_2 by another research team [20]. The incorporation of modified FA resulted in different levels of enhancement in the mechanical and flame-retardant performance of silicone rubber.

Another effective strategy for improving wettability between FA and polymer was to modify FA with a hydrophobic polymer. Bordoloi et al. engineered a surface-modified FA by depositing a hydrophobic polysulfide layer on FA [12]. There was excellent wettability between surface-modified FA and natural rubber. Other research teams have also reported similar hydrophobic coatings based on biopolymers for FA encapsulation, synthesized from waste sulfur and cooking oil [21].

As a commonly used matrix in rubber composites, the works on the SSBR modifying FA are seldom addressed in the literature. Our earlier research introduced an easy, highly efficient, and environmentally modification method for preparing SSBR-grafted silica via solution mechanochemical processing in a lab-scale planetary ball mill [22]. The surface modification of silica reduced filler–filler interactions while enhancing the rubber-silica interfacial adhesion, and the performance of the SiO_2-*g*-SSBR-filled SSBR composites was obviously improved. Inspired by these interesting results, two types of carboxyl-functionalized rubbers were subjected to wet ball milling with FA, aiming to prepare

https://doi.org/10.3390/polym18030348

hydrophobic FA (SSBR@FA) through in situ grafting-neutralization in this work. Ball milling was employed to decrease the particle size of FA and alter the structure of FA [2]. Under the dual effects of ball milling and SSBR modifiers, the mechanical properties, thermal conductivity, and flame retardancy of SSBR@FA-filled SBR vulcanizates have been improved, offering a practical and transformative solution for industrial-scale application of FA in rubber manufacturing.

2. Materials and Methods

2.1. Materials

FA (BET surface area of 3.38 m^2/g) was provided by a thermal power plant, and the composition is depicted in Table S1. SSBR (M_n = 74,300 g/mol, PDI = 1.03), with 32.4 wt% styrene and 47.9 wt% 1,2-polybutadiene units relative to polybutadiene, was supplied by Zhejiang Zhongli Synthetic Materials Technology Co., Ltd. (Jiaxing, China). 3-mercaptopropionic acid (MPA), 11-mercaptoundecanoic acid (MUA), and dilauroyl peroxide (LPO) (≥98%) were purchased from Adamas (Shanghai, China) and used in their original form. SBR1502 was purchased from Sinopec Qilu Petrochemical Company (Zibo, China). Other reactants, such as cyclohexane, zinc oxide, stearic acid, N-cyclohexylbenzothiazole-2-sulphenamide, 2-Mercaptobenzothiazole, and sulfur, were commercially sourced.

2.2. SSBR Functionalization

The procedure for carboxyl functionalization of SSBR through click reaction was explained in detail below. Briefly, under a nitrogen atmosphere, a predetermined amount of SSBR and cyclohexane were sequentially added to a glass reaction flask. The mixture underwent continuous stirring at 60 °C over a 6 h period until complete dissolution of SSBR in the cyclohexane, obtaining a homogeneous solution with a mass fraction of 10%. The SSBR solution subsequently received an injection of precisely measured thiol, either MPA or MUA. The mixture was heated at a temperature of 80 °C with simultaneous stirring for 10 min, and then a pre-prepared solution of LPO in cyclohexane was added to the mixture. The thiol-ene click reaction was maintained at 80 °C for 1 h under stirring conditions. The procedure for the post-treatment of carboxyl-functionalized SSBRs was similar to that of our previous work [22,23]. The final modified products were named as SSBR-*g*-MPA and SSBR-*g*-MUA, respectively.

2.3. Preparation of SSBR@FA

A Qm-2 laboratory planetary ball mill (Beijing New Lasers Technology Co., Ltd., Beijing, China) was employed to fabricate modified FA (SSBR@FA) with varying carboxyl-functionalized SSBR contents. The mill pot was sequentially charged with a cyclohexane solution of carboxyl-functionalized SSBR and FA at mass ratios of 0.01% and 0.03% (rubber to FA). A suitable amount of cyclohexane was then added to the mill pot to maintain a fly ash concentration of 40%. The FA and carboxyl-functionalized SSBR underwent grinding for 8 h with alternating clockwise and counterclockwise rotation. The planetary ball mill was operated at 260 rpm (revolution speed) and 530 rpm (rotation speed), using 30 zirconia balls (5 mm in diameter) and 18 zirconia balls (10 mm in diameter). To measure the typical structure of SSBR@FA, an appropriate amount of ball-milled FA was extracted using cyclohexane for 72 h to eliminate ungrafted SSBR. The purified SSBR@FA was dried in a vacuum drying oven at 50 °C for 36 h. The modified FA samples were named 1PFA, 3PFA, 1UFA, and 3UFA (e.g., 1PFA and 1UFA indicate that the mass ratio of SSBR-*g*-MPA and SSBR-*g*-MUA to FA was 1%, respectively).

https://doi.org/10.3390/polym18030348

2.4. Fabrication of SBR-Based Composites

SBR-based composites were fabricated by using traditional methods on a two-roll mill. The formulation for FA-filled SBR-based composites is shown in Table 1. The obtained composites filled by varied proportions of SSBR@FA were designated as follows: SBR/1PFA-15, SBR/1PFA-30, SBR/3PFA-15, SBR/3PFA-30, SBR/1UFA-15, SBR/1UFA-30, SBR/3UFA-15, and SBR/3UFA-30 (for example, SBR/1PFA-15 denotes a 15% mass ratio of 1PFA to SBR1502). As a contrast, SBR vulcanizate and SBR composites with raw FA were also prepared according to similar formulations, and the final products were termed as SBR, SBR/FA-15, and SBR/FA-30.

Table 1. Formulations of SBR/SSBR@FA composites.

Material	Amount/Phr [a]
SBR1502	100
Zinc oxide	2.18
Stearic acid	0.73
N-cyclohexylbenzothiazole-2-sulphenamide	1.09
2-Mercaptobenzothiazole	0.73
Sulfur	1.60
SSBR@FA	15/30

[a] Parts-per-hundred rubber.

2.5. Testing and Characterization Methods

The Fourier transform infrared spectroscopy (FTIR) analysis of SSBR and FA was conducted by a Nicolet iS20 spectrometer (Thermo Fisher Scientific, Waltham, MA, USA). ^{1}H nuclear magnetic resonance (^{1}H NMR) was conducted with a Bruker Plus spectrometer (Bruker Corporation, Karlsruhe, Germany) (600 MHz) to analyze the microstructure of SSBR using $CDCl_3$ as the solvent. The contact angles of FA with water and diiodomethane were determined by the SZ-CAMC32 equipment (Shanghai Xuanzhun Instrument Co., Ltd., Shanghai, China), and the surface energy was calculated via the Owens–Wendt equation. The thermal properties of FA were measured through thermal gravimetric analysis (TGA) with TGA/DSC3+ instruments (METTLER TOLEDO, Greifensee, Switzerland) from 30 to 800 °C. The temperature was increased at a rate of 10 °C/min. The specific surface area (SSA) of FA was determined using the BET method with an automated surface area and pore size analyzer (Quantachrome Nova 4000e, Boynton Beach, FL, USA) under nitrogen adsorption conditions. Prior to testing, the FA underwent degassing at 120 °C for 12 h. The surface morphology and elemental mapping of SSBR@FA and SBR/SSBR@FA vulcanizate were conducted by a scanning electron microscopy (SEM, TESCAN MIRA LMS, Brno, Czech Republic) equipped with energy-dispersive spectroscopy. The experimental cross-section of the SBR/SSBR@FA vulcanizate was obtained by fracturing after cryogenic embrittlement in liquid nitrogen. The morphology of the SSBR@FA was observed by using a transmission electron microscopy (TEM; H-800, Hitachi High-Technologies Corp., Tokyo, Japan). The mechanical properties of the vulcanizates were measured through a CMT4104 electronic tensile tester (Shenzhen SANS Test Machine Co., Ltd., Shenzhen, China) in accordance with ASTM D638 standards [24]. with a crosshead speed of 500 mm/min. The FA network was analyzed using an RPA 2000 instrument from (Alpha, CA, USA) at 60 °C. For the SBR/FA compounds, the strain range was 0.28% to 200% at a frequency of 1 Hz. For the SBR/FA vulcanizate, the strain range was 0.28% to 41.99% at a frequency of 10 Hz. To elucidate the viscoelastic properties of the SBR/FA vulcanizate, a VA3000 DMA (Metravib Corporation, Paris, France) was employed at 10 Hz in tension mode, heating at 3 °C/min from −60 to 90 °C. The strain amplitude of the test was 0.1%. The thermal conduction of the SBR/FA vulcanizate was assessed by the Hot Disk method TPS2500S

https://doi.org/10.3390/polym18030348

(Hot Disk, Gothenburg, Sweden). The flame-retardant property was evaluated according to ISO4589 [25] via a JF-3 oxygen index apparatus (Zhide Innovation Instrument Equipment Co., Ltd., Beijing, China).

3. Results and Discussion

3.1. Synthesis of the Functionalized SSBRs

To verify the click chemistry reaction between either MPA or MUA and SSBR, Figure 1 illustrates the FTIR spectra of pure SSBR and modified SSBR. It can be observed clearly that the peaks at 1709 cm^{-1} in SSBR-*g*-MPA and 1698 cm^{-1} in SSBR-*g*-MUA were assigned to the stretching vibrations of carboxyl moieties in hydrogen-bonded acid dimmer states, respectively [10,26]. The alkyl chain length of MUA was longer, and the carboxyl groups were positioned farther from the main chain of SSBR, thereby reducing the number of carboxyl groups embedded within the rubber matrix. This increased the probability of hydrogen–bonding and imposed greater constraints on the carboxyl groups. Compared with SSBR-*g*-MPA, the carboxyl groups' vibrational absorption peak in SSBR-*g*-MUA exhibited a red shift of 11 cm^{-1} due to these structural differences.

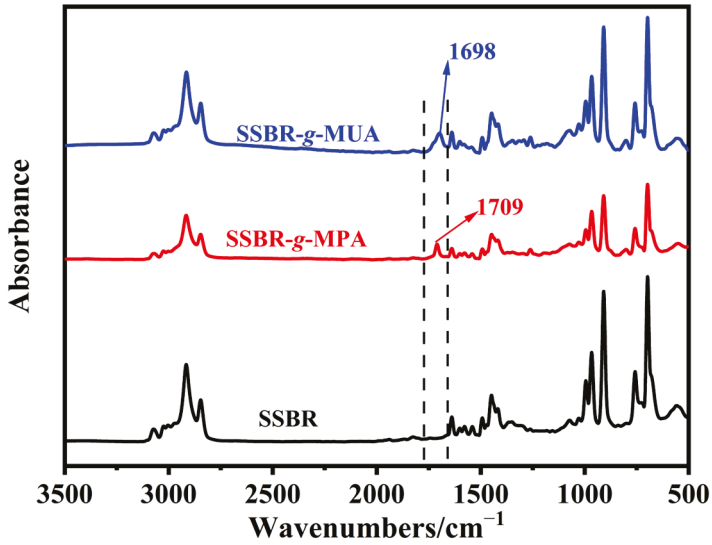

Figure 1. FTIR spectra of SSBR-*g*-MUA, SSBR-*g*-MPA, and SSBR.

Figure 2 displays the ^1H NMR result of rubber in this work. It should be noted that thiol-ene click chemistry predominantly occurred between 1,2-polybutadiene units (1,2-PB) and thiols [22,23,27–29]. Consequently, the content of 1,2-PB should decrease if the thiol-ene click occurred. According to the ^1H NMR spectra, a new characteristic peak at 2.76–2.88 ppm in SSBR-*g*-MPA was attributed to the methylene protons from -SCH_2CH_2COOH, and a new peak at 2.37–2.41 ppm stemmed from methylene protons (-CH_2COOH) in SSBR-*g*-MUA, respectively [23], which demonstrated that MPA and MUA were successfully grafted onto the SSBR chain. Furthermore, on the basis of the established equations in our previous work [23], the mass fraction of 1,2-PB (relative to PB) in SSBR decreased from 47.9% to 44.9% in SSBR-*g*-MPA and 47.3 in SSBR-*g*-MUA, which means that the grafting percentages of MPA and MUA were 6.3% and 4.7%, respectively.

3.2. FA Modification Through Ball-Milling-Induced Grafting of Carboxyl-SSBR

It is well known that the carboxyl group can undergo a chemical reaction with metal oxides on the surface of FA and form carboxyl–metal bonds [1,7,10,19] under heating conditions. A planetary ball mill generates significant friction and impact forces [30] in the process of grinding. This provides higher energy input and chemical reaction rates [31–33]

in comparison to the thermal-induced chemical reaction, and enables the mechanochemical activation at a lower temperature [34–36]. Therefore, carboxyl-metal chemical reactions are theoretically feasible under ball-milling conditions. Figure 3 presents the modification mechanism of FA.

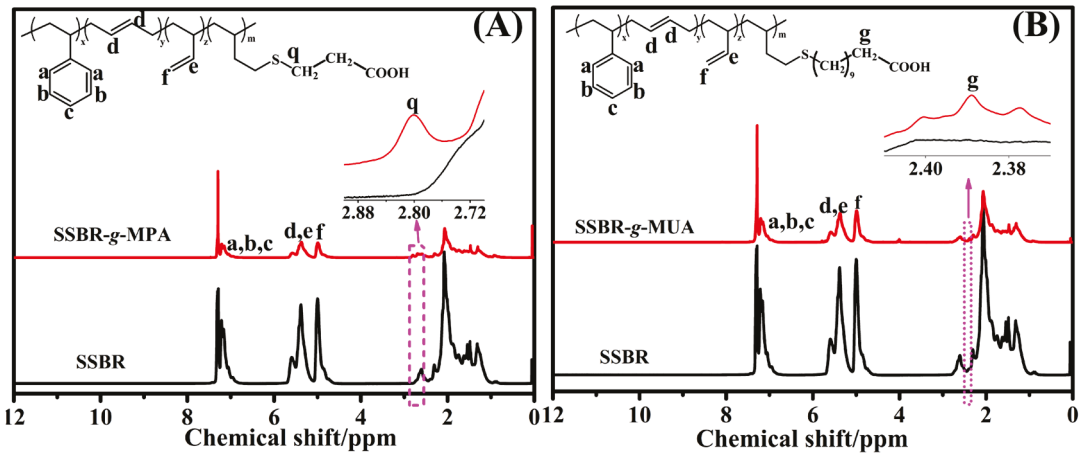

Figure 2. ^{1}H NMR spectra of (**A**) SSBR and SSBR-*g*-MPA and (**B**) SSBR and SSBR-*g*-MUA.

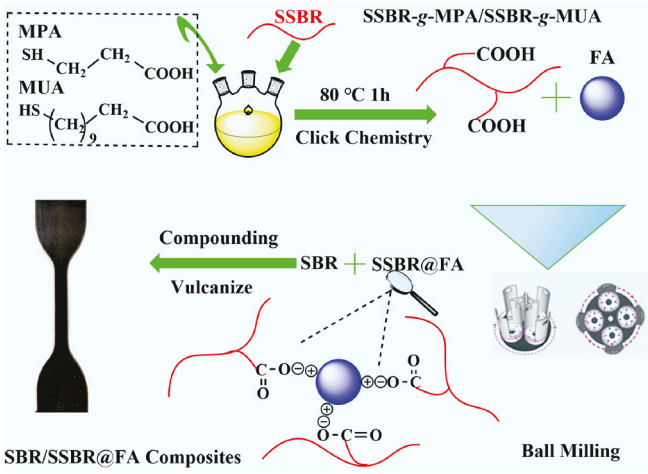

Figure 3. The design schematic of SBR/SSBR@FA composites.

It is reported that infrared spectroscopy exhibits high sensitivity to dipole moment changes in functional groups, making it a key analytical tool for investigating carboxyl-metal chemical reactions [1,7,10,19,26]. Figure 4 presents the corresponding spectrum of the SSBR@FA hybrid filler after extraction. After ball milling with FA, the disappearance of the stretching vibrations of carboxyl groups in hydrogen–bonded acid dimer states of two functionalized SSBRs indicated that the carboxyl groups underwent chemical reactions. The characteristic peaks of Si-O-Si in 3PFA and 3UFA became sharper, and the characteristic peak of Si-O-Si in 3UFA exhibited a slightly red shift (from 1105 cm^{-1} to 1103 cm^{-1}) compared to those of FA. The Si-O-Si groups on the FA surface, interacting with the carboxyl–metal bonding groups, experienced restricted vibrational motion [19,37–39]. In addition, the characteristic peak at 2915 cm^{-1} was attributed to the stretching vibration of methylene groups in SSBR [22]. Notably, this characteristic peak remained observable in the FTIR spectra of the extracted 3PFA and 3UFA samples. In conclusion, under the action of ball milling, the functionalized SSBRs were grafted onto the surface of FA. Similar experiment results also could be found anywhere [22].

https://doi.org/10.3390/polym18030348

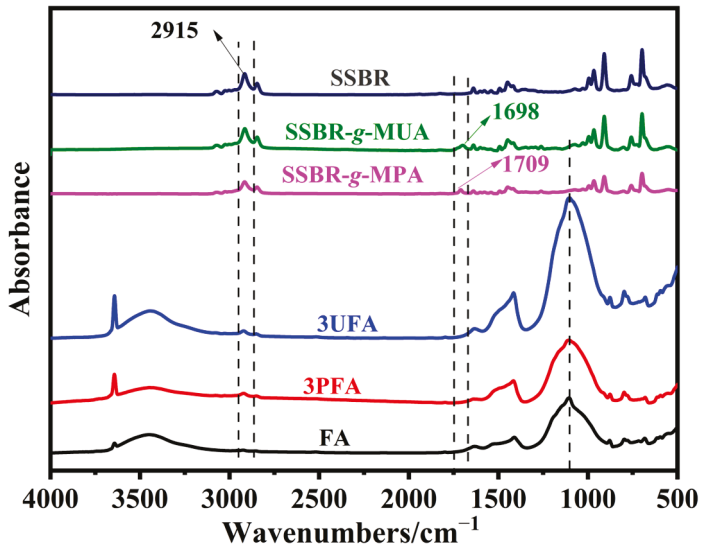

Figure 4. FTIR spectra of SSBR, functionalized SSBR, FA, and SSBR@FA after extraction.

The significant polarity difference between rubber and fillers leads to poor wettability, which not only hinders the dispersion of filler particles but also limits the enhancement of the composite composite's overall performance [10,22,23,40]. The static contact angle measurement was used to investigate the polarity changes in FA. As Figure 5A displays, it is clear that water spread quickly on the raw FA surface with a water contact angle (WCA) of 38.3°, which shows an obvious hydrophilic nature of FA. After the FA was treated with SSBR, the water displayed spherical droplets formed on the modified FA surface with a WCA consistently exceeding 90°. SSBR@FA showed a pronounced hydrophobicity and an obvious change in surface properties. The surface energy of FA was calculated using the Owens–Wendt equation by determining its contact angles with water and diiodomethane. The concrete values of FA, 1PFA, 3PFA, 1UFA, and 3UFA are displayed in Figure 5F. It showed that the surface energy of modified FA was significantly reduced. Compared with the raw FA (60.5 mN/m), the surface energy of 1PFA decreased remarkably by 35.9%. The reduction in surface energy contributed to the improvement of wetting between FA and rubber, thereby enhancing the interfacial interaction of the SSBR@FA hybrid filler with the SBR rubber matrix. To visually demonstrate the hydrophobicity of modified FA, we immersed raw FA, ball-mill-treated FA (BFA) without carboxyl functionalized SSBR, 3PFA, and 3UFA samples in cyclohexane (Figure S1). Initially, all samples were well-dispersed in the cyclohexane and formed a turbid suspension. After ten minutes, the raw FA and BFA gradually settled to the bottom of the container, leaving a transparent supernatant. While the 3PFA and 3UFA remained partially dispersed, maintaining a turbid appearance in the solution.

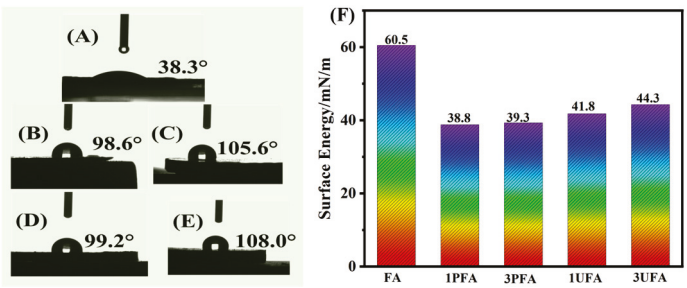

Figure 5. Water contact angle on the surface of (**A**) FA, (**B**) 1PFA, (**C**) 3PFA, (**D**) 1UFA, and (**E**) 3UFA. (**F**) Surface energy values of FA, 1PFA, 3PFA, 1UFA, and 3UFA.

https://doi.org/10.3390/polym18030348

Figure 6 displays the thermogravimetric curves for FA, SSBR@FA, SSBR-*g*-MPA, and SSBR-*g*-MUA. The TGA curve of FA exhibited three weight loss regions. In the initial region (40–210 °C), the weight loss resulted from the removal of the unbonded water evaporation located on the surface [41,42]. The second region (210–450 °C) was assigned to the desorption of hydration water and devolatilization [42]. The final stage (450–780 °C) was due to the decomposition of residual coal in the FA [43]. The functionalized SSBRs were primarily decomposed within the temperature range of 220–490 °C. The TGA curve of SSBR@FA showed a notable weight loss above 300 °C, corresponding to the decomposition of functionalized SSBR [21]. According to further calculations, the grafting percentages of modified SSBR based on FA observed for 1PFA, 3PFA, 1UFA, and 3UFA were 0.2%, 2.1%, 0.7%, and 2.4%, respectively. Even after 72 h of extraction, the SSBR was not entirely removed, confirming that the SSBR was firmly adsorbed onto the FA surface through chemical bonding [44]. Moreover, the grafting efficiency of SSBR-*g*-MUA based on FA was higher than that of SSBR-*g*-MPA.

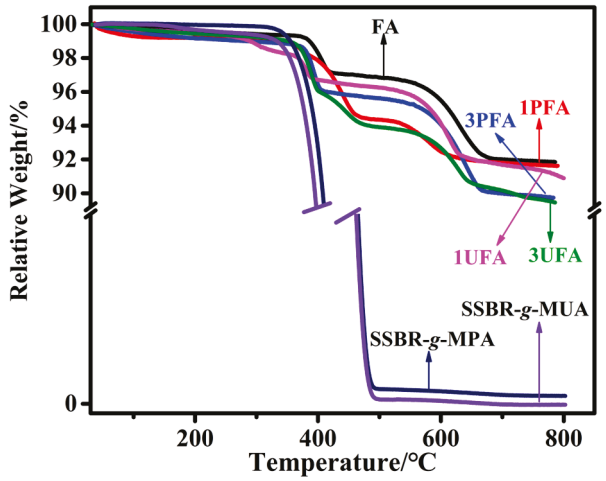

Figure 6. TGA curves of FA, functionalized SSBR, 1PFA, 3PFA, 1UFA, and 3UFA after extraction.

The SSBR molecular chains grafted onto the FA surface can be further confirmed by the chemical composition obtained from EDS. The EDS spectra of 3PFA and FA are shown in Figure 7A and Figure S2, respectively. The percentages of C, O, and S elements in 3PFA were all higher than those in FA, indicating that a SSBR layer was successfully coated on the FA. Furthermore, the SSAs of raw FA and SSBR@FA were determined by the BET method, and the corresponding data are presented in Figure 7B. Since ball milling can reduce FA particle size and change its morphology, the SSA of ball-mill-treated FA (BFA) without carboxyl functionalized SSBR was also measured. After ball milling, the SSA of BFA increased from 3.38 m^2/g to 5.21 m^2/g, representing a 54.1% increase compared to FA. While the SSAs of PFA and UFA were reduced compared to BFA, owing to the SSBR preventing nitrogen from accessing the pore area of FA [22,45,46]. However, the SSAs of SSBR@FA were still higher than those of raw FA. This promoted easier penetration of the rubber matrix into the pores of SSBR@FA and strengthened the interfacial bonding between the SSBR@FA hybrid filler and the rubber matrix. This was in agreement with Liu's work, which reported the surface modification of FA using waste engine oil under mechanical activation [44]. Figure S3 shows the TEM results of 1PFA and 3UFA. It was evident that SSBR was adsorbed on the FA surface, and the SSBR@FA exhibited a core–shell structure, which enhanced the wettability between FA and SBR matrix.

https://doi.org/10.3390/polym18030348

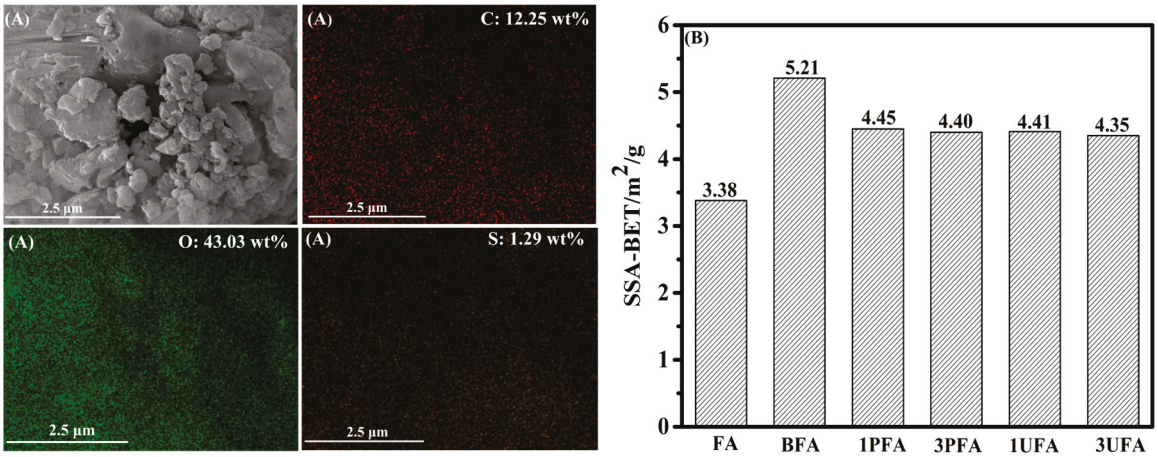

Figure 7. (**A**) SEM and EDS mapping diagrams of 3PFA and (**B**) SSA-BET values of FA, BFA, and SSBR@FA.

3.3. FA-Reinforced SBR Composites

Figure 8 shows the mechanical properties of all vulcanizates. According to the summarized results in Table 2, the addition of raw FA (15 phr) in SBR enhanced the tensile strength from 1.69 MPa to 1.95 MPa in comparison to pure vulcanized SBR, while the elongation at break was reduced from 345% to 284%. When the content of FA increased to 30 phr, the mechanical properties of SBR/FA further decreased, which demonstrated that the raw FA provided no reinforcement.

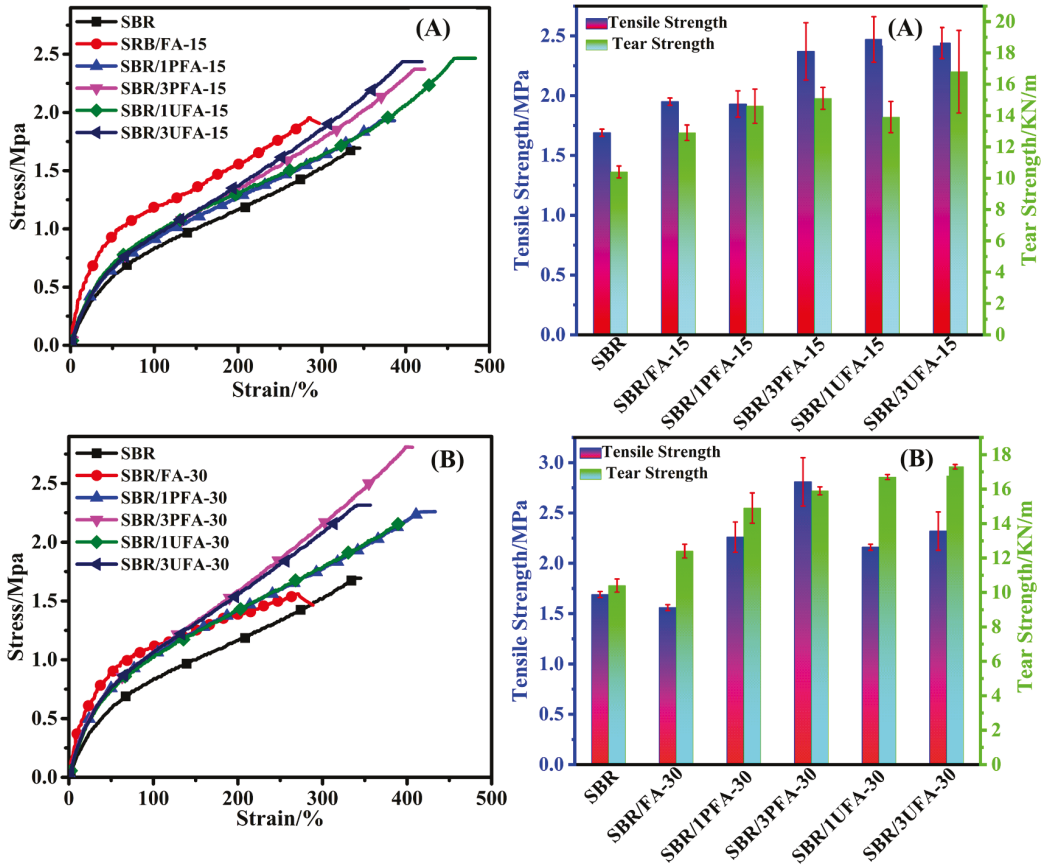

Figure 8. Stress–strain curves and mechanical properties of pure SBR, SBR/FA, and SBR/SSBR@FA vulcanizates with (**A**) 15 phr filler and (**B**) 30 phr filler.

https://doi.org/10.3390/polym18030348

Table 2. Mechanical properties of SBR, SBR/FA, and SBR/SSBR@FA vulcanizates.

Samples	Modulus at 100% Elongation/MPa	Modulus at 300% Elongation/MPa	Elongation at Break/%	Tensile Strength/MPa	Tear Strength/KN/m
SBR	0.84 ± 0.01	1.52 ± 0.04	345 ± 12	1.69 ± 0.03	10.4 ± 0.38
SBR/FA-15	1.19 ± 0.06	–	284 ± 3	1.95 ± 0.03	12.9 ± 0.50
SBR/FA-30	1.12 ± 0.05	–	270 ± 2	1.56 ± 0.03	12.4 ± 0.40
SBR/1PFA-15	0.91 ± 0.01	1.62 ± 0.04	387 ± 29	1.93 ± 0.11	14.6 ± 1.09
SBR/1PFA-30	1.04 ± 0.02	1.78 ± 0.01	433 ± 29	2.26 ± 0.15	14.9 ± 0.88
SBR/3PFA-15	0.95 ± 0.02	1.77 ± 0.04	423 ± 31	2.37 ± 0.24	15.1 ± 0.70
SBR/3PFA-30	1.07 ± 0.02	2.15 ± 0.02	406 ± 33	2.81 ± 0.24	15.9 ± 0.23
SBR/1UFA-15	0.96 ± 0.03	1.63 ± 0.06	483 ± 13	2.47 ± 0.19	13.9 ± 1.00
SBR/1UFA-30	1.02 ± 0.02	1.79 ± 0.11	396 ± 28	2.16 ± 0.03	16.7 ± 0.15
SBR/3UFA-15	0.94 ± 0.04	1.85 ± 0.11	419 ± 7	2.44 ± 0.13	16.8 ± 2.64
SBR/3UFA-30	1.06 ± 0.01	2.08 ± 0.09	357 ± 17	2.32 ± 0.19	17.3 ± 0.13

In contrast, the tensile strength, tear strength, and elongation at break of SBR/SSBR@FA vulcanizates were improved simultaneously, indicating that FA grafted with SSBR molecular chains not only served as a reinforcing filler but also further enhanced the elastic property of rubber-based composites in this system. This was in accordance with other work reporting the effects of filler modification on the properties of elastomeric composites [47]. For instance, the tensile strength, tear strength, and elongation at break of the SBR/3PFA-30 vulcanizate increased by 66.3%, 52.9%, and 17.7%, respectively, compared with those of the SBR vulcanizate. More interestingly, though adding the SSBR@FA into the SBR matrix, the modulus at 100% strain remained virtually unchanged, indicating that the dominant variable in the low-strain region is primarily determined by the changes in the bond angles of the rubber molecular chains [7,19]. Compared to pure SBR, the modulus of SBR/SSBR@FA in the 300% high-strain region increased, and this enhancement became more pronounced with higher SSBR@FA loading. This indicated that the SSBR@FA acted as a reinforcing filler.

The well-known Payne effect demonstrates that the storage modulus (G′) of composites declines as strain increases [48]. The RPA (Rubber Process Analyzer) testing method was employed to investigate the impact of ball-mill grafting modification on the filler-filler network and dispersion of FA fillers. The resulting curves of G′ versus strain are displayed in Figure 9, with the corresponding results presented in Table S2. In this study, the SBR/FA compounds and vulcanizates displayed the highest initial G′ value and most significant Payne effect, suggesting a robust filler–filler network structure formed due to weak SBR-FA interfacial interaction. After chemical grafting of functionalized SSBR onto FA surfaces, the initial G′ values of SBR/SSBR@FA composites decreased with a reduction in the Payne effect. This was because the FA–FA networks were damaged considerably after SSBR was chemically grafted onto the FA surface. For instance, the initial G′ values of the SBR/1UFA-30 compound and vulcanizate decreased by 28.4% and 39.4%, respectively. As depicted in Figure 9, compared to SBR/FA, the G′ values at which filler–filler structures began to break in SBR/SSBR@FA vulcanizates increased. This indicated that the strain dependence of the storage modulus is reduced, which further demonstrated that the FA-FA filler network structure was damaged after grafting modification [23].

The viscoelastic properties of the vulcanized rubber are displayed in Figure 10. The G′ values of vulcanized rubber in the rubbery plateau region were reported to reflect the filler–filler network [22,23,46,49]. A higher storage modulus value in the rubbery plateau indicates a stronger filler–filler network structure and poorer filler dispersion. The G′ values of the SBR/SSBR@FA vulcanizate, either filled with 15 phr SSBR@FA or 30 phr SSBR@FA in the rubbery plateau, are lower than those of the corresponding SBR/FA (Figure 10A). This indicated that the ball-mill-grafted modified FA reduced the filler–filler network structure

https://doi.org/10.3390/polym18030348

and improved the degree of dispersion in the SBR matrix. The results were consistent with the subsequent SEM results (Figure 11). As Figure 10B displays, the tan δ values at Tg (tan δ_{max}) of SBR/SSBR@FA vulcanizates were higher than those of corresponding SBR/FA, implying stronger interactions between SBR and SSBR@FA [1]. This result can be explained as follows: compared with FA, SSBR@FA demonstrated a higher SSA and lower surface energy. These properties increased the contact area and wettability between SSBR@FA and SBR and enhanced their interfacial interaction.

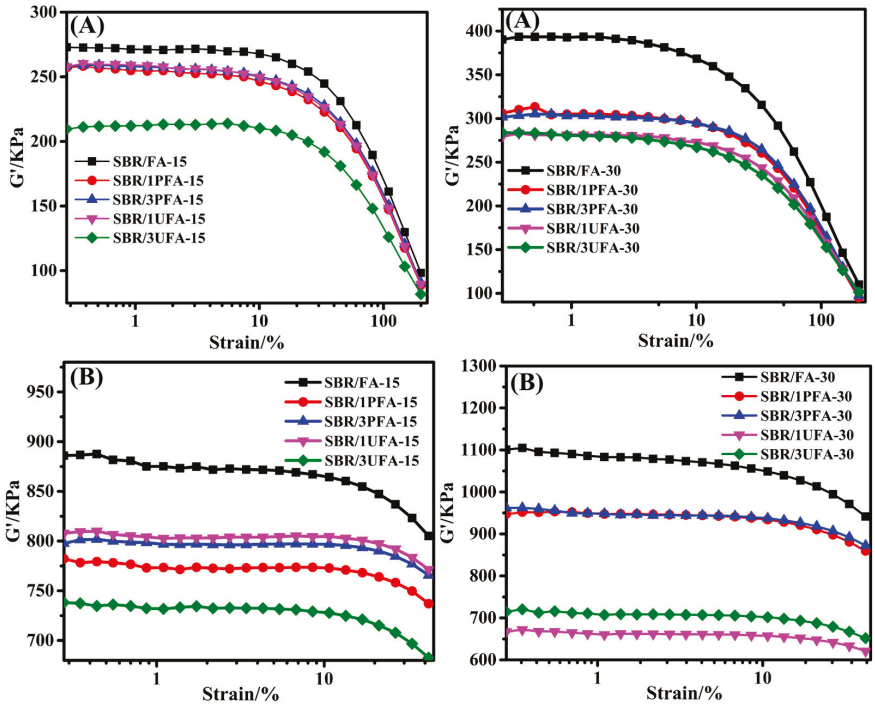

Figure 9. Payne effect study of SBR/FA and SBR/SSBR@FA composites: (**A**) compounds and (**B**) vulcanizates.

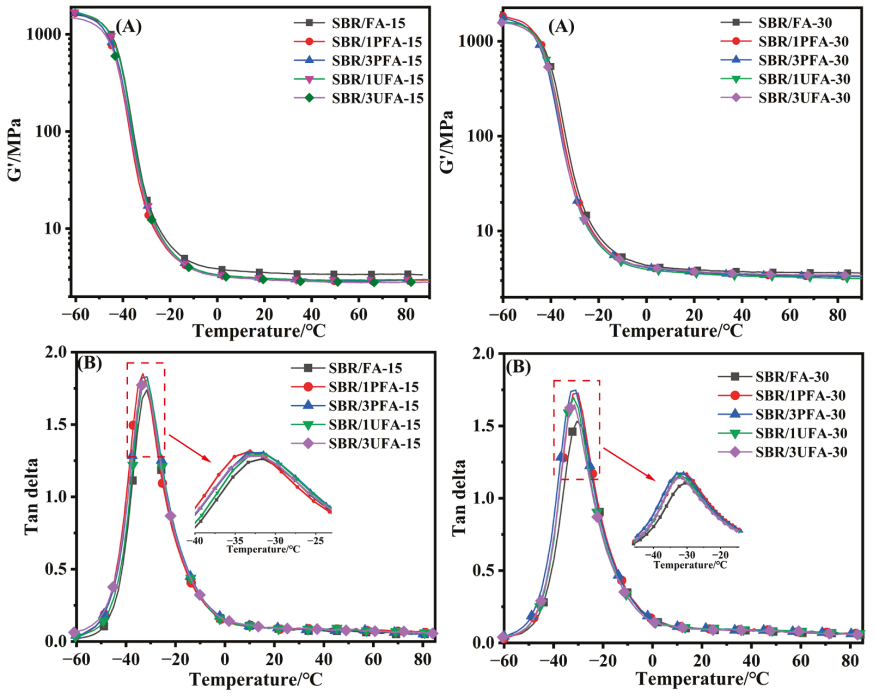

Figure 10. (**A**) G′-temperature curves and (**B**) loss factor–temperature curves of SBR/FA and SBR/SSBR@FA vulcanizates.

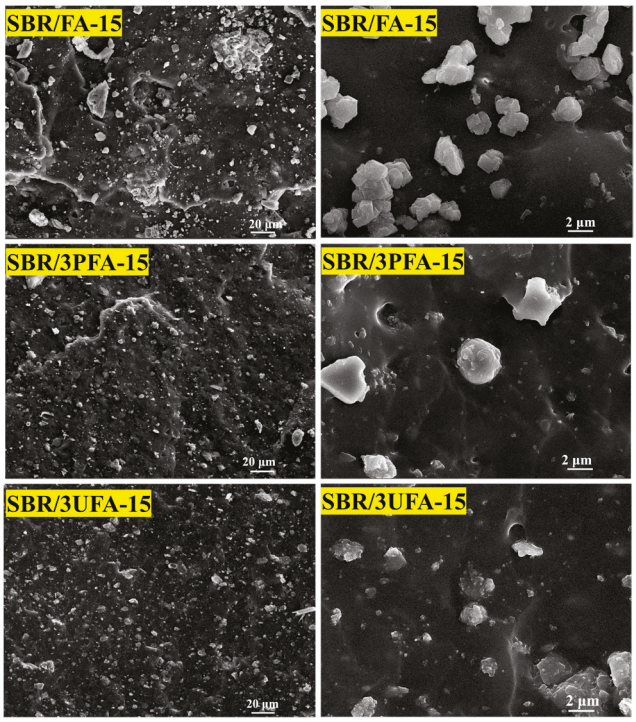

Figure 11. SEM images of SBR/FA-15, SBR/3PFA-15, and SBR/3UFA-15 with different magnifications.

Figure 11 presents the SEM images of SBR/FA-15, SBR/3PFA-15, and SBR/3UFA-15. The SEM micrographs of the cross-section of the SBR/FA composite after liquid nitrogen embrittlement fracture showed a multilamellar structure with concave holes. Furthermore, the micrograph showed obvious FA agglomeration, which had a bad influence on the composite's mechanical properties. The majority of FA were predominantly distributed on the SBR matrix surface, which indicated poor wetting behavior with minimized interfacial contact. The cross-section of the SBR/SSBR@FA composites showed reduced multilamellar structures and concave pits and presented a comparatively featureless fracture surface. Compared to SBR/FA, they showed a clearly distinct morphology. Moreover, SSBR@FA particles were embedded within the SBR matrix, which exhibited reduced interfacial chromatic contrast. This enhanced compatibility was a result of the dual effects of ball milling and SSBR modification, which increased FAs specific surface area and decreased its surface energy at the same time, thereby optimizing interfacial contact area and wettability with the rubber matrix [2,22]. This observation was consistent with the previously presented BET specific surface area and surface energy results.

It is well known that the mechanical properties of rubber composites are decided by a combination of factors, which include the filler's morphology and structure, the interfacial adhesion between rubber and filler, as well as the chemical crosslinking and confinement effects [47,50–53]. In this study, both ball milling and grafting can influence the aforementioned factors. Firstly, the intense friction and impact forces that were generated during the grinding process roughened the FA surface and increased its specific surface area. This increased in the contact area and mechanical adhesion between FA and the SBR matrix [47]. Secondly, the SSBR molecular chains grafted onto the FA surface through solution mechanochemistry and formed a rubber-constrained layer around the FA particles [10]. Also, grafted SSBR acted as a bridge between SBR and FA and further enhanced the interfacial interaction between them. Thirdly, the microscopic network structure formed by physical entanglement between grafted SSBR and SBR matrix enhanced constraint and improved the mechanical properties [1,7,10,19]. When the SBR/FA composite was

subjected to external force, stress spread along the macromolecular chains of the rubber to prevent stress concentration. Due to the increased contact area between SSBR@FA and the SBR matrix [2,20], the interfacial interaction was enhanced. As a result, the probability of SSBR@FA particle de-bondment at the interface was reduced. This made the transfer of external forces through the interface [22,54] more efficient and extended the propagation paths of tear cracks [22,49]. Thus, SBR/SSBR@FA could withstand greater external forces and exhibited improved mechanical properties.

The thermal conductivity and flame-retardant properties of SBR/FA and SBR/SSBR@FA composites were investigated by measuring the thermal conductivity and limiting oxygen index (LOI). The corresponding data are provided in Figure 12 and Table S3. Compared with pure SBR, the thermal conductivity values of SBR/3PFA-15, SBR/3PFA-30, SBR/3UFA-15, and SBR/3UFA-30 increased by 8.9%, 18.4%, 6.5%, and 16.7%, respectively. Meanwhile, the LOI values of SBR/3PFA-15, SBR/3PFA-30, SBR/3UFA-15, and SBR/3UFA-30 increased by 8.6%, 11.1%, 10.1%, and 13.6%, respectively. This enhancement can be attributed to the improved dispersion of FA in composites achieved through ball-mill graft modification, which effectively leveraged the heat-conduction [55,56] and flame-retardant effects of Al_2O_3 and SiO_2 in FA. Additionally, the increased SSA of SSBR@FA facilitated the distribution of CO2 generated during combustion within the pores on the surface of the FA, which created an oxygen barrier effect and further improved the flame-retardancy.

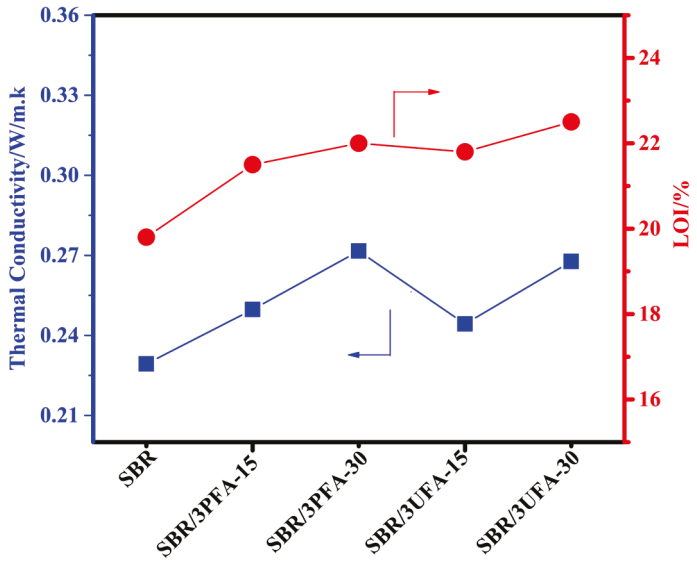

Figure 12. Thermal conductivity and LOI of SBR/FA and SBR/SSBR@FA vulcanizates.

4. Conclusions

The mechanochemical activation obtained through ball milling facilitated an in situ carboxylate reaction between carboxyl functional groups in SSBR and metal oxides on the FA surface. The results of FTIR confirmed the successful grafting of SSBR-*g*-MPA and SSBR-*g*-MUA onto FA, with maximum grafting percentages of 2.1% and 2.4%, respectively. Under the combined effects of ball milling and grafting, the modified FA exhibited hydrophobicity, an increase in specific surface area, and a reduction in surface energy. The SSBR@FA exhibited enhanced wettability with the SBR matrix, as confirmed by SEM results, as a result of the dual role of SSBR-*g*-MPA/SSBR-*g*-MUA, which served as both a dispersant and rubber matrix. With the enhanced interfacial interaction and a rubber-constrained layer surrounding the FA particles, external forces can be transferred at the interface more efficiently. As a result, the mechanical properties of the composites were enhanced. Even when 30 phr of SSBR@FA was added, the tensile strength, tear strength, and elongation

at break increased by 66.3%, 52.9%, and 17.7%, respectively, compared with those of pure SBR vulcanizate. The incorporation of SSBR@FA also led to an enhancement in both the thermal conductivity and flame resistance of the vulcanizates. For example, compared with those of pure SBR vulcanizate, the thermal conductivity and LOI values of SBR/3PFA-30 vulcanizate increased by 18.4% and 11.1%, respectively. This study is expected to offer significant insights for the widespread adoption of FA while mitigating environmental pollution simultaneously.

Supplementary Materials: The following supporting information can be downloaded at: https://www.mdpi.com/article/10.3390/polym18030348/s1, Figure S1. The dispersion of FA, BFA, 3PFA, and 3UFA in cyclohexane; Figure S2. SEM and EDS mapping diagrams of FA; Figure S3. TEM images of 1PFA and 3UFA; Table S1. The main chemical composition of FA; Table S2. Payne effect in SBR/FA and SBR/SSBR@FA composites; Table S3. Thermal conductivity and flame-retardant properties of SBR and SBR/SSBR@FA composites.

Author Contributions: Conceptualization, W.G.; Methodology, W.G. and Z.H.; Writing—original draft, W.G.; Writing-reviewing and editing, W.G., Z.H. and X.W.; Data curation, W.G.; Formal analysis, W.G., J.Z., W.Q., C.S., G.L., C.F. and X.Z. Funding acquisition, W.G. and Z.H. Investigation, W.G., J.Z., W.Q., C.F. and X.Z. Resources, W.G. and Z.H. All authors have read and agreed to the published version of the manuscript.

Funding: This work was supported by the Shandong Provincial Natural Science Foundation (ZR2022QE227), Qingchuang Science and Technology Plan of Shandong Province (2023KJ267), and Doctoral Foundation of Dezhou University (2019xjrc310).

Institutional Review Board Statement: Not applicable.

Data Availability Statement: The original contributions presented in this study are included in the article/Supplementary Materials. Further inquiries can be directed to the corresponding authors.

Conflicts of Interest: The authors declare no conflicts of interest.

References

1. Yang, S.; Tian, J.; Bian, X.; Wu, Y. High performance NBR/fly ash composites prepared by an environment-friendly method. *Compos. Sci. Technol.* **2020**, *186*, 107909. [CrossRef]
2. Ren, X.J.; Sancaktar, E. Use of fly ash as eco-friendly filler in synthetic rubber for tire applications. *J. Clean. Prod.* **2019**, *206*, 374–382. [CrossRef]
3. Oleksik, M.; Dobrotă, D.; Sabin, D.C.; Dumitrașcu, O.; Petrașcu, R. Advanced use of waste rubber and fly ash to ensure an efficient circular economy. *Ain Shams Eng. J.* **2024**, *15*, 102264. [CrossRef]
4. Das, D.; Rout, P.K. A review of coal fly ash utilization to save the environment. *Water Air Soil Pollut.* **2023**, *234*, 128. [CrossRef]
5. Yan, P.; Qin, T.; Li, T.; Jiang, S.; Liu, S. High-performance fly ash-reinforced engineering composites with thermosetting polyamine as matrix. *Polym. Compos.* **2025**, *46*, S413–S429. [CrossRef]
6. Navaratnarajah, S. Predicting compressive strength in cement mortar: The impact of fly ash composition through machine learning. *Sustainable Chem. Pharm.* **2025**, *43*, 101915.
7. Ma, C.; Wu, Y.; Zheng, H.; Liang, Y.; He, Z.; Liu, J.; Cai, W.; Liu, X.; Yang, S. Preparation of nitrile butadiene rubber/fly ash composites by designing a surficial immobile layer. *Polym. Compos.* **2022**, *43*, 7817–7825. [CrossRef]
8. Kuźnia, M. A review of coal fly ash utilization: Environmental, energy, and material assessment. *Energies* **2024**, *18*, 52. [CrossRef]
9. Saowapark, T.; Sombatsompop, N.; Sirisinha, C. Viscoelastic properties of fly ashfilled natural rubber compounds: Effect of fly ash loading. *J. Appl. Polym. Sci.* **2009**, *112*, 2552–2558. [CrossRef]
10. Yang, S.; Liang, P.; Hua, K.; Peng, X.; Zhou, Y.; Cai, Z. Preparation of carboxylated nitrile butadiene rubber/fly ash composites by in-situ carboxylate reaction. *Compos. Sci. Technol.* **2018**, *167*, 294–300. [CrossRef]
11. Krainoi, A.; Sripornsawat, B.; Toh-ae, P.; Kitisavetjit, W.; Pittayavinai, P.; Tangchirapat, W.; Kalkornsurapranee, E.; Johns, J.; Nakaramontri, Y. Utilization of high and low calcium oxide fly ashes as the alternative fillers for natural rubber composites: A waste to wealth approach. *Ind. Crops Prod.* **2022**, *188*, 115589. [CrossRef]
12. Bordoloi, S.; Devney, E.P.; Polyak, P.; Cornish, K.; Sharma, B.K.; Rajagopalan, N.; Puskas, J.E.; Baroi, C. Reducing the carbon footprint of Hevea rubber carbon composites using surface-modified fly ash. *Ind. Crops Prod.* **2024**, *220*, 119190. [CrossRef]

13. Sombatsompop, N.; Thongsang, S.; Markpin, T.; Wimolmala, E. Fly ash particles and precipitated silica as fillers in rubbers. I. Untreated fillers in natural rubber and styrene–butadiene rubber compounds. *J. Appl. Polym. Sci.* **2004**, *93*, 2119–2130. [CrossRef]
14. Thongsang, S.; Sombatsompop, N.; Ansarifar, A. Effect of fly ash silica and precipitated silica fillers on the viscosity, cure, and viscoelastic properties of natural rubber. *Polym. Adv. Technol.* **2008**, *19*, 1296–1304. [CrossRef]
15. Sombatsompop, N.; Wimolmala, E.; Markpin, T. Fly-ash particles and precipitated silica as fillers in rubbers. II. Effects of silica content and Si69-treatment in natural rubber/styrene-butadiene rubber vulcanizates. *J. Appl. Polym. Sci.* **2007**, *104*, 3396–3405. [CrossRef]
16. Maan, A.; Niyogi, U.; Singh, A.; Mehra, D.; Rattan, S. Studies on effect of a silane coupling agent (TESPT) on the properties of fly ash-natural rubber composite. *J. Polym. Mater.* **2015**, *32*, 45–55.
17. Garde, K.; McGill, W.; Woolard, C. Surface modification of fly ash-characterisation and evaluation as reinforcing filler in polyisoprene. *Plast. Rubber Compos.* **1999**, *28*, 1–10. [CrossRef]
18. Thongsang, S.; Sombatsompop, N. Effect of NaOH and Si69 treatments on the properties of fly ash/natural rubber composites. *Polym. Compos.* **2006**, *27*, 30–40. [CrossRef]
19. Yang, S.; Liang, P.; Peng, X.; Zhou, Y.; Hua, K.; Wu, W.; Cai, Z. Improvement in mechanical properties of SBR/fly ash composites by in-situ grafting-neutralization reaction. *Chem. Eng. J.* **2018**, *354*, 849–855. [CrossRef]
20. Kim, Y.; Hwang, S.; Choi, J.; Lee, J.; Yu, K.; Baeck, S.H.; Shim, S.E.; Qian, Y. Valorization of fly ash as a harmless flame retardant via carbonation treatment for enhanced fire-proofing performance and mechanical properties of silicone composites. *J. Hazard. Mater.* **2021**, *404*, 124202. [CrossRef] [PubMed]
21. Zhao, L.; Zaborowski, E.; Bordoloi, S.; Rajagopalan, N.; Sharma, B.K.; Baroi, C.; Xing, W.; Zhang, L. Characterization of novel polysulfide polymer coated fly ash and its application in mitigating diffusion of contaminants. *Environ. Pollut.* **2024**, *347*, 123706. [CrossRef] [PubMed]
22. Gao, W.; Lu, J.; Song, W.; Hu, J.; Han, B. Solution mechanochemical approach for preparing high-dispersion SiO_2-*g*-SSBR and the performance of modified silica/SSBR composites. *Ind. Eng. Chem. Res.* **2019**, *58*, 7146–7155. [CrossRef]
23. Gao, W.; Lu, J.; Song, W.; Hu, J.; Han, B. Interfacial interaction modes construction of various functional SSBR-silica towards high filler dispersion and excellent composites performances. *RSC Adv.* **2019**, *9*, 18888–18897. [CrossRef]
24. *ASTM D638*; Standard Test Method For Tensile Properties of Plastics. ASTM International: West Conshohocken, PA, USA, 2022.
25. *ISO 4589-2*; Plastics-Determination of Burning Behaviour by Oxygen Inde-Part 2: Room-Temperature Test. International Organization for Standardization: Geneva, Switzerland, 2017.
26. Li, L.; Ji, H.; Yang, H.; Sun, C.; Wang, R.; Hu, G.; Zhang, L. Dynamic evolution of ionic bonds and performance characteristics in bio-based dibutyl itaconate elastomers. *Polymer* **2025**, *334*, 128687. [CrossRef]
27. Qu, L.; Wang, L.; Xie, X.; Yu, G.; Bu, S. Contribution of silica-rubber interactions on the viscoelastic behaviors of modified solution polymerized styrene butadiene rubbers (M-S-SBRs) filled with silica. *RSC Adv.* **2014**, *4*, 64354–64363. [CrossRef]
28. Lotti, L.; Coiai, S.; Ciardelli, F.; Galimberti, M.; Passaglia, E. Thiol-ene radical addition of L-cysteine derivatives to low molecular weight polybutadiene. *Macromol. Chem. Phys.* **2009**, *210*, 1471–1483. [CrossRef]
29. Schapman, F.; Couvercelle, J.P.; Bunel, C. Low molar mass polybutadiene made crosslinkable by silane moities introduced via addition of thiol to double bond: 3. synthesis and kinetic study. *Polymer* **1998**, *39*, 4955–4962. [CrossRef]
30. Leonardi, M.; Villacampa, M.; Menendez, J.C. Multicomponent mechanochemical synthesis. *Chem. Sci.* **2018**, *9*, 2042–2064. [CrossRef] [PubMed]
31. Tullberg, E.; Peters, D.; Frejd, T. The heck reaction under ball-milling conditions. *J. Organomet. Chem.* **2004**, *689*, 3778–3781. [CrossRef]
32. Watanabe, H.; Hiraoka, R.; Senna, M. A diels-alder reaction catalyzed by eutectic complexes autogenously formed from solid state phenols and quinines. *Tetrahedron Lett.* **2006**, *47*, 4481–4484. [CrossRef]
33. Stolle, A.; Szuppa, T.; Leonhardt, S.E.S.; Ondruschka, B. Ball milling in organic synthesis: Solutions and challenges. *Chem. Soc. Rev.* **2011**, *40*, 2317–2329. [CrossRef]
34. Ye, G.; Troczynski, T. Mechanochemical activation-assisted low-temperature synthesis of $CaZrO_3$. *J. Am. Ceram. Soc.* **2007**, *90*, 287–290. [CrossRef]
35. Mergen, A. Mechanochemical synthesis of $MgTa_2O_6$ ceramic. *Ceram. Int.* **2009**, *35*, 1151–1157. [CrossRef]
36. James, S.L.; Adams, C.J.; Bolm, C.; Braga, D.; Collier, P.; Friscic, T.; Grepioni, F.; Harris, K.D.M.; Hyett, G.; Jones, W.; et al. Mechanochemistry: Opportunities for new and cleaner synthesis. *Chem. Soc. Rev.* **2012**, *41*, 413–447. [CrossRef] [PubMed]
37. Yang, S.; Liu, L.; Jia, Z.; Jia, D.; Luo, Y. Structure and mechanical properties of rareearth complex La-GDTC modified silica/SBR composites. *Polymer* **2011**, *52*, 2701–2710. [CrossRef]
38. Yang, S.; Liu, L.; Jia, Z.; Jia, D.; Luo, Y. Study on the curing properties of SBR/LaGDTC/SiO_2 composites. *J. Rare Earth* **2011**, *29*, 444–453. [CrossRef]
39. Yang, S.; Liu, L.; Jia, Z.; Jia, D.; Luo, Y.; Liu, Y. Studies on the influence of lanthanum glutamic dithiocarbamate on the interfacial reinforncement of SBR/SiO_2 composites by swelling equilibrium test. *Acta Polym. Sin.* **2011**, *7*, 709–717. [CrossRef]

40. Zhang, Y.; Gao, J.; Shen, P.; Zhu, K.; Li, J.; Wang, S.; Wu, Y.; Jin, H. Synthesizing ternary filler of multi-walled carbon nanotubes/silica/carbon for heightening fluororubber's mechanical performance. *Mater. Today Commun.* **2024**, *41*, 110461. [CrossRef]
41. Maryam, A.E.; Mohammad, K.H.; Khaled, Y.; Farah, E.; Hanin, M.; Mostafa, S.; Mohammad, I. Novel surface-treatment for bottom ash from municipal solid waste incineration to reduce the heavy metals leachability for a sustainable environment. *J. Environ. Manag.* **2023**, *347*, 119105. [CrossRef]
42. Sadiya, M.; Zaheer, A.; Rizwan, A.; Umair, A.; Sana, N.; Muhammad, A.; Bello, M.M. Surfactant modified waste ash for the removal of chloro and nitro group substituted benzene from wastewater. *Water Sci. Technol.* **2022**, *86*, 1969–1980. [CrossRef]
43. Aslam, Z. Carbonaceous adsorbent from waste oil fly ash: Surface treatments and hydrogen sulfide adsorption potential. *Chem. Pap.* **2022**, *76*, 5145–5158. [CrossRef]
44. Liu, Q.; Chen, S.; He, X.; Su, Y.; Zeng, J.; Zhu, Y.; Pan, Y.; Zhang, B.; Xu, H.; Wu, Y. Surface modification of fly ash by waste engine oil under mechanical activation enhanced the sustainable service life of asphalt. *J. Clean. Prod.* **2023**, *404*, 136785. [CrossRef]
45. Raut, P.; Swanson, N.; Kulkarni, A.; Pugh, C.; Jana, S.C. Exploiting arene-perfluoroarene interactions for dispersion of carbon black in rubber compounds. *Polymer* **2018**, *148*, 247–258. [CrossRef]
46. Li, Y.; Han, B.; Liu, L.; Zhang, F.; Zhang, L.; Wen, S.; Lu, Y.; Yang, H.; Shen, J. Surface modification of silica by two-step method and properties of solution styrene butadiene rubber (SSBR) nanocomposites filled with modified silica. *Compos. Sci. Technol.* **2013**, *88*, 69–75. [CrossRef]
47. Janík, R.; Labaj, I.; Skalková, P.; Ďurišová, S.; Moricová, K. Effects of filler modification on the properties of elastomeric composites. *Manuf. Technol.* **2024**, *24*, 365–377. [CrossRef]
48. Payne, A.R. The dynamic properties of carbon black-loaded natural rubber vulcanizates. Part I. *J. Appl. Polym. Sci.* **1962**, *6*, 57–63. [CrossRef]
49. Liu, X.; Zhao, S.; Zhang, X.; Li, X.; Bai, Y. Preparation, structure, and properties of solution-polymerized styrene-butadiene rubber with functionalized end-groups and its silica-filled composites. *Polymer* **2014**, *55*, 1964–1976. [CrossRef]
50. Zhong, B.; Jia, Z.; Hu, D.; Luo, Y.; Guo, B.; Jia, D. Surface modification of halloysite nanotubes by vulcanization accelerator and properties of styrene-butadiene rubber nanocomposites with modified halloysite nanotubes. *Appl. Surf. Sci.* **2016**, *366*, 193–201. [CrossRef]
51. Yang, S.; Wu, W.; Jiao, Y.; Cai, Z.; Fan, H. Preparation of NBR/Tannic acid composites by assembling a weak IPN structure. *Compos. Sci. Technol.* **2017**, *153*, 40–47. [CrossRef]
52. Yang, S.; Fan, H.; Jiao, Y.; Cai, Z.; Zhang, P.; Li, Y. Improvement in mechanical properties of NBR/$LiClO_4$/POSS nanocomposites by constructing a novel network structure. *Compos. Sci. Technol.* **2017**, *138*, 161–168. [CrossRef]
53. Qu, L.; Huang, G.; Zhang, P.; Nie, Y.; Weng, G.; Wu, J. Synergistic reinforcement of nanoclay and carbon black in natural rubber. *Polym. Int.* **2010**, *59*, 1397–1402. [CrossRef]
54. Godard, P.; Bomal, Y.; Biebuyck, J.J. Influence of interactions on the tensile behaviour of polystyrene filled with calcium carbonate. *J. Mater. Sci.* **1993**, *28*, 6605–6610. [CrossRef]
55. Oktaee, A.; Klier, K.; Giesen, R.U.; Heim, H.P. Thermal conductivity of silicone rubber composites: Effects of ceramic fillers, pressure, and temperature. *Adv. Eng. Mater.* **2025**, *27*, 2500444. [CrossRef]
56. Ji, X.; Lu, Z.; Wang, J.; Ye, N.; Zhang, H.; Zhou, L.; Li, J.; Lu, Y. Construction of micro-nano hybrid structure based on carbon nanotube whisker and alumina for thermally conductive yet electrically insulating silicone rubber composites. *Compos. Sci. Technol.* **2024**, *249*, 110495. [CrossRef]

polymers

MDPI

Article

Influence of Pretreatments on the Conductivity of Flexographic Printed Electronics on Flexible Substrates

Rocío Silvestre [1], Raúl Llinares Llopis [2,*], Cristian Ariel Olguín Pinatti [3], Josué Ferri [4], Ignacio Montava [5] and Eva Bou-Belda [5]

[1] Asociación de Investigación de la Industria Textil y Cosmética (AITEX), 03801 Alcoy, Spain; rsilvestre@aitex.es
[2] Departamento de Comunicaciones, Universitat Politècnica de València, 03801 Alcoy, Spain
[3] Instituto Interuniversitario de Investigación de Reconocimiento Molecular y Desarrollo Tecnológico (IDM), Universitat Politècnica de València, 46022 Valencia, Spain; criolpi@upv.es
[4] Centro Integrado Público de Formación Profesional BATOI, 03802 Alcoi, Spain; j.ferripascual@edu.gva.es
[5] Department of Textile and Paper Engineering, Universitat Politècnica de València, Plaza Ferrándiz y Carbonell s/n, 03801 Alcoy, Spain; imontava@upv.es (I.M.); evbobel@upvnet.upv.es (E.B.-B.)
* Correspondence: rllinares@dcom.upv.es

Abstract

The development of electronic textiles (e-textiles) has advanced significantly thanks to the integration of printing technologies such as flexography, which enables the efficient and reproducible production of conductive circuits on fabrics. This study evaluates the impact of different surface pretreatments (hydrophobic and oleophobic) on the electrical conductivity of flexographically printed circuits on a variety of polyester textile substrates. Key parameters such as grammage, fabric type and surface uniformity are analyzed using stereomicroscopy and profilometry techniques to characterize conductive ink distribution. The results demonstrate that oleophobic pretreatment is more effective at reducing the resulting electrical resistance, promoting better ink adhesion and distribution. Among the fabrics with the best results, those with a more regular and compact structure, such as 15 thread/cm and 666.7 dtex polyester taffeta, show homogeneous ink coverage and the lowest electrical resistance ($\sim$0.5 Ω/cm) compared to more irregular fabrics with discontinuities and higher resistance. The results show that uniformity in ink distribution, assessed by profilometry and color analysis, directly correlates with low electrical resistance. It can be concluded that the combination of a regular and compact textile structure, an adequate surface pretreatment, and a printing direction of the circuit pattern aligned with the weft permits optimizing the conductivity and quality of e-textiles produced by flexography.

Keywords: flexography; e-textiles; wearables; printed-electronics; textiles; electronic textiles

1. Introduction

Electronic textiles (e-textiles) have become a cornerstone in the development of wearable technologies, enabling garments to integrate sensing, communication, and energy functionalities in a seamless and unobtrusive manner. From early implementations using conductive threads for basic functions such as thermal regulation [1,2], physiological monitoring [3,4], pressure sensing [5] or antenna integration [6,7], the field has evolved toward more sophisticated and integrated systems. These initial approaches, while effective for proof-of-concept and low-complexity applications, presented limitations in terms of

circuit resolution, reproducibility, and scalability, especially when considering industrial production and long-term durability.

The need for more versatile, scalable, and precise fabrication methods has led to the adoption of printed electronics as a key enabling technology for e-textiles. Printed electronics allow for the direct deposition of conductive inks onto flexible substrates, offering a lightweight, low-profile alternative to traditional wiring and component integration. Their compatibility with textile substrates has opened new possibilities for integrating sensors [3,8], displays [9,10], and energy systems [11] directly into garments, supporting applications in health monitoring [12,13], sports performance [14], and interactive interfaces [15,16].

A wide range of printing techniques has been explored for this purpose, each with distinct advantages and constraints. Conventional methods such as screen printing and inkjet printing are widely used due to their accessibility and compatibility with various ink formulations. Screen printing is valued for its simplicity and ability to deposit thick ink layers, making it ideal for robust conductive paths [17–19]. It has been successfully applied in textile sensors and capacitive interfaces [20]. The process involves forcing ink through a mesh stencil onto the substrate, which allows for high ink volume transfer but limits resolution. In textile applications, screen printing benefits from its ability to accommodate the rough and porous nature of fabrics, although it requires careful control of ink viscosity and curing conditions. Inkjet printing, on the other hand, offers high precision and material efficiency [21,22], enabling fine patterning with minimal ink waste. However, it demands smooth surfaces and is sensitive to ink viscosity and surface energy, often necessitating substrate pretreatments or modifications [23,24].

Other printing techniques, such as aerosol jet printing, 3D printing, and transfer printing, offer additional capabilities but are generally less suited for large-scale textile production. Aerosol jet printing enables deposition on non-planar surfaces with fine resolution [25], though it is costly and technically demanding. Three-dimensional printing allows for multilayered and customized structures [26,27], and its ability to print directly onto curved or textured fabrics makes it attractive for specialized applications. Nevertheless, its slower speed, limited ink compatibility, and higher equipment costs restrict its use in industrial contexts. Transfer-based methods, including thermal transfer printing, are useful for integrating pre-fabricated circuits onto textiles [28]. These techniques facilitate the inclusion of microchips and passive components but often involve multiple steps and may compromise durability under mechanical stress or washing.

Flexographic printing is a particularly promising technique for the industrial-scale production of printed electronics on textiles. Originally developed for packaging, flexography offers high-speed processing, fine pattern resolution, and controlled ink deposition [29–31]. Its compatibility with roll-to-roll manufacturing and flexible substrates makes it particularly attractive for e-textile applications. Unlike other methods, flexography balances throughput and precision, making it suitable for large-scale production where consistency and cost-effectiveness are essential. Flexographic printing operates by transferring ink from an anilox roller to a flexible photopolymer plate, which then prints the pattern onto the substrate. The anilox roller plays a central role in controlling the ink volume: its engraved cells determine how much ink is transferred, and its geometry affects the uniformity and thickness of the printed layer. In textile applications, where surface roughness and porosity vary significantly, selecting the appropriate anilox configuration is crucial to achieving continuous and conductive traces.

Compared to other printing techniques, flexography offers a unique balance between resolution, throughput, and compatibility with textile substrates. Screen printing achieves very low sheet resistance (<0.5 Ω/sq) and excellent durability (up to 50 washing cycles) but

requires thick ink layers [32,33] and is constrained by its resolution (typically 100–500 μm), making scalability moderate [34]. Inkjet printing provides fine patterns (50–100 μm) but usually yields higher resistance (10–50 Ω/sq), reduced durability (5–10 washing cycles), and limited scalability due to slow processing and substrate preparation requirements [35–38]. Aerosol jet printing enables features below 50 μm with resistances in the 1–10 Ω/sq range, but its high cost and low throughput restrict widespread industrial adoption [25,39]. Three-dimensional (3D) printing allows multilayer structures and good mechanical durability but typically exhibits high linear resistances above 10 Ω/cm and suffers from very low scalability because of slow deposition rates [40,41]. In contrast, flexography combines moderate resolution (≈100–150 μm) with low linear resistance (≈0.5–2 Ω/cm under optimized conditions), high reproducibility, and compatibility with roll-to-roll manufacturing, achieving durability above 30 washing cycles when combined with appropriate pretreatments [15,42].

Despite its advantages, applying flexography to textiles presents challenges due to the fibrous and heterogeneous nature of fabrics, which can disrupt ink transfer and compromise electrical continuity [11,15]. Achieving reproducible and low-resistance conductive paths on textiles requires careful optimization of both the substrate and the printing process. The physical structure of the textile, such as weave type, yarn density, and grammage, plays a critical role in ink distribution and, therefore, in electrical performance. Fabrics with compact and regular structures tend to support more uniform ink coverage and lower resistance values [43–45].

A key strategy for improving print quality on textiles involves modifying the substrate's surface energy through chemical pretreatments. Hydrophobic and oleophobic coatings have proven effective in enhancing ink adhesion, minimizing spreading, and improving pattern definition by altering the wetting behavior of the fabric and facilitating the formation of continuous conductive traces [46,47]. Building on this foundation, the present study investigates the combined influence of surface pretreatments and textile morphology on the electrical performance of silver nanoparticle inks applied via flexographic printing. A range of polyester fabrics with distinct structural characteristics was analyzed to assess how pretreatment type and fabric architecture affect ink adhesion, distribution, and conductivity. A multiscale characterization approach, including electrical resistance measurements, stereomicroscopy, profilometry, and colorimetric analysis, was employed to correlate surface properties with functional performance and support the development of scalable, reliable, and high-performance e-textiles.

Building on insights from [43] regarding textile structure and composition in conductivity, this study complements those findings by introducing chemical surface modification. Specifically, it systematically evaluates the effect of hydrophobic and oleophobic pretreatments on polyester substrates and their interaction with textile architecture, an aspect not previously addressed. Furthermore, advanced characterization techniques such as optical profilometry and colorimetric analysis are incorporated to establish relations between surface morphology, ink coverage, and electrical performance, extending the methodological scope beyond conventional resistance measurements.

By focusing on industrially relevant polyester substrates and commercially available pretreatment agents, this work aims to identify the optimal combination of textile structure, surface pretreatment, and printing orientation to achieve low electrical resistance and high reproducibility. This integrated approach enhances ink adhesion, reduces variability, and supports industrial scalability.

2. Materials and Methods

2.1. Materials

Textile Substrates. Based on the results obtained in previous work by Rodes et al. [43], a selection of representative polyester fabrics was made for this study. The chosen materials vary in weave type, thread diameter, and fabric density. Table 1 shows the composition and ligament of the involved fabrics.

Table 1. Fabric characteristics (I): composition and ligament.

Fabric	Material	Ligament	Graphic Representation	Interlacing Coefficient (KL)
T1, T2, T3, T4	PES	Taffeta		1
T5, T6, T7, T8	PES	Twill		0.4

The fabric samples were produced by variation in the weft yarn count (333.3 dtex/666.7 dtex) without changing the warp count (167 dtex). The warp density is fixed as well at 60 threads/cm. The value of the linear yarn count is the same for all the fabrics, being 1.5%. Table 2 shows the size and weight of the different fabrics used.

Table 2. Fabric characteristics (II): size and weight characteristics.

Fabric	Weft Density (Thread/cm)	Weft Yarn Count (dtex)	Thickness (μm)	Grammage (g/m^2)
T1	10	333.3	515	154
T2	15	333.3	550	171
T3	10	666.7	622	191
T4	15	666.7	650	233
T5	10	333.3	705	160
T6	15	333.3	725	180
T7	10	666.7	744	222
T8	15	666.7	805	241

Figure 1 shows the graphic representation of the ligament and fabric used for the two groups of fabrics, taffeta and twill, varying the weft yarn count.

Pretreatment. Two different pretreatments have been applied to the textile substrates. The first one applies a hydrophobic agent, Smartrepel Hydro CMD liq from Archroma (Pratteln, Switzerland). This agent provides durable water repellence without the use of fluorocarbons, making it an environmentally friendly option. It ensures that the fabric remains breathable and comfortable while offering excellent resistance to water and stains. According to the technical data sheet, Smartrepel Hydro CMD liq presents a pH (5%) of about 5, a density (20°) of about 1.00 g/cm^3 and a flash point greater than 100 °C. The second pretreatment consists of the application of an oleophobic agent, Nuva N1811 from ARCHROMA. It is a C6-based fluorochemical microencapsulated coating that repels water, oil, alcohol, soil, and stains. After the treatment, the fabric is permeable to air, stays soft with no negative impact on abrasion resistance and tear strength. According to the technical data sheet, Nuva N1811 presents a pH (5%) of about 4–6, a density (20°) of about 1.05 g/cm^3 and a flash point greater than 100 °C.

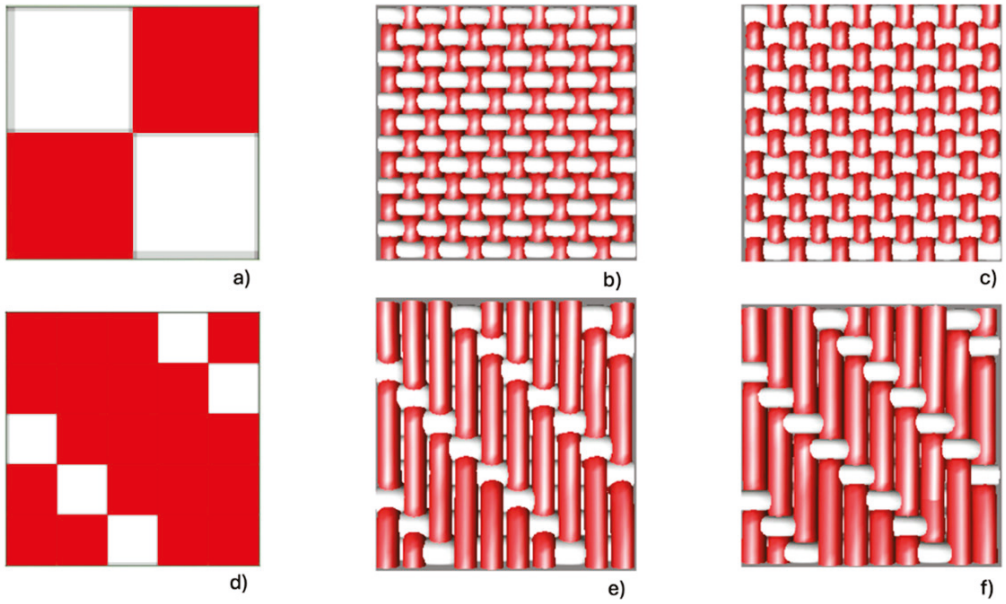

Figure 1. Graphic representation of ligament and fabric simulations of the two structures used: (**a**–**c**) Plain weave. (**a**) Diagram of the plain weave. (**b**) Simulation of the plain weave fabric with 333.3 dtex yarn. (**c**) Simulation of the plain weave fabric with 666.7 dtex yarn. (**d**–**f**) Twill weave. (**d**) Diagram of the twill weave. (**e**) Simulation of the twill weave fabric with 333.3 dtex yarn. (**f**) Simulation of the twill weave fabric with 666.7 dtex yarn.

Ink. The conductive ink employed in this study was PFI-RSA6004 from Novacentrix (Austin, TX, USA), selected for its high electrical performance (Table 3). This silver nanoparticle-based ink, formulated in an aqueous medium, is specifically designed for printing reflective and conductive patterns on smooth substrates. Its composition and rheological properties make it suitable for flexographic printing processes, including laboratory-scale and roll-to-roll applications.

Table 3. PFI-RSA6004 Silver ink characteristics.

Ink Code	Density (g/mL)	Solids (%)	Viscosity (Pas)	Volume Resistivity (μΩ·cm)	Curing	Properties
PFI-RSA6004	2.25	60 (±2)	50–150 @1000 s^{-1}	10–12	10–60 s 140 °C	- Fast Curing - Good Conductivity - Good Flexibility - Compatible with Polyester

Transmission Electron Microscopy (TEM) analysis of the ink shows the presence of silver nanoparticles with predominantly irregular to ellipsoidal morphologies. As shown in Figure 2, the particles exhibit sizes mainly in the range of 20–50 nm, with some smaller particles below 20 nm and occasional elongated structures exceeding 50 nm. The high-contrast regions observed within the particles suggest crystalline domains, consistent with metallic silver. These results support the claim of silver nanoparticle incorporation and provide evidence of their nanoscale dimensions and morphology.

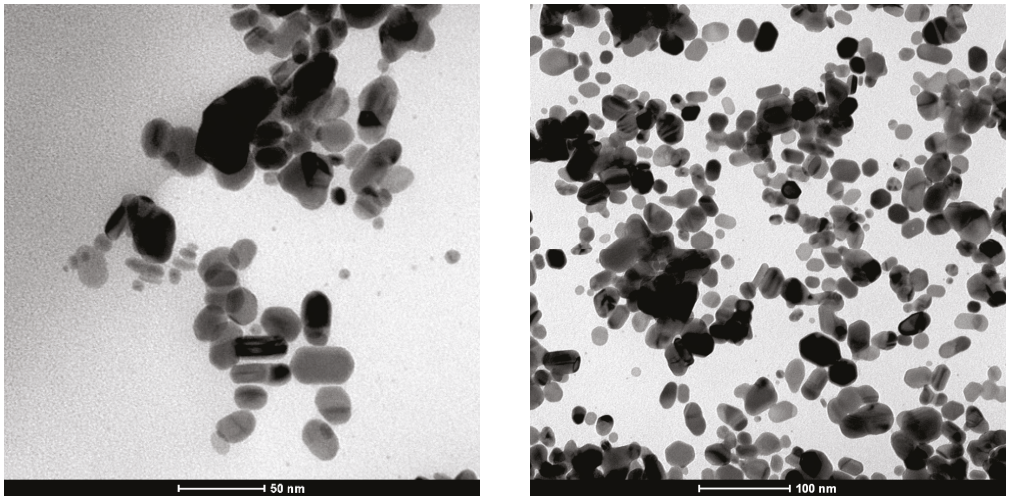

Figure 2. TEM micrograph images of PFI-RSA6004 Silver ink from Novacentrix: (**a**) Image taken at 1,000,000× magnification (scale bar = 50 nm). (**b**) Image taken at 500,000× magnification (scale bar = 100 nm). Images courtesy of Novacentrix.

2.2. Methods

Pretreatment. Hydrophobic and oleophobic pretreatments were applied to the selected fabrics with the purpose of reducing surface tension and modifying surface energy. These modifications were expected to influence the behavior of conductive ink deposition during flexographic printing by limiting ink spreading and promoting more uniform layer thickness. Additionally, such treatments may contribute to improved reproducibility of printed circuits and more consistent electrical performance across different batches and substrates.

For each one of the substrates, the pretreatment procedure consisted of 8 steps as reflected in Figure 3. Firstly, three samples were cut with a size of 190 × 120 mm approximately (one with no pretreatment for comparison purposes, one for the hydrophobic pretreatment, and the third one for the oleophobic pretreatment). Secondly, the samples were weighed before applying the pretreatment. Next, 400 mL of both pretreatments were prepared according to the manufacturer's specifications, 60 g/L for the hydrophobic one and 50 g/L for the oleophobic one. The pH of the oleophobic covering was corrected using acetic acid 96% with a concentration of 1 mL/L. Once the pretreatments were ready, the samples were impregnated by submersion in a bucket with each pretreatment for 30 s on each side (right and back). Afterwards, the samples were folded in half and proceeded to pass them through a manual pad to remove the excess of the product. This step was repeated 2 times. Next, the samples were weighed again to estimate the pick-up of the pretreatment. The pick-up indicates the quantity of absorbed chemical products after pretreatment. It is expressed as a percentage (I %) and defined by the following equation:

$$I(\%) = \frac{Wet\ Weigh - Dry\ Weigh}{Dry\ Weigh} \times 100 \quad (1)$$

Finally, the samples were dried and cured using a forced air oven, specifically the ArgoLab TCF 120 oven from Giorgio Bormac (Carpi, Italy). According to the manufacturer, the drying process needs 10 min at 120 °C, and the curing process must be carried out at 150 °C for 3 min. Lastly, before applying flexographic printing, the samples were ironed with an iron in nylon mode (1 black point) to ensure the best printing results.

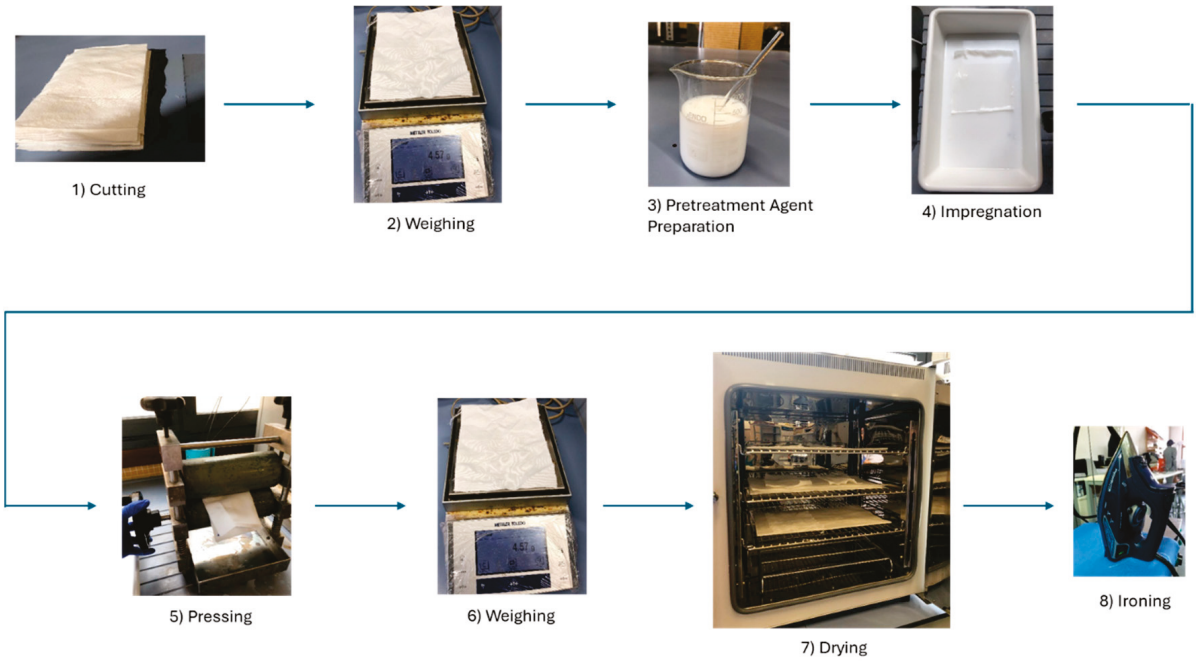

Figure 3. Steps for preparing the substrate textile samples before flexographic printing.

Once the three samples were prepared, the effectiveness of the applied pretreatment was evaluated using a drop situation test, such as the one used in UNE-EN ISO 14419:2010. The results of the pretreatments were compared with the untreated samples. Figure 4 shows the scale of the evaluation used in UNE-EN ISO 14419:2010.

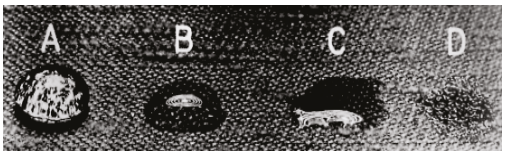

Figure 4. Value scale of drop situation for UNE-EN ISO 14419:2010. A: well-rounded drop. B: rounding drop with partial darkening. C: wicking apparent and/or complete wetting. D: complete wetting.

Printing. One-layer flexographic prints were carried out on the samples using the IGT F1 from IGT Testing Systems (Almere, The Netherlands). The printing plate used was based on a photopolymer specially developed for printed electronics applications from KodaK (Rochester, NY, USA). Figure 5 shows the flexographic printer, the anilox used in this work and the details of the anilox cells.

(**a**) (**b**) (**c**)

Figure 5. (**a**) Flexographic Printer used in the research. (**b**) Anilox used in the research. (**c**) Anilox cell detail.

The print patterns were designed as linear elements oriented at 0° and 90°, with varying line widths to evaluate their influence on electrical resistance (Figure 6). The minimum line width was established based on the thickest standard used by printed circuit board (PCB) manufacturers, Class 3, which corresponds to 0.25 mm. Then, the width is increased to 2 mm. This selection aims to assess the feasibility of achieving standardized printed circuits on textile substrates.

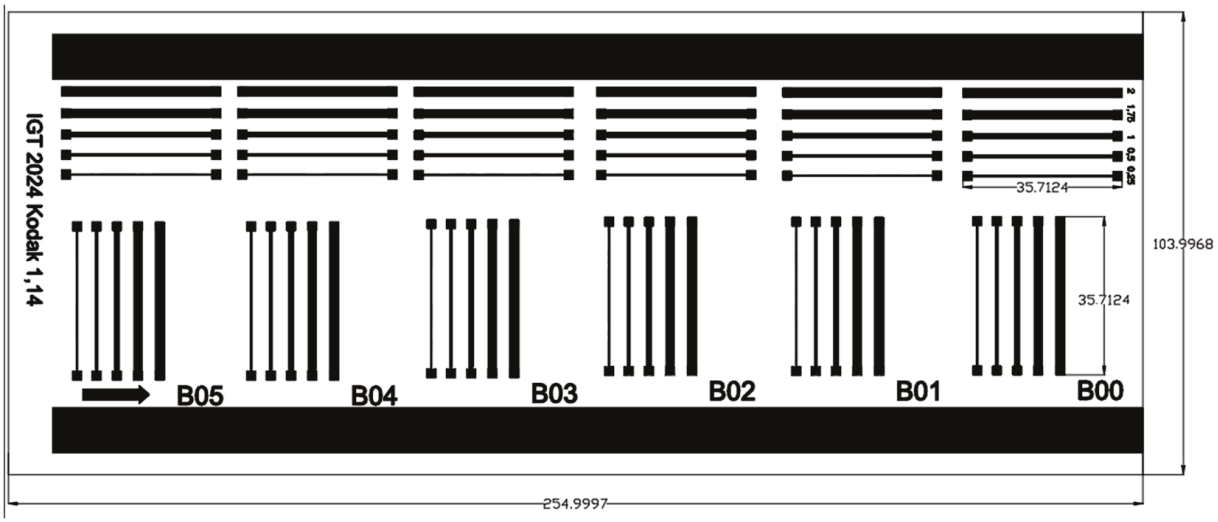

(**a**)

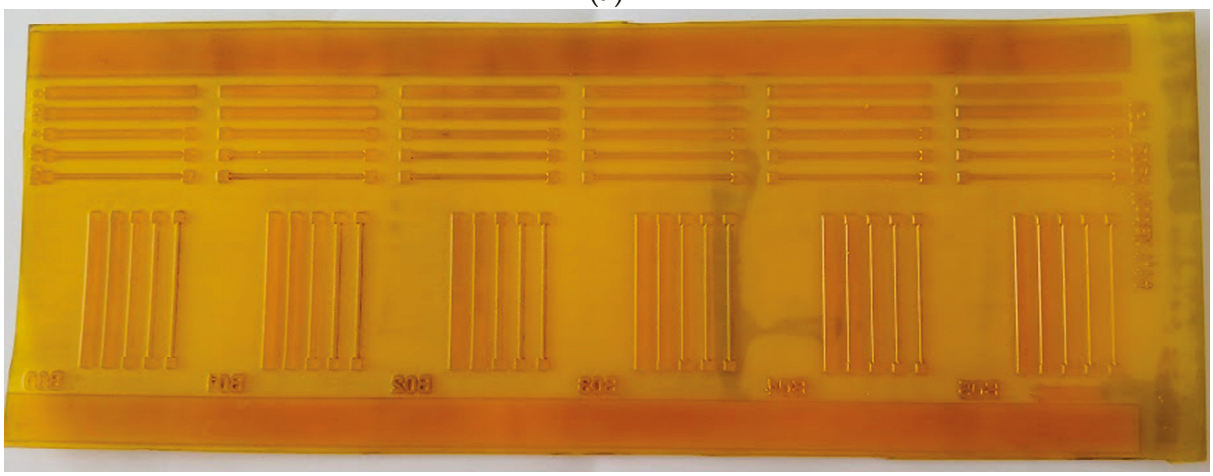

(**b**)

Figure 6. Printing plate applied on the flexographic prints: (**a**) dimensions, (**b**) final aspect of the printing plate.

Furthermore, the printing plate incorporates the full range of microstructures supported by KodakK, from B00 to B05. Among these, the B05 microstructure enables the highest ink transfer to the textile substrate. Ink transfer is a critical factor in achieving consistent conductivity and print quality, and, therefore, plays a key role in the overall performance of printed e-textiles.

The process began with the cleaning of the equipment prior to use to ensure the removal of any residual inks, dust, or contaminants that could interfere with print quality. The printing plate was cleaned with acetone to prevent clogging, while the anilox area was treated using enpurex Cleaning Liquid Power from TKM (Remscheid, Germany). Following this, the flexographic printing machine was configured according to the parameters listed in Table 4. To optimize the outcome, several secondary parameters were adjusted during printing trials, yielding the best results under the following conditions:

- Anilox Force: 150 N.
- Anilox Speed: 50%.
- Printing Force: 500 N.

Table 4. Printing Parameters.

Ink	Anilox Volume	Resolution	Printed Area	Speed	Curing
PFI-RSA6004—Silver Ink	11 cm^3/m^2	150 LPI	150 × 95 mm^2	0.5 m/s	60 s, 140 °C

Electrical characterization. Resistance measurements were made using a four-point probe configuration (Kelvin method) to minimize contact resistance effects, ensuring high accuracy and repeatability. A Keithley 2001 Series Digital Multimeter from Tektronix (Beaverton, OR, USA), a high-precision and low-noise-floor device, was employed to perform the resistance measurements. The probes were aligned to guarantee consistent spacing and contact pressure across all samples. For each sample, five consecutive resistance measurements were recorded to evaluate both repeatability and statistical dispersion.

Stereomicroscopy. Microstructural analysis of the fabric samples and printed ink was carried out using a MZ APO stereomicroscope from Leica (Wetzlar, Germany), equipped with a fully apochromatically corrected optical system. Samples were positioned on a flat, stable support to ensure consistent focus and minimize optical distortion. A zoom range from 8× to 80× was employed to examine the spatial distribution of the threads, the weave structure, and the interaction between the ink and the textile surface. The system's high numerical aperture (up to 0.2) enabled detailed visualization of fine features, supporting the qualitative assessment of thread alignment, fabric uniformity, and ink deposition.

Profilometry. Surface topography and geometric characterization of the fabric samples were conducted using a Profilm3D desktop optical profiler from KLA (Milpitas, CA, USA), which operates based on white light interferometry (WLI). Prior to measurement, the samples were mounted on the stage using a flat, non-reflective support to ensure stability and minimize light scattering. An objective 50× was used, enabling the determination of the geometric characteristics of the fabric, the sizes of the threads, their separation and arrangement of the weft and warp. Scans were performed over regions of interest, capturing representative areas of the fabric structure. Multiple scans ($n = 5$) were conducted at different locations on each sample to evaluate structural uniformity.

Color Measurement. Color measurements of the treated samples were performed using a CM-3600d reflectance spectrophotometer from Konica Minolta (Tokyo, Japan). The instrumental geometry was d/8 with the specular component excluded. The measurement area had a diameter of 25.4 mm. Ultraviolet energy was included. Measurements were carried out using the CIE 10° standard observer and the D65 standard illuminant over the wavelength range of 400–700 nm.

3. Results and Discussion

3.1. Pretreatments

Pick-Up. Pick-up values obtained after pretreatment are shown in Table 5. Both excessive and insufficient penetration can compromise the subsequent ink adhesion: deeper penetration may reduce the amount of treatment available at the surface for interaction with the ink, while shallow penetration may result in incomplete coverage of the fibers. Therefore, precise control of pick-up is essential to ensure that the surface is adequately modified for optimal ink deposition in the following printing step.

Table 5. Pick-up results for the different samples based on the used pretreatment.

	Hydrophobic Pretreatment (%)	Oleophobic Pretreatment (%)
T1	76.46	83.11
T2	72.87	77.02
T3	74.08	79.28
T4	64.73	66.98
T5	80.26	84.47
T6	78.80	87.51
T7	79.02	82.94
T8	74.39	78.92

Grouped bars in Figure 7 represent the percentage of treatment uptake for each fabric sample, highlighting differences in liquid absorption depending on substrate and type of pretreatment.

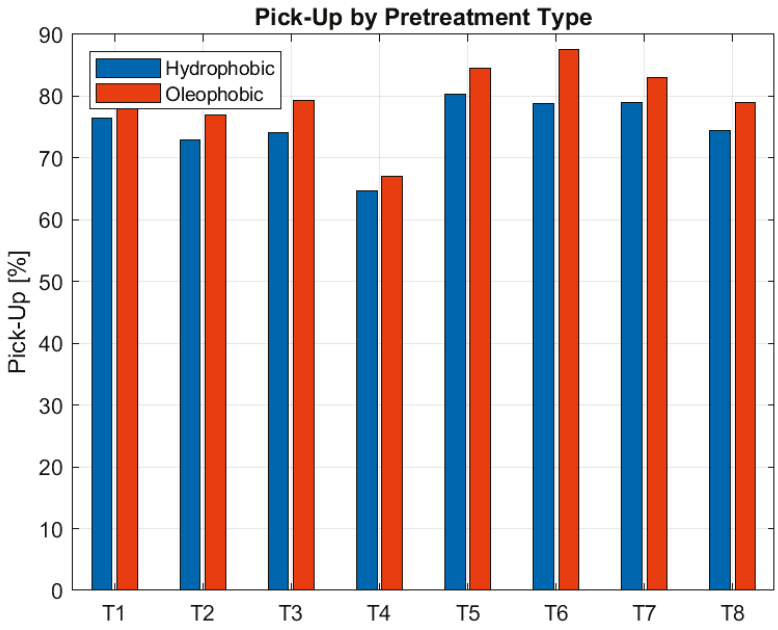

Figure 7. Comparison of Pick-Up percentage across textile substrates T1–T8 under hydrophobic and oleophobic surface treatments.

The pick-up results for hydrophobic and oleophobic pretreatments reveal a clear influence of both fabric structure and weave type on treatment absorption. Among all polyester fabrics studied, those with a plain weave and high weft density, T2 (72.87% hydrophobic, 77.02% oleophobic) and T4 (64.73%, 66.98%), consistently exhibit the lowest pick-up values. This behavior can be attributed to the combination of a tightly packed structure and the inherently closed nature of the plain weaves, which significantly restricts pore accessibility and internal capillarity, minimizing pretreatment penetration and retention.

In contrast, twill weave fabrics (T5–T8), characterized by their diagonal structure and increased porosity, show higher pick-up values overall. T5 (80.26%, 84.47%) and T7 (79.02%, 82.94%), both with low weft density, display the highest absorption due to their open structure and larger pore channels. T6 (78.80%, 87.51%), despite its high density, shows the highest oleophobic absorption, suggesting that yarn fineness and internal capillarity may override the density effect. T8 (74.39%, 78.92%), with high density and coarse yarn, stands out as the least absorbent twill fabric, though it still absorbs more than the most compact plain weaves.

These findings confirm that weave type can be a decisive factor in controlling pretreatment uptake: no twill fabric reaches the low absorption levels of the most compact plain weaves. Moreover, low pick-up is achieved only when both high weft density and a closed weave structure coincide, as in T2 and T4.

Drop Situation Test. The results of the drop test are presented in Table 6, following the assessment criteria of UNE-EN ISO 14419:2010, where repellence is graded from A (highest repellence) to D (lowest repellence).

Table 6. Drop situation results. A means highest repellence and D lowest repellence.

	Hydrophobic Pretreatment (%)	Oleophobic Pretreatment (%)
T1	A	A
T2	A	A
T3	A	A
T4	A	A
T5	A	A
T6	A	A
T7	A	A
T8	A	B

Most of the pretreated fabrics, regardless of whether hydrophobic or oleophobic agents were used, achieved the highest repellency rating (A), confirming the effectiveness of the applied pretreatments in modifying surface tension and enhancing liquid resistance. Notably, sample T8 treated with oleophobic agents exhibited a reduced performance (B rating), likely due to structural irregularities of the textile, which prevented uniform distribution of the agent.

Figure 8 shows the results for T4 for the cases studied, no pretreatment and both pretreatments. The last image of Figure 8, (d), shows the results for T8 with oleophobic pretreatment, where the drop does not have as much consistency as in the other cases shown.

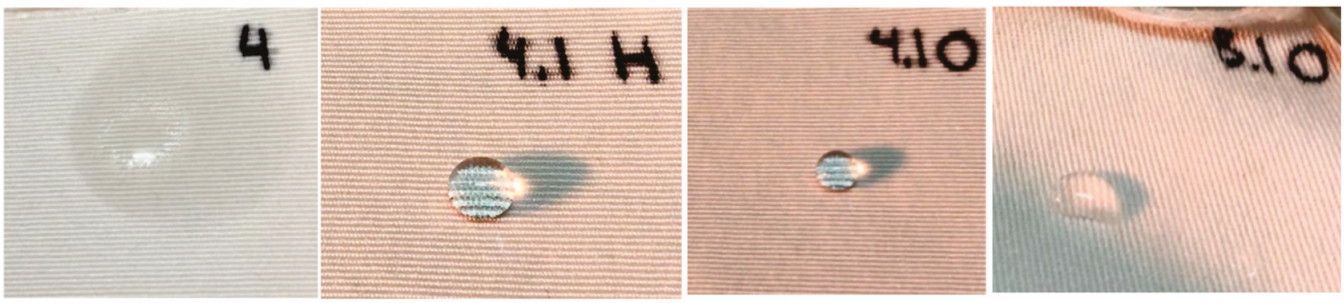

Figure 8. Drop Situation results for (**a**) T4-UT (Untreated), (**b**) T4-HT (Hydrophobic Pretreatment) and (**c**) T4-OT (Oleophobic Pretreatment). Figure (**d**) shows the worst result for a pretreatment (T8-OT).

All treatment formulations demonstrated an adequate level of water repellence across the available substrates. These results suggest that further optimization of the formulation could be explored to reduce production costs and improve process efficiency, without compromising functional performance.

3.2. Flexographic Printings

Printings. Before printing, each fabric was cut into two distinct orientations. One sample had its longer axis aligned with the weft direction (vertical yarns), while the other

was aligned with the warp direction (horizontal yarns). Each one of two samples of each fabric was printed once using flexographic printing. For the first sample, printing was performed with the printing direction aligned to the weft. For the second sample, the printing direction was aligned with the warp, following the horizontal yarn orientation. This setup enables evaluation of how fabric orientation relative to the printing direction influences ink deposition, image definition, and functional properties such as electrical resistance and color uniformity.

Figure 9 shows two examples of flexographic printing with silver conductive ink on two different fabrics cut in the warp orientation. The differences in printing will be analyzed in terms of the resistance values obtained.

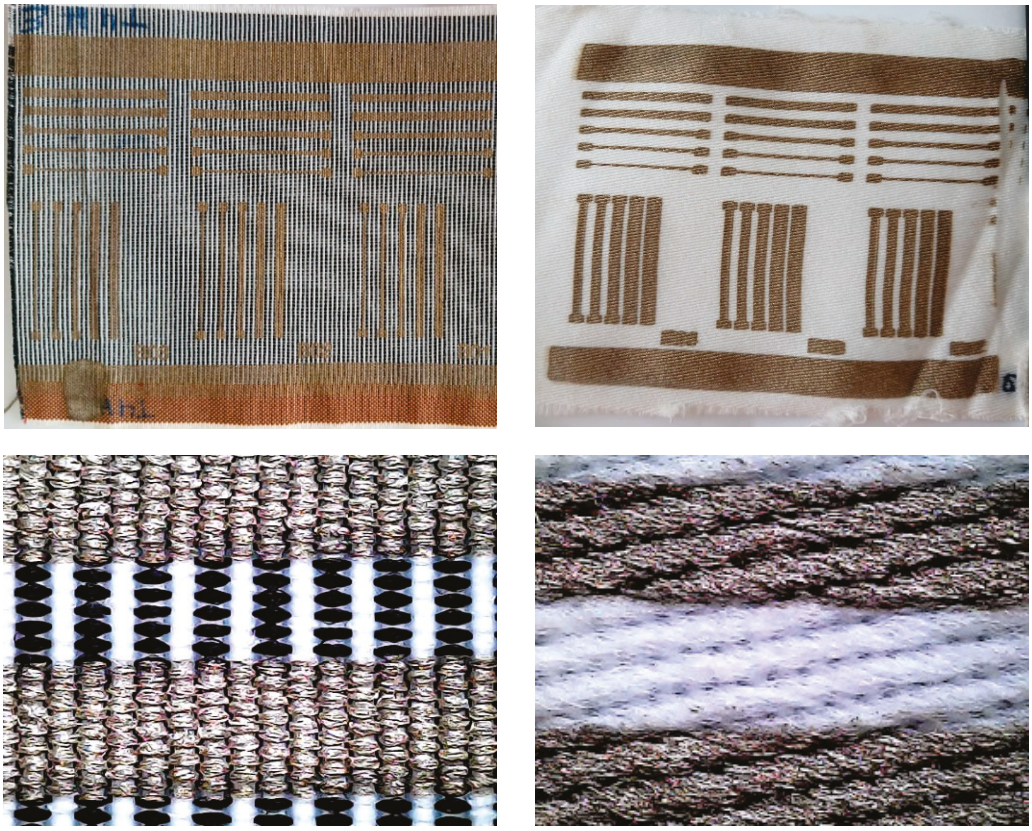

Figure 9. Example of pattern printing on a textile substrate. (**Left**) T4_HT printed on weft direction. (**Right**) T8_HT printed on warp direction.

3.3. Electrical Characterization

Resistance measurement. Measurements were performed considering the printing direction relative to the weft and warp orientations. Figure 10 illustrates the nomenclature applied according to the printing alignment. When the printing direction corresponds to the weft orientation, sample A refers to the measurement taken on a print oriented toward the warp, while sample B corresponds to the print aligned with the weft. Conversely, when the printing direction is aligned with the warp orientation, sample C represents the measurement on the print oriented toward the weft, and sample D corresponds to the one aligned with the warp.

For each printing, the minimum line width at which electrical conductivity was achieved was first identified. Fabrics T1 and T3 only exhibited conductive prints for sample B in the case of the Hydrophobic Pretreatment (in both fabrics) and for the same sample, B, for the Oleophobic Pretreatment (only in fabric T3). In all three cases, conductivity was obtained exclusively on the line with the largest width, 2 mm. The remaining fabrics

achieved conductivity at widths of 1.75 mm and 2 mm. For the 1.75 mm width, the lower one, five resistance measurements were taken for the line in the horizontal direction (sample B or D in Figure 10, depending on whether the printing direction aligns with the weft or warp orientation) and for the vertical line (sample A or C). These ten measurements were repeated for the six microstructures (B00 to B05). The procedure was applied to samples printed in both weft and warp directions, which yielded 30 measurements for each combination of printing direction and fabric orientation (A, B, C, and D). The mean and standard deviation were then calculated from these measurements.

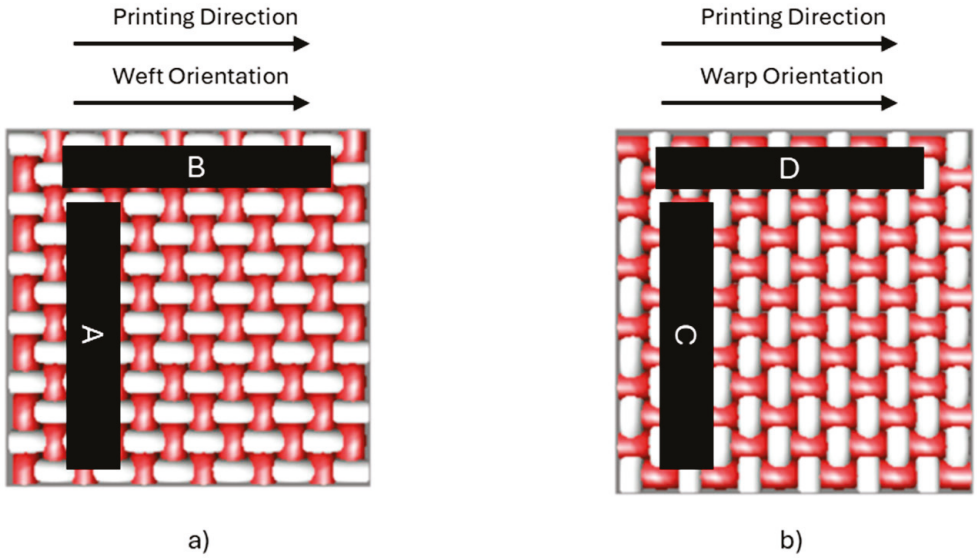

Figure 10. Designation of sample labels according to printing direction: (**a**) alignment with warp orientation; (**b**) alignment with weft orientation.

Table 7 summarizes the average electrical resistance values (Ω) along with the standard deviation obtained from each textile sample as a function of printing direction and fabric orientation (weft vs. warp), under three surface conditions: untreated (UT), oleophobic pretreatment (OT), and hydrophobic pretreatment (HT). The nomenclature follows the schema defined in Figure 10, where printing direction and fabric orientation combinations are labeled A–D for each pretreatment. Values marked as '–' indicate high impedance or open circuit conditions. This approach provides a comprehensive overview of the electrical behavior of each textile sample under different printing and surface treatment conditions. These averages provide a reliable basis for comparing fabrics and treatments, particularly in this exploratory context aimed at identifying general trends in conductivity improvement.

T1 and T3 exhibit open circuit behavior when untreated or after oleophobic treatment, only showing occasional tens to hundreds of ohms under hydrophobic treatment. T2 and T4 exhibit very low resistances (<10 Ω) after oleophobic pretreatment in all orientations, indicating excellent ink adhesion and conductivity. The surface tension of the fabrics achieved using the oleophobic agent facilitates better adhesion and distribution of the conductive ink, resulting in lower electrical resistance. T5 and T6, which initially showed resistance in the hundreds of ohms when untreated or oleophobic-treated, drop dramatically to around ten ohms with hydrophobic treatment. T7 displays an anomalous spike above 10^4 Ω under hydrophobic treatment, suggesting over-treatment or poor ink–substrate compatibility. Finally, T8 transitions from very high resistance (>10^5 Ω) when untreated to single-digit ohms after oleophobic treatment, then rises again under hydrophobic treatment, underscoring its strong sensitivity to pretreatment type.

Table 7. Electrical Resistance (Ω) (mean ± standard deviation) relative to Printing Direction and Fabric Orientation (Warp and Weft).

	Untreated (UT)				**Oleophobic Pretreatment (OT)**				**Hydrophobic Pretreatment (HT)**			
	A-UT	**B-UT**	**C-UT**	**D-UT**	**A-OT**	**B-OT**	**C-OT**	**D-OT**	**A-HT**	**B-HT**	**C-HT**	**D-HT**
T1	--	--	--	--	--	--	--	--	--	204 ± 20	--	--
T2	13.7 ± 0.5	13.3 ± 0.4	14.3 ± 0.6	15.2 ± 0.7	3.15 ± 0.11	2.17 ± 0.10	4.50 ± 0.15	5.60 ± 0.18	13.1 ± 0.5	12.7 ± 0.4	13.5 ± 0.6	14.2 ± 0.7
T3	--	180 ± 10	--	--	--	17.8 ± 1.2	--	--	--	38,000 ± 28.3	--	--
T4	3.10 ± 0.15	2.24 ± 0.12	3.60 ± 0.18	3.80 ± 0.20	0.90 ± 0.05	0.52 ± 0.03	1.20 ± 0.06	1.80 ± 0.09	1.90 ± 0.08	1.80 ± 0.07	2.10 ± 0.10	2.40 ± 0.12
T5	146 ± 2	140 ± 2	147 ± 2	150 ± 2	260 ± 3.5	255 ± 3.5	265 ± 3.5	269 ± 3.5	11.2 ± 2	10.3 ± 2	11.9 ± 2	12.5 ± 2
T6	255 ± 2	254 ± 2	256 ± 2	257 ± 2	64.1 ± 1	63.5 ± 1	65.2 ± 1	66.7 ± 1	47.1 ± 1	46.6 ± 1	48.2 ± 1	49.1 ± 1
T7	12.5 ± 0.2	11.9 ± 0.2	12.8 ± 0.2	13.5 ± 0.2	11.2 ± 0.2	10.4 ± 0.2	12.1 ± 0.2	13.2 ± 0.2	46,300 ± 32.7	46,100 ± 32.5	47,100 ± 33.2	47,200 ± 33.3
T8	145,000 ± 1020	144,000 ± 1010	146,000 ± 1030	147,000 ± 1040	7.2 ± 0.2	6.76 ± 0.2	7.9 ± 0.2	8.9 ± 0.2	122,000 ± 860	121,000 ± 850	123,000 ± 870	124,000 ± 880

Note: Unspecified data is high impedance (open circuit).

Although pretreatment absorption (pick-up) could be expected to influence conductivity, regression analysis between pick-up values (Table 5) and electrical resistance (Table 7) for oleophobic pretreatment yielded a weak correlation ($R^2 \approx 0.23$). The computed linear model was:

$$Resistance\ (\Omega)\ =\ \ 6.77\ \times Pick-Up\ (\%)-\ 480.66 \quad (2)$$

While some individual cases appear to suggest a trend, such as T4 (66.98%, ≈0.52 Ω/cm) compared to T5 (84.47%, ≈262 Ω/cm), the overall variability across fabrics indicates that absorption alone does not explain conductivity. For hydrophobic pretreatment, the correlation was even lower ($R^2 \approx 0.05$). Therefore, pretreatment pick-up cannot be considered a primary determinant of electrical performance.

The printing direction relative to the weft and warp of the fabric influences electrical resistance. When the printing direction of the circuit lines coincides with the weft direction, the best results are obtained (lower electrical resistance) for T4. Fabrics with a more regular and compact structure (such as T4) allow for a more homogeneous and continuous distribution of the conductive ink, which reduces electrical resistance. This aspect will be further investigated through microscopy and profilometry analyses to assess surface uniformity and roughness in fabrics T2 and T4.

Subsequent work will focus exclusively on substrates T2 and T4. These two samples were selected because they alone combine consistently low and reproducible electrical resistances across all printing orientations (A–D) and surface treatments. Figure 11 graphically illustrates the relationship between the measured electrical resistance and the printing orientation, as well as the applied surface treatment, for T2 and T4 textile substrates. The best results are obtained with T4 fabric when the print direction coincides with the weft direction, and the circuit line pattern is aligned with it. Error bars indicate standard deviation from four measurements per condition, showing variability across orientations.

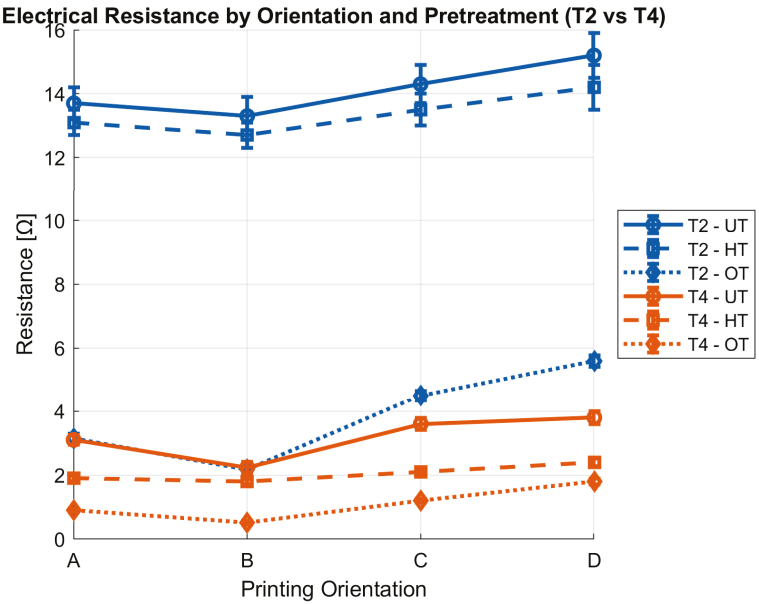

Figure 11. Electrical resistance of substrates T2 and T4 as a function of printing orientation (A–D) and surface treatment. Error bars represent standard deviation from multiple replicates.

Electrical resistance decreases with oleophobic pretreatment compared to hydrophobic pretreatment and to unpretreated samples. This is clearly observed in Figure 12, where (a) shows the absolute resistance values and (b) presents normalized resistance relative to the untreated condition. In both pretreatments, the resistance of printed linear elements on T4 (oleophobic) is significantly lower than on all samples of T2 and lower than on T4

untreated samples, confirming the effectiveness of the oleophobic treatment. Error bars in both subfigures indicate variability across four orientations (A–D).

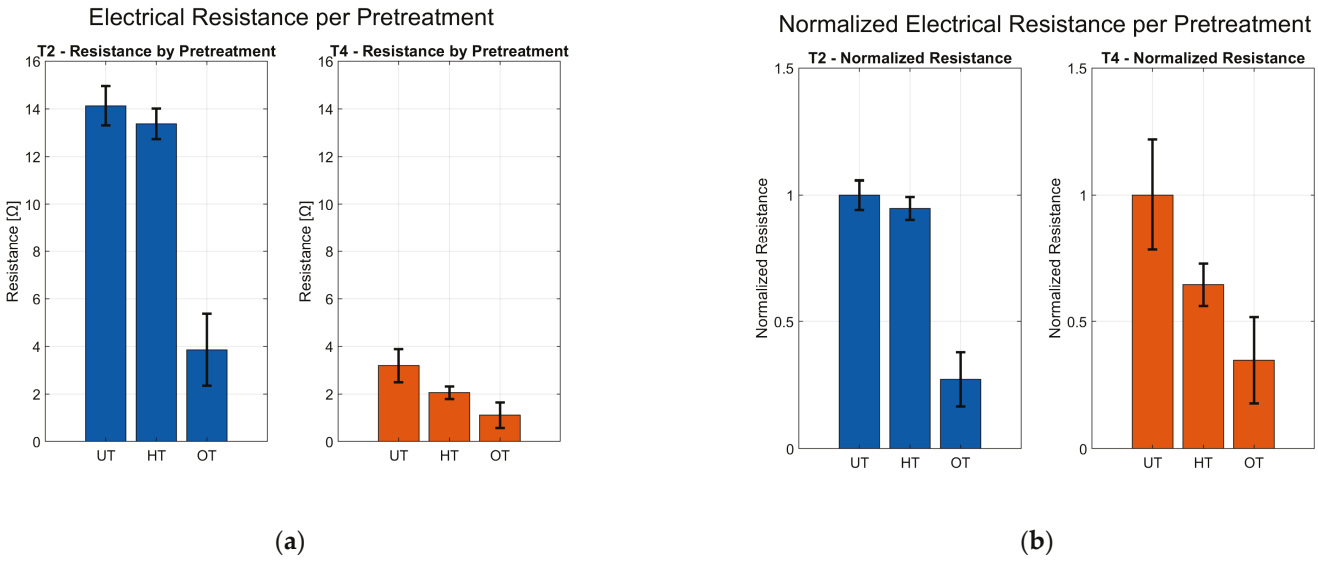

(**a**) (**b**)

Figure 12. (**a**) Electrical resistance for substrates T2 and T4 under untreated (UT), hydrophobic (HT), and oleophobic (OT) conditions, averaged across four printing orientations (A–D). (**b**) Normalized electrical resistance relative to the untreated condition for each substrate and treatment. Error bars represent standard deviation from four measurements per treatment.

3.4. Physical Characterization

Stereoscopic Microscopy. Stereoscopic microscopy evaluated flexographic printing quality on both textile substrates. The analysis focused on samples printed in the weft direction (sample B). Figures 13 and 14 present surface and cross-sectional views of the weft-oriented prints on fabrics T2 and T4, respectively.

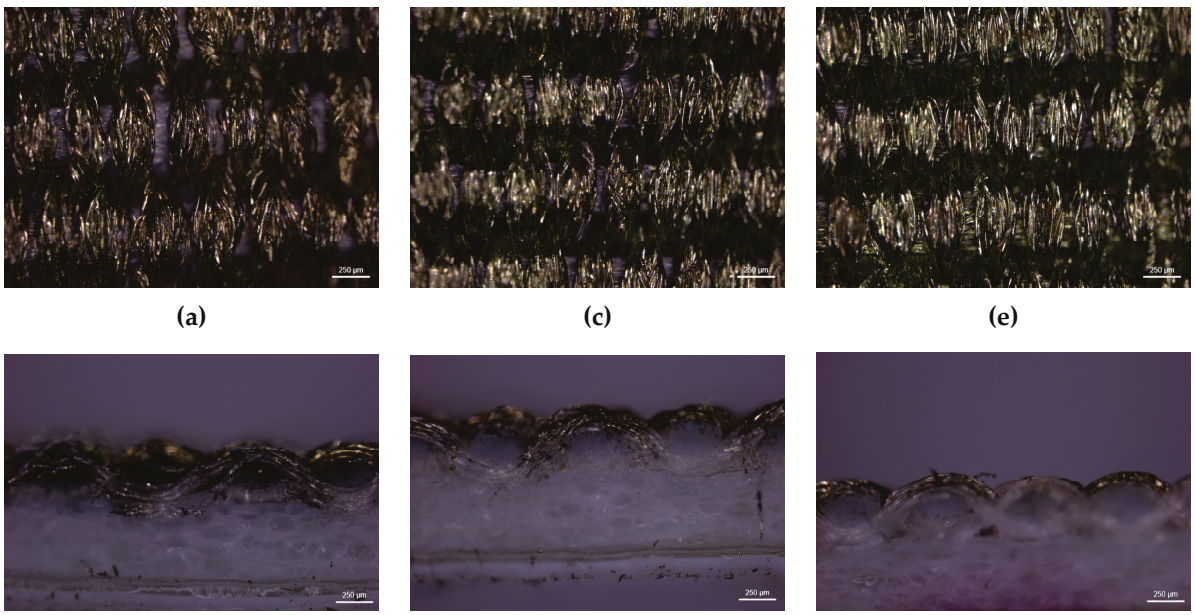

(**a**) (**c**) (**e**)

(**b**) (**d**) (**f**)

Figure 13. Surface (**top**) and cross-sectional (**bottom**) views of sample B of substrate T2 under different treatments (UT—Untreated, (**a**,**b**); HT—Hydrophobic treatment, (**c**,**d**); OT—Oleophobic treatment, (**e**,**f**)).

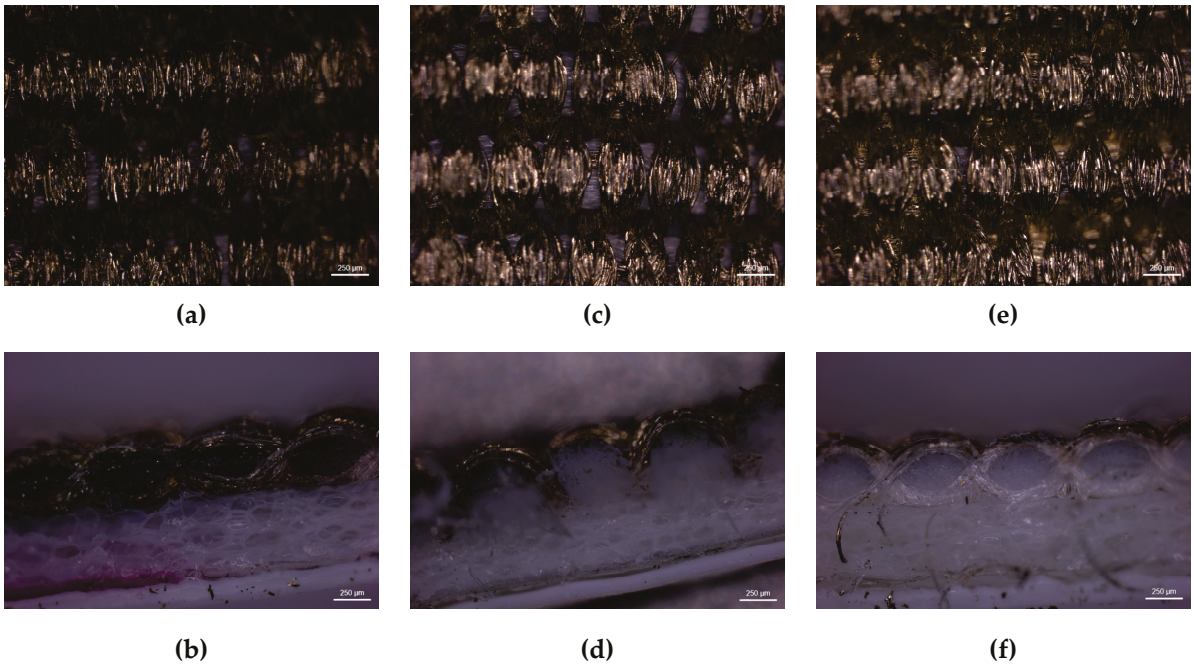

Figure 14. Surface (**top**) and cross-sectional (**bottom**) views of sample B of substrate T4 under different treatments (UT—Untreated, (**a**,**b**); HT—Hydrophobic treatment, (**c**,**d**); OT—Oleophobic treatment, (**e**,**f**)).

The stereomicroscopy and cross-sectional views of T2 reveal an irregular ink distribution, particularly in the untreated (UT) condition. Ink penetration varies depending on the treatment applied, with the oleophobic treatment resulting in the least penetration. This penetration is inconsistent across the treatments, with visible uncoated pores and fragmented conductive paths. Hydrophobic treatment (HT) slightly improves surface coverage with respect to UT, but still results in uneven ink deposition and accumulation zones, indicating poor compatibility between the treatment and the textile structure. Oleophobic treatment (OT), while more effective, still struggles to achieve full uniformity due to the fabric's inherent irregularity. Interestingly, cross-sectional observations suggest that lower penetration may favor electrical performance, as reflected in the electrical resistance values: UT and HT samples show resistances around 13.3 Ω/cm and 12.7 Ω/cm, respectively, while OT reduces resistance to approximately 2.17 Ω/cm.

T4 demonstrates much more favorable behavior across all treatments. The untreated sample already shows better ink coverage than T2, thanks to its compact and regular structure. Hydrophobic treatment (HT) enhances this further, yielding a more continuous ink layer with fewer discontinuities. Oleophobic treatment (OT) provides the best results, enabling uniform ink penetration and forming uninterrupted conductive traces. The cross-sectional analysis confirms consistent ink distribution throughout the textile thickness. As observed in T2 analysis, the sections suggest that controlled penetration, rather than excessive absorption, correlates with improved conductivity, reinforcing the importance of balanced ink interaction with the substrate. These structural advantages translate into significantly lower electrical resistance values: UT samples measure around 2.24 Ω/cm, HT samples drop to 1.80 Ω/cm, and OT samples achieve the lowest resistance at approximately 0.52 Ω/cm. The superior performance of T4 is directly linked to its dense weave and effective interaction with the oleophobic agent.

The comparison between T2 and T4 highlights the critical role of textile structure and surface treatment in determining ink absorption and electrical performance. While both fabrics benefit from oleophobic treatment, only T4 achieves optimal conductivity due to its compact and uniform morphology. The more irregular weave of T2 limits

the effectiveness of both pretreatments. Oleophobic treatment consistently outperforms hydrophobic and untreated conditions in both substrates, but its impact is maximized when paired with a structurally favorable fabric like T4. These findings underscore the importance of combining appropriate surface chemistry with textile engineering to optimize flexographic printing for e-textile applications.

Profilometry. The use of two different weft yarn thicknesses (333.3 dtex for T2 and 666.7 for T4) has a direct influence on pretreatment as well as on the posterior ink deposition, even when the fabric weave structure remains the same (plain for T2 and T4). This variation in weft yarn modifies the surface topography of the textile substrate, which significantly impacts the continuity and uniformity of the conductive ink deposited through flexographic printing.

To investigate this influence, this section analyzes oleophobic pretreated samples of T2 and T4 printed in the weft direction. Using optical profilometry techniques, a comparison of the surface morphology in both the weft and warp directions is carried out. Figures 15 and 16 show the topographic images obtained for each printed fabric, allowing the evaluation of key parameters such as regularity, thread spacing, and surface roughness, all of which are directly related to the quality and functionality of the resulting conductive traces.

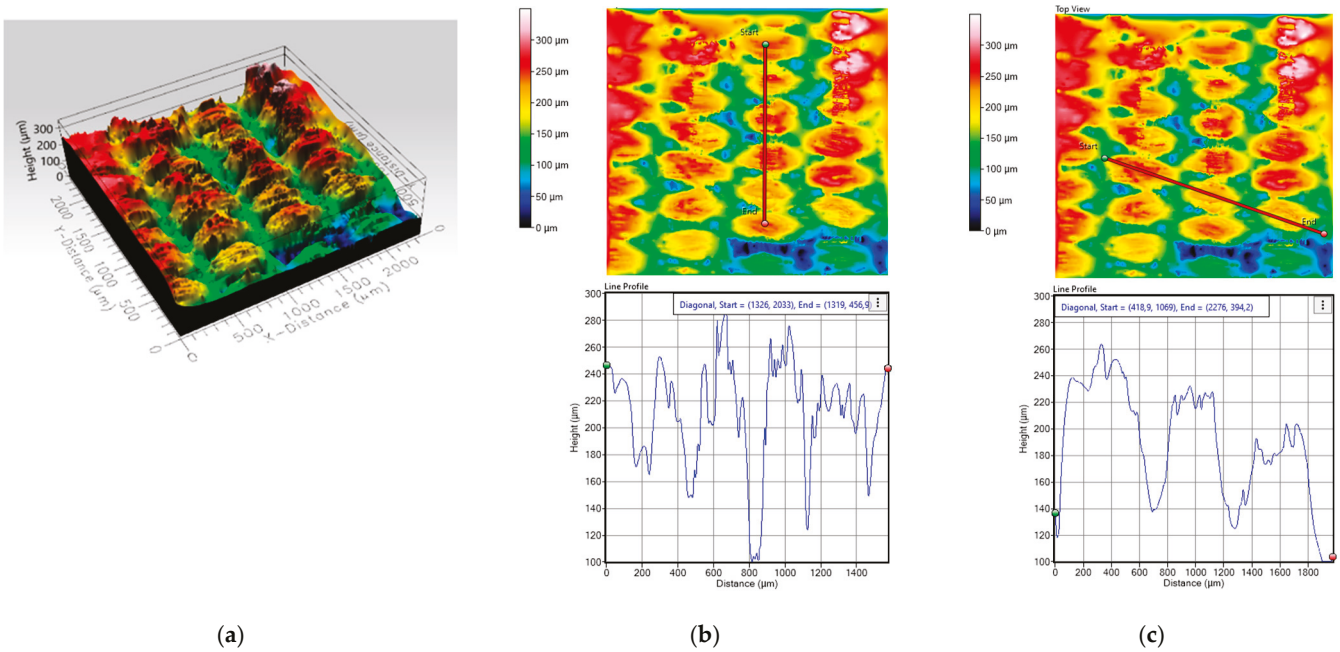

(**a**) (**b**) (**c**)

Figure 15. (**a**) Profile of the T2 substrate, (**b**) profile in the warp direction and (**c**) profile in slope in the weft direction.

The profilometric analysis of substrate T2 reveals a highly irregular surface morphology in both warp and weft directions. The 3D topography image shows alternating zones of red (≈250 µm), yellow (≈200 µm), and blue (≈50 µm), confirming the presence of abrupt height changes and a lack of surface uniformity. These color transitions visually reinforce the interpretation of high surface roughness and discontinuity, which negatively affect the formation of conductive traces. In the warp direction, peak heights reach 280 µm and 240 µm, with peak-to-valley differences ranging from 180 µm to 80 µm (100 µm of variation), depending on the region. This irregularity correlates with the electrical resistance measured in this direction under oleophobic treatment (A-OT ≈ 3.2 Ω/cm), indicating poorer ink continuity. In the weft direction, the surface remains uneven, with heights of 260 µm, 220 µm, and 200 µm, and peak-to-valley differences of 120 µm and 80 µm

(40 µm of variation). The corresponding electrical resistance (B-OT ≈ 2.2 Ω/cm) reflects the impact of these topographical variations, which hinder uniform ink deposition and reduce conductivity.

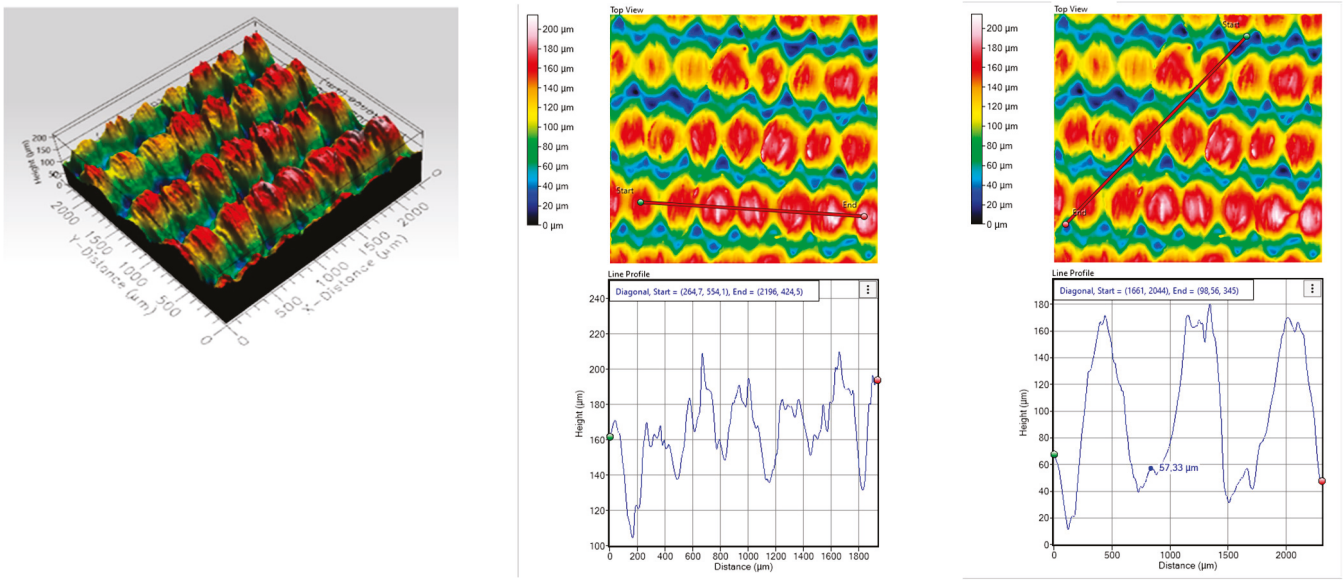

(**a**) (**b**) (**c**)

Figure 16. (**a**) Profile of the T4 substrate, (**b**) profile in the warp direction and (**c**) profile in slope in the weft direction.

Substrate T4 presents a significantly more regular and compact surface based on profilometric results. The 3D topography image is predominantly red, indicating a smooth and consistent surface with minimal height variation. This visual pattern confirms a uniform and compact surface, which facilitates better ink distribution and enhances conductivity. In the warp direction, excluding the initial peak, the surface heights stabilize around 200 µm and 180 µm, with consistent peak-to-valley differences of approximately 40 µm. This uniformity supports the formation of continuous conductive paths, resulting in a low electrical resistance (A-OT ≈ 0.9 Ω/cm) in this orientation. In the weft direction, the surface is even more homogeneous, with heights around 160 µm and peak-to-valley differences of ~100 µm, contributing to the lowest resistance observed (B-OT ≈ 0.5 Ω/cm).

The comparison between fabric printed results in T2 and T4 highlights the critical influence of surface topography and regularity on electrical performance. Substrate T2 exhibits pronounced irregularities and deep inter-yarn valleys, which disrupt ink continuity and lead to higher resistance values in both warp and weft directions. In contrast, substrate T4 demonstrates a smoother and more uniform surface, with shallower and consistently spaced valleys that facilitate better ink penetration and trace formation. Additionally, the weft direction consistently shows greater regularity than the warp direction, which is reflected in the lower resistance values obtained in weft-aligned prints for both substrates. The profilometric and colorimetric data directly support the electrical measurements, showing that lower surface roughness and higher regularity, especially in the weft direction, are essential for achieving low resistance and reliable conductivity in flexographically printed e-textiles.

Color Measurements. To evaluate the color obtained on the surface of the fabric treated by flexography, depending on the type of fabric and the pretreatments applied, the color of the samples was measured to investigate whether there is a relationship between the hue and lightness or darkness of the color and the resulting resistivity. Table 8 shows

the colorimetric coordinates (L*, a*, b*) in the CIELAB color space, as well as the color difference with respect to the reference sample.

Table 8. Color measurement. CIELAB.

Name	L*	a*	b*	ΔE*ab
Reference (untreated fabric)	92.3189	−0.7652	2.6213	
T2-UT	50.0492	0.1327	8.3465	42.665
T2-OT	52.7355	−0.607	9.9455	40.2556
T2-HT	54.7506	0.9541	9.2097	38.1804
T4-UT	52.5553	1.3045	9.4662	40.4015
T4-OT	53.3847	1.5468	9.0384	39.5271
T4-HT	54.7383	1.3473	10.0602	38.3679

The relationship between the resistance value of the samples and the color measurements is obtained with an R2 of 0.61, an adjusted R2 of 0.22, and a mean absolute error of 2.97, with the variables used being L*, a* and b*. Equation (3) shows this correlation.

$$R = 120.02 - 3.05 \cdot L^* + 7.05 \cdot a^* + 4.49 \cdot b^* \quad (3)$$

The scatter plot in Figure 17 compares predicted resistance values from the regression model against experimentally measured data. The diagonal dashed line represents the ideal fit (predicted = measured). Deviations from the line indicate estimation error and reflect sample-specific variability related to ink coverage and substrate structure. This model demonstrates a moderate correlation (R^2 = 0.61), suggesting that colorimetric measurements may serve as a complementary predictor of conductivity in printed fabrics. While the relationship is not perfect, a consistent trend is observed: increased ink deposition, reflected in greater color change, tends to result in lower electrical resistance. This moderate correlation is expected because colorimetry describes only the optical surface properties of the printed trace. Electrical performance, however, depends on additional microstructural factors such as porosity, surface roughness, yarn density, and, importantly, the depth-wise penetration of the conductive ink. These parameters influence the continuity and effective cross-section of the conductive path and are not captured by colorimetric data, thereby limiting the achievable correlation.

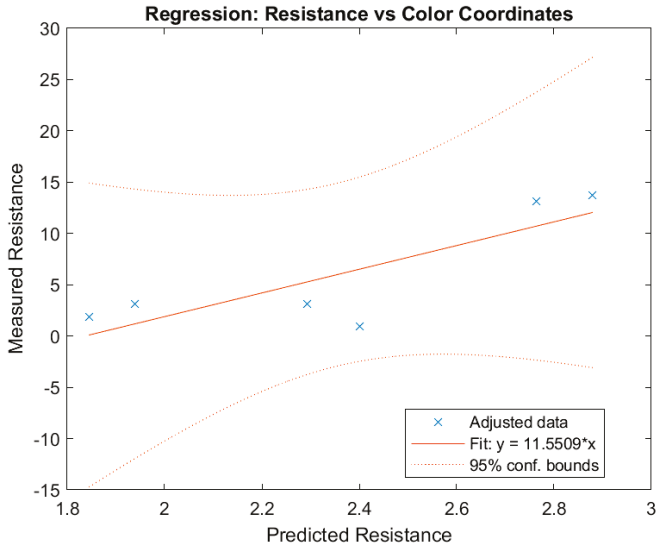

Figure 17. Regression analysis correlating CIELAB color coordinates (L*, a*, b*) with measured electrical resistance of textile samples.

On substrates such as T4, where ink coverage is homogeneous (as shown by microscopy and profilometry images), color measurement is also more uniform, resulting in less variability in resistance between samples. In contrast, on fabrics such as T2, where there are areas with less ink (less intense color), higher resistance and greater dispersion in the electrical results are observed. The correlation suggests that other factors, such as ink penetration into the textile structure or the presence of voids between threads, also influence conductivity and are not always reflected in the surface color measurement.

Objective color measurement complements physical and electrical characterization, since while microscopy and profilometry show the surface distribution and morphology of the ink, colorimetry provides quantitative data that is easy to compare and reproduce, useful for both laboratory quality control and industrial processes.

4. Conclusions

This study demonstrates that the combination of textile structure and surface pretreatment is critical for optimizing the electrical performance of flexographically printed e-textiles. The textile structure governs pretreatment effectiveness and determines ink deposition uniformity. Optimal electrical performance requires careful selection and matching of both pretreatment and textile architecture.

Oleophobic pretreatment consistently outperforms hydrophobic and untreated conditions, enabling lower electrical resistance by promoting better ink adhesion and more uniform distribution, especially when applied to fabrics with compact and regular morphology.

Profilometric analysis reveals that surface regularity and reduced roughness are essential for achieving continuous conductive traces. Substrates with higher weft yarn thickness (such as T4) exhibit shallower and more uniform valleys, which facilitate effective pretreatment absorption and homogeneous ink deposition. In contrast, fabrics with irregular and rough surfaces (such as T2) show deeper valleys and greater topographical variability, resulting in higher resistance values due to discontinuities in the printed paths.

A direct comparison between warp and weft directions further highlights the importance of structural regularity: the weft direction, which is more regular and compact, consistently yields lower electrical resistance than the warp direction for both substrates. These findings confirm that achieving low resistance and reliable conductivity in printed e-textiles requires not only the right chemical pretreatment but also careful selection of textile architecture and printing orientation. The integration of these factors is essential for the scalable production of high-performance, reproducible, and industrially viable e-textiles using flexography.

Additional observations indicate that electrical resistance decreases with increasing grammage and yarn linear density (dtex), and with lower pretreatment pick-up values, while no consistent correlation was found for weft density or substrate thickness. Furthermore, the lowest resistance values occur when the printing direction, warp/weft orientation, and circuit pattern alignment coincide. Finally, no significant correlation was found between pretreatment absorption and conductivity, reinforcing that textile structure and surface characteristics are more influential factors for achieving low electrical resistance.

In summary, the physical structure of the textile substrate, particularly its regularity and compactness, is as critical as chemical pretreatment for achieving low electrical resistance and high-quality printed electronics. Lower surface roughness favors the formation of continuous conductive layers, whereas irregular textures generate micro-cracks that increase resistivity. Fabrics such as T4, characterized by structural uniformity, exhibit reduced variability and improved reproducibility, supporting industrial scalability and minimizing defect rates.

Flexography, when combined with optimized pretreatments and structurally favorable substrates, emerges as a promising technique for industrial-scale production of high-performance e-textiles.

Author Contributions: Conceptualization, I.M., C.A.O.P. and E.B.-B.; methodology, I.M. and C.A.O.P.; validation, R.L.L. and C.A.O.P.; formal analysis, I.M. and R.L.L.; investigation, R.S. and E.B.-B.; resources, J.F.; writing—original draft preparation, J.F. and E.B.-B.; writing—review and editing, R.L.L., C.A.O.P. and R.S.; visualization, R.S. and R.L.L.; supervision, I.M., C.A.O.P. and E.B.-B.; funding acquisition, C.A.O.P. All authors have read and agreed to the published version of the manuscript.

Funding: This work was supported by the Spanish Government/FEDER funds (PID2024-155683OB-C44) (MINECO/FEDER).

Institutional Review Board Statement: Not applicable.

Data Availability Statement: The original contributions presented in this study are included in the article. Further inquiries can be directed to the corresponding author.

Conflicts of Interest: The authors declare no conflicts of interest.

Abbreviations

The following abbreviations are used in this manuscript:

PCB	Printed Circuit Board
LPI	Lines Per Inch
UT	Untreated
HT	Hydrophobic Pretreatment
OT	Oleophobic Pretreatment

References

1. Hu, R.; Liu, Y.; Shin, S.; Huang, S.; Ren, X.; Shu, W.; Cheng, J.; Tao, G.; Xu, W.; Chen, R.; et al. Emerging Materials and Strategies for Personal Thermal Management. *Adv. Energy Mater.* **2020**, *10*, 1903921. [CrossRef]
2. Caya, M.V.; Yrureta, R.G.; Chung, W.Y.; Flores-Payag, Z.P. Development of Conductive Thread Heating Element on Wireless Heating E-Textile Belt for Thermotherapy Application. *Automatika* **2021**, *62*, 293–299. [CrossRef]
3. Jia, J.; Xu, C.; Pan, S.; Xia, S.; Wei, P.; Noh, H.Y.; Zhang, P.; Jiang, X. Conductive Thread-Based Textile Sensor for Continuous Perspiration Level Monitoring. *Sensors* **2018**, *18*, 3775. [CrossRef]
4. Arquilla, K.; Webb, A.K.; Anderson, A.P. Textile Electrocardiogram (Ecg) Electrodes for Wearable Health Monitoring. *Sensors* **2020**, *20*, 1013. [CrossRef]
5. Moon, B.H.; Ryu, J.T. Efficient Placement of Pressure Sensors of a Sitting Cushion Stitched by Conductive Thread for Sitting Position. *Int. J. Adv. Sci. Eng. Inf. Technol.* **2021**, *11*, 603–609. [CrossRef]
6. Truong, T.; Kim, J.-S.; Kim, J. Design and Optimization of Embroidered Antennas on Textile Using Silver Conductive Thread for Wearable Applications. *Fibers Polym.* **2021**, *22*, 2900–2909. [CrossRef]
7. Shi, J.; Liu, S.; Zhang, L.; Yang, B.; Shu, L.; Yang, Y.; Ren, M.; Wang, Y.; Chen, J.; Chen, W.; et al. Smart Textile-Integrated Microelectronic Systems for Wearable Applications. *Adv. Mater.* **2020**, *32*, 1901958. [CrossRef]
8. Khan, A.; Winder, M.; Hossain, G. Modified Graphene-Based Nanocomposite Material for Smart Textile Biosensor to Detect Lactate from Human Sweat. *Biosens. Bioelectron. X* **2022**, *10*, 100103. [CrossRef]
9. Shi, X.; Zuo, Y.; Zhai, P.; Shen, J.; Yang, Y.; Gao, Z.; Liao, M.; Wu, J.; Wang, J.; Xu, X.; et al. Large-Area Display Textiles Integrated with Functional Systems. *Nature* **2021**, *591*, 240–245. [CrossRef]
10. Ferri, J.; Fuster, C.P.; Llopis, R.L.; Moreno, J.; Garcia-Breijo, E. Integration of a 2D Touch Sensor with an Electroluminescent Display by Using a Screen-Printing Technology on Textile Substrate. *Sensors* **2018**, *18*, 3313. [CrossRef] [PubMed]
11. Cherenack, K.; Van Pieterson, L. Smart Textiles: Challenges and Opportunities. *J. Appl. Phys.* **2012**, *112*, 091301. [CrossRef]
12. Wang, R.; Zhai, Q.; An, T.; Gong, S.; Cheng, W. Stretchable Gold Fiber-Based Wearable Textile Electrochemical Biosensor for Lactate Monitoring in Sweat. *Talanta* **2021**, *222*, 121484. [CrossRef]
13. Khan, A.; Haque, M.N.; Kabiraz, D.C.; Yeasin, A.; Rashid, H.A.; Sarker, A.C.; Hossain, G. A Review on Advanced Nanocomposites Materials Based Smart Textile Biosensor for Healthcare Monitoring from Human Sweat. *Sens. Actuators Phys.* **2023**, *350*, 114093. [CrossRef]

14. Júnior, H.L.O.; Neves, R.M.; Monticeli, F.M.; Dall Agnol, L. Smart Fabric Textiles: Recent Advances and Challenges. *Textiles* **2022**, *2*, 582–605. [CrossRef]
15. Islam, M.R.; Afroj, S.; Yin, J.; Novoselov, K.S.; Chen, J.; Karim, N. Advances in Printed Electronic Textiles. *Adv. Sci.* **2024**, *11*, 2304140. [CrossRef] [PubMed]
16. Liu, H.; Shi, Y.; Pan, Y.; Wang, Z.; Wang, B. Sensory Interactive Fibers and Textiles. *NPJ Flex. Electron.* **2025**, *9*, 23. [CrossRef]
17. He, P.; Cao, J.; Ding, H.; Liu, C.; Neilson, J.; Li, Z.; Kinloch, I.A.; Derby, B. Screen-Printing of a Highly Conductive Graphene Ink for Flexible Printed Electronics. *ACS Appl. Mater. Interfaces* **2019**, *11*, 32225–32234. [CrossRef] [PubMed]
18. Arapov, K.; Rubingh, E.; Abbel, R.; Laven, J.; De With, G.; Friedrich, H. Conductive Screen Printing Inks by Gelation of Graphene Dispersions. *Adv. Funct. Mater.* **2016**, *26*, 586–593. [CrossRef]
19. Hyun, W.J.; Secor, E.B.; Hersam, M.C.; Frisbie, C.D.; Francis, L.F. High-Resolution Patterning of Graphene by Screen Printing with a Silicon Stencil for Highly Flexible Printed Electronics. *Adv. Mater.* **2015**, *27*, 109–115. [CrossRef]
20. Ferri, J.; Llinares Llopis, R.; Moreno, J.; Vicente Lidón-Roger, J.; Garcia-Breijo, E. An Investigation into the Fabrication Parameters of Screen-Printed Capacitive Sensors on e-Textiles. *Text. Res. J.* **2020**, *90*, 1749–1769. [CrossRef]
21. Krykpayev, B.; Farooqui, M.F.; Bilal, R.M.; Vaseem, M.; Shamim, A. A Wearable Tracking Device Inkjet-Printed on Textile. *Microelectron. J.* **2017**, *65*, 40–48. [CrossRef]
22. Romaguera, V.S.; Madec, M.B.; Yeates, S.G. Inkjet Printing of Conductive Polymers for Smart Textiles and Flexible Electronics. *Mater. Res. Soc. Symp. Proc.* **2009**, *1192*, 15–20.
23. Loss, C.; Gonçalves, R.; Lopes, C.; Pinho, P.; Salvado, R. Smart Coat with a Fully-Embedded Textile Antenna for IoT Applications. *Sensors* **2016**, *16*, 938. [CrossRef] [PubMed]
24. Virkki, J.; Björninen, T.; Merilampi, S.; Sydänheimo, L.; Ukkonen, L. The Effects of Recurrent Stretching on the Performance of Electro-Textile and Screen-Printed Ultra-High-Frequency Radio-Frequency Identification Tags. *Text. Res. J.* **2015**, *85*, 294–301. [CrossRef]
25. Skarżyński, K.; Krzemiński, J.; Jakubowska, M.; Słoma, M. Highly Conductive Electronics Circuits from Aerosol Jet Printed Silver Inks. *Sci. Rep.* **2021**, *11*, 18141. [CrossRef] [PubMed]
26. Rao, C.H.; Avinash, K.; Varaprasad, B.K.S.V.L.; Goel, S. A Review on Printed Electronics with Digital 3D Printing: Fabrication Techniques, Materials, Challenges and Future Opportunities. *J. Electron. Mater.* **2022**, *51*, 2747–2765. [CrossRef]
27. Silvestre, R.; Garcia-Breijo, E.; Ferri, J.; Montava, I.; Bou-Belda, E. The Influence of the Structure of Cotton Fabrics on the Adhesion of Conductive Polymer Printed with 3D Printing Technology. *Polymers* **2023**, *15*, 668. [CrossRef]
28. Ding, C.; Wang, J.; Yuan, W.; Zhou, X.; Lin, Y.; Zhu, G.; Li, J.; Zhong, T.; Su, W.; Cui, Z. Durability Study of Thermal Transfer Printed Textile Electrodes for Wearable Electronic Applications. *ACS Appl. Mater. Interfaces* **2022**, *14*, 29144–29155. [CrossRef]
29. Nguyen, P.Q.M.; Yeo, L.P.; Lok, B.K.; Lam, Y.C. Patterned Surface with Controllable Wettability for Inkjet Printing of Flexible Printed Electronics. *ACS Appl. Mater. Interfaces* **2014**, *6*, 4011–4016. [CrossRef]
30. Roach, D.J.; Roberts, C.; Wong, J.; Kuang, X.; Kovitz, J.; Zhang, Q.; Spence, T.G.; Qi, H.J. Surface Modification of Fused Filament Fabrication (FFF) 3D Printed Substrates by Inkjet Printing Polyimide for Printed Electronics. *Addit. Manuf.* **2020**, *36*, 101544. [CrossRef]
31. Kim, S.; Sojoudi, H.; Zhao, H.; Mariappan, D.; McKinley, G.H.; Gleason, K.K.; Hart, A.J. Ultrathin High-Resolution Flexographic Printing Using Nanoporous Stamps. *Sci. Adv.* **2016**, *2*, e1601660. [CrossRef]
32. Wang, L.; Pan, Y.; He, D.; Qian, L.; Cao, X.; He, B.; Li, J. Conductive Polyester Fabrics with High Washability as Electrocardiogram Textile Electrodes. *ACS Appl. Polym. Mater.* **2022**, *4*, 1440–1447. [CrossRef]
33. Tao, X.; Koncar, V.; Huang, T.-H.; Shen, C.-L.; Ko, Y.-C.; Jou, G.-T.; Tao, X.; Koncar, V.; Huang, T.-H.; Shen, C.-L.; et al. How to Make Reliable, Washable, and Wearable Textronic Devices. *Sensors* **2017**, *17*, 673. [CrossRef]
34. Rubio, J.C.; Bolduc, M.; Rubio, J.C.; Bolduc, M. Screen Printing for Energy Storage and Functional Electronics: A Review. *Electron. Mater.* **2025**, *6*, 7. [CrossRef]
35. Dejene, B.K. Inkjet Printing of Conductive Nanomaterials on Textiles for Wearable Electronics: Advancements, Challenges, and Future Prospects. *Mater. Today Adv.* **2025**, *28*, 100629. [CrossRef]
36. Eghan, B.; Ofori, E.A.; Seidu, R.K.; Tawiah, B.; Acquaye, R. Systematic Review of Conductive Inks for E-Textiles: Formulation, Printing Methods, Challenges, and Opportunities. *AATCC J. Res.* **2025**, *12*, 24723444241303970. [CrossRef]
37. Islam, M.R.; Afroj, S.; Beach, C.; Islam, M.H.; Parraman, C.; Abdelkader, A.; Casson, A.J.; Novoselov, K.S.; Karim, N. Fully Printed and Multifunctional Graphene-Based Wearable e-Textiles for Personalized Healthcare Applications. *iScience* **2022**, *25*, 103945. [CrossRef] [PubMed]
38. Qi, X.; Luo, J.; Liu, H.; Fan, S.; Ren, Z.; Wang, P.; Yu, S.; Wei, J. Flexible Strain Sensors Based on Printing Technology: Conductive Inks, Substrates, Printability, and Applications. *Materials* **2025**, *18*, 2113. [CrossRef] [PubMed]
39. Yi, H.; Liu, Y.; Cao, H.; Luo, J.; Dong, X.; An, J.; Chua, C.K. Material and Process Integrated Innovations in Aerosol Jet Printing: A Review. *Mater. Today*, 2025; *in press*. [CrossRef]

40. Beniak, J.; Šooš, Ľ.; Križan, P.; Matúš, M.; Ruprich, V. Resistance and Strength of Conductive PLA Processed by FDM Additive Manufacturing. *Polymers* **2022**, *14*, 678. [CrossRef]
41. Manaia, J.P.; Cerejo, F.; Duarte, J. Revolutionising Textile Manufacturing: A Comprehensive Review on 3D and 4D Printing Technologies. *Fash. Text.* **2023**, *10*, 20. [CrossRef]
42. Zhong, Z.W.; Ee, J.H.; Chen, S.H.; Shan, X.C. Parametric Investigation of Flexographic Printing Processes for R2R Printed Electronics. *Mater. Manuf. Process.* **2020**, *35*, 564–571. [CrossRef]
43. Rodes-Carbonell, A.M.; Ferri, J.; Garcia-Breijo, E.; Montava, I.; Bou-Belda, E. Influence of Structure and Composition of Woven Fabrics on the Conductivity of Flexography Printed Electronics. *Polymers* **2021**, *13*, 3165. [CrossRef]
44. Rahmatinejad, J.; Khoddami, A.; Mazrouei-Sebdani, Z.; Avinc, O. Polyester Hydrophobicity Enhancement via UV-Ozone Irradiation, Chemical Pre-treatment and Fluorocarbon Finishing Combination. *Prog. Org. Coat.* **2016**, *101*, 51–58. [CrossRef]
45. Nadi, A.; Boukhriss, A.; Bentis, A.; Jabrane, E.; Gmouh, S. Evolution in the Surface Modification of Textiles: A Review. *Text. Prog.* **2018**, *50*, 67–108. [CrossRef]
46. Zhang, G.; Zhang, Q. Digital Imaging of the Oil Permeation Mechanism in an Oleophobic Textile. *Text. Res. J.* **2022**, *92*, 2662–2668. [CrossRef]
47. Melki, S.; Biguenet, F.; Dupuis, D. Hydrophobic Properties of Textile Materials: Robustness of Hydrophobicity. *J. Text. Inst.* **2019**, *110*, 1221–1228. [CrossRef]

polymers

MDPI

Article

A Composite Substrate of Ag Nanoparticle-Decorated Inverse Opal Polydimethylsiloxane for Surface Raman Fluorescence Dual Enhancement

Zilun Tang [1,2], Hongping Liang [2,*], Zhangyang Chen [1], Jianpeng Li [1], Jianyu Wu [3], Xianfeng Li [1] and Dingshu Xiao [1,2,*]

[1] School of Chemistry and Materials Engineering, Huizhou University, Huizhou 516007, China; tangzl@hzu.edu.cn (Z.T.); 18928934633@163.com (Z.C.); lijp@hzu.edu.cn (J.L.); lxfeng@hzu.edu.cn (X.L.)
[2] Guangdong Provincial Key Laboratory of Electronic Functional Materials and Devices, Huizhou University, Huizhou 516007, China
[3] Science and Technology on Reliability Physics and Application of Electronic Component Laboratory, China Electronic Product Reliability and Environmental Testing Research Institute, Guangzhou 511370, China; wujianyu@ceprei.com
* Correspondence: lianghp@hzu.edu.cn (H.L.); hgyjy@hzu.edu.cn (D.X.)

Abstract

It is difficult to simultaneously achieve surface-enhanced Raman scattering (SERS) and surface-enhanced fluorescence (SEF) for noble metals. Herein, a composite substrate is demonstrated based on the rational construction of Ag nanoparticles (Ag NPs) and inverse opal polydimethylsiloxane (PDMS) for surface Raman fluorescence dual enhancement. The well-designed Ag nanoparticle (Ag NP)-decorated inverse opal PDMS (AIOP) composite substrate is fabricated using the polystyrene (PS) photonic crystal method and the sensitization reduction technique. The inverse opal PDMS enhances the electromagnetic (EM) field by increasing the loading of Ag NPs and plasmonic coupling of Ag NPs, leading to SERS activity. The thin shell layer of polyvinyl pyrrolidone (PVP) in core–shell Ag NPs isolates the detected molecule from the Ag core to prevent the fluorescence resonance energy transfer and charge transfer to eliminate fluorescence quenching and enable SEF performance. Based on the blockage of the core–shell structure and the enhanced EM field originating from the inverse opal structure, the as-fabricated AIOP composite substrate shows dual enhancement in surface Raman fluorescence. The AIOP composite substrate in this work, which combines improved SERS activity and SEF performance, not only promotes the development of surface-enhanced spectroscopy but also shows promise for applications in flexible sensors.

Keywords: surface-enhanced Raman scattering; surface-enhanced fluorescence; polymer-based composite substrate; Ag nanoparticle; inverse opal structure

1. Introduction

Surface-enhanced spectroscopy is a highly important technology in analysis; it is essential for environmental monitoring [1,2], biochemical detection [3–5], and food safety [6,7]. Surface-enhanced Raman scattering (SERS) and surface-enhanced fluorescence (SEF) are two types of surface-enhanced spectroscopy that offer the benefits of high sensitivity, anti-photobleaching, and anti-interference [8–13]. In practical applications, SERS and SEF technologies are more competitive and promising than other surface-enhanced spectroscopy methods.

To the best of our knowledge, the electrons on the surface of noble metals are able to generate surface plasmon resonance (SPR) with the incidence of external light, leading to an improved electromagnetic (EM) field on the surface of noble metals [14–16]. The improved EM field can greatly increase the Raman scattering and fluorescence intensity of the detected molecules [17–20]. Theoretically, noble metals are considered ideal candidates for SERS and SEF technologies. Because Ag has the best SPR, it is the most widely used noble metal at present. To further improve the EM field, the optimization of noble metals' nanostructure and the composite of multiple noble metals are applied to improve plasmonic coupling [10,18,21–23]. In addition, noble metals have been incorporated into flexible substrates, such as PDMS [24–26], polyurethane (PU) [14,27], and poly (vinyl alcohol) (PVA) [28–30], to extend the application field in flexible sensors.

Generally, the detected molecules contact the surface of noble metals directly, which is beneficial for SERS but unfavorable for SEF. More specifically, the direct contact between detected molecules and a noble metal can promote their charge transfer, which can increase the Raman scattering intensity of the detected molecules [31,32]. However, fluorescence resonance energy transfer and charge transfer occur between detected molecules and noble metals because of their direct contact, leading to fluorescence quenching instead of enhanced fluorescence [33–36]. The noble metals that exhibit improved SERS activity tend to show limited SEF performance. To ensure improved SEF performance, an insulating layer was introduced to the surface of noble metals to avoid the occurrence of fluorescence resonance energy transfer and charge transfer [37–39]. However, the introduction of this layer inhibits the charge transfer between the detected molecules and the noble metal, reducing the SERS activity [40,41]. Thus, most studies only focus on SERS activity or SEF performance, and there are few reports regarding noble metals for surface Raman fluorescence dual enhancement. The development of strategies to endow noble metals with both improved SERS activity and SEF performance can promote the development of surface-enhanced spectroscopy.

In this work, a sacrificial polystyrene (PS) photonic crystal method was employed to fabricate the inverse opal PDMS, and the surface was decorated with Ag nanoparticles (Ag NPs) using the sensitization reduction method to obtain a Ag nanoparticle (Ag NP)-decorated inverse opal PDMS (AIOP) composite substrate. As shown in Scheme 1, a glass wafer with air plasma treatment was vertically placed into a diluted PS nanoparticle suspension. As the water solvent evaporated, the PS nanoparticles were deposited onto the surface of the glass wafer to form highly ordered PS photonic crystals. PDMS was selected as the flexible polymer substrate and drop-coated onto the surface of PS photonic crystals. After curing and peeling off, the PS/PDMS composite film was immersed in a solution of N, N-dimethylformamide (DMF) to etch the PS nanoparticles. The sample was removed and air-dried to obtain an inverse opal film. The obtained film was immersed in $SnCl_2$/HCl solution to anchor Sn^{2+} onto its surface. After that, the inverse opal film with the surface-anchoring Sn^{2+} was immersed in a $AgNO_3$/PVP solution for the growth of Ag NPs. Finally, the sample was removed, cleaned with deionized water, and air-dried to obtain the AIOP composite substrate. Because of the increased loading of Ag NPs onto the inverse opal structure and their improved plasmonic coupling from Ag NPs, as well as the fluorescence quenching prevented by their core–shell structure, the AIOP composite substrate exhibited surface Raman fluorescence dual enhancement, offering ideas for the study of noble metal-based dual-enhanced spectroscopy.

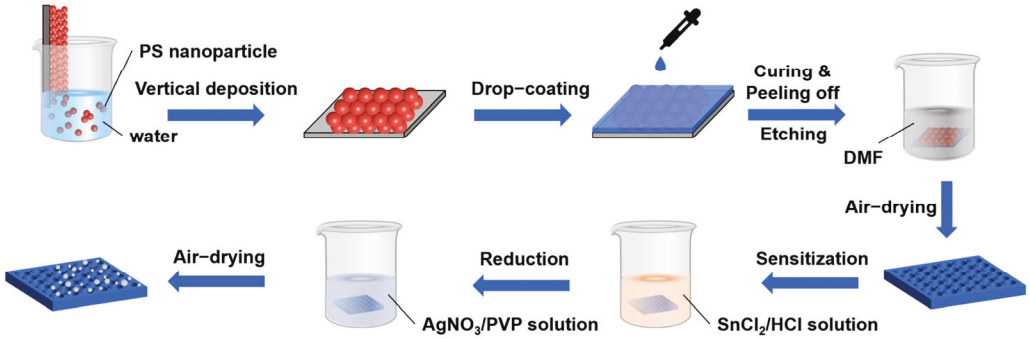

Scheme 1. Schematic process of fabrication of AIOP composite substrate.

2. Materials and Methods

2.1. Materials

Styrene, methylacrylic acid (MAA), potassium persulfate (KPS, 99.5%), polyvinyl pyrrolidone (PVP, 58000, K29-32), stannous chloride ($SnCl_2$, 99%), Rhodamine 6G (R6G), malachite green (MG), and crystal violet (CV) were purchased from Shanghai Macklin Biochemical Technology Co., Ltd. (Shanghai, China). PDMS prepolymer with curing agent (DC 184) was obtained from Dow Corning (Midland, MI, USA). Sodium dodecyl sulfate (SDS, ≥90.0%) and silver nitrate ($AgNO_3$, ≥99.8%) were purchased from Sinopharm Chemical Reagent Co., Ltd. (Shanghai, China). Hydrochloric acid (HCl) and N, N-dimethylformamide (DMF, 99.5%) were obtained from Guangzhou Chemical Reagent Factory (Guangzhou, China). Regioregular poly (3-hexylthiophene) (P3HT) was purchased from Luminescence Technology Corp (Hsinchu, China). All reagents and materials were used as received without further purification.

2.2. Synthesis of PS Nanoparticles

PS nanoparticles were synthesized according to our previous study [42]. Specifically, MAA (0.045 mL) and SDS (15 mg) were dissolved in deionized water (60 mL). When the above mixed solution was heated to 60 °C, styrene monomers were added and stirred for 30 min. The mixed solution was further heated to 80 °C. After that, 0.1 g/mL KPS aqueous solution was slowly added to the mixed solution and stirred for 10 h at 80 °C to obtain PS nanoparticles.

2.3. Preparation of PS/PDMS Composite Film

A total of 200 μL PS nanoparticle solution was added to 60 mL deionized water and stirred well to form dilute PS solution. The glass wafer was treated with air plasma for 10 min and then vertically placed into the dilute PS solution. As the water solvent evaporated, PS nanoparticles formed into a highly ordered nanostructure on the surface of the glass wafer. The mixture of PDMS prepolymer and curing agent in a ratio of 10:1 in mass was dropped onto the prepared highly ordered PS nanostructure. After curing at 60 °C in a vacuum oven for 12 h, the PS/PDMS composite film was obtained by peeling it off.

2.4. Fabrication of AIOP Composite Substrate

PS/PDMS composite film was immersed in DMF solution for 2 h. Based on the etching of DMF on PS, the inverse opal PDMS was obtained. Then, the inverse opal PDMS was removed from the DMF solution and dried naturally. In accordance with the sensitization reduction method in previous work [43], the resultant inverse opal PDMS was first immersed in $SnCl_2$/HCl solution (0.02 mol/L) for 1 min and then immersed in

Ag NO_3/PVP solution (0.01 mol/L) for 1 min. Finally, the AIOP composite substrate was obtained by cleaning it with deionized water and air-drying.

2.5. Characterization

The morphologies of PS nanoparticles, the PS/PDMS composite film, the inverse opal PDMS, and the AIOP composite substrate were observed with a scanning electron microscope (SEM, SU8010, Hitachi, Tokyo, Japan). The morphologies of Ag NPs and their crystal structures were measured using a transmission electron microscope (TEM, JEM-F200, JEOL, Tokyo, Japan). The chemical structure of PS nanoparticles was characterized with a Fourier transform infrared (FTIR) spectrometer (IS50R, Thermo Fisher, Waltham, MA, USA). The cavity depth of the inverse opal PDMS was determined with atomic force microscopy (AFM, Dimension FastScan, Bruker, Billerica, MA, USA). The surface analysis of the AIOP composite substrate was investigated using X-ray diffraction (XRD, miniflex600, Rigaku, Tokyo, Japan) with Cu Kα radiation at a Bragg angle ranging from 10 to 90° and X-ray photoelectron spectroscopy (XPS, Escalab 250Xi, Thermo Fisher, Waltham, MA, USA). The UV-Vis spectra of the AIOP composite substrate and regioregular P3HT were obtained using an ultraviolet spectrophotometer (UV-2600i, Shimadzu, Kyoto, Japan). The reflection spectra of PS nanoparticles after self-assembly and the PS/PDMS composite were obtained with a fiber spectrometer (PG2000-Pro-EX, Shanghai Fuxiang Optics Co., Ltd., Shanghai, China).

2.6. SERS and SEF Measurement

R6G was dissolved in deionized water to obtain aqueous solutions of different concentrations, from 1×10^{-4} M to 1×10^{-7} M, while MG and CV were dissolved in the deionized water to form an aqueous solution with a concentration of 1×10^{-4} M. The Raman spectra of R6G, MG, and CV on pure PDMS, Ag NP-decorated PDMS, and the AIOP composite substrate were collected using a micro confocal Raman spectrometer (in Via, RENISHAW, Wotton-under-Edge, UK) with a 633 nm excited laser and a 50× objective lens. The Raman measurements were performed with a 10 s acquisition time for one accumulation. A 633 nm excited laser was focused on a random area of 25×25 μm^2 using a 50× objective lens, and the peak of R6G at 1360 cm^{-1} was selected as the characteristic Raman signal for Raman mapping. The acquisition time was 10 s for one accumulation, and Raman mapping with a solution of 5×5 pixels was obtained. The fluorescence emission spectra of regioregular P3HT on the samples were measured with a fluorescence spectrometer (FLS1000, Edinburgh Instruments, Livingston, UK) ranging from 680 to 800 nm. A Xe lamp was used as the excited source, and its wavelength was set to 448 nm.

2.7. EM Field Simulation

EM field distributions among core–shell Ag NPs were calculated using COSMOL Multiphysics. Simulation models were constructed of the decoration of Ag NPs with a diameter ranging from 10 to 50 nm on the inverse opal PDMS and flat PDMS, which were arranged in the x–z plane. The wavelengths of incident plane waves were set at 633 and 448 nm, and the incident plane waves were polarized along the *x*-axis and incident along the *z*-axis.

3. Results and Discussion

3.1. Characterization of PS Nanoparticles

The morphology of as-synthesized PS nanoparticles is shown in Figure 1a. The PS nanoparticles had a spherical shape with a uniform particle size. Without any post-treatment, the as-synthesized PS nanoparticles were in a disordered arrangement. Accord-

ing to the size distribution histogram in Figure 1b, the diameter of the PS nanoparticles was 251 nm.

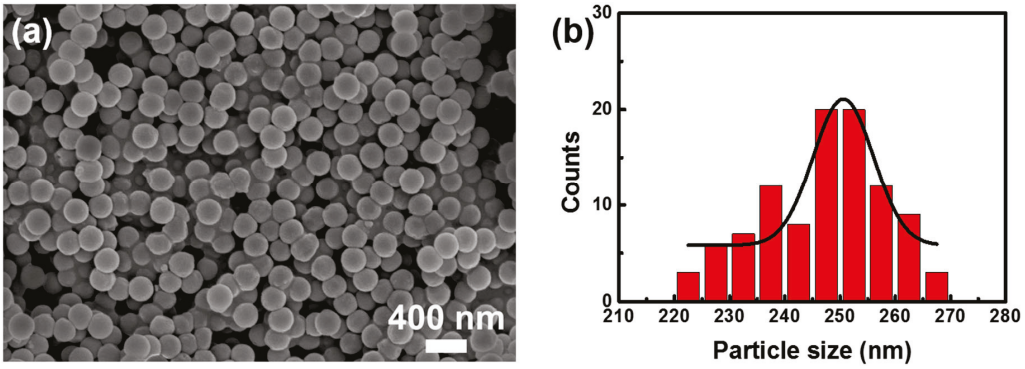

Figure 1. (**a**) SEM image and (**b**) size distribution histogram of PS nanoparticles.

To reveal the chemical structure of the PS nanoparticles, we used FTIR spectrometry (Figure S1). The absorption peaks at 1600, 1492, and 1450 cm^{-1} were attributed to the bending vibrations of the benzene ring skeleton. The absorption peaks at 3442, 1381, 912, and 1697 cm^{-1} were attributed to the stretching vibrations of -OH and -C=O in carboxyl groups [44]. These results confirmed that PS nanoparticles were successfully synthesized.

3.2. Self-Assembly and Transfer of PS Nanoparticles on PDMS

The PS photonic crystals on the glass wafer were formed via the self-assembly of vertical deposition, which shows an obvious structural color of green (Figure 2a). The reflection peak of the PS photonic crystals on the glass wafer was located at 526 nm (Figure S2a), which was within the wavelength range of green light [45]. Figure 2b shows an SEM image of the PS nanoparticles after self-assembly. They were arranged in an ordered hexagonal structure. As a result, Bragg diffraction was achieved, leading to the green structural color.

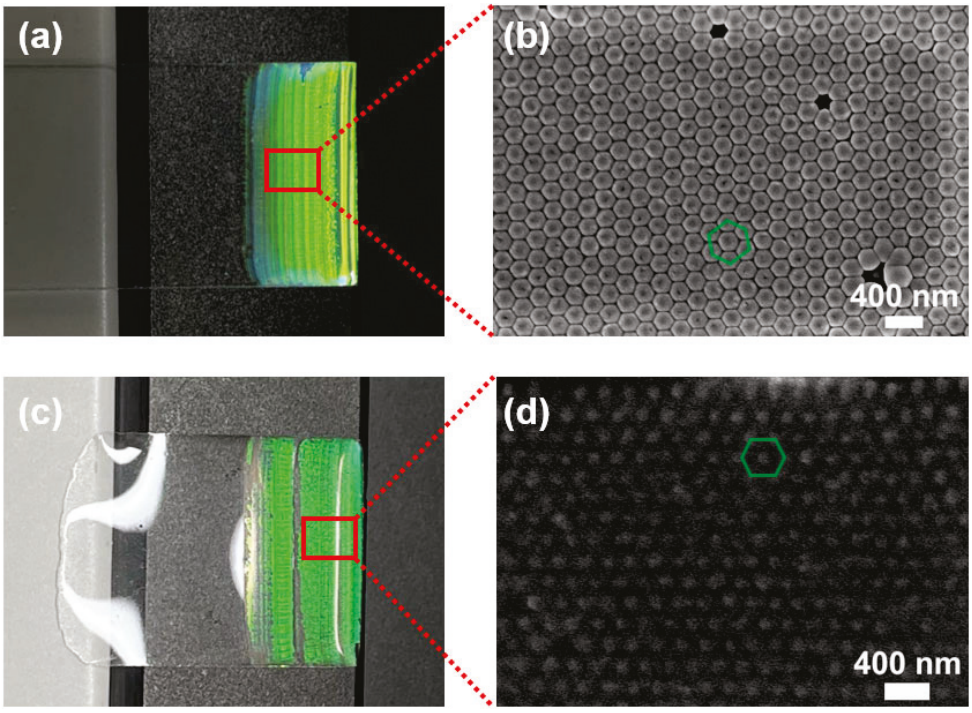

Figure 2. (**a**) Photograph and (**b**) SEM image of PS nanoparticles after self-assembly; (**c**) photograph and (**d**) SEM image of PS/PDMS composite film.

In this study, PDMS was chosen as the flexible substrate for PS photonic crystals. After transferring the PS photonic crystals onto PDMS, the PS/PDMS composite showed a green structural color (Figure 2c), and its reflection peak was in the wavelength range of green light, as before (Figure S2b). Figure 2d presents an SEM image of the PS/PDMS composite film. Each PS nanoparticle was partly embedded in the PDMS, while the remaining portion was exposed to the outside. The PS nanoparticles remained in a hexagonal arrangement, which indicated that the ordered hexagonal structure of the PS photonic crystals was not affected by the introduction of PDMS. All of these results confirmed that the PS nanoparticles with an ordered hexagonal arrangement were successfully transferred onto the PDMS substrate. Although PS photonic crystals had been transferred onto the PDMS substrate, the glass wafer after the transfer of PS photonic crystals still exhibited a green structural color (Figure S3), indicating that the transfer was incomplete.

3.3. Characterization and Surface Analysis of AIOP Composite Substrate

For PS/PDMS composite film, DMF is a good solvent for PS, but it does not provide a solvent for PDMS. Therefore, PS can be selectively etched with DMF to obtain the inverse opal PDMS, which is shown in Figure 3a. A monolayer of cavities was observed on the surface of PDMS. The cavities were still arranged in an ordered hexagonal structure, which illustrated that the arrangement of the PS nanoparticles was not destroyed by DMF during etching. The refractive index of air is 1.0, while that of PDMS is 1.4. There is a small refractive index difference (Δn = 0.4) between air and PDMS, which has an adverse effect on Bragg diffraction, resulting in weakened reflection. In addition, the obtained inverse opal structure consisted of cavities instead of complete spherical structures, which also resulted in weakened reflection. Thus, the inverse opal PDMS had no structural color, which is shown in the inset of Figure S4.

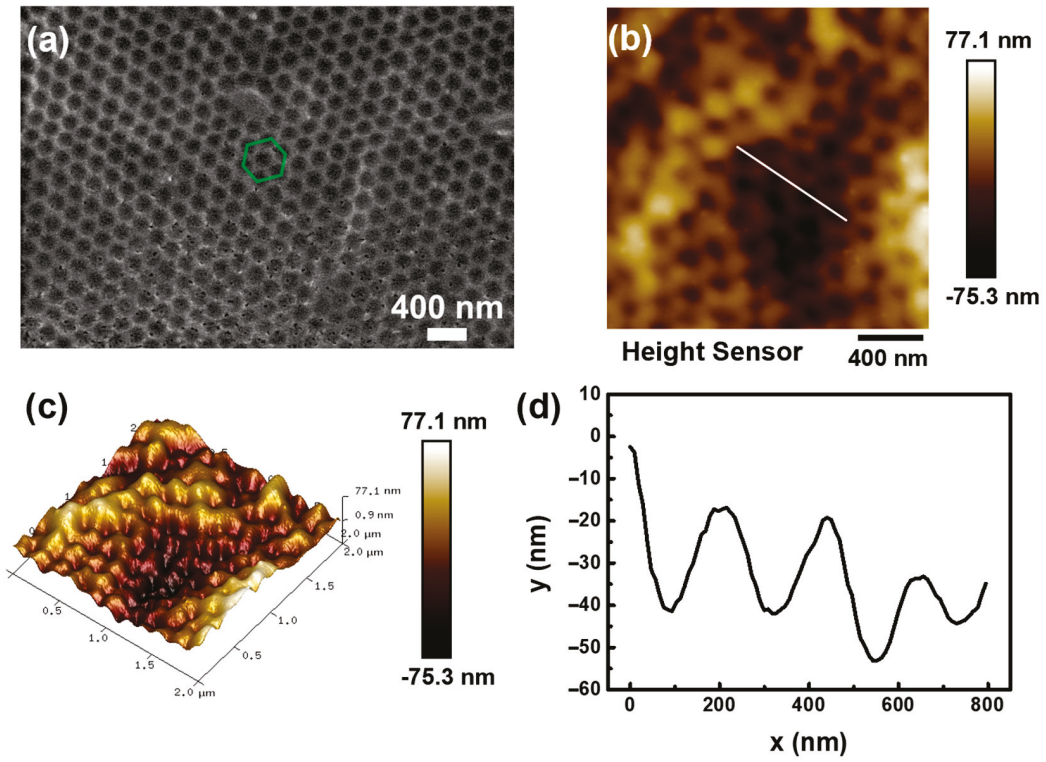

Figure 3. (**a**) SEM, (**b**) 2D, and (**c**) 3D AFM height images of the inverse opal PDMS; (**d**) roughness variation along the white line indicated in (**b**).

To measure the diameter and depth of the cavities, a roughness test was carried out. Figure 3b,c present 2D and 3D AFM height images of the inverse opal PDMS. The spherical dispersed phase consisted of cavities resulting from the etching of DMF on PS nanoparticles, while the continuous phase was a PDMS matrix. Figure 3d shows the roughness variation along the white line indicated in Figure 3b. The average diameter of the cavities was 200 nm—smaller than the 251 nm diameter of the PS nanoparticles—with an average depth of 40 nm. These results confirmed that the inverse opal PDMS was successfully fabricated.

As shown in Figure S5, only parts of the flat PDMS surface were decorated with Ag NPs. Because of its hydrophobicity [46,47], the flat PDMS could not be wetted by the Ag growth solution, leading to only parts of spots being decorated. Figure 4a shows the morphologies of the AIOP composite substrate. More spots of the inverse opal PDMS were decorated with Ag NPs because the inverse opal PDMS provided a higher surface area for the wetting of the Ag growth solution. Thus, the inverse opal structure was able to improve the loading of Ag NPs. Despite the higher surface area in contact with the Ag growth solution, certain spots remained uncovered by Ag NPs on the inverse opal PDMS surface. As shown in the inset of Figure 4a, Ag NPs with diameters ranging from 10 to 50 nm were distributed on the outer surface of cavities, whereas no Ag NPs were found on the inner surface of cavities. The Ag growth solution could not penetrate into the inner surface of the cavities due to its hydrophobicity in relation to PDMS. Instead, the Ag growth solution could only enrich near the rim of the cavities, leading to the aggregation of Ag NPs on their outer surface. Figure 4b shows the absorption spectrum of the AIOP composite substrate and Ag NP-decorated PDMS. The absorption peak at 450 nm was detected and attributed to the plasmon resonance of Ag NPs [48]. In comparison, the intensity of the plasmonic peak for the AIOP composite substrate was stronger than the Ag NP-decorated PDMS. Figure 4c, d present STEM and TEM images of Ag NPs from the AIOP composite substrate, which indicate that the Ag NPs possess a core–shell structure. During the fabrication of the AIOP composite substrate, PVP was introduced to the oxidation reduction of Ag NPs. On the one hand, PVP played an important role in protecting Ag NPs. On the other hand, PVP was able to facilitate the anchoring of Sn^{2+} onto the surface of Ag NPs, which was beneficial for the growth of Ag NPs. Therefore, the Ag NPs were encapsulated by the thin layer of PVP. As shown in Figure 4e, the d-spacing of the lattice fringe of the Ag NPs was 0.233 nm, which was attributed to the (111) plane of Ag NPs [49].

The surface elements of the AIOP composite substrate were measured with XPS. Figure 5a shows the XPS survey spectrum of the AIOP composite substrate. The C, O, Si, Ag, and Sn elements were detected. The C, O, and Si elements originated from the PDMS, while the Ag element originated from the Ag NPs. Because Ag NPs were prepared from the oxidation of Sn^{2+}, the appearance of the Sn element on the AIOP composite substrate was inevitable. Figure 5b shows the high-resolution XPS spectrum of the Ag 3d binding energy. Two peaks were detected at the positions of 373.8 and 367.8 eV, which corresponded to the peaks of Ag 3d3/2 and Ag 3d5/2, respectively [50]. Figure 5c,d present the XRD patterns of pure PDMS and AIOP composite substrate. In comparison, there was a weak peak at 38.15° for the diffraction pattern of the AIOP composite substrate, which corresponded to the (111) fraction direction of the Ag NPs [51], agreeing with the test results from HRTEM images of Ag NPs from AIOP composite substrate (Figure 4e). Because of the small size and core–shell structure of Ag NPs, only the diffraction peak of the (111) plane was detected in the XRD pattern of the AIOP composite substrate. The above SEM, STEM, TEM, UV-Vis, XPS, and XRD results confirmed the successful fabrication of AIOP composite substrate.

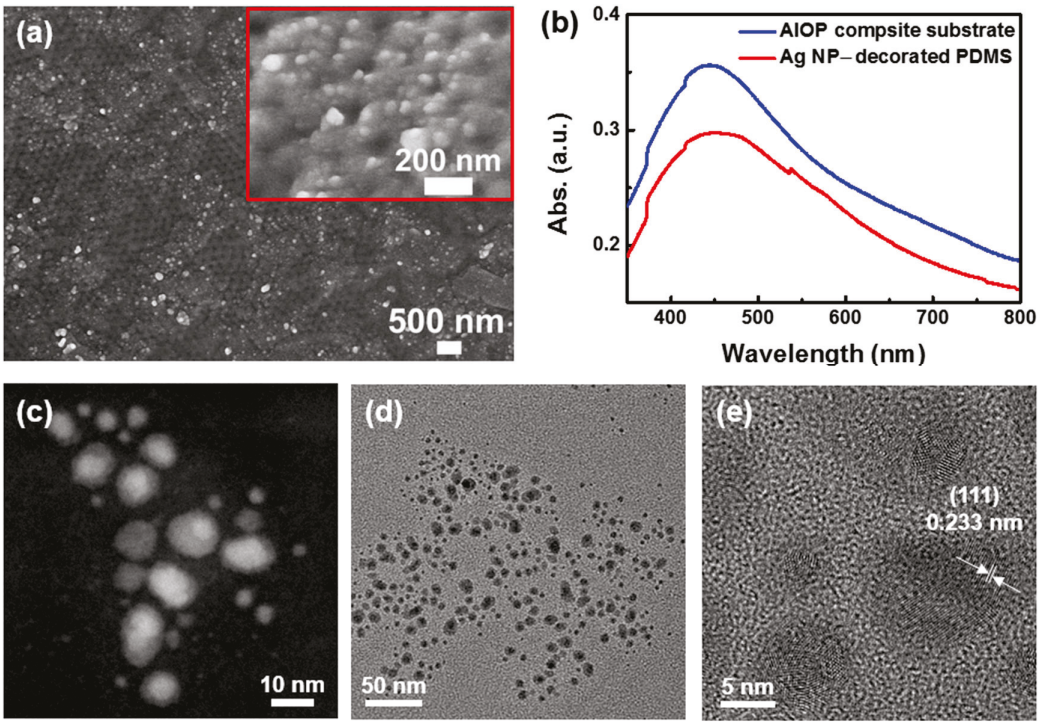

Figure 4. (**a**) SEM image of AIOP composite substrate; (**b**) absorption spectra of AIOP composite substrate and Ag NP-decorated PDMS; (**c**) STEM, (**d**) TEM, and (**e**) HRTEM images of Ag NPs from AIOP composite substrate.

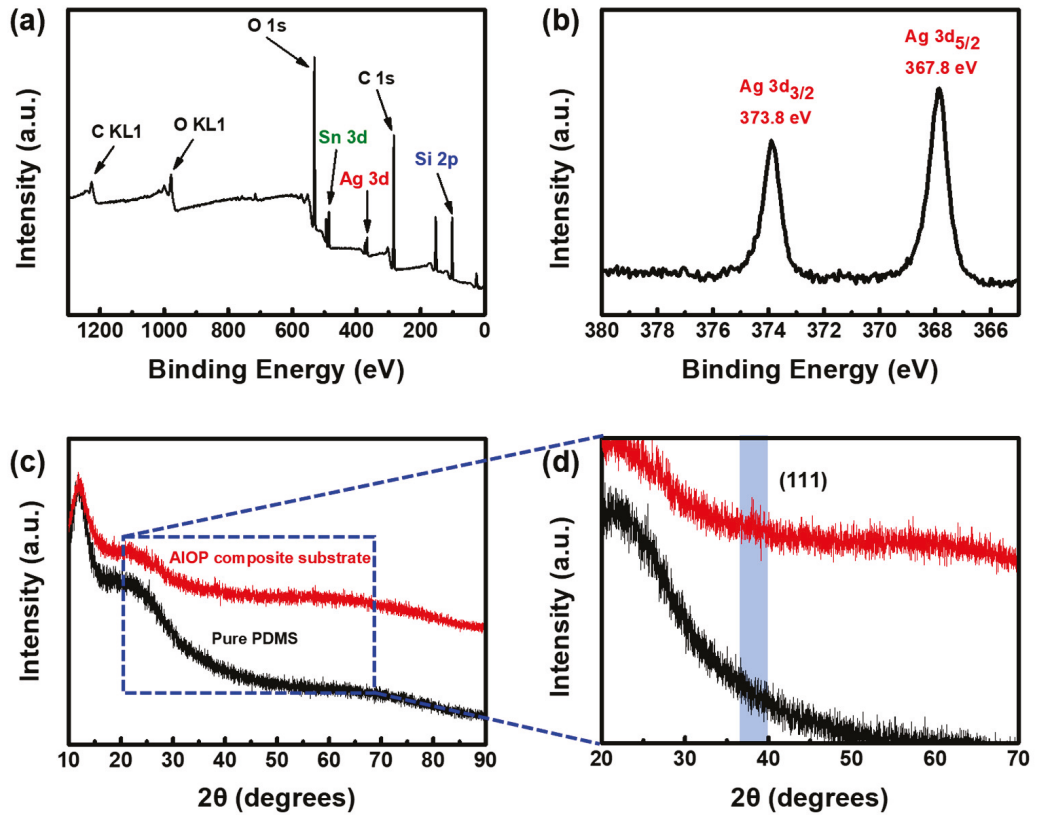

Figure 5. (**a**) XPS survey spectrum of AIOP composite substrate; (**b**) high-resolution XPS spectrum of Ag 3d binding energy; (**c**) XRD patterns of pure PDMS and AIOP composite substrate; (**d**) enlargement of the XRD patterns at specified positions for pure PDMS and AIOP composite substrate.

3.4. SERS Activity of AIOP Composite Substrate

To evaluate the SERS activity of AIOP composite substrate, Raman measurements of R6G probe molecule (1×10^{-4} M) were conducted on pure PDMS, Ag NP-decorated PDMS, and AIOP composite substrate, and a 633 nm excited laser was selected to ensure the Raman signals of R6G and reduce the interference of its fluorescence in Raman scattering (Figure 6a). Notably, the Raman characteristic peaks of R6G were clearly observed on the substrates of Ag NP-decorated PDMS and AIOP composite substrate, whereas the Raman characteristic peaks of R6G were not detected on pure PDMS substrate, even when magnified five times. The Raman peaks at 770 and 1187 cm^{-1} were attributed to C−H out-plane bending and C−H/N−H xanthene ring bending, while the Raman peak at 1306 cm^{-1} was due to C=C stretching. The Raman peaks at 1360 and 1502 cm^{-1} were attributed to C−C xanthene ring stretching, while the Raman peak at 1650 cm^{-1} was a result of C−C in-plane stretching (Table S1) [52,53]. In comparison, the AIOP composite substrate exhibited greater SERS activity than the Ag NP-decorated PDMS.

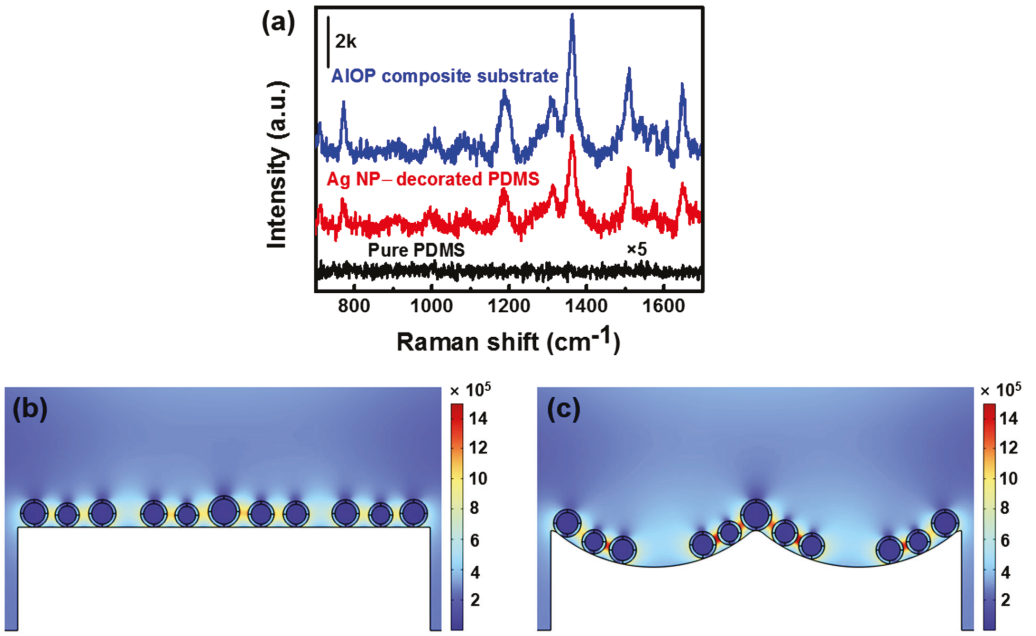

Figure 6. (**a**) Raman spectra of R6G (1×10^{-4} M) on pure PDMS, Ag NP-decorated PDMS, and AIOP composite substrate; EM field distributions of cross-section of (**b**) Ag NP-decorated PDMS and (**c**) AIOP composite substrate under excitation of 633 nm.

As shown in Figure 4c,d, the Ag NP-decorated inverse opal PDMS exhibited a core–shell structure, where Ag served as the core and PVP served as the shell. The PVP shell increased the distance of Ag NPs, which resulted in decreased plasmonic coupling between adjacent Ag NPs. As shown in Figure 6b, plasmonic coupling still occurred between adjacent Ag NPs on the flat PDMS despite the presence of the PVP shell. Based on the inverse opal structure, together with the hydrophobicity of PDMS, Ag NPs aggregated near the outer surface of cavities. The spacing between the aggregated Ag NPs was reduced for the AIOP composite substrate, which improved the plasmonic coupling to enhance the overlap of the EM field between adjacent Ag NPs. As shown in Figure 6c, the AIOP composite substrate exhibited stronger plasmonic coupling compared with the decoration of Ag NPs on the flat PDMS. Because of the higher loading of Ag NPs and the stronger interparticle plasmonic coupling, the intensity of the plasmonic peak for the AIOP composite substrate was stronger than that of the Ag NP-decorated PDMS (Figure 4b),

and Ag NPs on inverse opal PDMS exhibited greater SERS performance than those on flat PDMS (Figure 6a).

Typically, SERS enhancement mechanisms can be divided into the EM mechanism and the chemical mechanism (CM), where the EM mechanism originates from SPR in noble metals, while the CM mechanism relates to the charge transfer between the Raman probe molecule and the substrate surface [54]. The PVP shell blocked the charge transfer between Raman probe molecules and Ag NPs, which reduced the SERS activity via the CM mechanism. In contrast, the inverse opal structure from the AIOP composite substrate improved SERS activity via the EM mechanism [55]. It is well-established that the EM mechanism plays a predominant role in SERS activity compared with the CM mechanism. The inverse opal structure in the AIOP substrate improved SERS activity via increased loading of Ag NPs and enhanced plasmonic coupling between Ag NPs, compensating for SERS activity loss from the core–shell structure of Ag NPs. Therefore, the AIOP composite substrate still exhibited the improved SERS activity. In addition, the PVP shell was anchored onto the surface of Ag via strong chemical coordinate bonds, which prevented the whole PVP segment from detaching from the Ag NPs and dissolving [56,57]. Therefore, core–shell Ag NPs could stably exist in water, and the structural stability of the PVP shell layer remained unaffected during SERS measurements. We chose MG and CV as other analytes to investigate the SERS performance of pure PDMS, Ag NP-decorated PDMS, and the AIOP composite substrate (Figure S7). The Raman characteristic peaks of MG (916, 1171, 1294, 1365, 1589, 1641 cm^{-1}) and CV (915, 1171, 1371, 1531, 1629 cm^{-1}) were observed on the substrates of Ag NP-decorated PDMS and the AIOP composite substrate (Tables S2 and S3). Consistent with the results above, the AIOP composite substrate exhibited greater SERS activity.

To investigate the SERS sensitivity of the AIOP composite substrate, Raman measurements of R6G with serially diluted concentrations were carried out. As shown in Figure S3a, the Raman peaks at 770 and 1360 cm^{-1} were still observed even if the concentration of R6G decreased to 1×10^{-7} M. Thus, it can be concluded that the SERS sensitivity of the prepared AIOP composite substrate for R6G is 1×10^{-7} M. The Raman peak at 1360 cm^{-1} and the region of 25×25 μm^2 from the AIOP composite substrate were selected for Raman mapping. Figure S3b shows the Raman mapping at a resolution of 5×5 pixels of R6G (1×10^{-4} M) on the AIOP composite substrate. Few parts of spots exhibited low Raman intensity with a black color, which was due to the uneven distribution of Ag NPs on the AIOP composite substrate (Figure 4a). Overall, most of the spots exhibited similar blue colors, which demonstrated that their SERS activities were close to each other.

3.5. SEF Performance of AIOP Composite Substrate

In this study, regioregular P3HT was chosen as a fluorescence probe molecule to investigate SEF performance. Figure 7a shows the absorption spectrum of regioregular P3HT. It can be seen that the peaks at 265 and 448 nm appeared in this spectrum. The peak at 448 nm was stronger and very close to the plasmonic resonance peak of Ag NPs (Figure 4b), which was favorable for the improvement of the regioregular P3HT fluorescence excited rate.

Regioregular P3HT was dissolved in trichloromethane to form a mixed solution (1 mg/mL) and then spin-coated on the AIOP composite substrate. The excitation wavelength at 448 nm was chosen for the fluorescence test of regioregular P3HT. Figure S4 presents the fluorescence spectra of the AIOP composite substrate. There were no peaks for this substrate, which indicated that fluorescence did not occur in it with a wavelength range from 680 to 800 nm. Figure 7b shows the fluorescence spectrum of regioregular P3HT on pure PDMS, Ag NP-decorated PDMS, and the AIOP composite substrate. The fluorescence emission peaks at 725 nm of regioregular P3HT were detected in all substrates,

corresponding to the (0–1) transition of regioregular P3HT [58]. The fluorescence emission peak of regioregular P3HT was strongest on the AIOP composite substrate, followed by Ag NP-decorated PDMS, and weakest on pure PDMS.

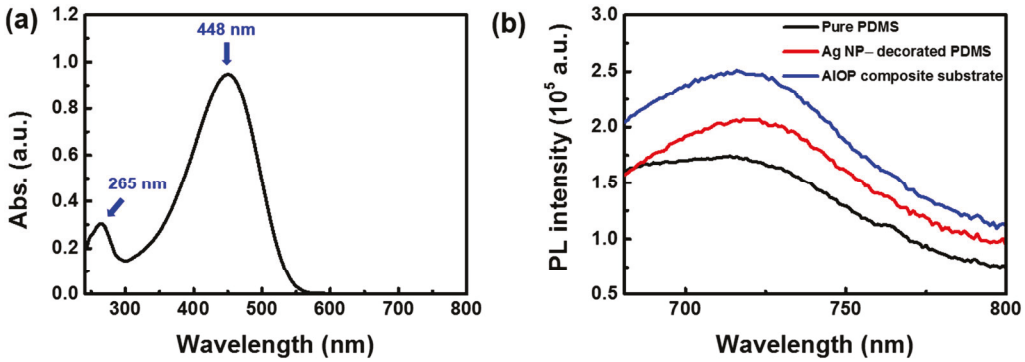

Figure 7. (**a**) Absorption spectrum of regioregular P3HT in trichloromethane; (**b**) fluorescence spectra of regioregular P3HT ranging from 680 to 800 nm on pure PDMS, Ag NP-decorated PDMS, and AIOP composite substrate.

The STEM and TEM images in Figure 4c,d indicate that the Ag NPs on the AIOP composite substrate had a core–shell structure, with Ag as the core and PVP as the shell. Because of the blocking of a thin layer of PVP, the fluorescence probe molecule P3HT was not directly in contact with Ag. There was no fluorescence resonance energy transfer or charge transfer between P3HT and Ag, avoiding the occurrence of fluorescence quenching. Under the excitation of 448 nm, strong plasmonic coupling still occurred between adjacent Ag NPs on the AIOP composite substrate. This plasmonic coupling was stronger than that of Ag NP-decorated PDMS, which is shown in Figure S5a,b. In addition, the inverse opal structure was able to improve the loading of Ag NPs. The blocking of PVP, the stronger plasmonic coupling, and the improved loading of Ag NPs improved the SEF performance of the AIOP composite substrate.

Overall, the Raman fluorescence dual enhancement of probe molecules of the AIOP composite substrate in this study can be achieved. In view of the combination of SERS activity and SEF performance, this work provides functional diversity for surface-enhanced spectroscopy. In addition, the AIOP composite substrate is fabricated based on a PDMS flexible polymer substrate. It is expected that this polymer-based material can be used in the practical application of flexible sensors.

4. Conclusions

In summary, we developed a polymer-based composite substrate of Ag NP-decorated inverse opal PDMS for surface Raman fluorescence dual enhancement. The AIOP composite substrate was fabricated using the sacrificial PS photonic crystals method and the sensitization reduction method. The inverse opal structure in the AIOP composite substrate improved the loading of Ag NPs and increased the plasmonic coupling of Ag NPs to compensate for the weakness in SERS activity originating from the core–shell structure of the Ag NPs, which improved the SERS activity of the AIOP composite substrate. Meanwhile, the core–shell structure of Ag NPs avoided the occurrence of fluorescence resonance energy transfer and charge transfer between detected molecules and Ag, which prevented fluorescence quenching, leading to SEF performance. The obtained AIOP composite substrate exhibited SERS activity and SEF performance simultaneously. This study is significant for the development of surface-enhanced spectroscopy and has promising application prospects in the field of flexible sensors.

Supplementary Materials: The following supporting information can be downloaded at https://www.mdpi.com/article/10.3390/polym17141995/s1: Figure S1: FTIR spectrum of PS nanoparticles; Figure S2: Reflection spectra of (a) PS nanoparticles after self-assembly and (b) PS/PDMS composite film; Figure S3: Photograph of the glass wafer after the transfer of PS photonic crystals; Figure S4: Photograph of the PS/PDMS composite film (a) before and (b) after the etching of DMF; Figure S5: SEM image of Ag NP-decorated PDMS; Figure S6: (a) Raman spectra of R6G with a concentration from 1×10^{-4} M to 1×10^{-7} M on the AIOP composite substrate; (b) Raman mapping at a resolution of 5×5 pixels of R6G (1×10^{-4} M) on the AIOP composite substrate; Figure S7: Raman spectra of (a) MG (1×10^{-4} M) and (b) CV (1×10^{-4} M) on pure PDMS, Ag NP-decorated PDMS, and AIOP composite substrate; Figure S8: Fluorescence spectra of AIOP composite substrate ranging from 680 to 800 nm; Figure S9: EM field distributions of cross-section of (a) Ag NP-decorated PDMS and (b) AIOP composite substrate under excitation of 448 nm; Table S1: Vibrational models of the Raman peaks for R6G molecules; Table S2: Vibrational models of the Raman peaks for MG molecules; Table S3: Vibrational models of the Raman peaks for CV molecules. References [52,53,59–61] are cited in the Supplementary Materials.

Author Contributions: Conceptualization, Z.T.; methodology, Z.T. and J.W.; software, J.W.; validation, Z.C. and J.W.; formal analysis, J.L., X.L., and Z.C.; investigation, Z.T., H.L., and Z.C.; writing—original draft preparation, Z.T.; writing—review and editing, H.L. and D.X.; visualization, D.X., J.L., and X.L.; supervision, H.L., J.W., and D.X.; funding acquisition, Z.T., H.L., D.X., and J.L. All authors have read and agreed to the published version of the manuscript.

Funding: This research was funded by the Youth Innovative Talents Program of Guangdong Colleges and Universities, grant number 2024KQNCX060; the Key Research Platforms and Projects of Guangdong Provincial Ordinary Universities, grant number 2019KCXTD019; the Guangdong Provincial Engineering Technology Research (and Development) Center of Ordinary Universities, grant number 2020GCZX001; the Professorial and Doctoral Scientific Research Foundation of Huizhou University, grant number 2022JB059; the Guangdong Basic and Applied Basic Research Foundation, grant numbers 2023A1515110940 and 2023A1515140081; the Huizhou Introduces and Cultivates Scientific and Technological Talents (Team) Project, grant number 2023EQ050033; and the Huizhou Social Development Science and Technology Projects, grant number 2024CQ010004.

Institutional Review Board Statement: Not applicable.

Data Availability Statement: The original contributions presented in this study are included in the article. Further inquiries can be directed to the corresponding authors.

Conflicts of Interest: The authors declare no conflicts of interest.

References

1. Li, D.; Wu, X.; Chen, Z.; Liu, T.; Mu, X. Surface-enhanced spectroscopy technology based on metamaterials. *Microsyst. Nanoeng.* **2025**, *11*, 60. [CrossRef]
2. Srivastava, S.; Wang, W.; Zhou, W.; Jin, M.; Vikesland, P.J. Machine learning-assisted surface-enhanced Raman spectroscopy detection for environmental applications: A review. *Environ. Sci. Technol.* **2024**, *58*, 20830–20848. [CrossRef]
3. Lu, Y.; Lin, L.; Ye, J. Human metabolite detection by surface-enhanced Raman spectroscopy. *Mater. Today Bio* **2022**, *13*, 100205. [CrossRef]
4. Li, Z.; Chen, M.; Liang, Q.-B.; Pan, X.-H.; Wang, J.-D.; Weng, Y.-H.; Cao, S.-H.; Li, Y.-Q. Covalent organic framework-based surface plasmon-enhanced fluorescence sensing for real-time monitoring of cell apoptosis. *Biosens. Bioelectron.* **2025**, *284*, 117569. [CrossRef]
5. Berger, L.M.; Duportal, M.; Menezes, L.d.S.; Cortés, E.; Maier, S.A.; Tittl, A.; Krischer, K. Improved In Situ Characterization of Electrochemical Interfaces Using Metasurface-Driven Surface-Enhanced IR Absorption Spectroscopy. *Adv. Funct. Mater.* **2023**, *33*, 2300411. [CrossRef]
6. Wu, T.; Mao, Y.; Wang, T.; Ma, L.; Cao, J.; Xie, B.; Weia, J.; Lia, P. Evolving trends in nanozyme-based SERS systems for food contaminant monitoring: A review. *Food Chem.* **2025**, *486*, 144621. [CrossRef] [PubMed]
7. Logan, N.; Cao, C.; Freitag, S.; Haughey, S.A.; Krska, R.; Elliott, C.T. Advancing Mycotoxin Detection in Food and Feed: Novel Insights from Surface-Enhanced Raman Spectroscopy (SERS). *Adv. Mater.* **2024**, *36*, 2309625. [CrossRef] [PubMed]

8. Xu, C.; Chen, S.; Sun, W.; Xu, R.; Yin, X.; Guo, D.; Yang, Y. Plasmon-enhanced fluorescence sensor based on Au nanocages for sensitive detection of norepinephrine. *Anal. Chim. Acta* **2025**, *1354*, 343995. [CrossRef] [PubMed]
9. Ge, Y.; Wang, H.; Li, Q.; Li, Q.; Yang, Y.; Zhu, R.; Yang, J.; Liu, X.; Zhang, Q.; Wang, Y. Rapid and Scalable Preparation of Highly Uniform, Atomically Thin MSe2 (M = Ti, Nb, Ta) Nanosheets as Ultra-Sensitive SERS Substrates for Lateral Flow Immunoassay. *Adv. Funct. Mater.* **2025**, *35*, 2420786. [CrossRef]
10. Huang, X.; Tian, H.; Huang, L.; Chen, Q.; Yang, Y.; Zeng, R.; Xu, J.; Chen, S.; Zhou, X.; Liu, G. Well-ordered Au nanoarray for sensitive and reproducible detection of hepatocellular carcinoma-associated miRNA via CHA-assisted SERS/fluorescence dual-mode sensing. *Anal. Chem.* **2023**, *95*, 5955–5966. [CrossRef]
11. Hang, Y.; Boryczka, J.; Wu, N. Visible-light and near-infrared fluorescence and surface-enhanced Raman scattering point-of-care sensing and bio-imaging: A review. *Chem. Soc. Rev.* **2022**, *51*, 329–375. [CrossRef]
12. Apostolaki, M.-A.; Sakellis, E.; Gardelis, S.; Likodimos, V. Interplay of plasmonic and charge transfer effects for ultrasensitive Ag–WO 3/TiO 2 photonic crystal SERS sensors. *Mater. Adv.* **2025**, *6*, 388–399. [CrossRef]
13. Wang, J.; Pinkse, P.W.; Segerink, L.I.; Eijkel, J.C. Bottom-up assembled photonic crystals for structure-enabled label-free sensing. *ACS Nano* **2021**, *15*, 9299–9327. [CrossRef] [PubMed]
14. Tang, Z.; Wu, J.; Yu, X.; Hong, R.; Zu, X.; Lin, X.; Luo, H.; Lin, W.; Yi, G. Fabrication of Au nanoparticle arrays on flexible substrate for tunable localized surface plasmon resonance. *ACS Appl. Mater. Interfaces* **2021**, *13*, 9281–9288. [CrossRef] [PubMed]
15. Deka, T.; Nair, R.G. Recent advancements in surface plasmon resonance and Schottky junction assisted photocatalytic water splitting of noble metal decorated Titania: A review. *Int. J. Hydrogen Energy* **2024**, *59*, 322–342. [CrossRef]
16. Cai, Y.Y.; Choi, Y.C.; Kagan, C.R. Chemical and Physical Properties of Photonic Noble-Metal Nanomaterials. *Adv. Mater.* **2023**, *35*, 2108104. [CrossRef]
17. Choi, J.-H.; Choi, J.-W. Metal-enhanced fluorescence by bifunctional Au nanoparticles for highly sensitive and simple detection of proteolytic enzyme. *Nano Lett.* **2020**, *20*, 7100–7107. [CrossRef]
18. Wang, D.; Xu, X.; Qiu, T.; Ren, N.; Liu, H.; Fang, G.; Liu, Z. Laser Construction TiOx-Ag heterostructure interface for high sensitive coupling resonance enhanced fluorescence in bacterial nucleic acid amplification sensor chip. *Sens. Actuators B Chem.* **2025**, *423*, 136727. [CrossRef]
19. Lin, L.L.; Alvarez-Puebla, R.; Liz-Marzán, L.M.; Trau, M.; Wang, J.; Fabris, L.; Wang, X.; Liu, G.; Xu, S.; Han, X.X. Surface-enhanced Raman spectroscopy for biomedical applications: Recent advances and future challenges. *ACS Appl. Mater. Interfaces* **2025**, *17*, 16287–16379. [CrossRef]
20. Zhao, J.; Chen, Y.; Tang, Y.; Li, B.; Wang, Q.; Wang, J.; Gao, X.; Zhang, Y.; Wang, J.; Lei, Z. Tandem Dual-Ratiometric SERS Probe Enables Raman Imaging of Neurological pH Fluctuations in Epilepsy. *Angew. Chem. Int. Ed.* **2025**, *64*, e202504822. [CrossRef]
21. Meng, T.; Shi, M.; Guo, Y.; Wang, H.; Fu, N.; Liu, Z.; Huang, B.; Lei, C.; Su, X.; Peng, B. Multifunctional Ag-coated CuO microbowl arrays for highly efficient, ultrasensitive, and recyclable surface-enhanced Raman scattering. *Sens. Actuators B Chem.* **2022**, *354*, 131097. [CrossRef]
22. Hu, X.; Mu, Z.; Li, Y.; Bai, L.; Qing, M. Metal–organic frameworks-scaffold gold nanoclusters enabled aggregation-induced enhanced fluorescent sensor array for high-throughput detection of heavy metal ions. *Microchem. J.* **2025**, *210*, 113020. [CrossRef]
23. Minamikawa, T.; Sakaguchi, R.; Harada, Y.; Tanioka, H.; Inoue, S.; Hase, H.; Mori, Y.; Takamatsu, T.; Yamasaki, Y.; Morimoto, Y. Long-range enhancement for fluorescence and Raman spectroscopy using Ag nanoislands protected with column-structured silica overlayer. *Light Sci. Appl.* **2024**, *13*, 299. [CrossRef]
24. Luo, J.; Wang, Z.; Li, Y.; Wang, C.; Sun, J.; Ye, W.; Wang, X.; Shao, B. Durable and flexible Ag-nanowire-embedded PDMS films for the recyclable swabbing detection of malachite green residue in fruits and fingerprints. *Sens. Actuators B Chem.* **2021**, *347*, 130602. [CrossRef]
25. Li, X.; Liu, H.; Gu, C.; Zhang, J.; Jiang, T. PDMS/TiO2/Ag hybrid substrate with intrinsic signal and clean surface for recyclable and quantitative SERS sensing. *Sens. Actuators B Chem.* **2022**, *351*, 130886. [CrossRef]
26. Choudhary, R.; Srivastava, S.K. Templating assisted fabrication of flexible, highly stable and uniform plasmonic platform for ultrahigh enhancement of Raman and fluorescence signals: Model sensing of rhodamine-6G. *Spectrochim. Acta Part A Mol. Biomol. Spectrosc.* **2025**, *338*, 126125. [CrossRef] [PubMed]
27. Yi, K.; Fan, Z.; Ran, Q.; Jia, K.; Liu, X.; Wang, L. Scalable fabrication of silver covered polyurethane nanofibers as flexible SERS nanosensors for aflatoxin detection. *Talanta* **2023**, *263*, 124636. [CrossRef] [PubMed]
28. Shao, T.; Xu, J.; Zhong, H.; Hu, Y.; Chen, J. A stable and flexible Au@ Ag NPs/PVA SERS platform for thiram residue detection on rough surface. *Talanta* **2024**, *274*, 126008. [CrossRef] [PubMed]
29. Chang, R.; Wang, T.; Liu, Q.; Tang, J.; Wu, D. Ag nanoparticles@ agar gel as a 3D flexible and stable SERS substrate with ultrahigh sensitivity. *Langmuir* **2022**, *38*, 13822–13832. [CrossRef]
30. Zhao, X.; Zhang, L.; Lv, X.; Liu, J.; Liu, X.; Zhang, Y.; Zhang, D.; Li, S.; Wang, Q. Large-area fluorescence enhancement of R6G based on a uniform PVA-Au plasmonic substrate. *Opt. Express* **2022**, *30*, 43281–43292. [CrossRef]

31. Ma, H.; Pan, S.-Q.; Wang, W.-L.; Yue, X.; Xi, X.-H.; Yan, S.; Wu, D.-Y.; Wang, X.; Liu, G.; Ren, B. Surface-enhanced Raman spectroscopy: Current understanding, challenges, and opportunities. *ACS Nano* **2024**, *18*, 14000–14019. [CrossRef]
32. Tang, X.; Hao, Q.; Hou, X.; Lan, L.; Li, M.; Yao, L.; Zhao, X.; Ni, Z.; Fan, X.; Qiu, T. Exploring and engineering 2D transition metal dichalcogenides toward ultimate SERS performance. *Adv. Mater.* **2024**, *36*, 2312348. [CrossRef]
33. Ma, Y.; Song, M.; Li, L.; Lao, X.; Liu, Y.; Wong, M.-c.; Yang, M.; Chen, H.; Hao, J. Attomolar-level detection of respiratory virus long-chain oligonucleotides based on FRET biosensor with upconversion nanoparticles and Au–Au dimer. *Biosens. Bioelectron.* **2024**, *243*, 115778. [CrossRef] [PubMed]
34. He, S.; Xiang, H.; Zhao, G.; Zhang, M.; Lin, J.; Yang, L.; Liu, H. A FRET assembly of fluorescent gold nanoclusters for ratiometric monitoring peroxynitrite in living cells and zebrafish. *Sens. Actuators B Chem.* **2023**, *378*, 133182. [CrossRef]
35. Yang, N.; Kang, Y.; Cong, Y.; Wang, X.; Yao, C.; Wang, S.; Li, L. Controllable gold nanocluster–emulsion interface for direct cell penetration and photothermal killing. *Adv. Mater.* **2023**, *35*, 2208349. [CrossRef] [PubMed]
36. Lai, X.; Zhang, G.; Deng, S.; Zhang, G.; Xiao, X.; He, W.; Su, L.; Liu, C.; Lai, W. Triple strategy-enhanced immunochromatographic assay based on APCB and AIEFM for the ultrasensitive detection of AFM1. *J. Hazard. Mater.* **2023**, *460*, 132438. [CrossRef]
37. Huang, K.; Le, N.; Wang, J.S.; Huang, L.; Zeng, L.; Xu, W.C.; Li, Z.; Li, Y.; Han, G. Designing next generation of persistent luminescence: Recent advances in uniform persistent luminescence nanoparticles. *Adv. Mater.* **2022**, *34*, 2107962. [CrossRef]
38. Cai, Y.; Lu, M.; Qin, X.; Jin, D.; Zhou, J. Understanding shell coating effects to overcome quenching in single anisotropic upconversion nanoparticles. *Nat. Commun.* **2025**, *16*, 4927. [CrossRef]
39. Qi, B.; Dai, W.; Lou, B.; Song, B.; Miao, Z.; Wei, Y.; Ma, C.; Wang, J. Amplifying Persistent Luminescence in Heavily Doped Nanopearls for Bioimaging and Solar-to-Chemical Synthesis. *ACS Nano* **2025**, *19*, 5818–5828. [CrossRef]
40. Zhu, Y.-Z.; Zhou, R.-Y.; Hu, S.; Li, J.-F.; Tian, Z.-Q. Shell-Isolated Nanoparticle-Enhanced Raman Spectroscopy: Toward High Sensitivity and Broad Applicability. *ACS Nano* **2024**, *18*, 32287–32298. [CrossRef]
41. Liu, Y.; Chui, K.K.; Fang, Y.; Wen, S.; Zhuo, X.; Wang, J. Metal–organic framework-enabled trapping of volatile organic compounds into plasmonic nanogaps for surface-enhanced raman scattering detection. *ACS Nano* **2024**, *18*, 11234–11244. [CrossRef]
42. Wu, J.; Li, J.; Liu, X.; Gong, L.; Chen, J.; Tang, Z.; Lin, W.; Mu, Y.; Lin, X.; Hong, W. Unclonable photonic crystal hydrogels with controllable encoding capacity for anticounterfeiting. *ACS Appl. Mater. Interfaces* **2021**, *14*, 2369–2380. [CrossRef]
43. Jiang, X.; Lai, Y.; Yang, M.; Yang, H.; Jiang, W.; Zhan, J. Silver nanoparticle aggregates on copper foil for reliable quantitative SERS analysis of polycyclic aromatic hydrocarbons with a portable Raman spectrometer. *Analyst* **2012**, *137*, 3995–4000. [CrossRef] [PubMed]
44. Huang, Z.; Liao, T.; Liu, X.; Wu, J.; Tang, Z.; Pan, G.; Liu, H.; Lin, X.; Lin, W.; Li, Y. Modified ethylene/α-octene co-polymer composites based on dual toughening of hydrogen bonding network and nanospheres. *Polym. Adv. Technol.* **2022**, *33*, 2313–2324. [CrossRef]
45. Truong, V.X.; Bachmann, J.; Unterreiner, A.N.; Blinco, J.P.; Barner-Kowollik, C. Wavelength-orthogonal stiffening of hydrogel networks with visible light. *Angew. Chem. Int. Ed.* **2022**, *61*, e202113076. [CrossRef] [PubMed]
46. Stanton, M.M.; Ducker, R.E.; MacDonald, J.C.; Lambert, C.R.; McGimpsey, W.G. Super-hydrophobic, highly adhesive, polydimethylsiloxane (PDMS) surfaces. *J. Colloid Interface Sci.* **2012**, *367*, 502–508. [CrossRef]
47. Ismail, A.E.; Grest, G.S.; Heine, D.R.; Stevens, M.J.; Tsige, M. Interfacial structure and dynamics of siloxane systems: PDMS− vapor and PDMS− water. *Macromolecules* **2009**, *42*, 3186–3194. [CrossRef]
48. Chen, Y.; Cao, J.; Wei, H.; Wu, Z.; Wang, X.; Pei, Y. Synthesis of polyvinyl alcohol/Ag electrospun nanofibers as highly efficient flexible SERS substrates. *Vib. Spectrosc.* **2021**, *114*, 103246. [CrossRef]
49. Wang, X.-Z.; Hu, Q.; Gao, M.; Liu, S.; Luo, J.-L. Tuning the subsurface oxygen of Ag2O-derived Ag nanoparticles to achieve efficient CO2 electroreduction to CO. *Electrochim. Acta* **2022**, *403*, 139656. [CrossRef]
50. Cao, T.; Zhou, Y.; Zhang, J.; Zhao, B. Clean preparation of Ag@ Au nanoparticle-modified cotton fabric with durable antimicrobial properties by adsorption. *Cellulose* **2025**, *32*, 613–628. [CrossRef]
51. Khan, J.; Naseem, I.; Bibi, S.; Ahmad, S.; Altaf, F.; Hafeez, M.; Almoneef, M.M.; Ahmad, K. Green synthesis of silver nanoparticles (Ag-NPs) using Debregeasia salicifolia for biological applications. *Materials* **2022**, *16*, 129. [CrossRef] [PubMed]
52. Liu, G.; Li, K.; Zhang, Y.; Du, J.; Ghafoor, S.; Lu, Y. A facile periodic porous Au nanoparticle array with high-density and built-in hotspots for SERS analysis. *Appl. Surf. Sci.* **2020**, *527*, 146807. [CrossRef]
53. Yu, H.; Chen, Y.; Wen, Z.; Wang, R.; Jia, S.; Zhu, W.; Song, Y.; Sun, H.; Liu, B. Selective SERS Sensing of R6G Molecules Using MoS2 Nanoflowers under Pressure. *Langmuir* **2024**, *40*, 21804–21813. [CrossRef] [PubMed]
54. Tang, Z.; Wu, J.; Liu, X.; Su, Q.; Yin, X.; Huang, Z.; Lin, X.; Lin, W.; Yi, G. Au-Nanoparticle-Array/Aligned-Ag-Nanowire-Based Flexible Dual Plasmonic Substrate for Sensitive Surface-Enhanced Raman Scattering Detection. *Part. Part. Syst. Charact.* **2021**, *38*, 2100160. [CrossRef]
55. Yang, B.; Chen, G.; Ghafoor, A.; Zhang, Y.F.; Zhang, X.B.; Li, H.; Dong, X.R.; Wang, R.P.; Zhang, Y.; Zhang, Y. Chemical Enhancement and Quenching in Single-Molecule Tip-Enhanced Raman Spectroscopy. *Angew. Chem. Int. Ed.* **2023**, *62*, e202218799. [CrossRef]

56. Yang, T.-H.; Ahn, J.; Shi, S.; Qin, D. Understanding the role of poly (vinylpyrrolidone) in stabilizing and capping colloidal silver nanocrystals. *ACS Nano* **2021**, *15*, 14242–14252. [CrossRef]
57. Badawy, A.M.E.; Luxton, T.P.; Silva, R.G.; Scheckel, K.G.; Suidan, M.T.; Tolaymat, T.M. Impact of environmental conditions (pH, ionic strength, and electrolyte type) on the surface charge and aggregation of silver nanoparticles suspensions. *Environ. Sci. Technol.* **2010**, *44*, 1260–1266. [CrossRef]
58. Dimitriev, O.P.; Blank, D.A.; Ganser, C.; Teichert, C. Effect of the polymer chain arrangement on exciton and polaron dynamics in P3HT and P3HT: PCBM films. *J. Phys. Chem. C* **2018**, *122*, 17096–17109. [CrossRef]
59. Rekha, C.; Sameera, S.; Nayar, V.; Gopchandran, K. Simultaneous detection of different probe molecules using silver nanowires as SERS substrates. *Spectrochim. Acta Part A Mol. Biomol. Spectrosc.* **2019**, *213*, 150–158. [CrossRef]
60. Xu, T.; Wang, X.; Huang, Y.; Lai, K.; Fan, Y. Rapid detection of trace methylene blue and malachite green in four fish tissues by ultra-sensitive surface-enhanced Raman spectroscopy coated with gold nanorods. *Food Control* **2019**, *106*, 106720. [CrossRef]
61. Fateixa, S.; Nogueira, H.I.; Trindade, T. Surface-enhanced Raman scattering spectral imaging for the attomolar range detection of crystal violet in contaminated water. *ACS Omega* **2018**, *3*, 4331–4341. [CrossRef]

polymers

MDPI

Article

Convenient Preparation of PEDOT-Based Conductive Fabrics via a Green Strategy for Morse Code Recognition

Hongjian Yu [1], Yifan Cui [2,*] and Miao Miao [3,*]

[1] College of Light Industry and Textile, Qiqihar University, Qiqihar 161006, China; qqhuyhj@163.com
[2] Xinjiang Production & Construction Corps Key Laboratory of Modern Textile Materials and Technology, College of Fashion and Textile, Tarim University, Alaer 843300, China
[3] State Key Laboratory of Separation Membranes and Membrane Processes, School of Textile Science and Engineering, Tiangong University, Tianjin 300387, China
* Correspondence: yfcui@taru.edu.cn (Y.C.); 2020010040@tiangong.edu.cn (M.M.)

Abstract

With the rapid development of Internet of Things (IoT) and bioscience technology, wearable smart devices are developing toward advanced trends such as flexibility, convenience and environmental-friendliness. Poly (p-styrenesulfonic acid) (PSS), as a common template and dispersant, is indispensable in the polymerization of conductive polymers. However, the doping amount of PSS has a significant effect on the electrical conductivity of the polymer. Herein, different molar quantities of PSS were used to assist the polymerization of 3,4-ethylenedioxythiophene (EDOT) monomer in a horseradish peroxidase/hydrogen peroxide (HRP/H_2O_2) low-temperature system to obtain conductive finishing solutions with more excellent electrical properties. Then, the polyester nonwoven fabric was immersed in the conductive finishing solution, and when the addition ratio of EDOT and PSS was 1:2, the conductive performance was optimal (3.27 KΩ cm^{-1}). Finally, the conductive fabric was assembled into a pressure sensor and a temperature sensor, which can transmit Morse code in the form of single-parameter (pressure response or temperature response) or collaboration. Overall, this research has great potential for production of poly(3,4-ethylenedioxythiophene) (PEDOT)-based composites and their applications in smart wearable device.

Keywords: doping amount; enzymatic polymerization; horseradish peroxidase; conductive polymer; pressure sensor; morse code

1. Introduction

Currently, the design and development of flexible electronic devices have attracted increasing attention by virtue of the advantages of textiles (comfortable to wear, breathable, and soft) [1,2]. Conductive polymers have been widely utilized as conductive layers in textile-based electronic devices due to their excellent mechanical properties and ease of processing. Generally, the preparation methods of conductive fabrics, which involve depositing conductive polymers onto textile surfaces, include dip-coating [3], vapor-phase deposition [4], electrochemical deposition [5], in-situ solution polymerization [6], and drop-injection [7]. Among these conductive polymers (such as polyaniline (PANI) [8,9], polypyrrole (PPy) [10,11], poly(3,4-ethylenedioxythiophene) (PEDOT) [12–14] and their derivatives [15,16]), PEDOT is considered as an ideal material for conductive layers due to its low cost, high conductivity, excellent environmental stability and promising commercial applications [17].

PEDOT can be synthesized by chemical, electrochemical and enzymatic polymerization. Enzymatic polymerization has the advantages of high efficiency, catalytic specificity, mild reaction conditions and environmental friendliness [12]. Natural enzymes such as horseradish peroxidase (HRP) [18], laccase [19] and soybean peroxidase (SBP) [20] can be used for the synthesis of PEDOT. Generally, templating agents are required for the synthesis of PEDOT. Generally, negatively charged linear polymers can serve as templates for the synthesis of PEDOT, such as poly(p-styrenesulfonic acid) (PSS) [21,22], sodium dodecyl sulfate (SDS) [23], sodium lignosulfonate (LS) [24], and p-toluenesulfonic acid (TsOH) [6]. Currently, numerous studies have focused on using water-soluble PSS as a template to assist in the polymerization of 3,4-ethylenedioxythiophene (EDOT) monomers. However, adding non-conductive PSS to PEDOT systems may affect the conductivity of the products. In previous research, a one-step enzymatic in-situ polymerization method was used to directly assemble PEDOT on the substrate surface with PSS as both the template and dopant [21]. This approach, however, yielded small sample sizes and required lengthy reaction times, hindering large-scale production. Therefore, investigating the impact of dopant content on the conductivity of poly(3,4-ethylenedioxythiophene):poly(styrene sulfonic acid) (PEDOT:PSS) represents a valuable research direction.

In this study, a green and eco-friendly HRP/H_2O_2 biocatalytic system was developed to synthesize PEDOT:PSS finishing solutions doped with varying molar amounts of the templating agent (PSS), with the aim of investigating the effect of doping levels on the conductivity of the resulting solutions. Additionally, pressure sensors and temperature sensors were prepared by coating the PEDOT:PSS finishing solutions onto nonwoven fabrics, and their capabilities for signal monitoring and transmission were evaluated. This research provides a new approach for mechanistic studies of conductive polymers and offers novel possibilities for the convenient fabrication of wearable electronic sensors.

2. Experimental Section

2.1. Materials and Reagents

PSS (Mw~75,000, 18 wt% in H_2O) and EDOT (99%) were acquired from Sigma-Aldrich (St. Louis, MO, USA). HRP (RZ: >2.0, freeze-dried powder, ≥300 units/mg) were acquired from Aladdin. H_2O_2 (≥30.0 wt%) was obtained from Sinopharm Chemical Reagent Co., Ltd. In addition, all of the reagents were analytical grade, were directly used without further purification, and were prepared with deionized water. PET nonwoven fabrics were purchased from Foshan Jiada Nonwoven Fabrics Co., Ltd. (Foshan, China), and were pretreated with deionized water and anhydrous ethanol.

2.2. Biocatalytic Preparation of PEDOT:PSS Conductive Finishing Solution

The polymerization of EDOT was catalyzed by HRP and the oxidizing agent (H_2O_2) under 4 °C (Figure 1). In brief, EDOT and PSS were added in 20 mL deionized water in the constant low-temperature device. After the solution homogeneous mixing, 6 mg of HRP solution (3 mg/mL of deionized water) and 50 mM of H_2O_2 solution were added and mixed. The reaction was carried out for 16 h to complete the polymerization process, and a characteristic dark-blue of PEDOT:PSS conductive finishing solution was obtained. The addition proportion of PSS & EDOT and the products' names were shown in Table 1.

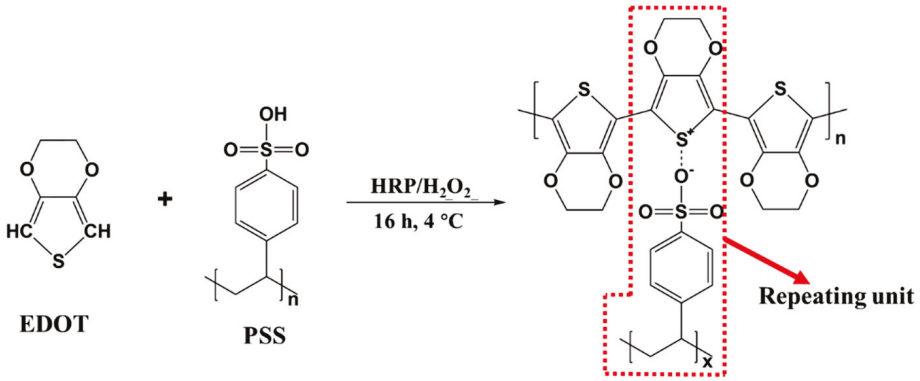

Figure 1. Scheme of enzymatic-catalyzed polymerization of PEDOT:PSS with HRP/H_2O_2 catalytic system.

Table 1. The addition proportion of PSS and EDOT and the products' names.

Samples	EDOT (mmol/L)	PSS (mmol/L)
PEDOT:PSS-21	50	25
PEDOT:PSS-11	50	50
PEDOT:PSS-12	50	100
PEDOT:PSS-13	50	150

2.3. Preparation of PEDOT:PSS Nonwoven Fabric and Assemble Devices

Firstly, commercialized nonwoven fabric was washed by alcohol and acetone to take away impurity substance. The washed nonwoven fabric was then dished in PEDOT:PSS conductive finishing solution and deposited for 1 h after 30 min ultrasonication. Finally, the modified nonwoven fabric was dried in an oven at 40 °C and designated as M-nonwoven-X, where X represents the molar ratio of PSS to EDOT. Among these samples, M-nonwoven-12 was selected for assembling the pressure sensor and the self-powered movement keyboard.

2.4. Characterization

UV–vis spectra were recorded on a spectrometer (UV-2808S, Shanghai Sunny Hengping Scientific Instrument Co., Ltd., Shanghai China) in the range of 200–1100 nm. In each measurement, deionized water was used as the control. Fourier transform infrared (FT-IR) (Nicolet iS 10, Thermo Fisher Scientific, Waltham, MA, USA) spectra were recorded on a spectrometer (at attenuated total reflection mode (ATR) with 32 scans and 4 cm^{-1} resolution in the scanning range of 4000–400 cm^{-1}). Raman spectra were recorded on a spectrometer (inVia Reflex, Renishaw plc, Wotton-under-Edge, UK). Collecting 5 spectra on different points of the sample on glass coupled. The laser wavelength was 532 nm and a range from 100 to 3100 cm^{-1}. Scanning electron microscopy (SEM) (JEOL Ltd., Akishima, Japan) was used to observe the microscopic view at 10 KV.

2.5. Electrical Property, Signal Monitoring, and Transmission Measurement

To examine the effect of the addition proportion of PSS and EDOT on electrical conductivity, electrical resistance of the modified nonwoven fabric was measured utilizing a digital precision multimeter (DMM 6550, Tektronix Inc., Solon, OH, USA). The signals were recorded in real-time using a Keithley 6550 multimeter. Each data point was measured twenty times, and the average value was subsequently recorded.

2.6. Pressure Sensor Assembly and Mechanism

The pressure sensor was fabricated by assembling a 1 cm × 3 cm strip of PEDOT-based conductive fabric using conductive silver paste and copper tape (Figure 2). When a finger adhered with a 2 cm × 2 cm patch of PEDOT-based conductive fabric presses the sensor, the instantaneous resistance decreases due to the creation of additional conductive paths. Specifically, the duration of each press directly translates into Morse code elements: a short press denotes a "dot" (·), while a long press signifies a "dash" (–).

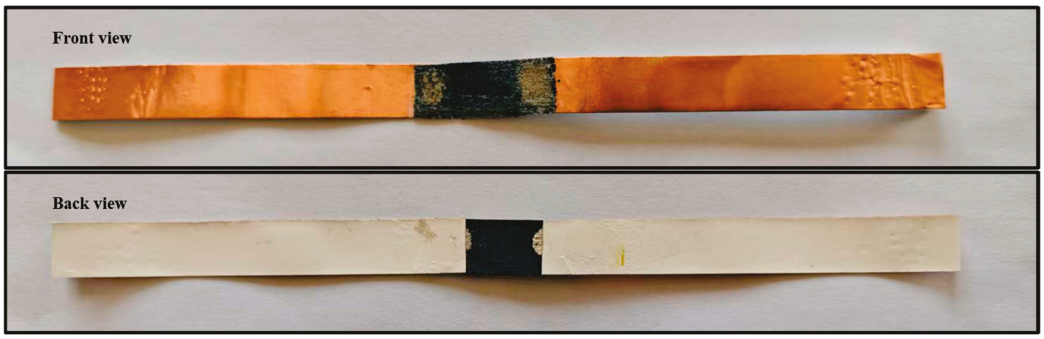

Figure 2. Physical images of pressure and temperature sensor devices.

2.7. Temperature Sensor Assembly and Mechanism

The temperature sensor was fabricated from a 1 cm × 3 cm strip of PEDOT-based conductive fabric, bonded with conductive silver paste and copper tape (Figure 2). The two ends of the strip serve as the hot and cold junctions, respectively. When the hot junction rapidly touches and separates from a heat source, it generates a positive voltage pulse corresponding to a "dot" (·) in Morse code. Conversely, maintaining prolonged contact produces a sustained positive voltage signal representing a "dash" (–). By modulating the thermal contact timing, various alphanumeric characters can be encoded through combinations of these "dot-dash" signals.

3. Results and Discussion

3.1. Chemical Structure of the PEDOT:PSS and Modified Nonwoven Fabric

The UV-Vis absorption spectra of obtained PEDOT:PSS with different addition proportions were shown in Figure 3a. As shown in the figure, the template agent PSS exhibits no significant absorption above 400 nm compared to PEDOT:PSS. The absorption bands of PEDOT:PSS in the range of 600–800 nm are attributed to π–π* transitions occurring within the PEDOT polymer chains [25]. To determine the chemical structure of the polymer, Figure 3b shows the FT-IR spectra of EDOT, PSS, and PEDOT:PSS-12. The characteristic peak (3111 cm^{-1}) of the EDOT monomer appears in FT-IR spectra, it is due to the C-H band stretching in the thiophene ring. However, the most notable feature was the absence of a peak at 3111 cm^{-1} in the PEDOT:PSS spectrum, which indicates the successful enzymatic polymerization of PEDOT. Furthermore, the characteristic bands of PEDOT were also observed. The classical band C=C antisymmetric stretching, C=C symmetric stretching, and C-C stretching of the thiophene ring are between 1353 cm^{-1} and 1490 cm^{-1}, C-O stretching at 1074 cm^{-1} and C-S stretching at 943 cm^{-1} [5,26].

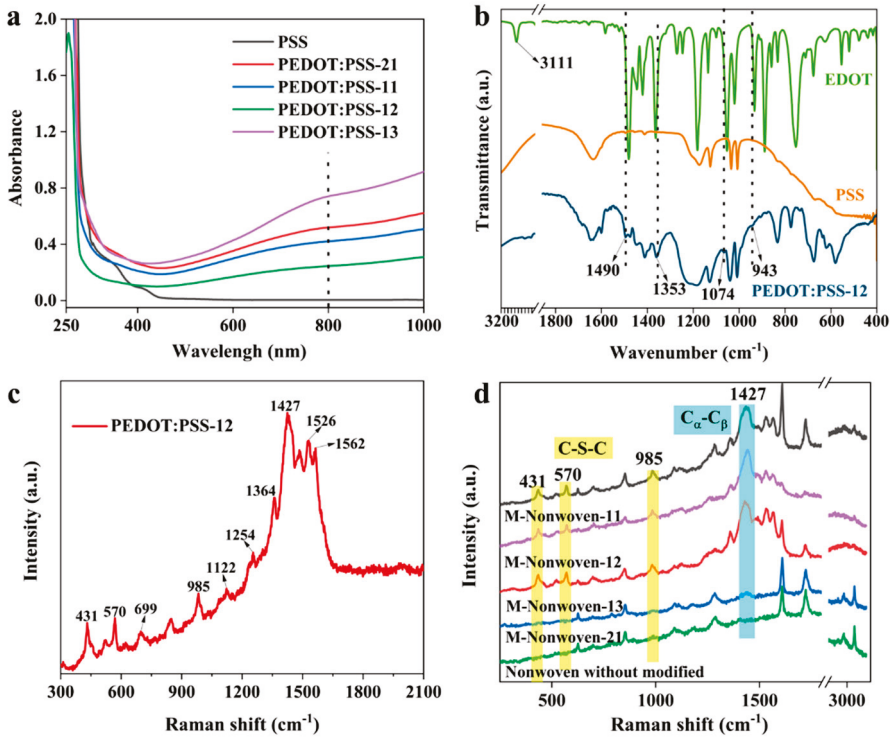

Figure 3. (**a**) The absorption spectra of PEDOT:PSS with different addition proportion. (**b**) The FT-IR spectra of EDOT, PSS and PEDOT:PSS-12. (**c**) The Raman spectrum of PEDOT:PSS-12. (**d**) The Raman spectra of nonwoven fabrics before and after modified.

To check the presence of PEDOT:PSS on nonwoven fabric, the samples were observed by Raman spectroscopy (Figure 3c,d). The Raman bands observed at 431, 570, and 985 cm^{-1} correspond to the deformation vibrations of the polyethylene ring, while those at 699 and 1122 cm^{-1} are attributed to the C–S–C and C–O–C bending modes, respectively. The bands at 1254 and 1364 cm^{-1} were C_α-C_α inter-ring stretching and C_β-C_β stretching, respectively. The bands at 1427, 1526, and 1562 cm^{-1} were the C_α-C_β symmetric stretching and C_α-C_β asymmetric mode, respectively. However, the spectrum of pristine PET was in absence of the C-S-C absorption band, the C_α-C_β symmetric stretching, and C_α-C_β asymmetric mode. This indicates that PEDOT:PSS was successfully deposited on nonwoven fabrics.

3.2. Surface Morphology and Composition of the PEDOT:PSS Modified Nonwoven Fabric

To observe the surface morphology of the fibers, nonwoven fabric and M-nonwoven-12 were observed by the scanning electron microscopy. Figure 4a–c presents SEM images of the nonwoven fabric and M-nonwoven-12. As observed from both the top view (Figure 4b) and the sectional view (Figure 4c), individual nonwoven fibers are uniformly coated with a substantial amount of PEDOT:PSS. At the same time, the gaps between the fibers are also filled with PEDOT:PSS. Figure 4d,e shows the EDS images of nonwoven fabric and M-nonwoven-12. It can be observed that element S is present in the elemental analysis of both the top and sectional views. Since the nonwoven fabric consists only of three elements (C, H, and O), this indicates that PEDOT:PSS, which contains sulfur (S), has been successfully deposited onto the nonwoven fabric. The presence of the conductive polymer PEDOT enables the nonwoven fabric to exhibit conductive properties.

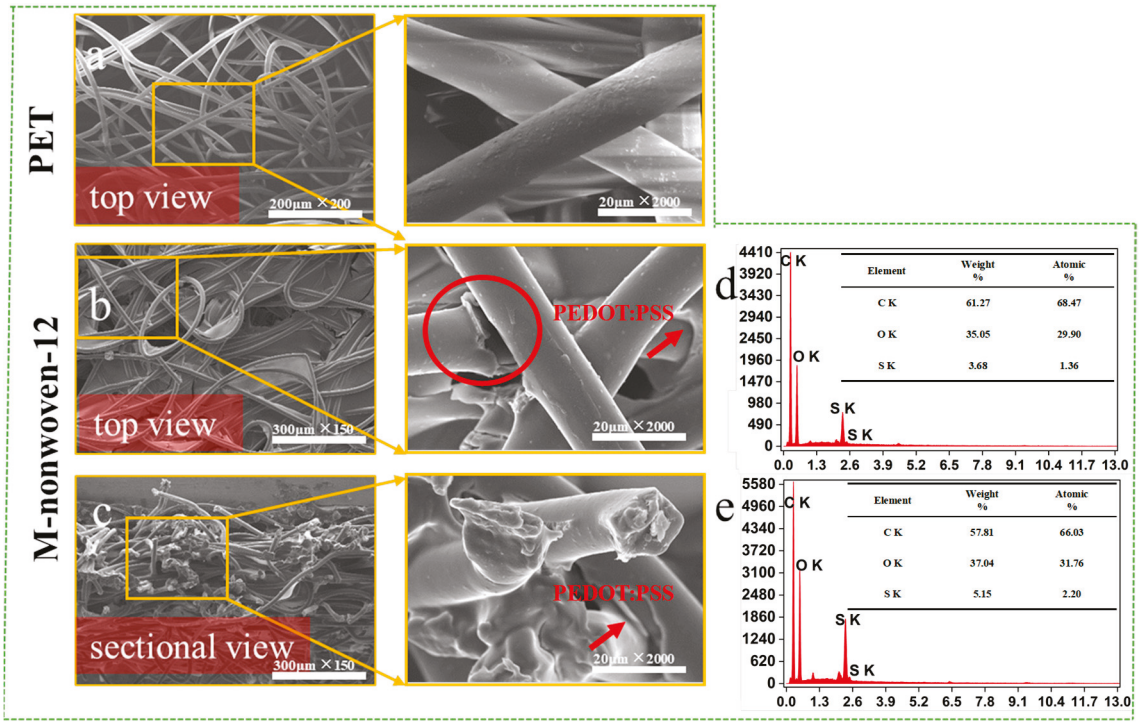

Figure 4. The SEM images of nonwoven fabric (**a**), and M-nonwoven-12 (**b**,**c**). The EDS image of M-nonwoven-12 (**d**,**e**).

3.3. Electrical Properties of the PEDOT:PSS Modified Nonwoven Fabric

To investigate the effect of PSS content on the electrical conductivity of PEDOT:PSS-modified nonwoven fabrics, electrical properties were systematically measured. Figure 5a shows the trend of electrical resistance. With the continuous growth of content of PSS, the electrical resistance drops first and then it increases. Compared with other samples, M-nonwoven-12 has excellent conductivity. In the reaction system, PSS serves not only as a template that facilitates the orderly and continuous arrangement of PEDOT, but also as a dispersant that ensures a uniform distribution of the monomer EDOT throughout the system (Figure 5b). However, excessive addition of PSS may counteract these beneficial effects, as PSS itself lacks electrical conductivity. Thus, in theory, the maximum electrical conductivity can be achieved when an equal or slightly excessive amount of PSS is introduced to disperse the monomer EDOT.

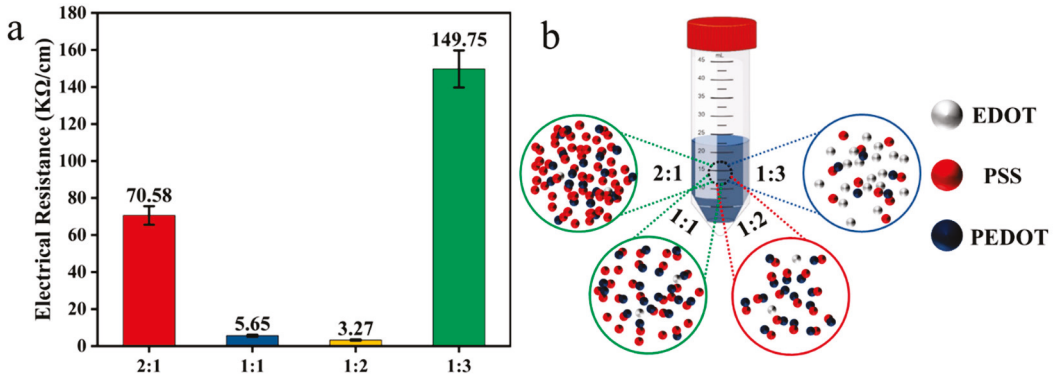

Figure 5. (**a**) The trend of electrical conductivity change. (**b**) Mechanism diagram of PSS doping at different ratios on PEDOT polymerization via HRP/H_2O_2 system.

3.4. Morse Code Recognition in Piezoresistive Mode

Morse code, a time-honored communication protocol, encodes information through standardized sequences of dots and dashes. Notably, this technology exhibits considerable potential in the field of medical health monitoring. It functions as a silent communication interface for non-verbal individuals, enabling them to express their needs by encoding "dot/dash" sequences through fingertip presses on the fabric. This approach enables real-time, highly precise communication, illustrating the transformative potential of smart textiles within the field of assistive technology. For example, in Morse code, four consecutive dots (....) represent the letter "H", a single dot (.) stands for "E", the dot-dash combination (.-..) denotes "L", and another combination (.--.) signifies "P"—these four symbols combined in sequence form the word "HELP" (Figure 6a). Furthermore, distress signals of varying urgency can be transmitted: a moderate "HELP", a more urgent "PANPAN" (Figure 6b), and a critical "SOS" (Figure 6c). The capabilities of this system extend beyond alphabetic words. Users can also send numeric distress signals, such as emergency phone numbers in the EU for 112 (Figure 6d), North America for 911 (Figure 6e), and the UK for 999 (Figure 6f). These demonstrations clearly highlight the device's potential as an efficient communication tool for the deaf and mute community, providing them with a reliable means to express their thoughts and needs in daily life.

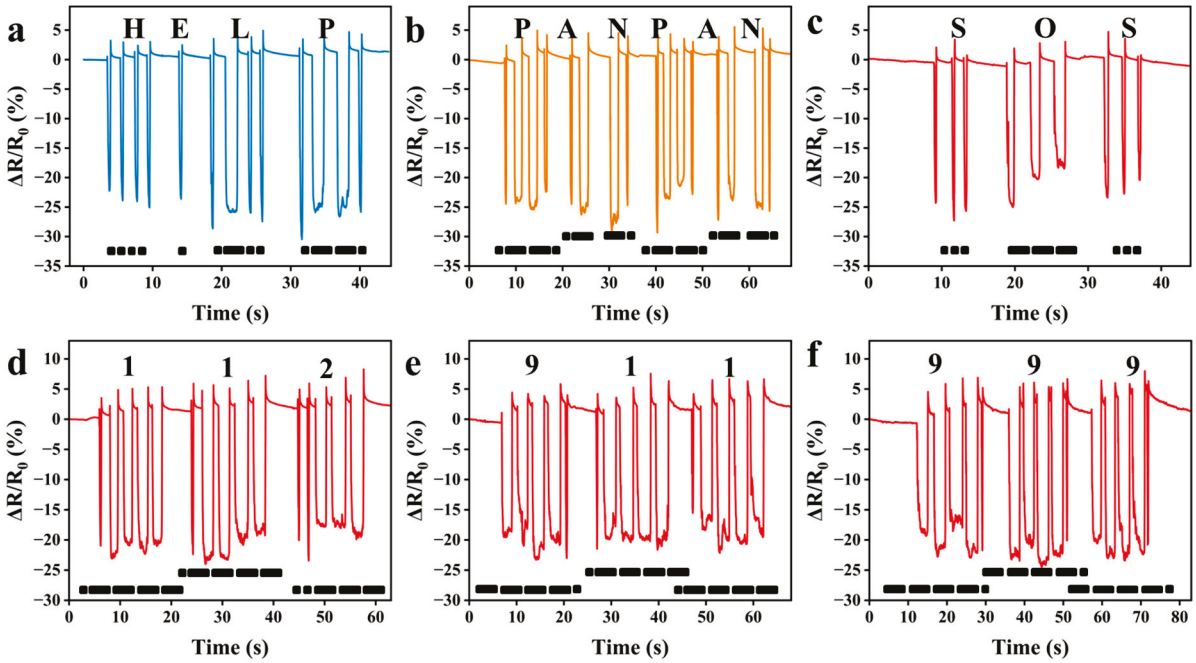

Figure 6. Images obtained by tapping Morse codes of letter combinations "HELP" (**a**), "PANPAN" (**b**), and "SOS" (**c**), or numeric combinations "112" (**d**), "911" (**e**), and "999" (**f**) with fingers.

3.5. Thermoelectric Performance

Figure 7a shows that, at room temperature (T_0 = 26 °C), there is a good linear relationship between the temperature difference (ΔT) across the composite fabric and the output thermal voltage. The slope of the curve is 12 μV/K, which corresponds to the Seebeck coefficient of the composite fabric. Therefore, temperature sensing can be realized by maintaining a constant temperature at one end of the composite fabric while varying the temperature at the other end. The study systematically investigated the output voltage response characteristics by establishing a temperature gradient ranging from 0 to 50 K between the two ends of the device. Experimental data indicate that, as the temperature difference gradually increases from 0 K to 50 K, the output voltage of the sensor exhibits a linear growth trend, eventually reaching nearly 600 μV (as shown in Figure 7b). These

results clearly demonstrate the sensor's exceptional capability to detect and respond to temperature variations across a broad temperature range.

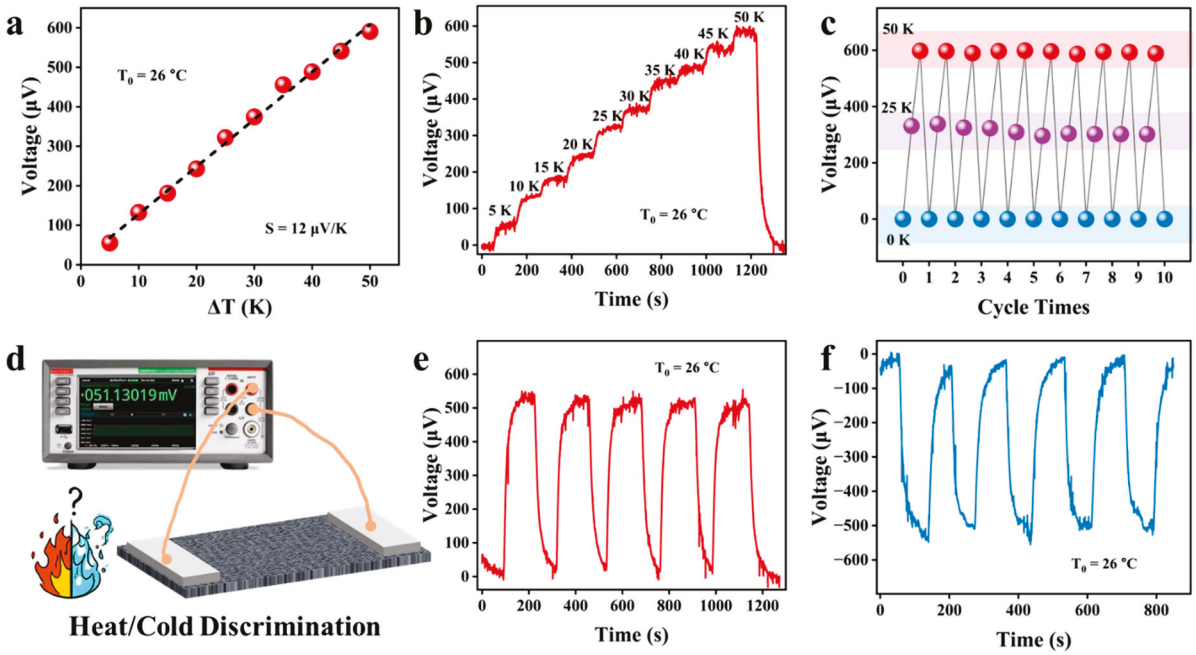

Figure 7. (**a**) At room temperature (T_0 = 26 °C), the temperature difference (ΔT) between the two ends of the composite fabric shows a good linear relationship with the output thermal voltage. (**b**) The output thermal voltage of the fabric under different temperature differences which shows good differentiation. (**c**) Multiple thermal voltage response of fabrics to different kind of temperature differences. (**d**) Schematic diagram of temperature sensing test for fabrics based thermoelectric effect. By, respectively, touching one end of the fabric with a high-temperature object (**e**) and a low-temperature object (**f**), output thermal voltage signals can be generated.

As shown in Figure 7c, temperature differences (0 K~25 K~50 K) were applied to the sensor to record its output thermal voltage. After ten cycles, the output signal of the device remained stable and reliable. Figure 7d presents a schematic diagram of the temperature sensing performance test conducted on the device based on the thermoelectric effect. As shown in Figure 7e, when a high-temperature object approaches one side of the device, a positive thermoelectric voltage is immediately generated. Conversely, when one end of the device is brought close to a low-temperature object, a negative thermoelectric voltage is rapidly generated within the device due to the Seebeck effect (Figure 7f). The excellent reproducibility of the temperature recognition process, as demonstrated through multiple repeated experiments, effectively confirms the device's stable and reliable temperature sensing performance.

3.6. Morse Code Recognition in Thermoelectric Mode

Based on the Seebeck effect, when two different conductive materials form a closed loop with a temperature difference at both ends, a thermoelectromotive force proportional to the temperature difference will be generated in the loop. Thermoelectric temperature sensing accurately measures the thermoelectromotive force to determine both the actual temperature difference between the sensor and its surroundings, and the true temperature of the target object. Thus, leveraging its excellent temperature detection and recognition capabilities, a self-powered telegraph was successfully developed. As shown in Figure 8a, "dot-dash-dash-dot" represents the letter "P", "dot" represents "E", and "dash" represents "T". The combination "PET" is exactly the abbreviation of the base material used in this study, Polyethylene Terephthalate (PET). Similarly, professional terms such as "HRP"

(horseradish peroxidase) and "Sensor" can also be transmitted (Figure 8b,c). In digital communication scenarios, the combinations "73" (Figure 8d) and "88" (Figure 8e) signify friendly greetings and farewells, respectively, while "222" is commonly used by radio enthusiasts to indicate "message received" (Figure 8f).

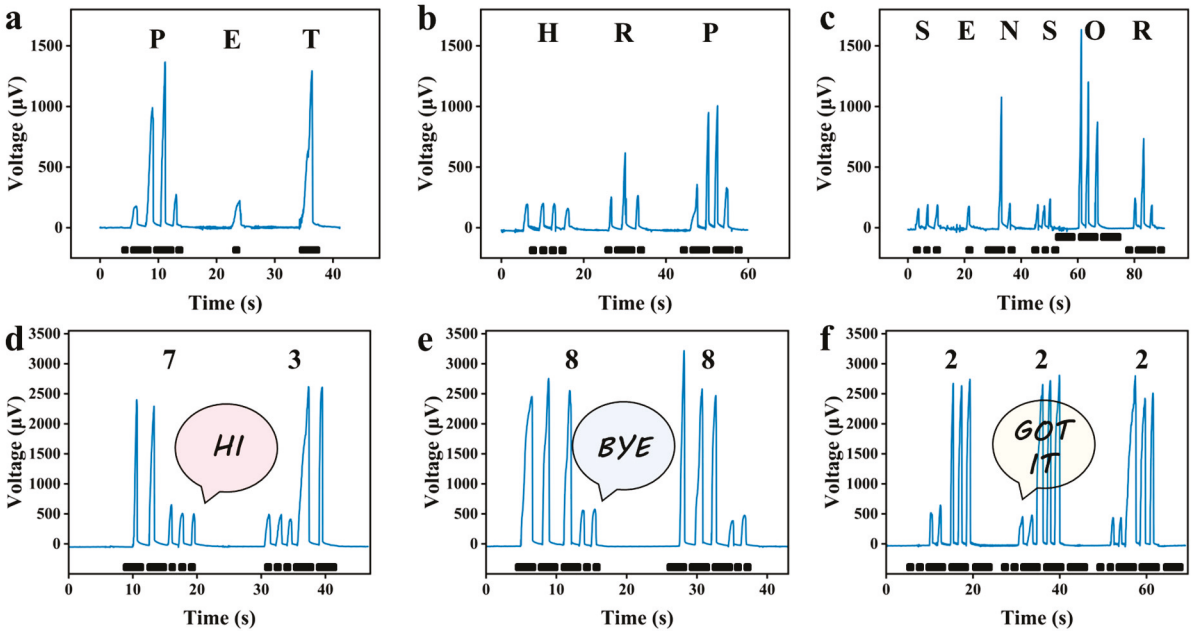

Figure 8. Images obtained by Morse codes of letter combinations "PET" (**a**), "HRP" (**b**), and "SENSOR" (**c**), or numeric combinations "73" (**d**), "88" (**e**), and "222" (**f**), composed of different output thermal voltages generated by touching with 1–2 fingers.

3.7. Morse Code Recognition in Collaborative Mode

Based on the aforementioned research findings, we have designed and developed an innovative dual-mode Morse code transceiver system. Through a sophisticated synchronous monitoring mechanism, the system can capture and analyze in real time the dynamic characteristics of voltage signals and the rate of resistance change, thereby enabling efficient encoding and precise decoding of letters and numbers. This provides users with a flexible and reliable channel for emotional communication and information transmission. The system demonstrates remarkable versatility in practical application scenarios. As shown in Figure 9a-d, through specific signal combinations, the system can accurately recognize the abbreviation codes for "Tarim University" and "College of Fashion and Textiles," clearly illustrating its information-expression and institutional-identification capabilities in campus environments. In the field of geographic information encoding, the numeric sequence "843300" transmitted in Figure 9e,f corresponds to the postal code of the location of Tarim University, whereas "0997" displayed in Figure 9g,h accurately represents the telephone area code of Alar City, where the university is situated. Through the deep mapping between digital signals and geographic identifiers, the system fully highlights its innovative application value in practical scenarios such as address encoding and regional information transmission. This achievement not only extends the application scope of Morse code within modern communication technologies, but also offers novel technical insights and practical cases for fields such as wearable devices and barrier-free communication, by virtue of its dual-mode signal monitoring mechanism design.

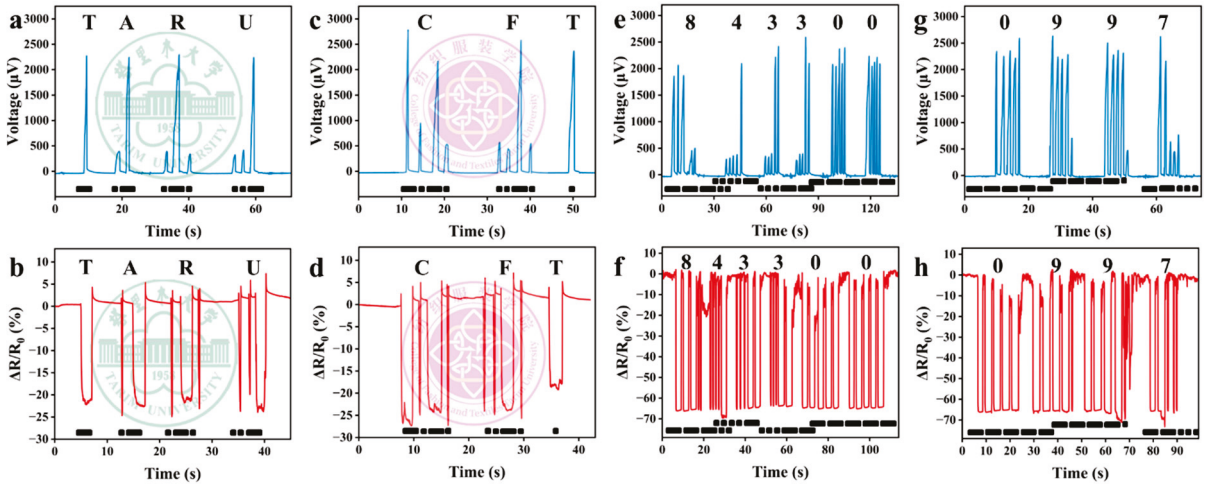

Figure 9. Response to changes in voltage and relative current when transmitting and recognizing Morse codes of letter combinations "TARU" (**a**–**b**) and "CFT" (**c**–**d**), or numeric combinations "843300" (**e**–**f**) and "0997" (**g**–**h**) in collaborative mode.

4. Conclusions

In this study, a PEDOT conductive finishing solution exhibiting excellent electrical conductivity was successfully synthesized through a green and straightforward approach, and the influence of PSS on the conductivity of the solution was systematically investigated. As an anionic long-chain polymer, PSS itself is electrically non-conductive and primarily functions as a dispersant and templating agent. The experimental results indicate that both insufficient and excessive amounts of PSS can significantly increase the resistance of the conductive finishing solution, thereby markedly reducing its electrical conductivity. When the molar ratios of PEDOT to PSS are 1:1 and 1:2, respectively, the finishing solution demonstrates extremely low resistance values. Additionally, this study verified another hypothesis: through an impregnation process, PEDOT:PSS was uniformly loaded onto the surface of nonwoven fabrics. The prepared flexible conductive nonwoven fabric can not only effectively recognize Morse code in either single-mode (piezoresistive or thermoelectric) operation or through collaborative dual-mode sensing, but also accurately monitor environmental temperature changes due to its sensitive temperature-responsive characteristics. This research achievement provides a new strategy for the green preparation of conductive finishing solutions. The prepared conductive finishing solution and its derivative materials, with their multifunctional properties, exhibit enormous application potential in cutting-edge fields such as intelligent sensing, human-computer interaction, and flexible electronics.

Author Contributions: Conceptualization, H.Y. and Y.C.; Methodology, H.Y. and Y.C.; Validation, H.Y.; Resources, H.Y.; Writing—review & editing, H.Y. and Y.C.; Software, Y.C.; Formal analysis, Y.C. and M.M.; Investigation, Y.C.; Writing—original draft, M.M. All authors have read and agreed to the published version of the manuscript.

Funding: This work was financially supported by the Tarim University President's Fund (TDZKBS202561).

Data Availability Statement: All the data generated or used during the study appear in the submitted article.

Acknowledgments: The project was funded by Xinjiang Production & Construction Corps Key Laboratory of Modern Textile Materials and Technology.

Conflicts of Interest: The authors declare no conflicts of interest.

References

1. Kayser, L.V.; Lipomi, D.J. Stretchable conductive polymers and composites based on PEDOT and PEDOT:PSS. *Adv. Mater.* **2019**, *31*, 1806133. [CrossRef] [PubMed]
2. Inoue, A.; Yuk, H.; Lu, B.Y.; Zhao, X.H. Strong adhesion of wet conducting polymers on diverse substrates. *Sci. Adv.* **2020**, *6*, eaay5394. [CrossRef] [PubMed]
3. Li, W.G.; Li, Z.; Bertelsmann, K.; Fan, D.E. Portable low-pressure solar steaming-collection unisystem with polypyrrole origamis. *Adv. Mater.* **2019**, *31*, 1900720. [CrossRef] [PubMed]
4. Zhang, L.S.; Baima, M.; Andrew, T.L. Transforming commercial textiles and threads into sewable and weavable electric heaters. *ACS Appl. Mater. Interfaces* **2017**, *9*, 32299–32307. [CrossRef]
5. Promsuwan, K.; Meng, L.G.; Suklim, P.; Limbut, W.; Thavarungkul, P.; Kanatharana, P.; Mak, W.C. Bio-PEDOT: Modulating carboxyl moieties in poly(3,4-ethylenedioxythiophene) for enzyme-coupled bioelectronic interfaces. *ACS Appl. Mater. Interfaces* **2020**, *12*, 39841–39849. [CrossRef]
6. Zhang, X.F.; Li, T.T.; Jiang, Q.; Wu, L.W.; Re, H.T.; Peng, H.K.; Shiu, B.C.; Wang, Y.T.; Lou, C.W.; Lin, J.H. Worm-Like PEDOT:Tos coated polypropylene fabrics via low-temperature interfacial polymerization for high-efficiency thermoelectric textile. *Prog. Org. Coat.* **2020**, *149*, 105919. [CrossRef]
7. Alamer, F.A.; Badawi, N.M.; Alodhayb, A.; Okasha, R.M.; Kattan, N.A. Effect of dopant on the conductivity and stability of three different cotton fabrics impregnated with PEDOT:PSS. *Cellulose* **2020**, *27*, 531–543. [CrossRef]
8. Tissera, N.D.; Wijesena, R.N.; Rathnayake, S.; Silva, R.; Silva, K. Heterogeneous in situ polymerization of polyaniline (PANI) nanofibers on cotton textiles: Improved electrical conductivity, electrical switching, and tuning properties. *Carbohydr. Polym.* **2018**, *186*, 35–44. [CrossRef]
9. Zhang, Y.; Fan, X.; Wang, Q.; Cavaco-Paulo, A. Preparation of functionalized cotton based on laccase-catalyzed synthesis of polyaniline in perfluorooctanesulfonate acid potassium salt (PFOS) template. *RSC Adv.* **2016**, *6*, 49272. [CrossRef]
10. Wang, B.; Yang, K.; Cheng, H.; Ye, T.; Wang, C. A hydrophobic conductive strip with outstanding one-dimensional stretchability for wearable heater and strain sensor. *Chem. Eng. J.* **2021**, *404*, 126393. [CrossRef]
11. Mule, A.; Dudem, B.; Patnam, H.; Graham, S.; Yu, J.S. Wearable single-electrode-mode triboelectric nanogenerator via conductive polymer-coated textiles for self-power electronics. *ACS Sustain. Chem. Eng.* **2019**, *7*, 16450–16458. [CrossRef]
12. Cui, Y.F.; He, X.Y.; Liu, W.D.; Zhu, S.Y.; Zhou, M.; Wang, Q. Highly Stretchable, Sensitive, and Multifunctional Thermoelectric Fabric for Synergistic-Sensing Systems of Human Signal Monitoring. *Adv. Fiber Mater.* **2024**, *6*, 170–180. [CrossRef]
13. Cui, Y.F.; Zheng, G.L.; Jiang, Z.; Zhou, M.; Wang, P.; Yu, Y.Y.; Wang, Q. Preparation of fabric-based electronic device via surface topological modification and enzymatic polymerization for personal thermal management, subtle motion detection, and ultraviolet protection. *Compos. Sci. Technol.* **2023**, *240*, 110098. [CrossRef]
14. Cui, Y.F.; Zheng; Jiang, Z.G.L.; Wang, W.D.; Zhou, M.; Wang, P.; Yu, Y.Y.; Wang, Q. Green preparation of PEDOT-based composites with outstanding electrothermal heating and durable rapid-response sensing performance for smart healthcare textiles. *Chem. Eng. J.* **2022**, *446*, 137189. [CrossRef]
15. Zhou, H.Y.; Zhao, Y.; Shen, X.F.; Ni, Z.H. Biocatalytically synthesized of water-soluble alkoxysulfonate-functionalized poly(3,4-ethylenedioxythiophene). *Mater. Chem. Phys.* **2018**, *208*, 91–96. [CrossRef]
16. Zhuang, A.; Pan, Q.C.; Qian, Y.; Fan, S.N.; Zhang, Y.; Song, L.J.; Zhu, B.; Zhang, Y.P. Transparent conductive silk film with a PEDOT-OH nano layer as an electroactive cell interface. *ACS Biomater. Sci. Eng.* **2021**, *7*, 1202–1215. [CrossRef]
17. Meng, W.; Ge, R.; Li, Z.; Tong, J.; Liu, T.; Zhao, Q.; Xiong, S.; Jiang, F.; Mao, L.; Zhou, Y. Conductivity enhancement of PEDOT:PSS films via phosphoric acid treatment for flexible all-plastic solar cells. *ACS Appl. Mater. Interfaces* **2015**, *7*, 14089–14094. [CrossRef]
18. Cui, Y.F.; Zheng, G.L.; Jiang, Z.; Zhou, M.; Wang, P.; Yu, Y.Y.; Wang, Q. Highly integrated smart mountaineering clothing with dual-mode synergistic heating and sensitive sensing for personal thermal management and human health monitoring. *J. Mater. Sci. Technol.* **2024**, *182*, 12–21. [CrossRef]
19. Vasil'eva, I.S.; Shumakovich, G.P.; Khlupova, M.E.; Vasiliev, R.B.; Emets, V.V.; Bogdanovskaya, V.A.; Morozova, O.V.; Yaropolov, A.I. Enzymatic synthesis and electrochemical characterization of sodium 1,2-naphthoquinone-4-sulfonate-doped PEDOT/MWCNT composite. *RSC Adv.* **2020**, *10*, 33010–33017. [CrossRef]
20. Nagarajan, S.; Kumar, J.; Bruno, F.F.; Samuelson, L.A.; Nagarajan, R. Biocatalytically synthesized poly(3,4-ethylenedioxythiophene). *Macromolecules* **2008**, *41*, 3049–3052. [CrossRef]
21. Cui, Y.F.; Jiang, Z.; Zhou, Y.; Wang, Q.; Zhou, M.; Wang, P.; Yu, Y.Y. Poly(3,4-ethylenedioxythiophene)-coated conductive polyester non-woven fabric prepared by enzymatic polymerization. *Fibers Polym.* **2022**, *23*, 1595–1601. [CrossRef]
22. He, X.Y.; Liu, M.Y.; Cai, J.X.; Li, Z.; Teng, Z.L.; Hao, Y.N.; Cui, Y.F.; Yu, J.Y.; Wang, L.M.; Qin, X.H. Waste Cotton-Derived Fiber-Based Thermoelectric Aerogel for Wearable and Self-Powered Temperature-Compression Strain Dual-Parameter Sensing. *Engineering* **2024**, *39*, 235–243. [CrossRef]

23. He, X.; Li, C.; Zhu, S.; Cai, J.; Yang, G.; Hao, Y.; Shi, Y.; Wang, R.; Wang, L.; Li, X.; et al. Layer-by-layer self-assembly of durable, breathable and enhanced performance thermoelectric fabrics for collaborative monitoring of human signal. *Chem. Eng. J.* **2024**, *490*, 151470. [CrossRef]
24. Wang, Q.H.; Pan, X.F.; Lin, C.M.; Lin, D.Z.; Ni, Y.H.; Chen, L.H.; Huang, L.L.; Cao, S.L.; Ma, X.J. Biocompatible, self-wrinkled, antifreezing and stretchable hydrogel-based wearable sensor with PEDOT:sulfonated lignin as conductive materials. *Chem. Eng. J.* **2019**, *370*, 1039–1047. [CrossRef]
25. Ouyang, J.Y.; Xu, Q.; Chu, C.W.; Yang, Y.; Li, G.; Shinar, J. On the mechanism of conductivity enhancement in poly(3,4-ethylenedioxythiophene):poly(styrene sulfonate) film through solvent treatment. *Polymer* **2004**, *45*, 8443–8450. [CrossRef]
26. Neves, M.F.F.; Damasceno, J.P.V.; Junior, O.D.L.; Zarbin, A.J.G.; Roman, L.S. Conductive ink based on PEDOT nanoparticles dispersed in water without organic solvents, passivant agents or metallic residues. *Synth. Met.* **2021**, *272*, 116657. [CrossRef]

polymers

MDPI

Review

Antibacterial Food Packaging with Chitosan and Cellulose Blends for Food Preservation

Tengfei Qu [1,*], Xiaowen Wang [2] and Fengchun Zhang [3,*]

[1] Xinjiang Key Laboratory of Clean Conversion and High Value Utilization of Biomass Resources, College of Chemistry and Chemical Engineering, Yili Normal University, Yining 835000, China
[2] Sichuan Water Development Group Co., Ltd., Chengdu 610000, China; wxwlx3041461@163.com
[3] School of Materials and Environmental Engineering, Chengdu Technological University, Chengdu 611730, China
* Correspondence: njuqtf@163.com (T.Q.); zfchun@cdtu.edu.cn (F.Z.)

Abstract

With the increasing demand for food quality and the need for green and sustainable development of food packaging materials in the environment, the preparation and optimization of multifunctional natural and renewable antibacterial packaging materials have become an important trend. This article aims to explore the development of chitosan–cellulose composite materials with good antibacterial properties and promote the widespread application of chitosan and cellulose in food packaging materials. Combining various natural polysaccharide polymers, we discuss the application of chitosan cellulose in meat, dairy products, fruits and vegetables, and fishery products. Meanwhile, we explore their antibacterial and antioxidant behaviors during their use as food packaging materials. This provides a reference for effectively improving the performance of modified chitosan and cellulose food packaging materials in the future. Based on the above explanation, we analyzed the advantages and disadvantages of modified chitosan and cellulose and looked forward to the future development trends of chitosan and cellulose blend films in food preservation. Chitosan–cellulose blends not only have important prospects in food packaging and preservation applications, but can also be combined with intelligent manufacturing to enhance their food preservation performance. The aim of this review is to provide valuable references for basic research on the antimicrobial properties of these composites and their practical application in smart food packaging.

Keywords: food packaging; chitosan; cellulose; food preservation

1. Introduction

Food spoilage is an important cause of food safety, as food becomes inedible due to spoilage [1]. Food spoilage leads to significant food waste and economic losses. About 1.3 billion tons of grain are wasted annually globally, and food companies lose USD 70 billion annually [2]. This waste also consumes other resources used in the food production process, such as water, energy, and labor [3]. At the same time, new opportunities and demands have emerged in the emerging market for fresh fruit and vegetable products. This demand stems from applying innovative packaging solutions and preservation technologies to ensure food quality and freshness [4,5]. Different antibacterial properties in food packaging are crucial for enhancing food safety and extending shelf life [6]. Antibacterial packaging is an effective measure to resist microbial contamination and foodborne diseases and to maintain the freshness of food by preventing the proliferation of these

microorganisms [7]. Furthermore, innovative antibacterial packaging solutions can gain a market advantage [8]. This method can also reduce the dependence of food on chemical preservatives. In short, new food packaging is crucial for safeguarding public health and promoting the development of high-quality food products.

Traditional food packaging materials include plastics (e.g., polyethylene, polypropylene), glass, and metal. They have long been used to protect food from spoilage by providing barriers to moisture, oxygen, light, and contaminants [9–11]. However, these materials come with some limitations. Primarily, traditional plastics lack inherent antimicrobial properties. They are rarely able to inhibit the growth of bacteria, molds, and pathogens [3,12]. Secondly, many of these materials are derived from non-renewable resources. It is contributing to significant environmental pollution. The worst thing is that if applied improperly, certain synthetic food packaging materials may leach harmful substances that may pose potential risks to food health. Additionally, glass has several drawbacks, including brittleness, heavy weight, and high processing costs. Metals also have their own disadvantages, such as high costs and difficulties in recycling and disposal.

In contrast, some antibacterial food packaging is made from chitosan and cellulose blends. They offer a more effective and sustainable solution for food preservation [13]. Chitosan possesses natural antimicrobial properties. Combining it with cellulose produces a packaging material that actively inhibits microbial growth [14]. These biopolymers are biodegradable and derived from renewable resources. They are an environmentally friendly alternative to traditional materials. Moreover, chitosan–cellulose blends can be engineered to improve mechanical strength and barrier properties. These properties contain moisture and gas permeability more effectively than conventional packaging [15]. This innovation reduces environmental impact and meets food packaging demand.

Chitosan and cellulose are natural polysaccharides. Their structures and chemical compositions vary depending on their sources. Common natural polysaccharides include cellulose, chitosan, lignin, and so on, as shown in Figure 1. These polysaccharides are typically formed by different monosaccharide units linked together by glycosidic bonds. Chitosan and cellulose play important roles in various applications across multiple industries [16]. Chitosan is derived from chitin, a polysaccharide found in the exoskeletons of crustaceans and certain fungi. Through deacetylation, chitin is converted into chitosan, resulting in a biopolymer that exhibits excellent biocompatibility, biodegradability, and antimicrobial properties [17,18]. These characteristics make chitosan particularly valuable in biomedical applications, food preservation, and agriculture [19]. Cellulose is the most abundant biopolymer on Earth. It is primarily present in the cell walls of plants, algae, and some bacteria [20]. Composed of long chains of β-D-glucose units linked by β-1,4-glycosidic bonds, cellulose provides structural strength to plant cells [21,22]. It is known for its exceptional tensile strength, hydrophilicity, and biodegradability. Due to these properties, cellulose is extensively used in textiles, paper, and packaging material [23,24].

Both chitosan and cellulose are increasingly being explored for their potential in innovative applications [25]. Their natural origins and favorable properties position them as key players in biodegradable materials [26]. Chitosan exhibits good antibacterial properties; however, its mechanical performance is suboptimal, which is improved through blending with cellulose. Chitosan is distributed within the cellulose matrix, forming a composite structure. The presence of cellulose not only serves as a carrier for chitosan but also facilitates the controlled release of the antimicrobial agent—chitosan [19,21,27]. Researchers continue to enhance these materials' functionality through chemical modifications. So, it is beneficial for a more sustainable future of antibacterial food packaging.

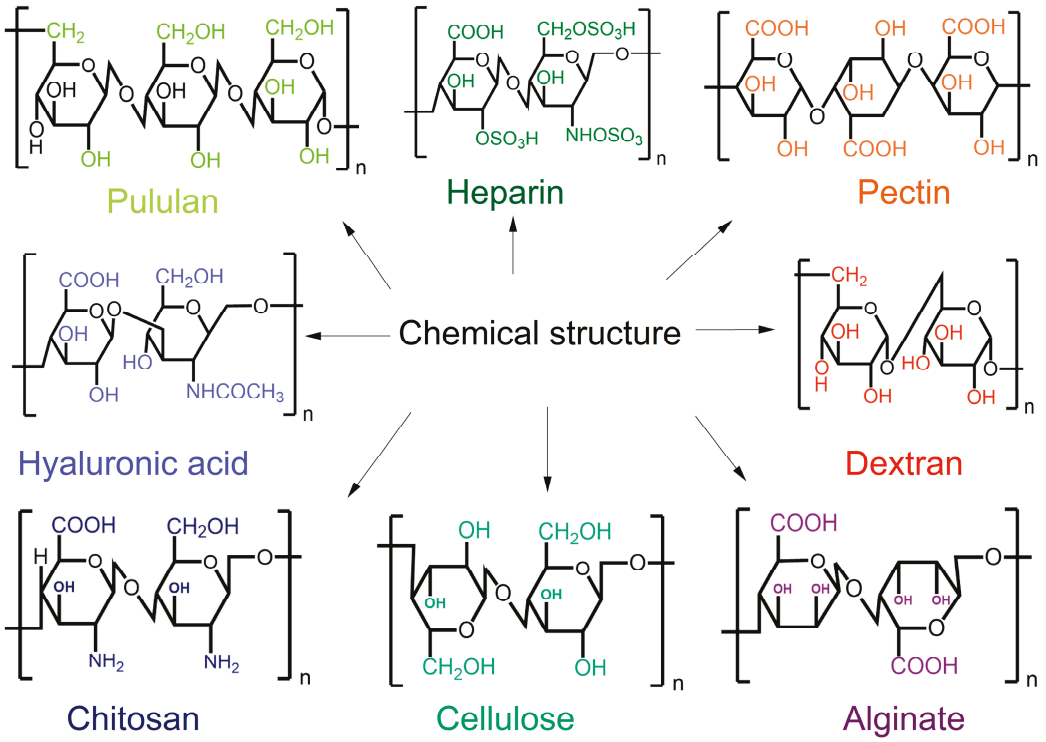

Figure 1. The chemical structures of different natural polysaccharides.

Concern over food safety, quality, and sustainability is becoming increasingly prominent. It is urgent to explore innovative packaging solutions. This review aims to provide insight into the role of chitosan and cellulose blends in antibacterial food packaging materials, to enhance food preservation. First, we explore their chemical and physical properties, elucidating their contributions to antimicrobial activity and packaging performance. Secondly, this review details the mechanisms of their microbial growth inhibition, including their effects on microbial cell membranes. Furthermore, this review analyzes current methods for preparing chitosan–cellulose blends and discusses their different properties, advantages, and drawbacks. Case studies highlighting the application of these materials in various food products have been included. Finally, this review addresses the environmental impact and application potential of chitosan and cellulose in food packaging. Overall, this review seeks to provide an integrated understanding of the antibacterial properties of chitosan and cellulose blends, fostering further research and development in food packaging.

2. Applications and Preparations of Chitosan–Cellulose Packaging in Food Preservation

Fresh meat, dairy products, fruits, and vegetables are prone to spoilage, often due to microbial contamination. Therefore, developing effective food packaging strategies is crucial. The combination of chitosan and cellulose has shown promising potential in antimicrobial food packaging, as it offers a new solution for extending the shelf life of food and enhancing safety. Fresh produce, particularly delicate items like berries, cut fruits, and leafy greens, has a short shelf life and is prone to spoilage. Utilizing packaging made from chitosan–cellulose mixtures can significantly improve its freshness and nutritional quality. This material provides effective moisture and toxin barriers that inhibit the growth of spoilage microorganisms, thereby reducing food waste.

Due to differences in their characteristics, meat and poultry products have varied preservation requirements. Chicken, a high-protein and perishable fresh ingredient, is par-

ticularly susceptible to microbial contamination during storage. Therefore, strict control of microbial growth is essential to maintain its freshness [27]. In contrast, beef features coarser fibers and varied fat distribution, necessitating preservation methods that inhibit surface microbial proliferation and prevent the deterioration of meat quality due to oxidation and other factors [28].

Dairy products are rich in moisture and nutrients, making them highly susceptible to microbial contamination and rapid oxidation [29]. Their preservation must focus on the dual needs of inhibiting microbial growth and preventing oxidation. Therefore, it is essential to choose packaging materials that effectively suppress microbes, provide good sealing performance, and are opaque to block light, which can lead to nutrient degradation.

Bread, when fresh, has a soft and tender texture; however, its high moisture content makes it particularly vulnerable to drying out and mold growth [30]. The preservation of bread must address the need to inhibit microbial growth and prevent oxidation while also maintaining moisture levels. Thus, it is important to select packaging materials that can fulfill these requirements and possess a certain level of compressive strength to protect the bread from damage during transport and storage.

Sausages, as processed meat products, have complex compositions containing various spices, additives, and so forth. Their preservation must address the dual challenge of inhibiting microbial growth and preventing the oxidation and rancidity of fats [31]. Cooked foods, having undergone preparation, are more easily exploited by microorganisms, and their flavor compounds are prone to volatilization [32]. Thus, besides antibacterial action, preservation of these products requires efforts to maintain flavor and texture.

The advanced antibacterial packaging technology made from chitosan and cellulose specifically addresses these diverse needs [33–35]. For chicken, it significantly reduces surface microbial loads, minimizing spoilage risks. For beef, it suppresses bacteria while slowing down oxidation processes. In the case of sausages, it effectively prevents fat oxidation and inhibits bacterial growth. For cooked foods, this packaging minimizes flavor loss, ensuring food safety while maximizing the preservation of the texture, quality, and unique flavors of various products, ultimately enhancing preservation effectiveness and consumer experience. This type of packaging is particularly vital in retail environments, where the risk of contamination can be higher due to extended display times [34,35]. Table 1 showcases specific cases of chitosan and cellulose blends applied in preserving fresh meat, dairy products, fruits, and vegetables, clearly delineating their potential in food packaging.

Table 1. The application of different antibacterial films of chitosan and cellulose blends.

Evaluation Criteria			
Materials Components	**Preparation Approaches**	**Applications**	**References**
1. Alkylation of chitosan	Chitosan undergoes N-alkylation through the formation of Schiff bases	Antibacterial, food, and pharmaceutical	[36]
2. Cellulose alkylation	Alkylation of micro-fibrillated cellulose	Food preservation	[37]
3. Chitosan acylation	Chitosan acylation, biocatalytic enzyme activity	Food preservation	[38]
4. Acetylated cellulose	Reacetylation method; banana pseudostem cellulose was extracted and acetylated to prepare	Beef preservation; antimicrobial against Staphylococcus aureus and Escherichia coli	[34,35]

Table 1. *Cont.*

Evaluation Criteria			
Materials Components	**Preparation Approaches**	**Applications**	**References**
5. Hydroxychitosan	Hydroxyl substitution of flavonols on chitosan	The preservation of fatty and water-based meats	[39]
6. Imine-based chitosan/quaternized chitosan-based nanofibers	Ammoniated chitosan, vanillin, and polyethylene oxide electrospun into fiber materials	Antibacterial activity of Escherichia coli, Staphylococcus aureus, and Candida albicans	[40]
7. Shellac quaternized chitosan nanoparticles	Quercetin-loaded shellac quaternized chitosan nanoparticles	Cosmetics, pharmaceuticals, and food preservation	[41]
8. Quaternary ammonium chitosan, cellulose	Deacetylated quaternized chitosan and its use as cellulose nanofiber-based film	Extend the raw salmon's shelf life	[42]
9. Amphiphilic quaternized chitosan derivatives	Amphiphilic quaternized chitosan derivatives	Antibacterial experiment of Streptococcus mutans, the pathogen of dental caries	[43]
10. Polyvinyl alcohol/quaternized cellulose	Blending of quaternized cellulose with polyvinyl alcohol matrix	Antibacterial experiments on Gram-positive (Staphylococcus aureus) and Gram-negative (Escherichia coli) bacteria	[44]
11. derivatives of cellulose, chitin and chitosan	Introduced multifunctional groups	Fruits, antibacterial field, fuel cell, drug delivery, immunotherapy, etc.	[45]
12. Cellulose nanofibers, chitosan/modified cellulose	Physical mixing	Beefcake food preservation	[46]
13. Cellulose, gelatin, starch chitosan nanocomposite film	Single-layered films through film casting technique	Meat preservation	[47]
14. Microfibrillated cellulose, chitosan and polypyrrole	Coasting method	Cherry tomato preservation	[48]
15. Cellulose nanocrystals, polyvinyl alcohol, chitosan nanoparticle	The solvent casting method	The packaging of fresh fruits	[49]
16. Carboxymethyl cellulose, chitosan-based carbon quantum dots	Carboxymethyl cellulose-based functional film integrated with chitosan-based carbon quantum dots.	Lemon fruit preservation	[50]
17. Chitosan, lignin-containing cellulose nanofibrils bio-composite	Combining hydrothermal pretreatment, mechanical fibrosis, and casting.	Green food packaging	[51]
18. Hydrophobic-modified cellulose nanofibrils, chitosan, zein coating	Multi-coating method	Meat packaging	[52]
19. chitosan/cellulose acetate hybrid nanostructure, Ziziphora clinopodioides essential oils.	Ion gel, electric spray, and electrospinning process	Fresh beef preservation	[53]
20. Cellulose and chitosan and volatile antibacterial benzyl isothiocyanate.	The layer-by-layer self-assembly approach	Chicken preservation	[54]

Table 1. *Cont.*

Evaluation Criteria			
Materials Components	**Preparation Approaches**	**Applications**	**References**
21. Aluminum chloride, chitosan, cellulose	Ternary composite approach	Gram microbiota experiment	[55]
22. Chitosan, bacterial cellulose, ε—polylysine	Casting method	Tilapia preservation	[56]
23. Corn alcohol soluble protein, cinnamaldehyde, chitosan, dialdehyde carboxymethyl cellulose	Loading and doping method	Strawberry preservation	[57]
24. Composed of cellulose, bentonite, and chitosan, Aspergillus Niger extract	Ternary composite approach	Sherbet berry preservation	[58]

In addition to fresh produce and meats, the dairy industry can reap significant benefits from using chitosan–cellulose blends in food packaging. Products such as cheese, yogurt, and milk are susceptible to microbial spoilage, affecting their taste, texture, and safety. The incorporation of biodegradable and antibacterial packaging can extend the shelf life of these items by controlling microbial growth and moisture loss. For instance, soft cheeses and yogurts, which have higher moisture content, are especially prone to spoilage, and chitosan's antimicrobial properties can help preserve their quality throughout the storage period [59].

Bakery products represent another category where chitosan and cellulose blends can improve packaging effectiveness. Bread and pastries are common victims of mold growth and staleness due to moisture absorption [60]. Antibacterial packaging, which uses chitosan to inhibit mold formation while regulating moisture levels, can help maintain the freshness and palatability of baked goods. This is particularly beneficial for artisanal breads and goods with no preservatives, ensuring that consumers receive products that are not only safe but also have desirable textures and flavors when consumed.

Seafood is another highly perishable category that stands to benefit significantly from chitosan–cellulose packaging. Fish and shellfish are particularly prone to spoilage and bacterial growth, necessitating careful preservation methods. Antibacterial packaging can help extend the shelf life of seafood by minimizing microbial contamination, thus ensuring quality and safety. Whether dealing with fresh fish or ready-to-eat seafood salads, the use of these bio-based packaging materials can significantly enhance the product's longevity without compromising flavor or texture [61]. Finally, the blending of chitosan and cellulose for antibacterial food packaging presents a multi-faceted solution that can enhance the safety, quality, and shelf life of a wide range of food products, from fresh produce and meats to dairy, bakery, seafood, and ready-to-eat meals. This innovation not only aids in reducing food waste but also aligns with the growing consumer demand for sustainable and health-conscious packaging solutions.

3. Antibacterial Action and Antioxidant Properties

3.1. Interaction of Cellulose Blends with Microbials

Cellulose is a natural polysaccharide primarily found in plant cell walls and does not possess antimicrobial activity. However, after chemical modification or when combined with other active components, it may acquire certain antimicrobial functions. Cellulose blends exhibit unique interactions with microbials in food preservation [13]. These blends

create a physical barrier that can prevent microbial access to food surfaces, reducing the likelihood of contamination. The high surface area of cellulose fibers facilitates the adsorption of antimicrobial compounds released from chitosan. It promotes a synergistic effect that actively disrupts microbial growth. This interaction can significantly lower the initial microbial load on food products, improving safety and extending shelf life. The synergistic effects of cellulose with other natural compounds, such as essential oils, metal oxides, or plant extracts, were explored. The schematic of the interaction of cellulose blends with microbials is shown in Figure 2 [62]. These potential applications of cellulose in food preservation are expected to expand further [63].

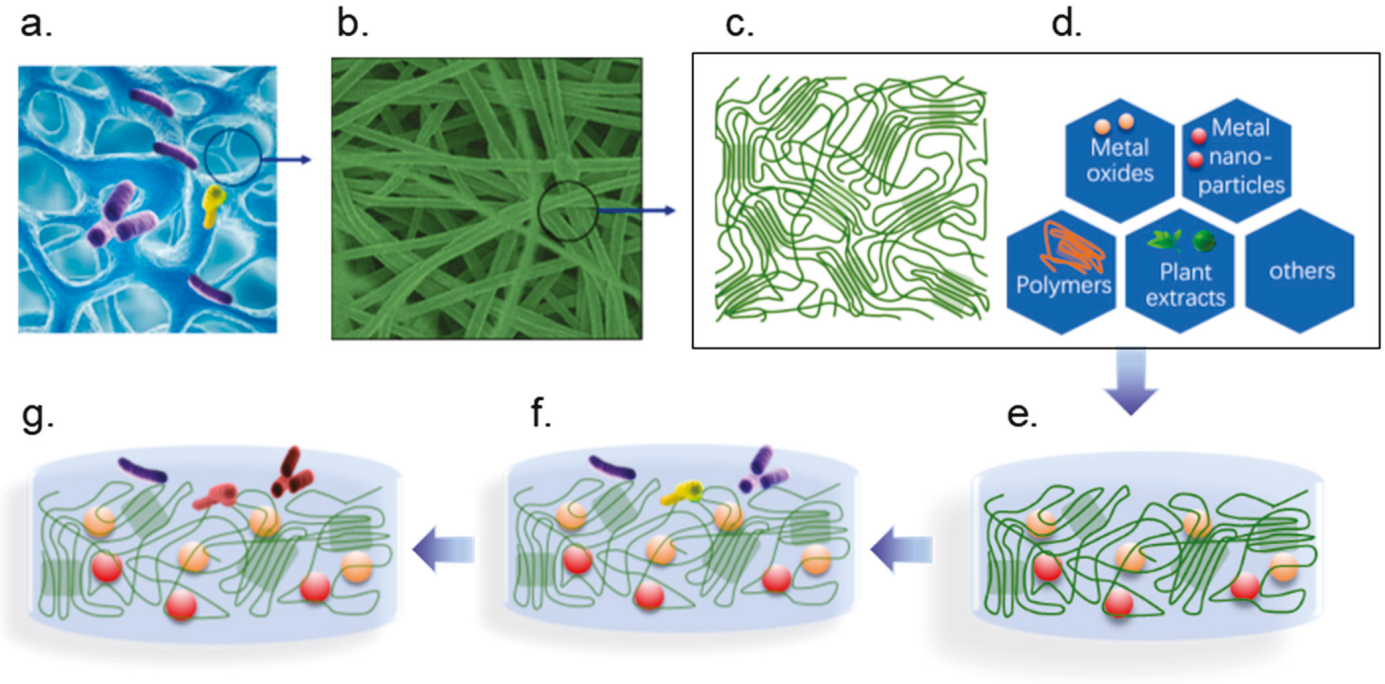

Figure 2. The schematic of the interaction of cellulose blends with microbials. (**a**) The surface of the cellulose with microbials; (**b**,**c**) the microstructure of the cellulose is composed of the crystalline fraction and the amorphous fraction; (**d**) the cellulose composite with different antibacterial active substances; (**e**–**g**) the antibacterial process of the cellulose composite with different antibacterial active substances. (Green thread represents cellulose, purple and yellow cylinders represent active bacteria, and reddish-brown cylinders represent dead bacteria.)

Once microbial cells interact with cellulose–chitosan blends, several mechanisms can cause cell damage or death. Chitosan's cationic nature allows it to interact electrostatically with negatively charged microbial cell membranes and the cell membranes in a destabilized state [64]. This disruption increases the permeability of the cell, causing essential intracellular components to leak out and ultimately leading to cell lysis. Additionally, binding chitosan to the cell surface can interfere with microbial metabolic processes, hindering their growth and reproduction. This dual action—physical barrier and chemical interaction—makes cellulose blends particularly effective against pathogens, including bacteria and fungi.

Moreover, adding cellulose blends into food packaging offers the potential for sustained release of active compounds. This slow-release mechanism ensures that antimicrobial activity is maintained over an extended period. It provides continuous protection against microbial contamination. The biocompatibility and non-toxicity of cellulose and its blends make them suitable for contact with food because they do not pose risks of harmful chemical migration. Ultimately, the interaction of cellulose blends with microbial

cells represents a promising approach to developing effective, safe, and environmentally friendly food packaging solutions.

3.2. Chitosan Antibacterial Activity

Chitosan is a natural biopolymer derived from chitin [14]. The effectiveness of chitosan as an antibacterial agent can be primarily attributed to its chemical structure. The interactions of chitosan with the microbial cell (Figure 3a) membranes are shown in Figure 3b. Chitosan is a cationic polymer with positive charges. It plays a pivotal role in its antibacterial mechanism. When the positively charged chitosan is introduced to bacterial cells, it interacts with the negatively charged components of the bacterial cell membrane, destroying the membrane integrity as shown in Figure 3c,d. This disruption can result in increased permeability and ultimately leakage of essential intracellular components, leading to cell death. High-molecular-weight chitosan typically has a molecular weight exceeding 100,000 Mw, making it relatively difficult to dissolve in neutral pH environments. In contrast, low-molecular-weight chitosan usually has a molecular weight below 50,000 Mw, which allows for better solubility and a wider range of applications. A blend of high- and low-molecular-weight chitosan components demonstrates robust antifungal activity. The high-molecular-weight components disrupt the stability of fungal membranes, facilitating the penetration of low-molecular-weight components into the cells, where they interfere with vital cellular processes [64–67].

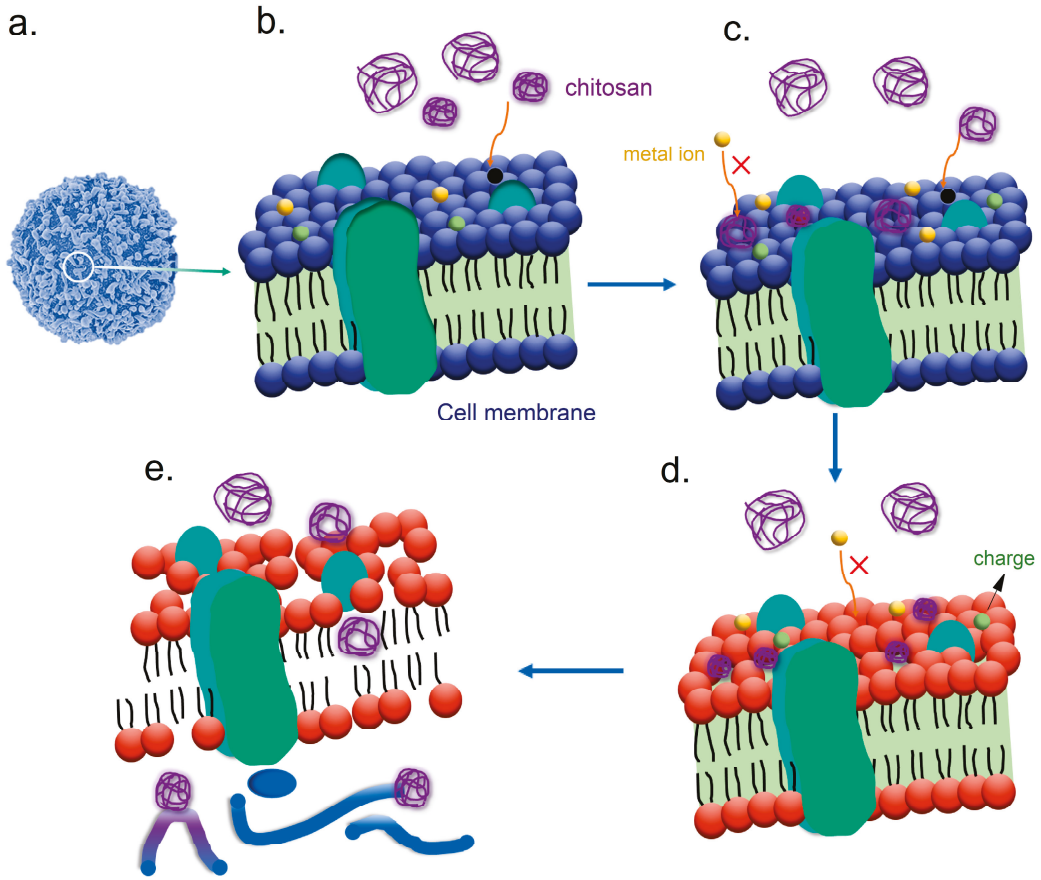

Figure 3. Schematic mechanisms of the antibacterial activity of chitosan. (**a**) A schematic of a microbial cell. (**b**) Microbial cell membranes. (**c**–**e**) The different-molecular-weight chitosan interacts with the microbial cell membranes and the internal DNA fractions.

In addition to membrane disruption, chitosan can affect microbial physiology by interfering with cellular processes. Once chitosan penetrates the bacterial cell wall, it can inhibit

vital metabolic functions by interacting with intracellular proteins and nucleic acids. This interaction not only halts protein synthesis but may also impair DNA replication, which is critical for the survival and proliferation of bacteria, as shown in Figure 3e. Consequently, the broad-spectrum antibacterial activity of chitosan makes it effective against various microbes, including both Gram-positive and Gram-negative bacteria. Its ability to inhibit the growth of pathogenic bacteria, such as Escherichia coli and Staphylococcus aureus, highlights its potential applicability in food preservation and packaging [64,68].

Additionally, the antibacterial efficacy of chitosan can be affected by various factors, such as its molecular weight, degree of deacetylation, and concentration in formulations. Generally, chitosan with a lower molecular weight demonstrates greater effectiveness against bacteria. This enhanced performance is attributed to its improved solubility and greater capacity to interact with microbial cells. The degree of deacetylation, which refers to the extent to which chitin has been converted to chitosan, affects the polymer's charge density and, consequently, its antibacterial activity. Studies have shown that chitosan with a higher degree of deacetylation exhibits enhanced antibacterial properties. Furthermore, variations in pH and ionic strength can also impact chitosan's performance. They are the important factors in optimizing chitosan's application in food packaging [64–67]. So, incorporating chitosan into food packaging materials effectively inhibits microbial growth. It also meets the increasing consumer demand for natural and environmentally friendly additives in food packaging materials.

3.3. Synergistic Effects of Chitosan and Cellulose Blends in Antibacterial Activity

The synergistic effects of chitosan and cellulose in blends are pivotal in enhancing the functional properties of food packaging materials [13,15]. Chitosan has a cationic nature. When blended with cellulose, these two biopolymers complement each other, improving the overall performance of this kind of material [69]. The synergy between chitosan and cellulose arises from their properties to combine strong antimicrobial action with structural integrity and biodegradability.

One significant aspect of this synergy is the improved antimicrobial efficacy observed when chitosan is incorporated into cellulose matrices. The presence of cellulose not only serves as a carrier for chitosan but also facilitates the controlled release of antimicrobial agents. This slow-release mechanism prolongs the antimicrobial effect, allowing for sustained inhibition of microbial growth over time [59–64]. The cellulose blend enhances the solubility and bioavailability of chitosan's active components. So, it increases the contact between the antimicrobial agents and microbials. The result is particularly advantageous for food preservation. The schematic of chitosan and cellulose in blends interacting with microbials is displayed in Figure 4.

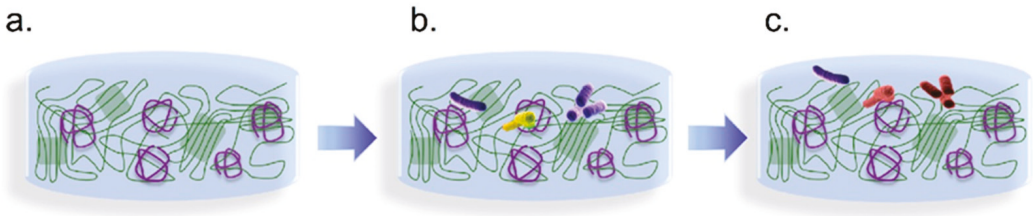

Figure 4. A schematic of chitosan and cellulose in blends interacting with microbials. (**a**–**c**) The antibacterial process of chitosan and cellulose in blends. (Purple thread represents chitosan, green thread represents cellulose, purple and yellow cylinders represent active bacteria, and reddish-brown cylinders represent dead bacteria.)

In addition, the mechanical and barrier properties are significantly improved through blending. Cellulose fibers provide strength and a higher degree of flexibility. It makes the

resulting material more resilient for food packaging applications. Chitosan incorporation in blends enhances the tensile strength of the blend. It is essential for maintaining the freshness of food products [70]. The packaging materials with this combination can adapt to different types of food.

3.4. Antioxidant Properties of Chitosan–Cellulose Blended Films

Antioxidant properties also play a crucial role in food packaging materials. Oxidation can lead to the degradation of food quality, resulting in the loss of flavor, color, and nutritional value. Antibacterial chitosan–cellulose blended films in food packaging have garnered significant attention. Researchers have developed innovative packaging solutions by incorporating chitosan [13]. They help food to mitigate oxidative stress caused by environmental factors such as light, heat, and oxygen exposure [71]. These biopolymer blends inhibit microbial growth and provide a barrier against the food's oxidative reactions.

Reactive oxygen species (ROS) refer to molecules, atoms, or ions that contain unpaired electrons. Three significant types of reactive oxygen species are superoxide anion radicals, hydroxyl radicals, and alkyl radicals. These free radicals exhibit high reactivity and are associated with over 100 diseases [72,73]. Moreover, reactive oxygen species can accelerate the aging and spoilage of fruits, vegetables, and fruit juices during storage, negatively impacting their quality and taste [74]. Therefore, researching and developing substances with antioxidant properties is significant. These substances can help mitigate the damaging effects of ROS, preserving the quality of food products.

Experimental studies have demonstrated that chitosan can scavenge free radicals and protect the body from oxidative damage [75]. Research indicates that low-molecular-weight chitosan has superior antioxidant properties compared with high-molecular-weight chitosan [76]. However, as molecular weight increases, the antioxidant capacity may decline. A similar trend has been observed in studies involving DPPH (1,1-diphenyl-2-picrylhydrazyl) radical scavenging [75,77].

Microorganisms such as bacteria, molds, and yeasts significantly contribute to the spoilage of fruits, vegetables, meat, and seafood, leading to a reduced shelf life for these products [32]. The application of chitosan in food preservation can be classified into three categories: (1) the use of unmodified chitosan, as illustrated in Figure 5a; (2) modified chitosan; and (3) composite chitosan formulations. Unmodified chitosan possesses natural antimicrobial properties, effectively inhibiting the growth of spoilage-causing microorganisms [78].

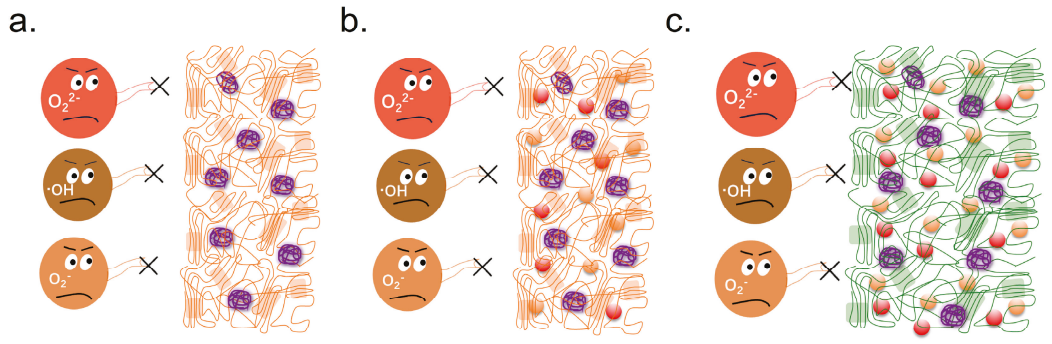

Figure 5. A schematic of different chitosan materials for free radical scavenging. (**a**) Chitosan and polymer film materials. (**b**) Modified chitosan and polymer composite film materials. (**c**) Modified chitosan and cellulose composite film materials. (Purple thread represents chitosan, green thread represents cellulose, orange thread represents other polymers.)

Modified chitosan typically incorporates additional functional groups or nanoparticles to enhance its antimicrobial activity. The reason is that the functional groups or nanoparti-

cles provide improved efficacy against a wider array of pathogens [79]. Composite chitosan, on the other hand, combines chitosan with other natural or synthetic materials to harness synergistic effects, resulting in even greater food preservation capabilities [80]. During the modification process of chitosan, its properties can be enhanced to improve its applicability, as shown in Figure 5b. For instance, chitosan's poor water solubility and relatively weak antibacterial activity limit its practical use. Various modification techniques, such as acylation, esterification, and alkylation, can be employed to improve its solubility. Additionally, processes like sulfation, oxidation, reaction with heterocyclic compounds, and grafting can enhance its biological activity. Physical modifications can also be used to improve the mechanical properties of chitosan [80–83].

Modified chitosan and cellulose composite film materials can enhance antibacterial performance by adding preservatives or antibacterial agents to chitosan solutions. It has a better food preservation effect compared to using unmodified chitosan alone, as shown in Figure 5c. For example, antimicrobial agents such as sodium lactate, tea polyphenols, film-forming agents like glycerol, and antioxidants such as phytic acid can be incorporated to enhance their efficacy. Furthermore, adding other materials like silica, Tween, and nanomaterials can improve certain properties of chitosan [81]. Composite chitosan films demonstrate significantly better preservation performance than monolithic coatings. By leveraging these various additives, composite chitosan material maintains the desired functionalities and extends the shelf life of perishable products more effectively [82]. This adaptability makes composite chitosan an attractive option for food preservation and other related applications.

4. The Preparation of Chitosan–Cellulose Blends and Their Benefits and Drawbacks

4.1. The Preparation of Chitosan–Cellulose Blends

The preparation process of chitosan–cellulose blends involves several methods. It focuses on the dissolution of biopolymers and subsequent mixing to create a homogeneous material. One common approach begins with the dissolution of chitosan in an acidic solvent, such as acetic acid. Acetic acid is beneficial for dissolving polymers while maintaining their inherent properties [13]. When components are effectively dissolved, they can be mixed in varying ratios. The process can help people to explore the optimal blend composition for the desired functionality. This blending process may also include the addition of plasticizers, such as glycerol, to enhance flexibility and processing characteristics. Different modified chitosan and cellulose can further enrich their applications. An illustration of chitosan and cellulose modifications in their blends for potential antibacterial food packaging is shown in Figure 6. For different modification studies, it is to optimize their performance in application fields such as food, sewage treatment, additives, etc., to meet practical application needs.

The significance and necessity of antimicrobial modifications in food packaging materials are multifaceted, primarily concerning food safety and sustainability. Antimicrobial packaging can inhibit the growth of bacteria, molds, and yeasts, thereby reducing the risk of foodborne pathogens, extending the shelf life of products, and minimizing food waste. These technologies cater to growing health awareness among consumers, differentiate products in the market, and assist companies in complying with food safety regulations, thereby enhancing consumer trust. Additionally, as the globalization of food progresses, food safety issues during long-distance transportation have become increasingly prominent, and antimicrobial packaging offers effective solutions to address these emerging challenges. In summary, antimicrobial food packaging not only helps improve product safety and freshness but also contributes to sustainable development, enhancing the integrity of the

food supply chain. Based on these considerations, we explore the applications of chitosan and cellulose in green, renewable food packaging materials and the advantages and disadvantages brought about by their modifications, with the aim of providing a reference for their broader research and application.

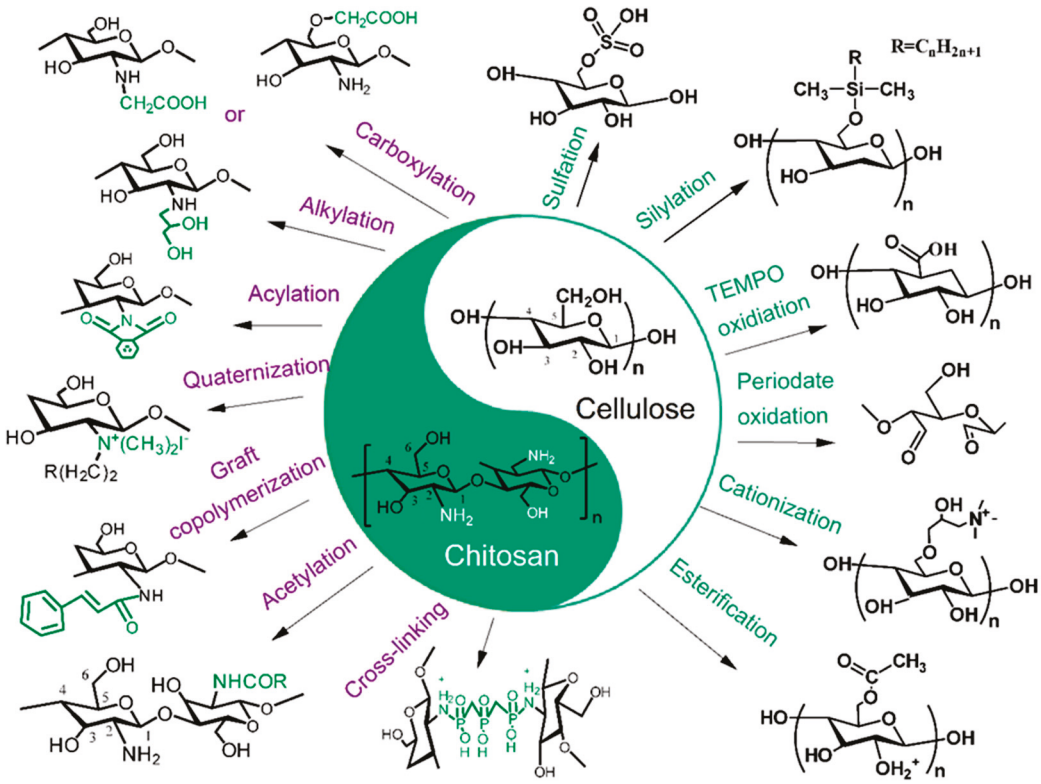

Figure 6. The different modifications of chitosan and cellulose in their blends for potential antibacterial food packaging.

For ease of understanding, we have conducted a comparative analysis of their different modification methods. Carboxymethyl chitosan is obtained after the carboxylation modification of chitosan. Compared with unmodified chitosan, its water solubility has been improved. In the chitosan molecule, the amino group at the C2 position and the hydroxyl groups at the C3 and C6 positions can be carboxylates. However, carboxylation of the hydroxyl group at the C3 position faces steric hindrance, making it less reactive, whereas carboxylation at the C2 amino and C6 hydroxyl groups is more common [83]. Alkylation is effective in food preservation because higher degrees of substitution and the presence of longer alkyl graft chains enhance coagulation-promoting effects. This leads to the improved stability and shelf life of food products [84,85]. The acylation modification of chitosan involves the reaction of its amino and hydroxyl groups with organic acyl chlorides or anhydrides. It produces O-acylated and N-acylated forms, increasing solubility and altering physicochemical properties according to reaction conditions. Research has found that the degree of acetylation significantly affects the properties of chitosan. Further research is crucial for fully understanding the behavior of modified chitosan and cellulose in food preservation applications. They include molecular interaction studies measured using surface force devices [75].

The quaternization reaction of chitosan is completed at the amino group on the C2 position, and it is typically carried out in two main ways. One is the direct quaternization of chitosan using alkyl halides. The other is grafting small molecules containing quaternary ammonium salt groups onto chitosan to achieve quaternized chitosan [86]. Chemical modi-

fications of natural polysaccharides enable diverse applications. And the development of tailored hybrid substances is completed through graft copolymerization methods. By grafting synthetic monomers onto natural chitosan, desired properties can be enhanced, thereby expanding the range of potential applications by incorporating various side chains [87]. In chitosan molecules, the amino and hydroxyl groups can react with cross-linking agents such as polyaldehydes, polycarboxylic acids, epichlorohydrin, episulfides, polycarboxylic anhydrides, and polyethers. These reactions increase intermolecular cross-linking, resulting in more stable chitosan derivatives, although their solubility decreases [88].

Negatively charged sulfate polysaccharides play a crucial role in their biological activity, promoting both specific and non-specific interactions with positively charged proteins. Additionally, the antibacterial properties of sulfate cellulose, combined with its promising biomedical applications, make it one of the most valuable cellulose derivatives on the market [89]. In recent years, research into silylation technology has deepened to further enhance the performance of cellulose. Silylation involves incorporating multifunctional silane compounds into cellulose fibers or nanocrystals, endowing them with unique characteristics based on specific functional groups within glucose units. This process not only increases the crystallinity and tensile strength of cellulose materials but also improves their functional capabilities, such as water vapor barrier properties and thermal resistance, making them more suitable for various applications [90]. Meanwhile, since 2017, the application range of TEMPO-oxidized cellulose nanofibers (TOCNFs) has also expanded significantly. This type of material has a carboxylate content of approximately 1.7 mmol/g and is increasingly favored in various fields due to its uniform width, excellent crystallinity, and high tensile strength. TOCNF is widely used in adhesives, hydrogels, membranes, and medical applications [91]. The enhancement of these properties is closely related to advancements in sulfation and silylation technologies, providing new opportunities for the development of cellulose-based materials in the biomedical field. Therefore, the processing techniques of sulfation, silylation, and TEMPO oxidation together drive the diversified applications of cellulose-based materials, opening new avenues for future research and development.

Periodate oxidation has proven effective for isolating nanocellulose. Particularly, when the oxidation degree is carefully controlled, it leads to advances in nanofibrillation techniques. This method has gained attention for producing dialdehyde cellulose nanocellulose. It also shows great potential for further functionalization and diverse applications in nanocellulosic material development [92,93]. Cellulose cationization was achieved through direct or indirect graft polymerizations. The graft methods were then evaluated for their effects on functionalization degree, thermal stability, crystallinity, and antiviral activity of cellulose. Indirect cationization yielded the highest polymer grafting, enhancing particle size and thermal stability. And the antiviral efficacy depended on the specific structure of functional groups and surface charge density. These changes demonstrate their potential for applications in textiles and packaging [94]. Cellulose esters are promising bio-based materials with potential applications in coatings, films, and plastics. These applications are based on their internal plasticization properties. Various esterification methods can synthesize cellulose esters with different side chain lengths. The acyl chloride method proved to be the most effective under homogeneous conditions [95,96].

4.2. The Benefits and Drawbacks of Different Modifications of Chitosan–Cellulose Blends

To facilitate the analysis and understanding of the benefits and drawbacks of different modifications of chitosan and cellulose in their blends for potential antibacterial food packaging, we present these aspects in the form of radial bar figures in Figure 7. Solid circles of different colors represent various modified chitosan samples, while hollow circles of different colors represent various modified cellulose samples. In the left figure (Figure 7a),

the advantages of modified chitosan and cellulose can be directly observed. Similarly, in the right figure (Figure 7b), the drawbacks of the modified chitosan and cellulose are clearly represented. Some modified chitosan samples, such as chitosan cross-linking (indicated by the blue solid circle), exhibit five advantages (Figure 7a), while the corresponding drawbacks associated with the modifications amount to four (Figure 7b). This figure can also be a reference for future research on modified chitosan and cellulose blends in different application scenarios.

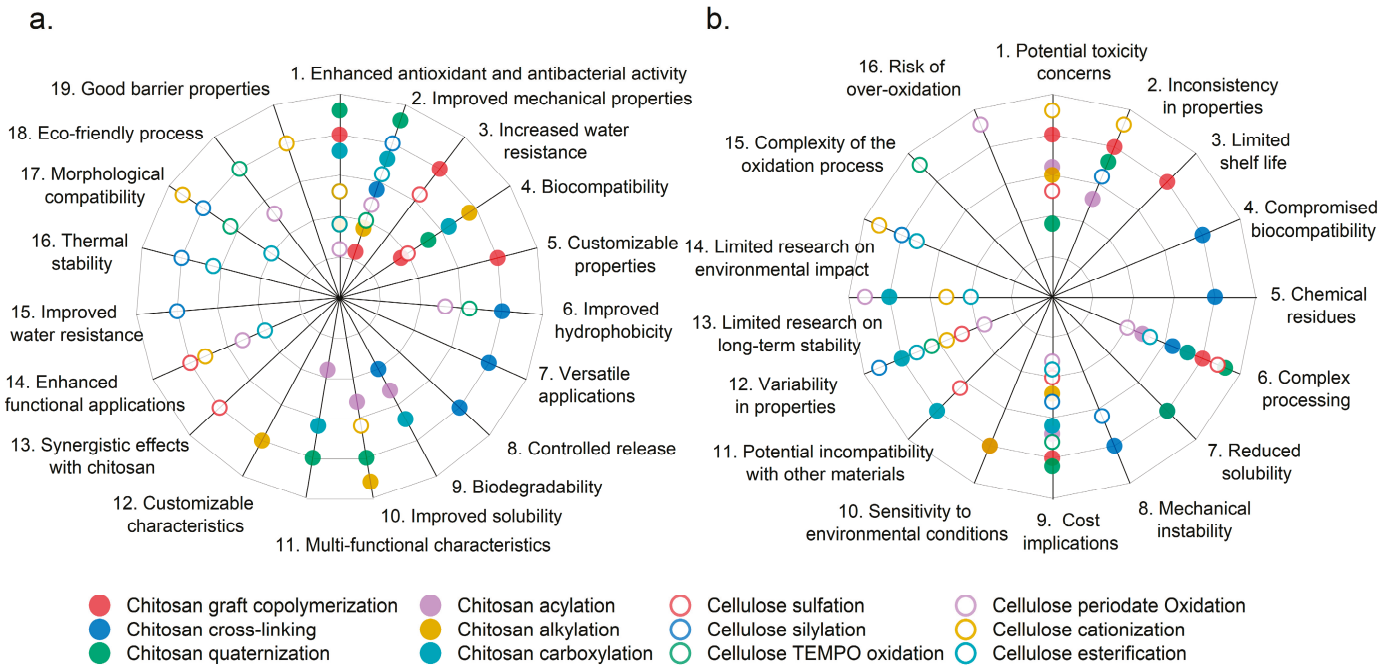

Figure 7. The benefits (**a**) and drawbacks (**b**) of different modifications of chitosan and cellulose in their blends for potential antibacterial food packaging.

Chitosan graft copolymerization in Figure 7 offers significant advantages, including enhanced antibacterial properties, improved mechanical strength, increased water resistance, and customizable characteristics, making it a valuable choice for food packaging applications. However, it poses challenges such as higher costs, complex manufacturing processes, potential toxicity concerns, inconsistent material properties, and limited shelf life [56,97,98]. Chitosan cross-linking enhances mechanical properties, hydrophobicity, and versatility for applications in packaging and biomedicine. Meanwhile, it retains biodegradability and facilitates controlled release of active ingredients. However, it may compromise biocompatibility, introduce chemical residues, complicate processing, reduce solubility, and create mechanical instability over time [99–101]. Chitosan quaternization significantly enhances antibacterial activity, solubility, biocompatibility, mechanical properties, and multifunctional characteristics, making it suitable for various food packaging applications. Nevertheless, it involves higher costs, a complex manufacturing process, potential toxicity concerns, and inconsistencies in material properties, and it may exhibit limited stability over time [45,102,103]. Chitosan acylation enhances antibacterial properties, allows for targeted functionalization, improves mechanical and barrier properties, offers customizable solubility, and maintains biodegradability, making it suitable for food packaging applications. Nonetheless, the process can be complex and costly, potentially leading to inconsistencies in material properties, raising toxicity concerns depending on the acylating agents, and exhibiting sensitivity to environmental conditions [38,79,104]. Chitosan alkylation enhances antibacterial activity, solubility, mechanical properties, and biocompatibility while allowing for customizable characteristics tailored for specific food

packaging applications. On the other hand, it involves complex processing, higher costs, potential inconsistencies in material properties, toxicity concerns regarding alkylating agents, and sensitivity to environmental conditions [36,75,105,106]. Chitosan carboxylation enhances antibacterial activity, solubility, and mechanical properties, and it allows for tailored functionalities, making it suitable for eco-friendly food packaging applications. However, the process is complex, may increase production costs, can lead to material compatibility issues, exhibits variability in different properties, and has limited research on long-term stability under various environmental conditions [107–109].

Cellulose sulfation enhances antibacterial properties, solubility, and functional applications while allowing for synergistic effects with chitosan, making it advantageous for food packaging. Nonetheless, the process is complex, may increase production costs, can alter mechanical properties, leads to variability in material consistency, and has limited research on its long-term environmental impact [110–113]. Cellulose sialylations enhance mechanical properties, water resistance, thermal stability, and compatibility with chitosan, making it effective for durable food packaging applications. On the other hand, the process is complex and costly, raises potential toxicity concerns, reduces biodegradability, and may lead to variability and incompatibility with other materials [112,114,115]. Cellulose TEMPO oxidation enhances mechanical properties, hydrophilicity, antibacterial activity, and compatibility with chitosan, while also being an eco-friendly modification process. The disadvantage is that this method is complex and costly, which may lead to performance changes; has limited long-term stability data; and may affect biodegradability [91,116–118]. Cellulose periodate oxidation enhances functionalization, antibacterial properties, mechanical strength, and modifiable hydrophilicity, making it compatible with eco-friendly packaging materials. Nonetheless, the process can be complex and costly, with risks of over-oxidation, variability in product quality, and limited long-term stability data [92,93]. Cellulose cationization improves antibacterial properties, water solubility, compatibility with chitosan, and barrier performance, making it beneficial for packaging applications. However, the complexity of the cationization process, potential cost implications, changes in properties, and limited long-term stability data may hinder its commercial viability [119–121]. Cellulose esterification enhances barrier properties, mechanical strength, and compatibility with chitosan while allowing for tailored functional properties and improved antioxidant and antibacterial activity, making it beneficial for food packaging applications. Nevertheless, the complexity of the process, potential cost increases, variability in product quality, limited long-term stability data, and concerns about biodegradability limit its commercial applicability [122–124].

In the above content, we analyzed the advantages and disadvantages of different modification methods for chitosan and cellulose through Figure 6. Modified chitosan and cellulose materials exhibit excellent performance in enhancing antioxidant and antibacterial activity, improving mechanical properties, and biocompatibility. These materials may not be satisfactory in terms of complex processing, potential toxicity issues, variability in performance, and cost impact, but these are also important research areas for future development.

5. Future Directions for Chitosan–Cellulose Blends

The future of chitosan–cellulose blends holds remarkable potential for innovation. These improving aspects include enhancing their properties to address the growing demands for effective, sustainable, and multifunctional packaging solutions.

5.1. Integration of Nanotechnology

One of the most promising areas for innovation is the integration of nanotechnology into chitosan–cellulose blends. Incorporating nanoparticles, such as silver, titanium dioxide, or even quantum dot materials, can significantly enhance the packaging material's antibacterial properties and mechanical strength [125]. M.M. Abutalib synthesized silver (Ag) nanoparticles with an average crystal size of 20 nm using water extract of fresh quinoa leaves, combined with 15 nm TiO_2 nanoparticles, and added Ag and TiO2 nanoparticles to the polymer blend system. The activity indices (%) of the antibacterial activity of the sample mixture + (0.3%) Ag + (0.8%) TiO_2 against Escherichia coli, Staphylococcus aureus, Candida albicans, and Aspergillus niger were 32%, 45.8%, 77.8%, and 92%, respectively. This provides new insights into the applicability of nanocomposites in food packaging applications [126]. Recently, quantum dots of MXene have been integrated into thermoplastic chitosan through wet chemical blending method, resulting in nanocomposite films with excellent UV resistance (>90%), antioxidant activity (>78%), and good flexibility at $-30\ ^{\circ}C$. This makes it a promising alternative material for sustainable and high-performance food packaging solutions [127].

These nanoparticles can provide a larger surface area for antimicrobial activity and improved interaction with the food products. Furthermore, nanomaterials can bolster the barrier properties against gases and liquids, extending shelf life while maintaining freshness. Advances in nanotechnology also allow for the precise control of the size, shape, and distribution of particles within the polymer matrix, leading to the optimization of overall performance.

5.2. Functionalization and Surface Modification

Functionalization techniques that modify the chemical structure of chitosan and cellulose can yield significant improvements in their properties. Methods such as graft copolymerization or blending with other biopolymers can create new materials with enhanced properties, such as improved adhesion, water resistance, and flexibility. For example, introducing functional groups that react favorably with food products can improve the seal ability of packaging, thereby enhancing its protective characteristics. The hydrophobicity of polyvinyl alcohol (PVA) and chitosan (CS) composite films is stronger than that of PVA films. This composite film has higher mechanical properties, with a Young's modulus, tensile strength, and elongation at break of 344.99 MPa, 39.12 MPa, and 507.09%, respectively [128]. Hydrophobic microcrystalline cellulose ester was prepared using microcrystalline cellulose and long-chain stearic acid. The above sample was applied onto the surface of sugarcane bagasse fiber paper to form a continuous hydrophobic film. This material exhibited good water repellency and oxygen blocking activity. The coated material samples also showed excellent dimensional stability, good wet tensile strength of 16 MPa, and good antibacterial performance in water [129]. Research has shown that modified composite films can extend the shelf life of antibacterial packaging. Surface modifications, such as creating hydrophobic or hydrophilic surfaces, can help tailor the blends for specific applications, allowing for better compatibility with various types of food items and environments.

5.3. Smart Packaging Solutions

The emergence of smart packaging is set to revolutionize food packaging made from chitosan–cellulose blends. Integrating sensors that monitor temperature, humidity, and the presence of spoilage indicators can provide real-time data on food quality and safety.

Zhiming Guo et al. recently developed a detector for collecting volatile gases from apples infected with acute anthrax, Botrytis cinerea, and Botrytis cinerea using deep learning

and variable selection algorithms. This device can transmit data in real-time and monitor remotely, achieving effective analysis and grading alerts for apple spoilage. It is expected that when combined with other different food packaging materials, it can achieve intelligent and powerful real-time monitoring and improve food quality. In addition, this study applied a collaborative interval gated cyclic unit model to construct an optimal warning model for multi-environmental factor detection [130]. In addition, color-changing indicators can alert consumers to potential spoilage, enhancing food safety and reducing waste. Vânia Gomes researched intelligent labels for freshness monitoring in food packaging. In summary, 0.2% (*w*/*w*) pyranoyl pigment and 30% (*w*/*w*) glycerol were added to a cellulose solution. Thin films with different pH response properties (pH 4 to 8) were prepared by the solvent casting method. In the preservation of fish and meat, freshness monitoring of fish samples can be carried out. As the fish meat rots, the yellow label begins to turn purple, effectively helping people detect the beginning of the fish meat spoilage process [131]. These innovations will benefit consumers and empower manufacturers to track product conditions better throughout the supply chain. Smart packaging can help people store food under optimal conditions.

5.4. Advanced Processing Techniques

The advancement of processing techniques will play a crucial role in the future of chitosan–cellulose blends. Techniques such as 3D printing and electrospinning can create structures with highly tailored properties, enabling the design of innovative packaging solutions. For example, electrospinning can produce ultrafine fibers that enhance the surface area available for antibacterial action [132]. Meanwhile, 3D printing allows for customizable shapes and designs that improve the packaging's protective capabilities and consumer appeal. Three-dimensional printing technology is expected to be applied in food production for different populations with varying demands by adding different food ingredients and additives. The demands mainly include customized printing of food, personalized nutrition, and food packaging applications.

In addition to meeting the requirements of color, size, and design, additive manufacturing technology through 3D printing can also reduce waste of packaging materials. On the other hand, customized food packaging can be achieved through 3D printing to explore the optimal application process and conditions of additive manufacturing in food packaging. Three-dimensional printing technology is also used to develop machine parts for packaging production lines in the food packaging process. These include picking and placing robots. This innovation reduces the time and resources required for outsourcing design and manufacturing operations [133]. In addition, by combining the characteristics of 3D printing with thermal environment temperature sensing systems in the production process of food packaging, research can be conducted to improve the thermal performance and environmental adaptability of food packaging [134]. So, 3D printing developments in bio-composite processing will facilitate large-scale manufacturing and integration with existing packaging technologies.

6. Conclusions

Chitosan and cellulose are gaining attention in the food industry due to their eco-friendly characteristics and broad application prospects. Both biopolymers are derived from renewable sources, making them sustainable alternatives to conventional plastic materials, a significant consumer concern today. One of the most promising applications of chitosan and cellulose blends lies in food packaging. Chitosan possesses notable antimicrobial properties that can inhibit the growth of bacteria and fungi, while cellulose provides essential structural integrity, mechanical strength, and flexibility. This combina-

tion enhances food preservation and contributes to reducing plastic waste, aligning with global sustainability goals.

Moreover, the development of chitosan and cellulose blends involves various preparation methods that can be tailored to enhance their properties. Research is progressing toward customizing these blends for specific food types and applications, increasing their effectiveness in preserving food quality and safety. As consumer preferences shift towards safer and more sustainable packaging options, innovation in using chitosan and cellulose blends is poised to play a crucial role in the future of the food packaging industry. This paper aims to encourage further research on the structure and properties of these blends following various modifications, highlighting their potential to revolutionize food packaging and contribute to environmental sustainability.

Author Contributions: Writing—original draft, supervision, funding acquisition, and conceptualization, T.Q.; review, editing, and conceptualization, X.W.; supervision and conceptualization, F.Z. All authors have read and agreed to the published version of the manuscript.

Funding: This research was supported by the Project of the University and College Key Lab of Natural Product Chemistry and Application in Xinjiang (No. 2022YSHXZD003), the Tianshan Talents Program of Xinjiang, China (2025–2028) (No. 2024TSYCJC0030), and the Natural Science Foundation Project of Xinjiang Uygur Autonomous Region (No. 2021D01C470). The APC was funded by Yili Normal University.

Institutional Review Board Statement: Not applicable.

Data Availability Statement: No new data were created or analyzed in this study. Data sharing does not apply to this article.

Conflicts of Interest: The author Xiaowen Wang is employed by the company Sichuan Water Development Group Co., Ltd. The remaining authors declare that the research was conducted in the absence of any commercial or financial relationships that could be construed as potential conflicts of interest.

References

1. Madhumala, Y.; Soraganvi, V.S. Microbiology of Food Spoilage. In *Frontiers in Food Biotechnology*; Yaradoddi, J.S., Meti, B.S., Mudgulkar, S.B., Agsar, D., Eds.; Springer Nature: Singapore, 2024; pp. 67–80.
2. Roy, P.; Mohanty, A.K.; Dick, P.; Misra, M. A Review on the Challenges and Choices for Food Waste Valorization: Environmental and Economic Impacts. *ACS Environ. Au* **2023**, *3*, 58–75. [CrossRef] [PubMed]
3. Mc Carthy, U.; Uysal, I.; Badia-Melis, R.; Mercier, S.; O'Donnell, C.; Ktenioudaki, A. Global food security—Issues, challenges and technological solutions. *Trends Food Sci. Technol.* **2018**, *77*, 11–20. [CrossRef]
4. Heydari, M. Cultivating sustainable global food supply chains: A multifaceted approach to mitigating food loss and waste for climate resilience. *J. Clean. Prod.* **2024**, *442*, 141037. [CrossRef]
5. Ma, Y.; Liu, Y. Turning food waste to energy and resources towards a great environmental and economic sustainability: An innovative integrated biological approach. *Biotechnol. Adv.* **2019**, *37*, 107414. [CrossRef] [PubMed]
6. Sharma, R.; Jafari, S.M.; Sharma, S. Antimicrobial bio-nanocomposites and their potential applications in food packaging. *Food Control* **2020**, *112*, 107086. [CrossRef]
7. El-Saber Batiha, G.; Hussein, D.E.; Algammal, A.M.; George, T.T.; Jeandet, P.; Al-Snafi, A.E.; Tiwari, A.; Pagnossa, J.P.; Lima, C.M.; Thorat, N.D.; et al. Application of natural antimicrobials in food preservation: Recent views. *Food Control* **2021**, *126*, 108066. [CrossRef]
8. Jagtiani, E. Advancements in nanotechnology for food science and industry. *Food Front.* **2022**, *3*, 56–82. [CrossRef]
9. Akelah, A. Polymers in Food Packaging and Protection. In *Functionalized Polymeric Materials in Agriculture and the Food Industry*; Akelah, A., Ed.; Springer: Boston, MA, USA, 2013; pp. 293–347.
10. Bopp, A.F. The Evolution of Food Preservation and Packaging. In *Chemistry's Role in Food Production and Sustainability: Past and Present*; American Chemical Society: Washington, DC, USA, 2019; Volume 1314, pp. 211–228.
11. Marsh, K.; Bugusu, B. Food Packaging—Roles, Materials, and Environmental Issues. *J. Food Sci.* **2007**, *72*, R39–R55. [CrossRef]
12. Kaur, K.; Reddy, S.; Barathe, P.; Oak, U.; Shriram, V.; Kharat, S.S.; Govarthanan, M.; Kumar, V. Microplastic-associated pathogens and antimicrobial resistance in environment. *Chemosphere* **2022**, *291*, 133005. [CrossRef]

13. Ambaye, T.G.; Vaccari, M.; Prasad, S.; van Hullebusch, E.D.; Rtimi, S. Preparation and applications of chitosan and cellulose composite materials. *J. Environ. Manag.* **2022**, *301*, 113850. [CrossRef]
14. Priyadarshi, R.; Rhim, J.-W. Chitosan-based biodegradable functional films for food packaging applications. *Innov. Food Sci. Emerg. Technol.* **2020**, *62*, 102346. [CrossRef]
15. Abdul Khalil, H.P.S.; Saurabh, C.K.; Adnan, A.S.; Nurul Fazita, M.R.; Syakir, M.I.; Davoudpour, Y.; Rafatullah, M.; Abdullah, C.K.; Haafiz, M.K.M.; Dungani, R. A review on chitosan-cellulose blends and nanocellulose reinforced chitosan biocomposites: Properties and their applications. *Carbohydr. Polym.* **2016**, *150*, 216–226.
16. Khattak, S.; Wahid, F.; Liu, L.-P.; Jia, S.-R.; Chu, L.-Q.; Xie, Y.-Y.; Li, Z.-X.; Zhong, C. Applications of cellulose and chitin/chitosan derivatives and composites as antibacterial materials: Current state and perspectives. *Appl. Microbiol. Biotechnol.* **2019**, *103*, 1989–2006. [CrossRef] [PubMed]
17. Kurita, K. Chitin and Chitosan: Functional Biopolymers from Marine Crustaceans. *Mar. Biotechnol.* **2006**, *8*, 203–226. [CrossRef]
18. Joseph, S.M.; Krishnamoorthy, S.; Paranthaman, R.; Moses, J.A.; Anandharamakrishnan, C. A review on source-specific chemistry, functionality, and applications of chitin and chitosan. *Carbohydr. Polym. Technol. Appl.* **2021**, *2*, 100036. [CrossRef]
19. Azmana, M.; Mahmood, S.; Hilles, A.R.; Rahman, A.; Arifin, M.A.B.; Ahmed, S. A review on chitosan and chitosan-based bionanocomposites: Promising material for combatting global issues and its applications. *Int. J. Biol. Macromol.* **2021**, *185*, 832–848. [CrossRef] [PubMed]
20. Praveen Kumar, G.; Shreeya Sai, R.; Deepali Venkatesh, P.; Priyadharsini, V.; Vidhya, S.; Chandrananthi, C.; Shreya, C.; Krithika, S.; Keerthana, G. An Update on Overview of Cellulose, Its Structure and Applications. In *Cellulose*; Alejandro Rodríguez, P., María, E.E.M., Eds.; IntechOpen: Rijeka, Croatia, 2019; Chapter 4.
21. Elango, B.; Shirley, C.P.; Okram, G.S.; Ramesh, T.; Seralathan, K.-K.; Mathanmohun, M. Structural diversity, functional versatility and applications in industrial, environmental and biomedical sciences of polysaccharides and its derivatives—A review. *Int. J. Biol. Macromol.* **2023**, *250*, 126193. [CrossRef]
22. Payne, C.M.; Knott, B.C.; Mayes, H.B.; Hansson, H.; Himmel, M.E.; Sandgren, M.; Ståhlberg, J.; Beckham, G.T. Fungal Cellulases. *Chem. Rev.* **2015**, *115*, 1308–1448. [CrossRef]
23. Zanchetta, E.; Damergi, E.; Patel, B.; Borgmeyer, T.; Pick, H.; Pulgarin, A.; Ludwig, C. Algal cellulose, production and potential use in plastics: Challenges and opportunities. *Algal Res.* **2021**, *56*, 102288. [CrossRef]
24. Zhou, S.; Nyholm, L.; Strømme, M.; Wang, Z. Cladophora Cellulose: Unique Biopolymer Nanofibrils for Emerging Energy, Environmental, and Life Science Applications. *Acc. Chem. Res.* **2019**, *52*, 2232–2243. [CrossRef]
25. Christina, K.; Subbiah, K.; Arulraj, P.; Krishnan, S.K.; Sathishkumar, P. A sustainable and eco-friendly approach for environmental and energy management using biopolymers chitosan, lignin and cellulose—A review. *Int. J. Biol. Macromol.* **2024**, *257*, 128550. [CrossRef]
26. Xiong Chang, X.; Mujawar Mubarak, N.; Ali Mazari, S.; Sattar Jatoi, A.; Ahmad, A.; Khalid, M.; Walvekar, R.; Abdullah, E.C.; Karri, R.R.; Siddiqui, M.T.H.; et al. A review on the properties and applications of chitosan, cellulose and deep eutectic solvent in green chemistry. *J. Ind. Eng. Chem.* **2021**, *104*, 362–380. [CrossRef]
27. Silva, F.; Domingues, F.C.; Nerín, C. Trends in microbial control techniques for poultry products. *Crit. Rev. Food Sci. Nutr.* **2018**, *58*, 591–609. [CrossRef] [PubMed]
28. Deshpande, A. *Meat Technology and Processing*; Educohack Press: Delhi, India, 2025.
29. Ntuli, V.; Sibanda, T.; Elegbeleye, J.A.; Mugadza, D.T.; Seifu, E.; Buys, E.M. Chapter 30—Dairy production: Microbial safety of raw milk and processed milk products. In *Present Knowledge in Food Safety*; Knowles, M.E., Anelich, L.E., Boobis, A.R., Popping, B., Eds.; Academic Press: Cambridge, MA, USA, 2023; pp. 439–454.
30. Magan, N.; Aldred, D.; Arroyo, M. Chapter 18—Mold prevention in bread. In *Breadmaking*, 3rd ed.; Cauvain, S.P., Ed.; Woodhead Publishing: Sawston, UK, 2012; pp. 541–560.
31. Bolívar-Monsalve, J.; Ramírez-Toro, C.; Bolívar, G.; Ceballos-González, C. Mechanisms of action of novel ingredients used in edible films to preserve microbial quality and oxidative stability in sausages—A review. *Trends Food Sci. Technol.* **2019**, *89*, 100–109. [CrossRef]
32. Mafe, A.N.; Edo, G.I.; Makia, R.S.; Joshua, O.A.; Akpoghelie, P.O.; Gaaz, T.S.; Jikah, A.N.; Yousif, E.; Isoje, E.F.; Igbuku, U.A.; et al. A review on food spoilage mechanisms, food borne diseases and commercial aspects of food preservation and processing. *Food Chem. Adv.* **2024**, *5*, 100852. [CrossRef]
33. Pongchaiphol, S.; Preechakun, T.; Raita, M.; Champreda, V.; Laosiripojana, N. Characterization of Cellulose–Chitosan-Based Materials from Different Lignocellulosic Residues Prepared by the Ethanosolv Process and Bleaching Treatment with Hydrogen Peroxide. *ACS Omega* **2021**, *6*, 22791–22802. [CrossRef]
34. Lim, C.; Hwang, D.S.; Lee, D.W. Intermolecular interactions of chitosan: Degree of acetylation and molecular weight. *Carbohydr. Polym.* **2021**, *259*, 117782. [CrossRef] [PubMed]

35. Pereira, N.R.L.; Lopes, B.; Fagundes, I.V.; de Moraes, F.M.; Morisso, F.D.P.; Parma, G.O.C.; Zepon, K.M.; Magnago, R.F. Biopackaging based on cellulose acetate from banana pseudostem and containing Butia catarinensis extracts. *Int. J. Biol. Macromol.* **2022**, *194*, 32–41. [CrossRef]
36. Paula, H.C.B.; Silva, R.B.C.; Santos, C.M.; Dantas, F.D.S.; de Paula, R.C.M.; de Lima, L.R.M.; de Oliveira, E.F.; Figueiredo, E.A.T.; Dias, F.G.B. Eco-friendly synthesis of an alkyl chitosan derivative. *Int. J. Biol. Macromol.* **2020**, *163*, 1591–1598. [CrossRef]
37. Lepetit, A.; Drolet, R.; Tolnai, B.; Montplaisir, D.; Zerrouki, R. Alkylation of microfibrillated cellulose—A green and efficient method for use in fiber-reinforced composites. *Polymer* **2017**, *126*, 48–55. [CrossRef]
38. Linhorst, M.; Wattjes, J.; Moerschbacher, B.M. Chitin Deacetylase as a Biocatalyst for the Selective N-Acylation of Chitosan Oligo- and Polymers. *ACS Catal.* **2021**, *11*, 14456–14466. [CrossRef]
39. Zhang, N.; Bi, F.; Xu, F.; Yong, H.; Bao, Y.; Jin, C.; Liu, J. Structure and functional properties of active packaging films prepared by incorporating different flavonols into chitosan based matrix. *Int. J. Biol. Macromol.* **2020**, *165*, 625–634. [CrossRef]
40. Andreica, B.-I.; Anisiei, A.; Rosca, I.; Marin, L. Quaternized chitosan-based nanofibers with strong antibacterial and antioxidant activity designed as ecological active food packaging. *Food Packag. Shelf Life* **2023**, *39*, 101157. [CrossRef]
41. Zhang, H.; Wang, J.; Sun, X.; Zhang, Y.; Dong, M.; Wang, X.; Li, L.; Wang, L. Fabrication and Characterization of Quercetagetin-Loaded Nanoparticles Based on Shellac and Quaternized Chitosan: Improvement of Encapsulation Efficiency and Acid and Storage Stabilities. *J. Agric. Food Chem.* **2021**, *69*, 15670–15680. [CrossRef]
42. Kim, Y.H.; Kim, H.-J.; Yoon, K.S.; Rhim, J.-W. Cellulose nanofiber/deacetylated quaternary chitosan composite packaging film for growth inhibition of Listeria monocytogenes in raw salmon. *Food Packag. Shelf Life* **2023**, *35*, 101040. [CrossRef]
43. Phuangkaew, T.; Booranabunyat, N.; Kiatkamjornwong, S.; Thanyasrisung, P.; Hoven, V.P. Amphiphilic quaternized chitosan: Synthesis, characterization, and anti-cariogenic biofilm property. *Carbohydr. Polym.* **2022**, *277*, 118882. [CrossRef]
44. Hu, D.; Wang, L. Preparation and characterization of antibacterial films based on polyvinyl alcohol/quaternized cellulose. *React. Funct. Polym.* **2016**, *101*, 90–98. [CrossRef]
45. Huang, K.-X.; Zhou, L.-Y.; Chen, J.-Q.; Peng, N.; Chen, H.-X.; Gu, H.-Z.; Zou, T. Applications and perspectives of quaternized cellulose, chitin and chitosan: A review. *Int. J. Biol. Macromol.* **2023**, *242*, 124990. [CrossRef]
46. Deng, Z.; Jung, J.; Zhao, Y. Development, characterization, and validation of chitosan adsorbed cellulose nanofiber (CNF) films as water resistant and antibacterial food contact packaging. *LWT Food Sci. Technol.* **2017**, *83*, 132–140. [CrossRef]
47. Noorbakhsh-Soltani, S.M.; Zerafat, M.M.; Sabbaghi, S. A comparative study of gelatin and starch-based nano-composite films modified by nano-cellulose and chitosan for food packaging applications. *Carbohydr. Polym.* **2018**, *189*, 48–55. [CrossRef]
48. Gao, Q.; Lei, M.; Zhou, K.; Liu, X.; Wang, S.; Li, H. Preparation of a microfibrillated cellulose/chitosan/polypyrrole film for Active Food Packaging. *Prog. Org. Coat.* **2020**, *149*, 105907. [CrossRef]
49. Dey, D.; Dharini, V.; Periyar Selvam, S.; Rotimi Sadiku, E.; Mahesh Kumar, M.; Jayaramudu, J.; Nath Gupta, U. Physical, antifungal, and biodegradable properties of cellulose nanocrystals and chitosan nanoparticles for food packaging application. *Mater. Today Proc.* **2021**, *38*, 860–869. [CrossRef]
50. Riahi, Z.; Rhim, J.-W.; Bagheri, R.; Pircheraghi, G.; Lotfali, E. Carboxymethyl cellulose-based functional film integrated with chitosan-based carbon quantum dots for active food packaging applications. *Prog. Org. Coat.* **2022**, *166*, 106794. [CrossRef]
51. Xu, K.; Li, Q.; Xie, L.; Shi, Z.; Su, G.; Harper, D.; Tang, Z.; Zhou, J.; Du, G.; Wang, S. Novel flexible, strong, thermal-stable, and high-barrier switchgrass-based lignin-containing cellulose nanofibrils/chitosan biocomposites for food packaging. *Ind. Crops Prod.* **2022**, *179*, 114661. [CrossRef]
52. Yi, C.; Yuan, T.; Xiao, H.; Ren, H.; Zhai, H. Hydrophobic-modified cellulose nanofibrils (CNFs)/chitosan/zein coating for enhancing multi-barrier properties of heat-sealable food packaging materials. *Colloids Surf. A Physicochem. Eng. Asp.* **2023**, *666*, 131245. [CrossRef]
53. Nazari, M.; Majdi, H.; Gholizadeh, P.; Kafil, H.S.; Hamishehkar, H.; Zarchi, A.A.K.; Khoddami, A. An eco-friendly chitosan/cellulose acetate hybrid nanostructure containing Ziziphora clinopodioides essential oils for active food packaging applications. *Int. J. Biol. Macromol.* **2023**, *235*, 123885. [CrossRef]
54. Jiang, J.; Chen, X.; Zhang, G.-L.; Hao, H.; Hou, H.-M.; Bi, J. Preparation of chitosan-cellulose-benzyl isothiocyanate nanocomposite film for food packaging applications. *Carbohydr. Polym.* **2022**, *285*, 119234. [CrossRef]
55. Beji, E.; Keshk, S.M.A.S.; Douiri, S.; Charradi, K.; Ben Hassen, R.; Gtari, M.; Attia, H.; Ghorbel, D. Bioactive film based on chitosan incorporated with cellulose and aluminum chloride for food packaging application: Fabrication and characterization. *Food Biosci.* **2023**, *53*, 102678. [CrossRef]
56. Liao, W.; Liu, X.; Zhao, Q.; Lu, Z.; Feng, A.; Sun, X. Physicochemical, antibacterial and food preservation properties of active packaging films based on chitosan/ε-polylysine-grafted bacterial cellulose. *Int. J. Biol. Macromol.* **2023**, *253*, 127231. [CrossRef]
57. Wang, K.; Li, W.; Wu, L.; Li, Y.; Li, H. Preparation and characterization of chitosan/dialdehyde carboxymethyl cellulose composite film loaded with cinnamaldehyde@zein nanoparticles for active food packaging. *Int. J. Biol. Macromol.* **2024**, *261*, 129586. [CrossRef]

58. Latif, S.; Ahmed, M.; Ahmed, M.; Ahmad, M.; Al-Ahmary, K.M.; Ali, I. Development of Plumeria alba extract supplemented biodegradable films containing chitosan and cellulose derived from bagasse and corn cob waste for antimicrobial food packaging. *Int. J. Biol. Macromol.* **2024**, *266*, 131262. [CrossRef]
59. Hasannezhad, H.; Bakhshi, A.; Mozafari, M.R.; Naghib, S.M. A review of chitosan role in milk bioactive-based drug delivery, smart packaging and biosensors: Recent advances and developments. *Int. J. Biol. Macromol.* **2024**, *294*, 139248. [CrossRef]
60. Qian, M.; Liu, D.; Zhang, X.; Yin, Z.; Ismail, B.B.; Ye, X.; Guo, M. A review of active packaging in bakery products: Applications and future trends. *Trends Food Sci. Technol.* **2021**, *114*, 459–471. [CrossRef]
61. Inanli, A.G.; Tümerkan, E.T.A.; Abed, N.E.; Regenstein, J.M.; Özogul, F. The impact of chitosan on seafood quality and human health: A review. *Trends Food Sci. Technol.* **2020**, *97*, 404–416. [CrossRef]
62. Tian, B.; Liu, J.; Yang, W.; Wan, J.-B. Biopolymer Food Packaging Films Incorporated with Essential Oils. *J. Agric. Food Chem.* **2023**, *71*, 1325–1347. [CrossRef]
63. Shen, Y.; Seidi, F.; Ahmad, M.; Liu, Y.; Saeb, M.R.; Akbari, A.; Xiao, H. Recent Advances in Functional Cellulose-based Films with Antimicrobial and Antioxidant Properties for Food Packaging. *J. Agric. Food Chem.* **2023**, *71*, 16469–16487. [CrossRef] [PubMed]
64. Nasaj, M.; Chehelgerdi, M.; Asghari, B.; Ahmadieh-Yazdi, A.; Asgari, M.; Kabiri-Samani, S.; Sharifi, E.; Arabestani, M. Factors influencing the antimicrobial mechanism of chitosan action and its derivatives: A review. *Int. J. Biol. Macromol.* **2024**, *277*, 134321. [CrossRef]
65. Minh, N.C.; Van Hoa, N.; Trung, T.S. Chapter 15—Preparation, properties, and application of low-molecular-weight chitosan. In *Handbook of Chitin and Chitosan*; Gopi, S., Thomas, S., Pius, A., Eds.; Elsevier: Amsterdam, The Netherlands, 2020; pp. 453–471.
66. Park, Y.; Kim, M.-H.; Park, S.-C.; Cheong, H.; Jang, M.-K.; Nah, J.-W.; Hahm, K.-S. Investigation of the antifungal activity and mechanism of action of LMWS-chitosan. *J. Microbiol. Biotechnol.* **2008**, *18*, 1729–1734.
67. Seyfarth, F.; Schliemann, S.; Elsner, P.; Hipler, U.C. Antifungal effect of high- and low-molecular-weight chitosan hydrochloride, carboxymethyl chitosan, chitosan oligosaccharide and N-acetyl-d-glucosamine against *Candida albicans*, *Candida krusei* and *Candida glabrata*. *Int. J. Pharm.* **2008**, *353*, 139–148. [CrossRef]
68. Mumtaz, S.; Ali, S.; Mumtaz, S.; Mughal, T.A.; Tahir, H.M.; Shakir, H.A. Chitosan conjugated silver nanoparticles: The versatile antibacterial agents. *Polym. Bull.* **2023**, *80*, 4719–4736. [CrossRef]
69. Goel, S.; Bano, Y. Chapter 13—Chitosan-based nanofibrous membranes for antibacterial filter applications. In *Antimicrobial Materials and Coatings*; Singh, A.K., Dhayal, M., Hussain, C.M., Eds.; Woodhead Publishing: Sawston, UK, 2025; pp. 425–447.
70. Bhowmik, S.; Agyei, D.; Ali, A. Enhancement of mechanical, barrier, and functional properties of chitosan film reinforced with glycerol, COS, and gallic acid for active food packaging. *Sustain. Mater. Technol.* **2024**, *41*, e01092. [CrossRef]
71. Kuai, L.; Liu, F.; Chiou, B.-S.; Avena-Bustillos, R.J.; McHugh, T.H.; Zhong, F. Controlled release of antioxidants from active food packaging: A review. *Food Hydrocoll.* **2021**, *120*, 106992. [CrossRef]
72. Averill-Bates, D. Reactive oxygen species and cell signaling. Review. *Biochim. Biophys. Acta Mol. Cell Res.* **2024**, *1871*, 119573. [CrossRef]
73. Zaric, B.L.; Macvanin, M.T.; Isenovic, E.R. Free radicals: Relationship to Human Diseases and Potential Therapeutic applications. *Int. J. Biochem. Cell Biol.* **2023**, *154*, 106346. [CrossRef] [PubMed]
74. Zhao, H.; Zhang, S.; Ma, D.; Liu, Z.; Qi, P.; Wang, Z.; Di, S.; Wang, X. Review of fruits flavor deterioration in postharvest storage: Odorants, formation mechanism and quality control. *Food Res. Int.* **2024**, *182*, 114077. [CrossRef]
75. Harugade, A.; Sherje, A.P.; Pethe, A. Chitosan: A review on properties, biological activities and recent progress in biomedical applications. *React. Funct. Polym.* **2023**, *191*, 105634. [CrossRef]
76. Anraku, M.; Gebicki, J.M.; Iohara, D.; Tomida, H.; Uekama, K.; Maruyama, T.; Hirayama, F.; Otagiri, M. Antioxidant activities of chitosans and its derivatives in in vitro and in vivo studies. *Carbohydr. Polym.* **2018**, *199*, 141–149. [CrossRef]
77. Negm, N.A.; Kana, M.T.H.A.; Abubshait, S.A.; Betiha, M.A. Effectuality of chitosan biopolymer and its derivatives during antioxidant applications. *Int. J. Biol. Macromol.* **2020**, *164*, 1342–1369. [CrossRef]
78. Moratti, S.C.; Cabral, J.D. 2—Antibacterial properties of chitosan. In *Chitosan Based Biomaterials*; Jennings, J.A., Bumgardner, J.D., Eds.; Woodhead Publishing: Sawston, UK, 2017; Volume 1, pp. 31–44.
79. Yu, Y.; Su, Z.; Peng, Y.; Zhong, Y.; Wang, L.; Xin, M.; Li, M. Recent advances in modifications, biotechnology, and biomedical applications of chitosan-based materials: A review. *Int. J. Biol. Macromol.* **2025**, *289*, 138772. [CrossRef]
80. Thomas, D.; Thomas, S. Chemical Modification of Chitosan and Its Biomedical Application. In *Biopolymer Nanocomposites*; Springer: Cham, Switzerland, 2013; pp. 33–51.
81. Wang, J.; Zhuang, S. Chitosan-based materials: Preparation, modification and application. *J. Clean. Prod.* **2022**, *355*, 131825. [CrossRef]
82. Barik, M.; BhagyaRaj, G.V.S.; Dash, K.K.; Shams, R. A thorough evaluation of chitosan-based packaging film and coating for food product shelf-life extension. *J. Agric. Food Res.* **2024**, *16*, 101164. [CrossRef]
83. Geng, Y.; Xue, H.; Zhang, Z.; Panayi, A.C.; Knoedler, S.; Zhou, W.; Mi, B.; Liu, G. Recent advances in carboxymethyl chitosan-based materials for biomedical applications. *Carbohydr. Polym.* **2023**, *305*, 120555. [CrossRef]

84. Niu, X.; Zhu, L.; Xi, L.; Guo, L.; Wang, H. An antimicrobial agent prepared by N-succinyl chitosan immobilized lysozyme and its application in strawberry preservation. *Food Control* **2020**, *108*, 106829. [CrossRef]
85. Caetano, D.; Junior, L.A.; Carneiro, J.; Ducatti, D.R.B.; Gonçalves, A.G.; Noseda, M.D.; Duarte, M.E.R. Semisynthesis of new sulfated heterorhamnan derivatives obtained from green seaweed *Gayralia brasiliensis* and evaluation of their anticoagulant activity. *Int. J. Biol. Macromol.* **2024**, *267*, 131506. [CrossRef]
86. Moustafa, A.M.Y.; Fawzy, M.M.; Kelany, M.S.; Hassan, Y.A.; Elsharaawy, R.F.; Mustafa, F.H. Synthesis of new quaternized chitosan Schiff bases and their N-alkyl derivatives as antimicrobial and anti-biofilm retardants in membrane technology. *Int. J. Biol. Macromol.* **2024**, *267*, 131635. [CrossRef]
87. Kumar, D.; Gihar, S.; Shrivash, M.K.; Kumar, P.; Kundu, P.P. A review on the synthesis of graft copolymers of chitosan and their potential applications. *Int. J. Biol. Macromol.* **2020**, *163*, 2097–2112. [CrossRef] [PubMed]
88. Ribeiro, E.F.; de Barros-Alexandrino, T.T.; Assis, O.B.G.; Junior, A.C.; Quiles, A.; Hernando, I.; Nicoletti, V.R. Chitosan and crosslinked chitosan nanoparticles: Synthesis, characterization and their role as Pickering emulsifiers. *Carbohydr. Polym.* **2020**, *250*, 116878. [CrossRef]
89. Normakhamatov, N.; Mischnick, P.; Muhitdinov, B.; Mukhamedov, I.; Turaev, A. Sodium cellulose sulfate and its antimicrobial activity. *React. Funct. Polym.* **2023**, *191*, 105672. [CrossRef]
90. Liu, X.; Qin, Z.; Ma, Y.; Liu, H.; Wang, X. Cellulose-Based Films for Food Packaging Applications: Review of Preparation, Properties, and Prospects. *J. Renew. Mater.* **2023**, *11*, 3203–3225. [CrossRef]
91. Tang, Z.; Lin, X.; Yu, M.; Mondal, A.K.; Wu, H. Recent advances in TEMPO-oxidized cellulose nanofibers: Oxidation mechanism, characterization, properties and applications. *Int. J. Biol. Macromol.* **2024**, *259*, 129081. [CrossRef]
92. Sun, X.; Jiang, F. Periodate oxidation-mediated nanocelluloses: Preparation, functionalization, structural design, and applications. *Carbohydr. Polym.* **2024**, *341*, 122305. [CrossRef] [PubMed]
93. Fernández-Santos, J.; Valls, C.; Cusola, O.; Roncero, M.B. Periodate oxidation of nanofibrillated cellulose films for active packaging applications. *Int. J. Biol. Macromol.* **2024**, *267*, 131553. [CrossRef]
94. Madani, M.; Borandeh, S.; Teotia, A.K.; Seppälä, J.V. Direct and Indirect Cationization of Cellulose Nanocrystals: Structure–Properties Relationship and Virus Capture Activity. *Biomacromolecules* **2023**, *24*, 4397–4407. [CrossRef]
95. Willberg-Keyriläinen, P.; Ropponen, J. Evaluation of esterification routes for long chain cellulose esters. *Heliyon* **2019**, *5*, e02898. [CrossRef]
96. Li, M.-L.; Hou, D.-F.; Li, P.-Y.; Feng, Z.-W.; Huang, Y.-H.; Wang, F.; Zhai, Y.-M.; Sun, X.-R.; Zhang, K.; Yin, B.; et al. One-Step Solvent-Free Strategy to Efficiently Synthesize High-Substitution Cellulose Esters. *ACS Sustain. Chem. Eng.* **2024**, *12*, 9669–9681. [CrossRef]
97. Sanchez-Salvador, J.L.; Balea, A.; Monte, M.C.; Negro, C.; Blanco, A. Chitosan grafted/cross-linked with biodegradable polymers: A review. *Int. J. Biol. Macromol.* **2021**, *178*, 325–343. [CrossRef]
98. Zhang, W.; Hadidi, M.; Karaca, A.C.; Hedayati, S.; Tarahi, M.; Assadpour, E.; Jafari, S.M. Chitosan-grafted phenolic acids as an efficient biopolymer for food packaging films/coatings. *Carbohydr. Polym.* **2023**, *314*, 120901. [CrossRef] [PubMed]
99. Bisla, V.; Yoshitake, H. Control of mechanical and hydrophobic properties of silylated chitosan-starch films by cross-linking using carboxylic acids. *Carbohydr. Polym. Technol. Appl.* **2024**, *7*, 100462. [CrossRef]
100. Liu, B.; Ye, H.-B.; Liang, Q.-Y.; Jiang, L.-L.; Chen, M.-M.; Yang, S.-B. Development and characterization of pectin and chitosan films incorporated with a new cross-linking agent. *J. Sci. Food Agric.* **2023**, *103*, 1964–1973. [CrossRef]
101. Patiño-Ruiz, D.A.; De Ávila, G.; Alarcón-Suesca, C.; González-Delgado, Á.D.; Herrera, A. Ionic Cross-Linking Fabrication of Chitosan-Based Beads Modified with FeO and TiO_2 Nanoparticles: Adsorption Mechanism toward Naphthalene Removal in Seawater from Cartagena Bay Area. *ACS Omega* **2020**, *5*, 26463–26475. [CrossRef]
102. Andreica, B.-I.; Cheng, X.; Marin, L. Quaternary ammonium salts of chitosan. A critical overview on the synthesis and properties generated by quaternization. *Eur. Polym. J.* **2020**, *139*, 110016. [CrossRef]
103. Andreica, B.-I.; Anisiei, A.; Rosca, I.; Sandu, A.-I.; Pasca, A.S.; Tartau, L.M.; Marin, L. Quaternized chitosan/chitosan nanofibrous mats: An approach toward bioactive materials for tissue engineering and regenerative medicine. *Carbohydr. Polym.* **2023**, *302*, 120431. [CrossRef] [PubMed]
104. Morandi, P.; Berthalon, S.; David, G.; Lebrun, A.; Parra, K.; Negrell, C. Selective acylation of chitosan oligomers by several cyclic anhydrides as a 13C NMR quantification method. *Carbohydr. Polym. Technol. Appl.* **2024**, *7*, 100498. [CrossRef]
105. Elnaggar, E.M.; Abusaif, M.S.; Abdel-Baky, Y.M.; Ragab, A.; Omer, A.M.; Ibrahim, I.; Ammar, Y.A. Insight into divergent chemical modifications of chitosan biopolymer: Review. *Int. J. Biol. Macromol.* **2024**, *277*, 134347. [CrossRef]
106. Chen, W.-C.; Chien, H.-W. Enhancing the antibacterial property of chitosan through synergistic alkylation and chlorination. *Int. J. Biol. Macromol.* **2022**, *217*, 321–329. [CrossRef]
107. Zhuxin, L.; Biao, Y.; Badamkhand, D.; Yifan, C.; Honghong, S.; Xiao, X.; Mingqian, T.; Zhixiang, W.; Chongjiang, C. Carboxylated chitosan improved the stability of phycocyanin under acidified conditions. *Int. J. Biol. Macromol.* **2023**, *233*, 123474. [CrossRef]

108. Chen, Y.; Liu, Y.; Dong, Q.; Xu, C.; Deng, S.; Kang, Y.; Fan, M.; Li, L. Application of functionalized chitosan in food: A review. *Int. J. Biol. Macromol.* **2023**, *235*, 123716. [CrossRef]
109. Su, J.; Zhang, W.; Moradi, Z.; Rouhi, M.; Parandi, E.; Garavand, F. Recent functionality developments of carboxymethyl chitosan as an active food packaging film material. *Food Chem.* **2025**, *463*, 141356. [CrossRef] [PubMed]
110. He, X.; Lu, W.; Sun, C.; Khalesi, H.; Mata, A.; Andaleeb, R.; Fang, Y. Cellulose and cellulose derivatives: Different colloidal states and food-related applications. *Carbohydr. Polym.* **2021**, *255*, 117334. [CrossRef]
111. Thivya, P.; Akalya, S.; Sinija, V.R. A comprehensive review on cellulose-based hydrogel and its potential application in the food industry. *Appl. Food Res.* **2022**, *2*, 100161. [CrossRef]
112. Ma, G.; Zhang, Z.; Chen, J.; Yang, G.; He, M. Facile sulfation of cellulose via recyclable ternary deep eutectic solvents for low-cost cellulose nanofibril preparation. *Nanoscale Adv.* **2023**, *5*, 356–360. [CrossRef]
113. Lu, Z.; Zhang, H.; Toivakka, M.; Xu, C. Current progress in functionalization of cellulose nanofibers (CNFs) for active food packaging. *Int. J. Biol. Macromol.* **2024**, *267*, 131490. [CrossRef] [PubMed]
114. Shao, G.; Cao, J.; Wu, X.; Qin, B.; Wang, Z.; Wang, Y.; Zhang, Y.; Wang, T.; Fu, Y. Molecularly imprinted polymer on silylated cellulose matrix via dummy template for detoxification of ginkgolic acids. *Ind. Crops Prod.* **2022**, *188*, 115644. [CrossRef]
115. Chetia, P.; Bharadwaj, C.; Purbey, R.; Bora, D.; Yadav, A.; Lal, M.; Rajulu, A.V.; Sadiku, E.R.; Selvam, S.P.; Jarugala, J. Influence of silylated nano cellulose reinforcement on the mechanical, water resistance, thermal, morphological and antibacterial properties of soy protein isolate (SPI)-based composite films. *Int. J. Biol. Macromol.* **2023**, *242*, 124861. [CrossRef]
116. Wen, Y.; Liu, J.; Jiang, L.; Zhu, Z.; He, S.; He, S.; Shao, W. Development of intelligent/active food packaging film based on TEMPO-oxidized bacterial cellulose containing thymol and anthocyanin-rich purple potato extract for shelf life extension of shrimp. *Food Packag. Shelf Life* **2021**, *29*, 100709. [CrossRef]
117. Rahmadiawan, D.; Abral, H.; Azka, M.A.; Sapuan, S.M.; Admi, R.I.; Shi, S.-C.; Zainul, R.; Azril; Zikri, A.; Mahardika, M. Enhanced properties of TEMPO-oxidized bacterial cellulose films via eco-friendly non-pressurized hot water vapor treatment for sustainable and smart food packaging. *RSC Adv.* **2024**, *14*, 29624–29635. [CrossRef]
118. Hassan, S.H.; Velayutham, T.S.; Chen, Y.W.; Lee, H.V. TEMPO-oxidized nanocellulose films derived from coconut residues: Physicochemical, mechanical and electrical properties. *Int. J. Biol. Macromol.* **2021**, *180*, 392–402. [CrossRef] [PubMed]
119. Pedrosa, J.F.S.; Rasteiro, M.G.; Neto, C.P.; Ferreira, P.J.T. Effect of cationization pretreatment on the properties of cationic Eucalyptus micro/nanofibrillated cellulose. *Int. J. Biol. Macromol.* **2022**, *201*, 468–479. [CrossRef]
120. Rana, V.; Malik, S.; Joshi, G.; Rajput, N.K.; Gupta, P.K. Preparation of alpha cellulose from sugarcane bagasse and its cationization: Synthesis, characterization, validation and application as wet-end additive. *Int. J. Biol. Macromol.* **2021**, *170*, 793–809. [CrossRef]
121. Yang, Y.; Lu, Y.-T.; Zeng, K.; Heinze, T.; Groth, T.; Zhang, K. Recent Progress on Cellulose-Based Ionic Compounds for Biomaterials. *Adv. Mater.* **2021**, *33*, 2000717. [CrossRef]
122. Ragavan, K.V.; Hernandez-Hernandez, O.; Martinez, M.M.; Gutiérrez, T.J. Organocatalytic esterification of polysaccharides for food applications: A review. *Trends Food Sci. Technol.* **2022**, *119*, 45–56. [CrossRef]
123. LakshmiBalasubramaniam, S.; Patel, A.S.; Nayak, B.; Howell, C.; Skonberg, D. Antioxidant and antimicrobial modified cellulose nanofibers for food applications. *Food Biosci.* **2021**, *44*, 101421. [CrossRef]
124. Yang, M.; Chen, Y.; Abdalkarim, S.Y.H.; Chen, X.; Yu, H.-Y. Efficient cellulose dissolution and derivatization enabled by oxalic/sulfuric acid for high-performance cellulose films as food packaging. *Int. J. Biol. Macromol.* **2024**, *276*, 133799. [CrossRef] [PubMed]
125. Gupta, R.K.; Gawad, F.A.E.; Ali, E.A.E.; Karunanithi, S.; Yugiani, P.; Srivastav, P.P. Nanotechnology: Current applications and future scope in food packaging systems. *Meas. Food* **2024**, *13*, 100131. [CrossRef]
126. Abutalib, M.M.; Rajeh, A. Enhanced structural, electrical, mechanical properties and antibacterial activity of Cs/PEO doped mixed nanoparticles (Ag/TiO_2) for food packaging applications. *Polym. Test.* **2021**, *93*, 107013. [CrossRef]
127. Althawab, S.A.; Alzahrani, A.; Alohali, B.M.; Alsulami, T. Flexible N-doped MXene quantum dot–biopolymer films with antibacterial and antioxidant functions for active food packaging. *Colloids Surf. A Physicochem. Eng. Asp.* **2025**, *722*, 137291. [CrossRef]
128. Liu, F.; Zhang, X.; Xiao, X.; Duan, Q.; Bai, H.; Cao, Y.; Zhang, Y.; Alee, M.; Yu, L. Improved hydrophobicity, antibacterial and mechanical properties of polyvinyl alcohol/quaternary chitosan composite films for antibacterial packaging. *Carbohydr. Polym.* **2023**, *312*, 120755. [CrossRef]
129. Huang, H.; Mao, L.; Wang, W.; Li, Z.; Qin, C. A facile strategy to fabricate antibacterial hydrophobic, high-barrier, cellulose papersheets for food packaging. *Int. J. Biol. Macromol.* **2023**, *236*, 123630. [CrossRef]
130. Guo, Z.; Zhang, Y.; Xiao, H.; Jayan, H.; Majeed, U.; Ashiagbor, K.; Jiang, S.; Zou, X. Multi-sensor fusion and deep learning for batch monitoring and real-time warning of apple spoilage. *Food Control* **2025**, *172*, 111174. [CrossRef]
131. Gomes, V.; Bermudez, R.; Mateus, N.; Guedes, A.; Lorenzo, J.M.; de Freitas, V.; Cruz, L. FoodSmarTag: An innovative dynamic labeling system based on pyranoflavylium-based colorimetric films for real-time monitoring of food freshness. *Food Hydrocoll.* **2023**, *143*, 108914. [CrossRef]

132. El kalaaoui, K.; Bili, O.; Boukhriss, A.; Gmouh, S. 27—Electrospinning process: Fiber composition and applications. In *Synthetic and Mineral Fibers, Their Composites and Applications*; Rangappa, S.M., Ayyappan, V., Manik, G., Siengchin, S., Eds.; Woodhead Publishing: Sawston, UK, 2024; pp. 719–744.
133. Nachal, N.; Moses, J.A.; Karthik, P.; Anandharamakrishnan, C. Applications of 3D Printing in Food Processing. *Food Eng. Rev.* **2019**, *11*, 123–141. [CrossRef]
134. Li, H.; Qi, G. Product packaging design for hybrid manufacturing process based on 3D printing and thermal environment sensors. *Int. J. Adv. Manuf. Technol.* **2024**. [CrossRef]

polymers

MDPI

Article

Fabrication of Poly(s-triazine-*co*-*o*-aminophenol) Conducting Polymer via Electropolymerization and Its Application in Aqueous Charge Storage

Xueting Bai [1], Bo Lan [1], Xinyang Li [1], Xinlan Yi [2], Shaotong Pei [1] and Chao Wang [3,4,*]

[1] Hebei Provincial Key Laboratory of Power Transmission Equipment Security Defense, North China Electric Power University, Baoding 071003, China; xt_baii@163.com (X.B.); rambo596596@163.com (B.L.); lxygerenyouxiang@163.com (X.L.); peishaotong@ncepu.edu.cn (S.P.)
[2] Economic Management Department, North China Electric Power University, Baoding 071003, China; yixinlan1006@163.com
[3] School of Renewable Energy, Inner Mongolia University of Technology, Ordos 017010, China
[4] Inner Mongolia Key Laboratory of New Energy and Energy Storage Technology, Hohhot 010051, China
* Correspondence: cwang@imut.edu.cn

Abstract: Designing conducting polymers with novel structures is essential for electrochemical energy storage devices. Here, copolymers of s-triazine and o-aminophenol are electropolymerized from an aqueous solution onto a carbon cloth substrate using the galvanostatic method. The poly(s-triazine-*co*-*o*-aminophenol) (PT-*co*-oAP) is characterized, and its charge storage properties are investigated in 1 M H_2SO_4 and in 1 M $ZnSO_4$. At 1 A g^{-1}, the specific capacities of PT-*co*-oAP reach 101.3 mAh g^{-1} and 84.4 mAh g^{-1} in 1 M H_2SO_4 and in 1 M $ZnSO_4$, respectively. The specific capacity of PT-*co*-oAP maintains 90.3% of its initial value after cycling at 10 A g^{-1} for 2000 cycles in 1 M H_2SO_4. The high specific capacity achieved originates from abundant surface active sites, facile ion diffusion, with optimized active site structure achieved by forming copolymer. The charge storage mechanism involves the redox processes of amino/imino groups and hydroxyl/carbonyl groups in the copolymer, together with the insertion of cations. Two electrode devices using two PT-*co*-oAP and aqueous 1 M H_2SO_4 are assembled, and the maximum energy density reaches 63 Wh kg^{-1} at 0.5 A g^{-1} with a power density of 540 W kg^{-1}. The capacity retention of the device after 3000 cycles at 10 A g^{-1} reaches 81.2%.

Keywords: conducting polymer; PT-*co*-oAP; electropolymerization; aqueous electrolyte; electrochemical energy storage

1. Introduction

Electrode materials are essential for high-performance energy storage devices. Conducting polymers, including polyaniline and polypyrrole [1,2], are environmentally benign, conductive, and inexpensive, and they are considered promising electrode materials for charge storage [3]. However, due to the repetitive ion insertion and extraction during charging and discharging, as the electrode material, the stability of conducting polymers needs improvement [4]. Therefore, designing new conductive polymers with novel morphologies and novel chemical structures is a promising route to achieve high specific capacity and stability [5–7].

S-triazine-based covalent bonded frameworks were recently reported to exhibit excellent charge storage capacity [8]. S-triazine derivatives with aromatic rings exhibit good thermal stability and a conjugated D-π-A structure, which facilitates charge separation and

charge transport. The s-triazine ring is capable of binding with cations via π interactions and with anions through σ interactions. In this way, abundant charge can be stored, endowing s-triazine a promising monomer to construct conducting polymers [9]. *O*-aminophenol contains amino and phenolic hydroxyl groups and is also reported to act as a monomer to construct conducting polymers for charge storage [10]. In poly(*o*-aminophenol) (PoAP), hydroxyl/carbonyl and amino/imino groups can serve as active sites to store charge. Graphene nanosheets-PoAP nanocomposites prepared by potential cycling on a platinum surface by Heli et al. exhibit a specific capacitance of 281.1 F g^{-1} at 0.1 A g^{-1} [11]. Functionalized graphene oxide nanosheets/PoAP were prepared by Ehsani et al., and the specific capacitance reached 251.15 F g^{-1} [12]. Maryam Naseri et al. used electropolymerization to prepare PoAP/ZnO, which exhibits a specific capacitance of 223 F g^{-1} [13]. Depending on the electrochemical method adopted, different structures of poly(*o*-aminophenol), including line-shaped and ladder-shaped repeating units, can be constructed.

Electropolymerization offers a facile route to construct copolymers, either layer-by-layer or random copolymers [14,15]. Copolymers exhibit unique charge storage properties by combining the functional groups of two monomers. For example, poly(5-amino-naphthalene sulfonic acid-*co*-*o*-aminophenol) (PANS-*co*-oAP) was electropolymerized on a carbon cloth (CC) substrate in an aqueous acid electrolyte with both monomers, exhibiting superior charge storage performance compared to PANS and PoAP [16]. The simultaneous presence of electron-donating (amino and hydroxyl) and electron-absorbing (sulfonic acid) groups in copolymers facilitates charge separation and the generation of active sites. S-triazine is electron-deficient, and constructing copolymers with electron-rich monomers is desirable to achieve efficient charge separation and the generation of active sites [17]. Therefore, the copolymer of s-triazine and oAP is constructed using electropolymerization. The copolymer is characterized, and its charge storage properties are investigated.

2. Experimental

The following reagents are used without further purification: 1,3,5-triazine ($C_3H_3N_3$, AR, 97%, Shanghai BiDe Pharmaceutical Technology Co., Ltd., Shanghai, China), *o*-aminophenol (C_6H_7NO, AR, 99%, Shanghai Aladdin Biochemical Technology Co., Ltd., Shanghai, China), concentrated sulfuric acid (H_2SO_4, AR, 98.0%, Shanghai HaoHong Bio-Pharmaceutical Technology Co., Ltd., Shanghai, China), zinc sulfate ($ZnSO_4$, AR, 99.8%, Shanghai HaoHong Bio-Pharmaceutical Technology Co., Ltd., Shanghai, China), carbon cloth (SCC130, Suzhou ShengErNuo Technology Co., Ltd., Suzhou, China), and distilled water.

Electropolymerization was used to obtain copolymers with CC as the substrate in aqueous acidic solution. The CC was first cut into small pieces of 1 × 2 cm^2, washed repeatedly with water for 30 min, and calcined at 400 °C for 90 min. When used as the working electrode, about a 1 × 1 cm^2 surface area was immersed in the electrolyte. Electropolymerization was carried out using the galvanostatic method, which can deposit measurable amounts of polymer on CC in a short time. A cleaned graphite rod was used as the counter electrode, and a saturated calomel electrode (SCE) was used as the reference in the three-electrode system setup. The electrolyte was a 1 M H_2SO_4 aqueous solution containing 5 mM s-triazine and 2 mM oAP. A constant current density of 0.01 A cm^{-2} was applied to construct PT-*co*-oAP. The mass of the PT-*co*-oAP film obtained by electropolymerization on CC was measured to be 1.0 mg cm^{-2} using a laboratory balance. The PT and PoAP were prepared using a similar method, with the electrolyte containing only 5 mM s-triazine or 2 mM oAP, respectively, and the deposited masses were 0.4 mg cm^{-2} and PoAP 0.3 mg cm^{-2}, respectively. Information about instrumentation and equations is provided in the Supporting Information.

3. Results and Discussion

Electropolymerization using the galvanostatic method enables a controlled electropolymerization rate to be achieved, and large quantities of polymers can be generated in a short period [18,19]. The PT-*co*-oAP, PT, and PoAP were electrochemically polymerized onto a CC substrate from 1 M H_2SO_4 (Figure S1, Supporting Information). Electropolymerization is initiated by the generation of radicals at the N sites in oAP and s-triazine. The radicals can attack adjacent neutral monomers or couple with another radical to form oligomers. With the repetitive generation of radicals and the growth of the oligomer chain, deposition happens when the concentration of the oligomer near the electrode surface exceeds solubility [20]. Solid-state radical generation and coupling form the three-dimensional connected film at the electrode surface. Figure 1 shows the proposed structure of the PT-*co*-oAP film. Figure 2a–c show the scanning electron micrographs (SEM) of PT, PT-*co*-oAP, and PoAP, and the SEM of the bare CC is provided in Figure S5. In Figure 2a, the CC surface is covered by a layer of PT, and the surface appears rough. In Figure 2b, the PT-*co*-oAP exhibits a small granular structure of about 300 nm in size. Figure 2c displays the SEM of PoAP, which also exhibits a granular structure. Figure 2d shows the electron diffraction spectroscopy (EDS) elemental mapping of PT-*co*-oAP. The N is from both PT and oAP, and the uniform distribution of N and O indicates the successful formation of PT-*co*-oAP on CC. Note that small amounts of S are also detected from the PT-*co*-oAP, which result from the intercalated anions (SO_4^{2-}) during electropolymerization to balance the positive charge of the polymer [21].

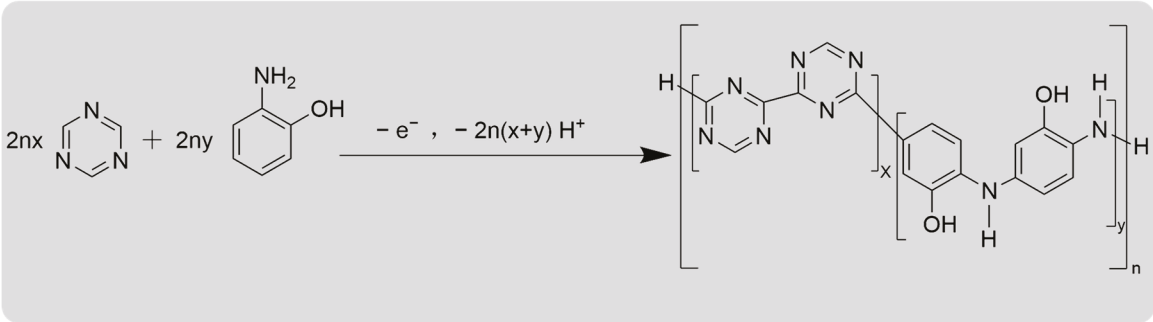

Figure 1. Proposed structure of PT-*co*-oAP.

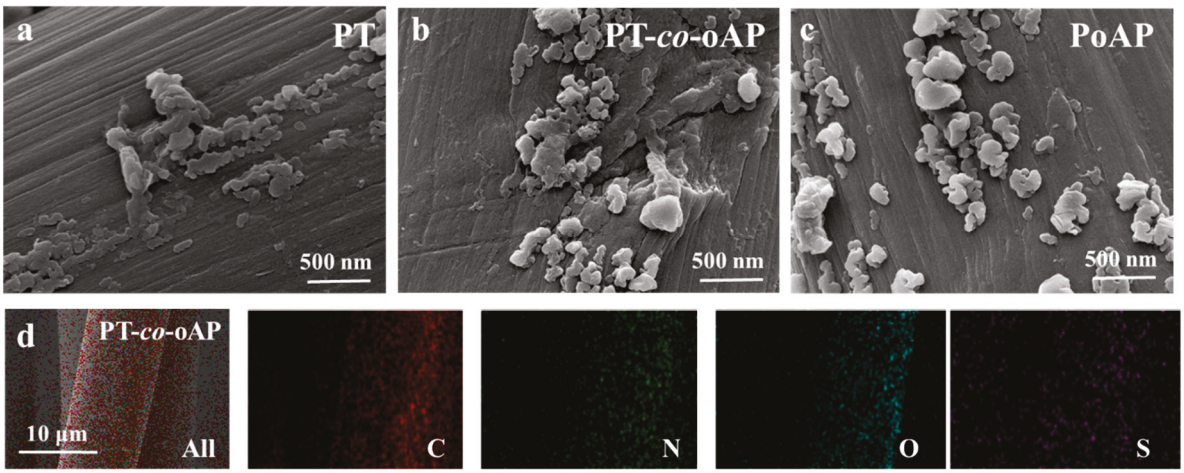

Figure 2. SEM images of (**a**) PT, (**b**) PT-*co*-oAP, and (**c**) PoAP; (**d**) EDS elemental mapping of PT-*co*-oAP.

The surface state of the deposited PT-*co*-oAP was investigated by X-ray photoelectron spectroscopy (XPS, Figure 3). Figure 3a shows the deconvoluted high-resolution XPS

spectra of the C 1s region of PT-*co*-oAP. The deconvolved peaks at 284.7, 286.8, and 289.0 eV correspond to the C-C/C=C, C-N/C-O, and C=N/C=O bonds, respectively [22]. The N 1s spectra (Figure 3b) can be deconvoluted into 399.2, 400.1, 400.5, and 401.3 eV peaks assignable to neutral amine (-NH-), neutral imine (-N=), protonated amine (-NH^+-), and protonated imine (-NH^+=), respectively [23]. The doping level calculated by analyzing the ratio of protonated amino and imino groups to the total N content is 0.51, which is a typical doping level for conducting polymers [22,24]. This indicates that approximately half of the N is protonated. Figure 3c shows the deconvoluted high-resolution XPS spectra of the O 1s region, with peaks at 531.9, 533.0, and 533.6 eV, corresponding to C=O, C-O/S-O, and C-O-C bonds, respectively. The C=O bonds originate from the carbonyl groups formed by the oxidation of the hydroxyl groups on the oAP or the carbonyl groups generated during the oxidative electropolymerization of s-triazine [9,16]. Figure 3d shows the XPS deconvoluted spectra of the S 2p region, with peaks at 169.1 ($2p_{1/2}$) and 168.2 eV ($2p_{3/2}$) corresponding to S in the intercalated sulfate groups [25]. These characterizations show that the PT-*co*-oAP film is successfully electropolymerized onto the CC surface.

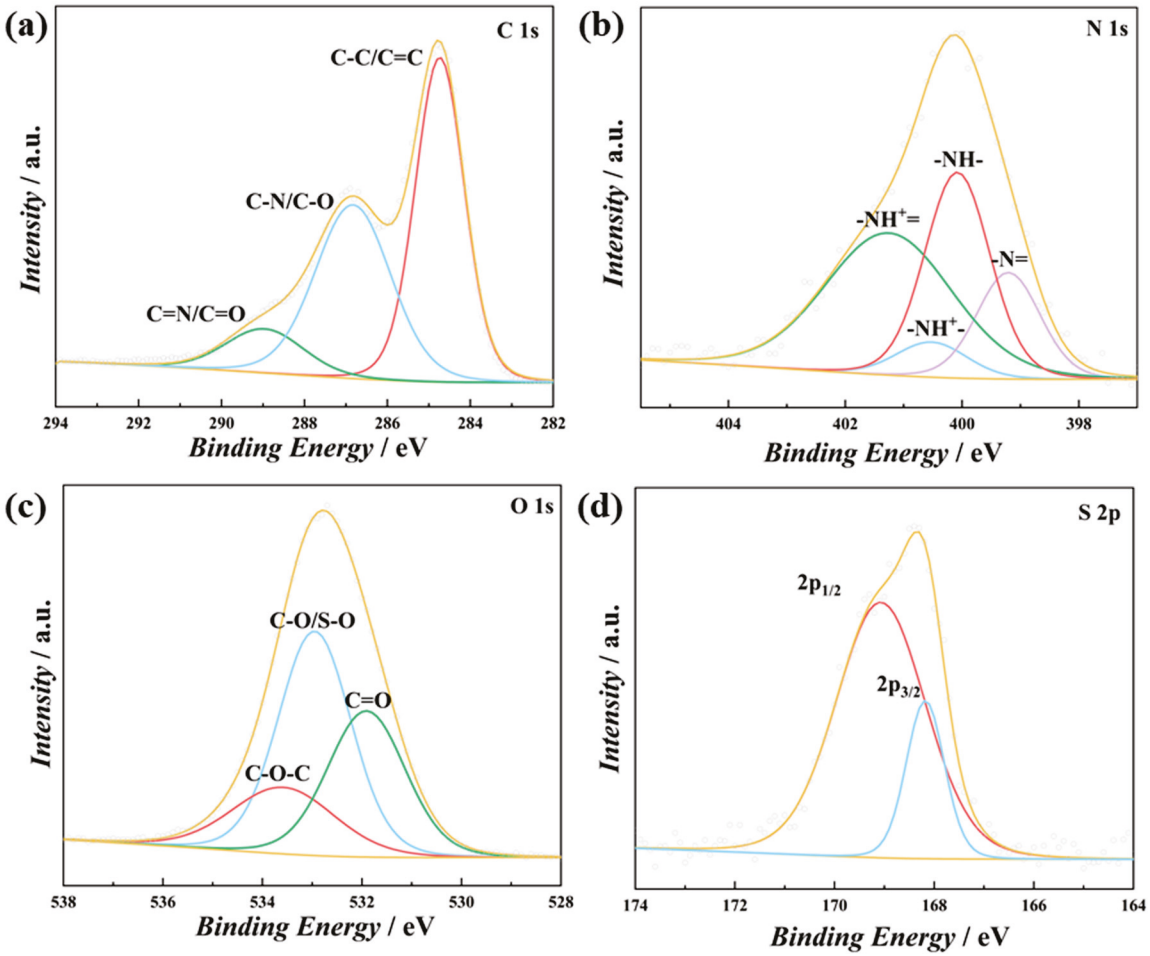

Figure 3. XPS spectra of (**a**) C 1s, (**b**) N 1s, (**c**) O 1s, and (**d**) S 2p regions of PT-*co*-oAP.

Three electrode tests were carried out to investigate the charge storage properties of PT, PoAP, and PT-*co*-oAP in 1 M H_2SO_4. The cyclic voltammetry (CV) of PT, PoAP, and PT-*co*-oAP in 1 M H_2SO_4 in the range of −0.4–1.2 V_{SCE} at 20 mV s^{-1} are shown in Figure 4a. For the PT, the redox peaks are at 0.51 V_{SCE} (ox.) and 0.23 V_{SCE} (red.), which is consistent with reference [9]. For the PoAP, two pairs of redox peaks are present, and the redox peaks at 0.45 V_{SCE} (ox.)/0.3 V_{SCE} (red.) are significantly higher than those at 0.2 V_{SCE} (ox.)/ 0.1 V_{SCE} (red.). This indicates that the linear structure is predominant in PoAP, not the

ladder structure, and that phenoxazine units are predominant. The redox peaks of PT-*co*-oAP are at 0.46 V_{SCE} (ox.)/0.27 V_{SCE} (red.), which are in the middle of PoAP and PT. This implies that a random copolymer is formed, and the redox properties are tuned through the electron interaction between the s-triazine and oAP units. The redox peaks originate from the redox of hydroxyl/carbonyl groups and amino/imino groups, accompanied with cation insertion and extraction. The GCD curves of PT, PoAP, and PT-*co*-oAP (Figure 4b) in 1 M H_2SO_4 at 1 A g^{-1} all show a small plateau around 0.46 V_{SCE}. The GCD curves of PT and PoAP are consistent with the CV of PT and PoAP. The potential of this plateau matches the redox peak potential observed in CV. The specific capacities of PT, PoAP, and PT-*co*-oAP in 1 M H_2SO_4 are calculated by GCD to be 83.8, 62.8, and 101.3 mAh g^{-1}, respectively. The PT-*co*-oAP exhibits higher specific capacity than PT and PoAP. The specific capacities of PT, PoAP, and PT-*co*-oAP at different current densities are shown in Figure 4c. When discharged at 2, 3, 5, and 10 A g^{-1}, the calculated specific capacities of PT-*co*-oAP are 93.3, 90.8, 87.8, and 84.4 mAh g^{-1}, respectively. The decrease in specific capacity with increasing current density is due to the slow kinetics of the redox process limited by ion insertion and extraction [26,27]. The capacity retention values of PT, PoAP, and PT-*co*-oAP are 47.0%, 53.2%, and 61.2%, respectively, when the GCD current density changes from 1 to 10 A g^{-1}. PT-*co*-oAP exhibits the highest capacity retention among these electrodes.

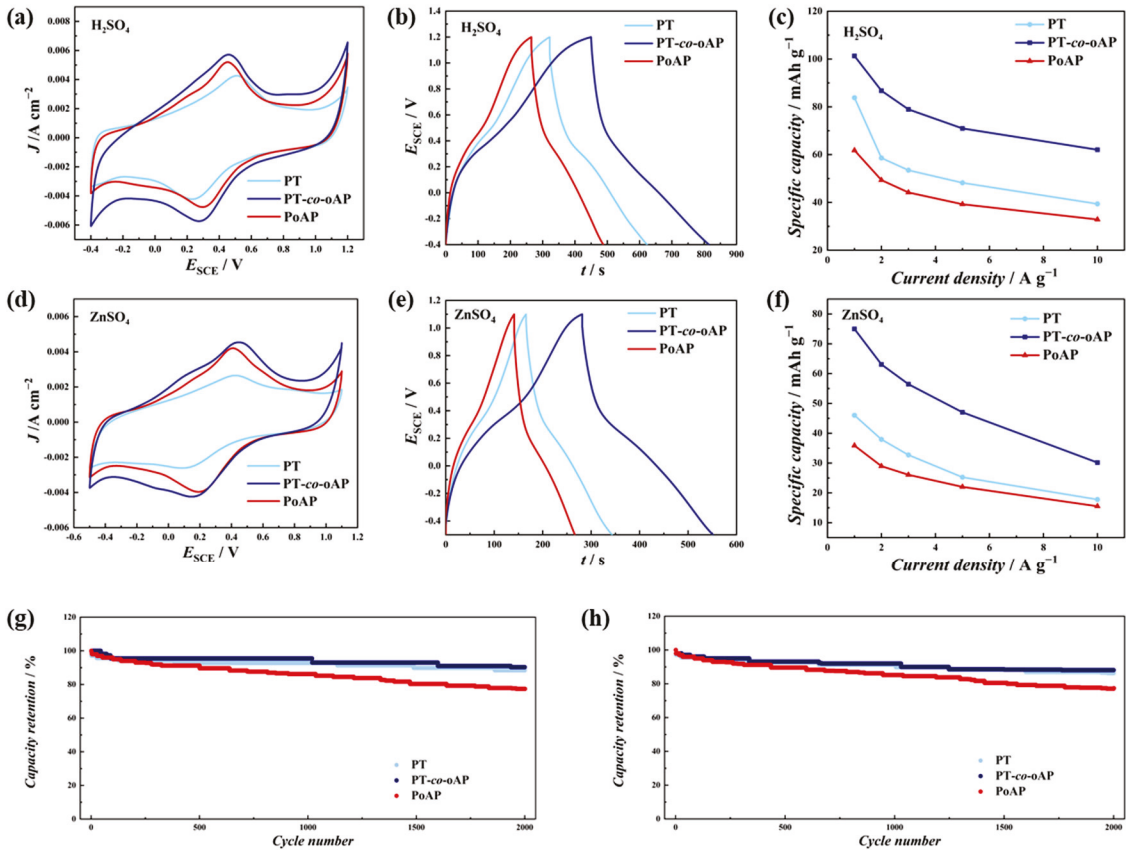

Figure 4. (**a**) CV of PT, PoAP, and PT-*co*-oAP from −0.4 to 1.2 V_{SCE} at scan rate of 20 mV s^{-1} in 1 M H_2SO_4; (**b**) GCD curves of these electrodes at 1 A g^{-1} charge and discharge current density in 1 M H_2SO_4; (**c**) GCD specific capacities versus current densities in 1 M H_2SO_4; (**d**) CV of these electrodes from −0.5 to 1.1 V_{SCE} at scan rate of 20 mV s^{-1} in 1 M $ZnSO_4$; (**e**) GCD curves at 1 A g^{-1} in 1 M $ZnSO_4$; (**f**) GCD specific capacities versus current densities in 1 M $ZnSO_4$. Cycle stability of these electrodes at 10 A g^{-1} in (**g**) 1 M H_2SO_4 and in (**h**) 1 M $ZnSO_4$.

As increasing attention is being paid to energy storage systems in aqueous electrolytes with zinc ions, zinc sulfate solution was used as the electrolyte to evaluate the charge

storage properties [28,29]. The CV values of PT, PoAP, and PT-*co*-oAP in 1 M $ZnSO_4$ are given in Figure 4a. The redox peaks of PT are located at 0.42 V_{SCE} (ox.)/0.09 V_{SCE} (red.), while those of PoAP are located at 0.41 V_{SCE} (ox.)/0.19 V_{SCE} (red.). The PT-*co*-oAP exhibits redox peaks at 0.45 V_{SCE}/0.15 V_{SCE}. These redox peaks also originate from the redox processes of hydroxyl/carbonyl groups and amino/imino groups, accompanied with cation insertion and extraction. The GCD curves of these electrodes at 1 A g^{-1} are shown in Figure 4e. The specific capacities of PT, PoAP, and PT-*co*-oAP are 46.0, 35.9, and 75.0 mAh g^{-1}, respectively. When discharged at 2, 3, 5, and 10 A g^{-1}, the specific capacities of PT-*co*-oAP are 63.1, 56.4, 47.0, and 30.2 mAh g^{-1}, respectively (Figure 4f). When the GCD current density is in the range of 1 to 10 A g^{-1}, the capacity retention values of PT, PoAP, and PT-*co*-oAP are 38.6%, 43.3% and 40.3%, respectively, and significantly lower capacity retention is observed in 1 M $ZnSO_4$ compared to 1 M H_2SO_4, which might result from the complex side reactions in 1 M $ZnSO_4$ that limit the kinetics at high charge and discharge rates [30–32]. The cycling stability of these electrodes in 1 M H_2SO_4 and 1 M $ZnSO_4$ at 10 A g^{-1} is also investigated, and the results are shown in Figure 4g,h. After 2000 cycles, the specific capacity retention values of PT, PoAP, and PT-*co*-oAP are 88.4%, 77.4%, and 90.3% in 1 M H_2SO_4, respectively, and 86.3%, 77.1%, and 88.1% in 1 M $ZnSO_4$, respectively. This indicates that PT-*co*-oAP exhibits the best cycling stability in both electrolytes. In addition, PT-*co*-oAP also sustains the 10,000-cycle stability test (Figure S4). SEM and XPS after the stability test (Figures S6 and S9) indicate no significant physical detachment of the PT-*co*-oAP from the CC substrate. This implies that specific capacity degradation is induced from the structural change that leads to a loss of active sites.

Electrochemical impedance spectroscopy was then carried out [33]. Figure 5a shows the 3D Bode plot of PT-*co*-oAP obtained in 1 M H_2SO_4 [34]. The 3D Bode plot shows a low frequency peak at -0.2–0.8 V_{SCE}, which is consistent with the redox peak potential in CV. Together with the redox peaks in CV and the asymmetric shape of the GCD curves, the peak in the 3D Bode plot implies that the PT-*co*-oAP is a battery-type charge storage material. The Nyquist plots of these electrodes are shown in Figure 5b. The high-frequency semicircles of the Nyquist plots of PT, PoAP, and PT-*co*-oAP can be observed, whose diameter is related to the charge transfer resistance (R_{CT}) [35]. The R_{CT} of PT-*co*-oAP is the largest, which indicates that the redox kinetics of PT-*co*-oAP is the most sluggish. The low-frequency region Z' versus $\omega^{-1/2}$ in 1 M H_2SO_4 is shown in Figure 5c. The slope ∂ (Warburg factor) is related to ion diffusion impedance [36,37]. ∂ is the smallest for PT-*co*-oAP (40 $\Omega\ s^{-1/2}\ rad^{1/2}$), which indicates that ion diffusion is the most facile for PT-*co*-oAP. The ∂ values are 70 and 23 $\Omega\ s^{-1/2}\ rad^{1/2}$ for PT and PoAP, respectively. Figure 5d exhibits the 3D Bode plot for PT-*co*-oAP in 1 M $ZnSO_4$, with low-frequency peaks in the range of -0.2–0.7 V_{SCE}. PT-*co*-oAP behaves as a battery-type electrode material in 1 M $ZnSO_4$. The Nyquist plots of PT, PoAP, and PT-*co*-oAP in 1 M $ZnSO_4$ (Figure 5e) are typical for capacitive behavior, where a straight line close to the $-Z''$ axis is shown. The R_{CT} of PT-*co*-oAP is lower than that of PT but higher than that of PoAP. In both electrolytes, the R_{CT} of PoAP is the lowest, which indicates its most facile redox kinetics. The ∂ values of PT, PoAP, and PT-*co*-oAP are 20, 15, and 26 $\Omega\ s^{-1/2}\ rad^{1/2}$, respectively. In both electrolytes, PT exhibits the highest diffusion impedance, which is probably a result of the thick-layered morphology of PT. In contrast, PT-*co*-oAP exhibits the most facile diffusion, probably originating from the porous granular shape of the deposits. Also, the change in interfacial hydrogen bonding structure can affect the ion diffusion processes. However, the R_{CT} of PT-*co*-oAP is not the lowest, which implies that the redox kinetics is not accelerated, which is possibly limited by the electron transfer process induced by the formation of copolymers. In addition, the structure of the active sites is altered, and the electron interaction may also affect the redox kinetics. From the CV, PT-*co*-oAP exhibits the largest integrated area, which indicates that

the number of active sites is the highest. Though redox kinetics is not the most facile, the abundant number of electrochemically active sites and facile diffusion enhance the charge storage performance of PT-*co*-oAP. The SEM images show that these electrodeposited films consist of granular and aggregated structures. Though this morphology is common for electrodeposited films, a highly porous substrate is desirable for polymer deposition to expose a higher number of electrochemically active sites for charge storage.

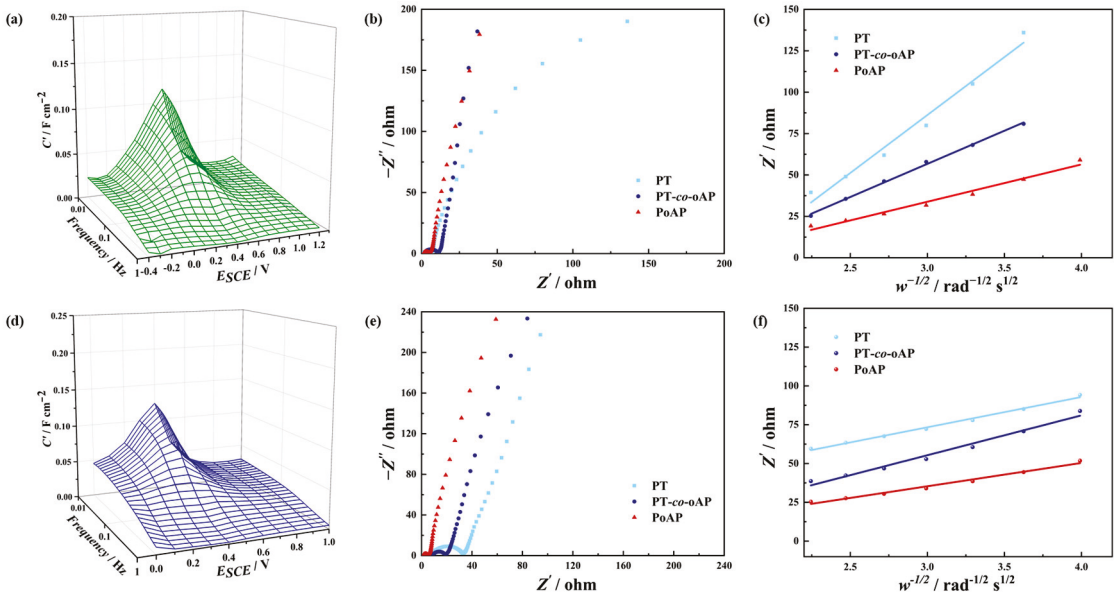

Figure 5. (**a**) Three-dimensional Bode plots of C′ vs. f vs. E of PT-*co*-oAP in 1 M H_2SO_4. (**b**) Nyquist plots of PT-*co*-oAP in 1 M H_2SO_4. (**c**) Plot of Z′ vs. $\omega^{-1/2}$ of PT-*co*-oAP in 1 M H_2SO_4. (**d**) Three-dimensional Bode plots of PT-*co*-oAP in 1 M $ZnSO_4$. (**e**) Nyquist plots of PT-*co*-oAP in 1 M $ZnSO_4$. (**f**) Plot of Z′ vs. $\omega^{-1/2}$ of PT-*co*-oAP in 1 M $ZnSO_4$.

The charge storage mechanism of the PT-*co*-oAP was further investigated in both 1 M H_2SO_4 and 1 M $ZnSO_4$ since the copolymer exhibits the highest specific capacity among these electrodes. Ex situ XPS was carried out to investigate the charge storage mechanism [38]. The high-resolution spectra were deconvoluted, and the percentages of each component in the deconvolution high-resolution XPS spectra are provided in the Supporting Information. In 1 M H_2SO_4, the imino groups (-N= and -NH^+=) account for 63.94% of the total N at the charged state. In the discharged state, the content of imino groups decreases to 37.79% (Figure 6a,c). The results indicate that amines are oxidized to produce imines during charging, while the opposite process occurs during discharging [39]. The ratio of C=O to C-O in the deconvolution O 1s spectra also decreases at the discharged state (Figure 6b,d). These observations are consistent with the redox peaks observed in CV. In 1 M $ZnSO_4$, the content of imino groups in the N 1s spectra decreases from 29.96% at the charged state to 12.22% at the discharged state. The ratio of C=O to C-O decreases from 0.71 at the charged state to 0.43 at the discharged state. Figure 7c and f show the variation in Zn peak intensity in 1 M $ZnSO_4$, which is lower at the charged state and higher at the discharged state. This also indicates that Zn^{2+} is inserted into the polymer at the discharged state. Figure 7g displays the proposed charge storage mechanism of PT-*co*-oAP.

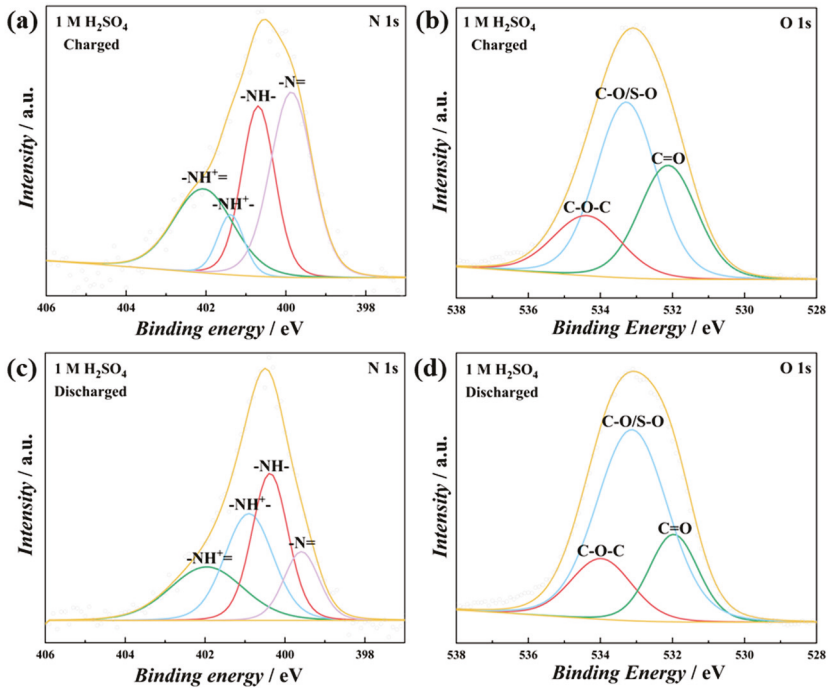

Figure 6. Deconvoluted XPS spectra of PT-*co*-oAP. (**a**) N 1s region and (**b**) O 1s region when charged to 1.2 V; (**c**) N 1s region and (**d**) O 1s region when discharged to −0.4 V in 1 M H_2SO_4.

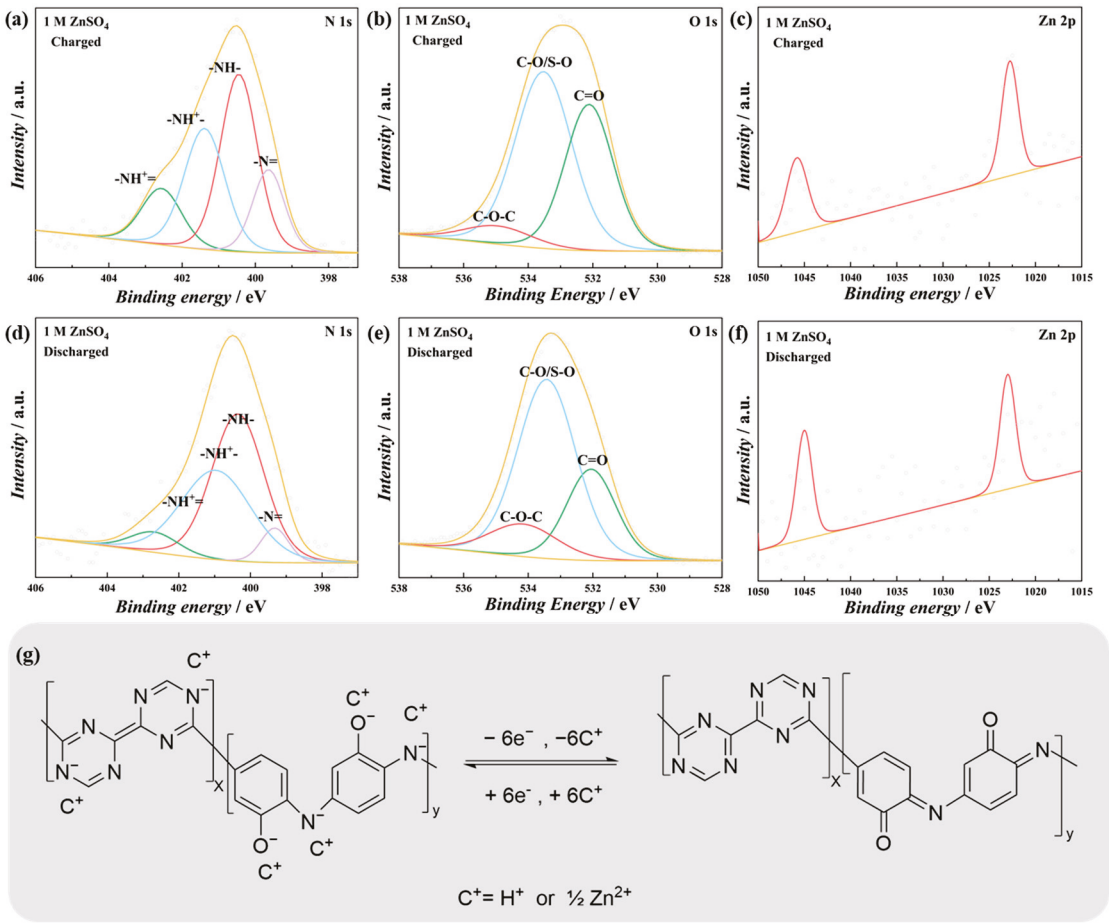

Figure 7. Deconvoluted XPS spectra of PT-*co*-oAP in 1 M $ZnSO_4$. (**a**) N 1s region, (**b**) O 1s region, and (**c**) Zn 2p region when charged to 1.1 V; (**d**) N 1s region, (**e**) O 1s region, and (**f**) Zn 2p region when discharged to −0.5 V. (**g**) Proposed charge–discharge mechanism of PT-*co*-oAP.

A two-electrode test was further carried out, with two PT-*co*-oAP electrodes and aqueous 1 M H_2SO_4 as the electrolyte, to construct a charge storage device (Figure 8). Figure 8a shows the CV of this device at various scan rates. The CV increases in current density with an increased scan rate, and redox peaks are observed. The GCD curve also shows plateaus, which implies its battery-type behavior [40,41]. The specific capacities at 0.5, 1, 2, 3, and 5 A g^{-1} are 30, 24.9, 18.5, 16.1, and 13.1 mAh g^{-1}, respectively (Figure 8b). Figure 8c shows the Ragone plots comparing this device with those reported in the literature [42]. The maximum energy density of the device reaches 63 Wh kg^{-1} at 0.5 A g^{-1}. The C' and C'' vary with frequency (Figure 8d), and the dielectric relaxation time constant τ_0 of the device was calculated to be 1.32 s. This value is lower than that of some carbon-based supercapacitor electrode materials, which shows its ability to charge and discharge rapidly [43,44]. The stability analysis of the discharging device is performed, as shown in Figure 8e. The device shows high stability (81.2%, 3000 cycles).

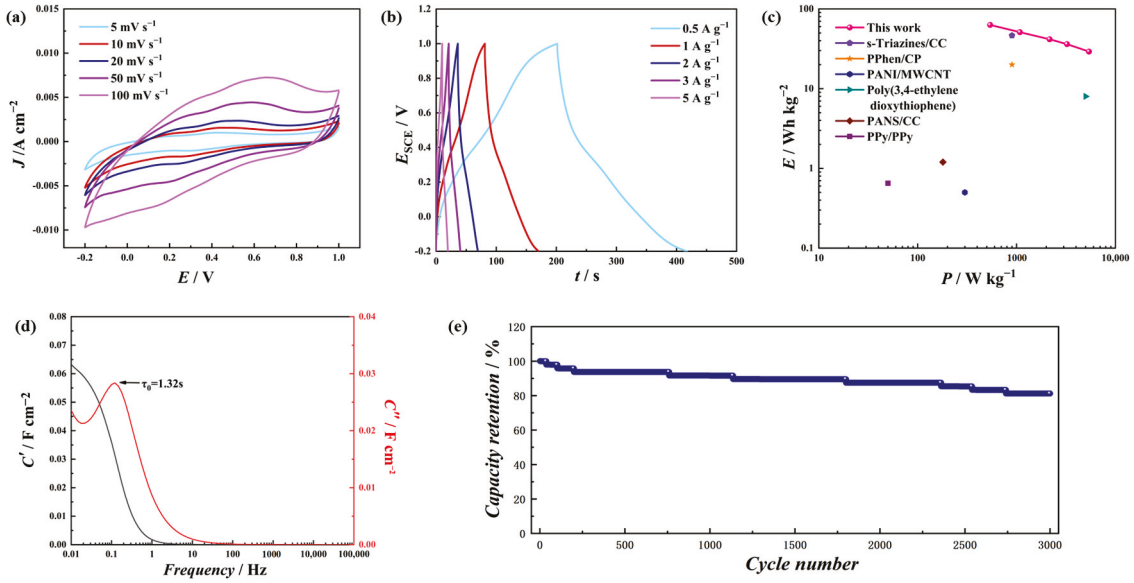

Figure 8. (**a**) CV of the device with 1 M H_2SO_4 aqueous electrolyte; (**b**) the GCD profiles of the device at different current densities; (**c**) the Ragone plot comparing the device in this work with systems in the literature based on conducting polymers; (**d**) the dependence of C' and C'' over frequency; (**e**) capacity retention versus cycle numbers of the device at 10 A g^{-1}.

4. Conclusions

Copolymers of s-triazine and oAP are electropolymerized on the CC substrate using a galvanostatic method. The PT-*co*-oAP exhibits a rough surface and can be used as a battery-type electrode material to electrochemically store charge in both 1 M H_2SO_4 and 1 M $ZnSO_4$ aqueous solutions. At 1 A g^{-1}, the specific capacities of PT-*co*-oAP are 101.3 mAh g^{-1} and 75.0 mAh g^{-1} in 1 M H_2SO_4 and in 1 M $ZnSO_4$, respectively, higher than those of PT and PoAP. The high specific capacity of PT-*co*-oAP stems from the increased number of active sites and the improved diffusion kinetics, induced by the unique structure owing to the formation of a copolymer. The charge storage mechanism involves the redox processes of amino/imino groups and hydroxyl/carbonyl groups in the copolymer, together with the insertion of cations (Zn^{2+} and/or H^+). The PT-*co*-oAP exhibits high stability towards GCD cycling. The two-electrode device with PT-*co*-oAP exhibits a 63 Wh kg^{-1} energy density at a 540 W kg^{-1} power density, with 81.2% of the initial specific capacity being maintained after 3000 cycles. This study demonstrates that forming copolymers by electropolymerization is an effective method to improve the specific capacity and energy density of charge storage materials. Further studies focusing

on precisely controlling the repeating unit of the polymer by electropolymerization are desirable to achieve high charge storage performance.

Supplementary Materials: The following supporting information can be downloaded at https://www.mdpi.com/article/10.3390/polym17091160/s1, Figure S1: *E-t* curve for electropolymerization of 5 mM s-triazine and 2 mM oAP in 1 M H_2SO_4 at 0.01 A cm^{-2}. Working electrode is CC; Figure S2: (a) CV of PT-*co*-oAP at scan rates ranging from 5 to 100 mV s^{-1} in 1 M H_2SO_4; (b) Log (*i*, mA) versus (c) log (*v*, mV s^{-1}) plots in 1 M H_2SO_4.; Figure S3: (a) CV of PT-*co*-oAP at scan rates ranging from 5 to 100 mV s^{-1} in 1 M $ZnSO_4$; (b) Log (*i*, mA) versus (c) log (*v*, mV s^{-1}) plots in 1 M $ZnSO_4$; Figure S4: The cycle stability of these electrodes at 10 A g^{-1} in (a) 1 M H_2SO_4 and in (b) 1 M $ZnSO_4$; Figure S5: SEM images of the CC substrate; Figure S6: SEM images of the PT-*co*-oAP after GCD cycling at 10 A g^{-1} for 10,000 cycles in 1 M H_2SO_4; Figure S7: XPS survey spectrum of PT-*co*-oAP; Figure S8: XPS survey spectrum of PT-*co*-oAP under various conditions. (a) Charged to 1.2 V_{SCE} and (b) discharged to −0.4 V_{SCE} in 1 M H_2SO_4; (c) charged to 1.1 V_{SCE} and (d) discharged to −0.5 V_{SCE} in 1 M $ZnSO_4$; Figure S9: XPS spectra of (a) C 1s, (b) N 1s, and (c) O 1s regions of PT-*co*-oAP after GCD cycling at 10 A g^{-1} for 10,000 cycles in 1 M H_2SO_4. Table S1: Components of deconvoluted C 1s XPS spectra of PT-*co*-oAP in 1 M H_2SO_4; Table S2: Components of deconvoluted N 1s XPS spectra of PT-*co*-oAP in 1 M H_2SO_4; Table S3: Components of deconvoluted O 1s XPS spectra of PT-*co*-oAP in 1 M H_2SO_4; Table S4: Components of deconvoluted N 1s XPS spectra of charged or discharged PT-*co*-oAP in different solutions; Table S5: Components of deconvoluted O 1s XPS spectra of charged or discharged PT-*co*-oAP in different solutions; Table S6: R_{CT} of Nyquist plot in H_2SO_4; Table S7: R_{CT} of Nyquist plot in $ZnSO_4$; Table S8: Comparison of specific capacity and cyclic stability among some previously reported polymer-based electrochemical energy storage systems. References [9,45–49] are cited in the Supplementary Materials.

Author Contributions: Conceptualization, S.P., X.B., and C.W.; Methodology, C.W., B.L., and X.B.; Formal Analysis, X.B., B.L., X.Y., and C.W.; Data Curation, B.L., X.L. and X.B.; Writing—Original Draft, X.B. and X.L.; Writing—Review and Editing, B.L. and C.W.; Supervision, C.W., S.P., and X.Y.; Funding Acquisition, S.P. and C.W. All authors have read and agreed to the published version of the manuscript.

Funding: Funding was provided by the National Natural Science Foundation of China (No. 22308206), the Renewable Energy Strategic Pilot Project of Ordos, and the Inner Mongolia University of Technology.

Data Availability Statement: The original contributions presented in this study are included in the article/Supplementary Materials. Further inquiries can be directed to the corresponding author.

Acknowledgments: The authors thank the Inner Mongolia University of Technology for providing funding.

Conflicts of Interest: The authors declare no conflicts of interest.

References

1. Li, Z.; Gong, L. Research Progress on Applications of Polyaniline (PANI) for Electrochemical Energy Storage and Conversion. *Materials* **2020**, *13*, 548. [CrossRef] [PubMed]
2. Alam, S.; Jadoon, S.; Iqbal, M.Z.; Hegazy, H.H.; Ahmad, Z.; Yahia, I.S. Recent progress in polypyrrole and its composites with carbon, metal oxides, sulfides and other conducting polymers as an emerging electrode material for asymmetric supercapacitors. *J. Energy Storage* **2024**, *85*, 110955. [CrossRef]
3. Bashir, S.; Hasan, K.; Hina, M.; Ali Soomro, R.; Mujtaba, M.A.; Ramesh, S.; Ramesh, K.; Duraisamy, N.; Manikam, R. Conducting polymer/graphene hydrogel electrodes based aqueous smart Supercapacitors: A review and future prospects. *J. Electroanal. Chem.* **2021**, *898*, 115626. [CrossRef]
4. del Valle, M.A.; Gacitúa, M.A.; Hernández, F.; Luengo, M.; Hernández, L.A. Nanostructured Conducting Polymers and Their Applications in Energy Storage Devices. *Polymers* **2023**, *15*, 1450. [CrossRef]
5. Kim, J.; Lee, J.; You, J.; Park, M.-S.; Hossain, M.S.A.; Yamauchi, Y.; Kim, J.H. Conductive polymers for next-generation energy storage systems: Recent progress and new functions. *Mater. Horiz.* **2016**, *3*, 517–535. [CrossRef]

6. Shi, Y.; Peng, L.; Ding, Y.; Zhao, Y.; Yu, G. Nanostructured conductive polymers for advanced energy storage. *Chem. Soc. Rev.* **2015**, *44*, 6684–6696. [CrossRef]
7. Sumdani, M.G.; Islam, M.R.; Yahaya, A.N.A.; Safie, S.I. Recent advancements in synthesis, properties, and applications of conductive polymers for electrochemical energy storage devices: A review. *Polym. Eng. Sci.* **2022**, *62*, 269–303. [CrossRef]
8. Xiong, P.; Zhang, S.; Wang, R.; Zhang, L.; Ma, Q.; Ren, X.; Gao, Y.; Wang, Z.; Guo, Z.; Zhang, C. Covalent triazine frameworks for advanced energy storage: Challenges and new opportunities. *Energy Environ. Sci.* **2023**, *16*, 3181–3213. [CrossRef]
9. Pei, S.; Lan, B.; Bai, X.; Liu, Y.; Li, X.; Wang, C. Electropolymerization of s-Triazines and Their Charge Storage Performance in Aqueous Acidic Electrolytes. *Polymers* **2024**, *16*, 3266. [CrossRef]
10. Tucceri, R.; Arnal, P.M.; Scian, A.N. Poly(o-aminophenol) film electrodes: Synthesis and characterization and formation mechanisms—A review article. *Can. J. Chem.* **2013**, *91*, 91–112. [CrossRef]
11. Heli, H.; Yadegari, H.; Jabbari, A. Graphene nanosheets-poly(o-aminophenol) nanocomposite for supercapacitor applications. *Mater. Chem. Phys.* **2012**, *134*, 21–25. [CrossRef]
12. Ehsani, A.; Mohammad, S.H.; Kowsari, E.; Safari, R.; Torabian, J.; Kazemi, S. Nanocomposite of p-type conductive polymer/functionalized graphene oxide nanosheets as novel and hybrid electrodes for highly capacitive pseudocapacitors. *J. Colloid Interface Sci.* **2016**, *478*, 181–187. [CrossRef] [PubMed]
13. Naseri, M.; Fotouhi, L.; Ehsani, A.; Shiri, H.M. Novel electroactive nanocomposite of POAP for highly efficient energy storage and electrocatalyst: Electrosynthesis and electrochemical performance. *J. Colloid Interface Sci.* **2016**, *484*, 308–313. [CrossRef] [PubMed]
14. Yan, S.; Fu, H.; Zhang, L.; Dong, Y.; Li, W.; Ouyang, M.; Zhang, C. Conjugated polymer multilayer by in situ electrochemical polymerization for black-to-transmissive eletrochromism. *Chem. Eng. J.* **2021**, *406*, 126819. [CrossRef]
15. Jadoun, S.; Riaz, U. A review on the chemical and electrochemical copolymerization of conducting monomers: Recent advancements and future prospects. *Polym. Plast. Technol. Mater.* **2020**, *59*, 484–504. [CrossRef]
16. Wang, C.; Yang, Y.; Zhou, Z.; Li, Y.; Li, Y.; Hou, W.; Liu, S.; Tian, Y. Electrodeposited Poly(5-Amino-2-Naphthalenesulfonic Acid-co-o-Aminophenol) as the Electrode Material for Flexible Supercapacitor. *Small* **2024**, *20*, 2305994. [CrossRef]
17. Mansha, M.; Ahmad, T.; Ullah, N.; Akram Khan, S.; Ashraf, M.; Ali, S.; Tan, B.; Khan, I. Photocatalytic Water-Splitting by Organic Conjugated Polymers: Opportunities and Challenges. *Chem. Rec.* **2022**, *22*, e202100336. [CrossRef]
18. An, N.; Guo, C.; Li, W.; Wei, M.; Liu, L.; Meng, C.; Sun, D.; Lei, Y.; Hu, Z.; Zhao, L. Electropolymerization nanoarchitectonics of polyaminoanthraquinone/carbon cloth flexible electrode with nano-spines array structure for high-performance supercapacitor. *J. Energy Storage* **2024**, *75*, 109558. [CrossRef]
19. Li, J.; Zhao, L.; Liu, P. Boosting electrochemical property of carbon cloth for supercapacitors with electrodeposited aniline-based copolymers. *Electrochim. Acta* **2023**, *462*, 142706. [CrossRef]
20. Heinze, J.; Frontana-Uribe, B.A.; Ludwigs, S. Electrochemistry of Conducting Polymers—Persistent Models and New Concepts. *Chem. Rev.* **2010**, *110*, 4724–4771. [CrossRef]
21. Inzelt, G. Conducting polymers: Past, present, future. *J. Electrochem. Sci. Eng.* **2018**, *8*, 3–37. [CrossRef]
22. Snook, G.A.; Kao, P.; Best, A.S. Conducting-polymer-based supercapacitor devices and electrodes. *J. Power Sources* **2011**, *196*, 1–12. [CrossRef]
23. Yan, H.; Mu, X.; Song, Y.; Qin, Z.; Guo, D.; Sun, X.; Liu, X.-X. Protonating imine sites of polyaniline for aqueous zinc batteries. *Chem. Commun.* **2022**, *58*, 1693–1696. [CrossRef] [PubMed]
24. Meng, Q.; Cai, K.; Chen, Y.; Chen, L. Research progress on conducting polymer based supercapacitor electrode materials. *Nano Energy* **2017**, *36*, 268–285. [CrossRef]
25. Ahn, H.J.; Kim, S.J.; Kim, H.G.; Jee, Y.; Huh, S.H. Two-Dimensional Hydration and Triple-Interlayer Lattice Structures in Sulfate-Intercalated Graphene Oxide Nanosheets. *Minerals* **2024**, *14*, 1030. [CrossRef]
26. Chun, S.-E.; Evanko, B.; Wang, X.; Vonlanthen, D.; Ji, X.; Stucky, G.D.; Boettcher, S.W. Design of aqueous redox-enhanced electrochemical capacitors with high specific energies and slow self-discharge. *Nat. Commun.* **2015**, *6*, 7818. [CrossRef] [PubMed]
27. Hu, X.; Liu, Y.; Chen, J.; Yi, L.; Zhan, H.; Wen, Z. Fast Redox Kinetics in Bi-Heteroatom Doped 3D Porous Carbon Nanosheets for High-Performance Hybrid Potassium-Ion Battery Capacitors. *Adv. Energy Mater.* **2019**, *9*, 1901533. [CrossRef]
28. Zeng, X.; Hao, J.; Wang, Z.; Mao, J.; Guo, Z. Recent progress and perspectives on aqueous Zn-based rechargeable batteries with mild aqueous electrolytes. *Energy Storage Mater.* **2019**, *20*, 410–437. [CrossRef]
29. Mittal, U.; Kundu, D. Electrochemical Stability of Prospective Current Collectors in the Sulfate Electrolyte for Aqueous Zn-Ion Battery Application. *J. Electrochem. Soc.* **2021**, *168*, 090560. [CrossRef]
30. Ye, S.; Sheng, S.; Yao, H.; Chen, Q.; Meng, L.; Yang, Y. One-stone-for-two-birds strategy to enhance the zinc ion storage performance of PANI in low-cost ZnSO4 electrolyte. *J. Energy Storage* **2024**, *100*, 113674. [CrossRef]
31. Yue, J.; Chen, S.; Yang, J.; Li, S.; Tan, G.; Zhao, R.; Wu, C.; Bai, Y. Multi-Ion Engineering Strategies toward High Performance Aqueous Zinc-Based Batteries. *Adv. Mater.* **2024**, *36*, 2304040. [CrossRef]
32. Chen, X.; Xie, X.; Ruan, P.; Liang, S.; Wong, W.-Y.; Fang, G. Thermodynamics and Kinetics of Conversion Reaction in Zinc Batteries. *ACS Energy Lett.* **2024**, *9*, 2037–2056. [CrossRef]

33. Wang, S.; Zhang, J.; Gharbi, O.; Vivier, V.; Gao, M.; Orazem, M.E. Electrochemical impedance spectroscopy. *Nat. Rev. Methods Primers* **2021**, *1*, 41. [CrossRef]
34. Patil, S.S.; Patil, P.S. 3D Bode analysis of nickel pyrophosphate electrode: A key to understanding the charge storage dynamics. *Electrochim. Acta* **2023**, *451*, 142278. [CrossRef]
35. Yuan, M.; Liu, H.; Ran, F. Fast-charging cathode materials for lithium & sodium ion batteries. *Mater. Today* **2023**, *63*, 360–379. [CrossRef]
36. Cha, H.L.; Park, J.W.; Yun, J.-I. Determination of the Diffusion Coefficient in Electrodeposition Reactions by Electrochemical Impedance Spectroscopy: A Case Study of Cobalt in Molten LiCl-KCl Salt. *J. Electrochem. Soc.* **2024**, *171*, 036503. [CrossRef]
37. Perdana, M.Y.; Johan, B.A.; Abdallah, M.; Hossain, M.E.; Aziz, M.A.; Baroud, T.N.; Drmosh, Q.A. Understanding the Behavior of Supercapacitor Materials via Electrochemical Impedance Spectroscopy: A Review. *Chem. Rec.* **2024**, *24*, e202400007. [CrossRef]
38. Patra, A.; Namsheer, K.; Jose, J.R.; Sahoo, S.; Chakraborty, B.; Rout, C.S. Understanding the charge storage mechanism of supercapacitors: In situ/operando spectroscopic approaches and theoretical investigations. *J. Mater. Chem. A* **2021**, *9*, 25852–25891. [CrossRef]
39. Shi, H.-Y.; Ye, Y.-J.; Liu, K.; Song, Y.; Sun, X. A Long-Cycle-Life Self-Doped Polyaniline Cathode for Rechargeable Aqueous Zinc Batteries. *Angew. Chem. Int. Ed.* **2018**, *57*, 16359–16363. [CrossRef]
40. Xie, J.; Yang, P.; Wang, Y.; Qi, T.; Lei, Y.; Li, C.M. Puzzles and confusions in supercapacitor and battery: Theory and solutions. *J. Power Sources* **2018**, *401*, 213–223. [CrossRef]
41. Shaikh, N.S.; Kanjanaboos, P.; Lokhande, V.C.; Praserthdam, S.; Lokhande, C.D.; Shaikh, J.S. Engineering of Battery Type Electrodes for High Performance Lithium Ion Hybrid Supercapacitors. *ChemElectroChem* **2021**, *8*, 4686–4724. [CrossRef]
42. Beyers, I.; Bensmann, A.; Hanke-Rauschenbach, R. Ragone plots revisited: A review of methodology and application across energy storage technologies. *J. Energy Storage* **2023**, *73*, 109097. [CrossRef]
43. Khanra, P.; Kuila, T.; Bae, S.H.; Kim, N.H.; Lee, J.H. Electrochemically exfoliated graphene using 9-anthracene carboxylic acid for supercapacitor application. *J. Mater. Chem.* **2012**, *22*, 24403–24410. [CrossRef]
44. Ganesh, V.; Lakshminarayanan, V.; Pitchumani, S. Assessment of Liquid Crystal Template Deposited Porous Nickel as a Supercapacitor Electrode Material. *Electrochem. Solid-State Lett.* **2005**, *8*, A308. [CrossRef]
45. Wang, C.; Zhou, Z.; Tian, Q.; Cao, X.; Wu, Y.; Liu, S.; Wang, J. Electropolymerized 1, 10-phenanthroline as the electrode material for aqueous supercapacitors. *Chem. Eng. J.* **2022**, *433*, 134483. [CrossRef]
46. Khan, M.Z.; Gul, I.H.; Baig, M.M.; Akram, M.A. Facile synthesis of a multifunctional ternary SnO2/MWCNTs/PANI nanocomposite: Detailed analysis of dielectric, electrochemical, and water splitting applications. *Electrochim. Acta* **2023**, *441*, 141816. [CrossRef]
47. Lv, T.R.; Zhang, W.H.; Yang, Y.Q.; Zhang, J.C.; Yin, M.J.; Yin, Z.; Yong, K.T.; An, Q.F. Micro/Nano-Fabrication of Flexible Poly (3, 4-Ethylenedioxythiophene)-Based Conductive Films for High-Performance Microdevices. *Small* **2023**, *19*, 2301071. [CrossRef]
48. Tian, Y.; Yang, Y.; Wu, Y.; Zhou, Z.; Li, Y.; Wang, J.; Liu, S.; Wang, C. Electropolymerization of 5-amino-2-naphthalenesulfonic acid and their application as the electrode material for supercapacitors. *J. Energy Storage* **2023**, *72*, 108308. [CrossRef]
49. Zhuo, H.; Hu, Y.; Chen, Z.; Zhong, L. Cellulose carbon aerogel/PPy composites for high-performance supercapacitor. *Carbohydr. Polym.* **2019**, *215*, 322–329. [CrossRef]

polymers

MDPI

Article

Bicomponent Electrospinning of PVDF-Based Nanofiber Membranes for Air Filtration and Oil–Water Separation

Tianxue Feng [1], Lin Fu [2], Zhimei Mu [1], Wenhui Wei [1], Wenwen Li [1], Xiu Liang [1], Liang Ma [3], Yitian Wu [1], Xiaoyu Wang [1], Tao Wu [1], Meng Gao [1], Guanchen Xu [1] and Xingshuang Zhang [1,*]

[1] Advanced Materials Institute, Qilu University of Technology (Shandong Academy of Sciences), Jinan 250014, China
[2] Sino Science and Technology Co., Ltd., Dongying 257000, China
[3] Guochen Industrial Group Co., Ltd., Jinan 250300, China
* Correspondence: xszhang@qlu.edu.cn

Abstract: Particulate matter (PM) and water pollution have posed serious hazards to human health. Nanofiber membranes (NFMs) have emerged as promising candidates for the elimination of PMs and the separation of oil–water mixtures. In this study, a polyvinylidene difluoride (PVDF)-based nanofiber membrane with an average diameter of approximately 150 nm was prepared via a double-nozzle electrospinning technology, demonstrating high-efficiency PM filtration and oil–water separation. The finer fiber diameter not only enhances PM filtration efficiency but also reduces air resistance. The high-voltage electric field and mechanical stretching during electrospinning promote high crystallization of β-phase PVDF. Additionally, the electrostatic charges generated on the surface of β-phase PVDF facilitate the adsorption of PM from the atmosphere. The introduction of polydopamine (PDA) in PVDF produces abundant adsorption sites, enabling outstanding filtration performance. PVDF-PVDF/PDA NFMs can achieve remarkable $PM_{0.3}$ filtration efficiency (99.967%) while maintaining a low pressure drop (144 Pa). PVDF-PVDF/PDA NFMs are hydrophobic, and its water contact angle (WCA) is 125.9°. It also shows excellent resistance to both acidic and alkaline environments, along with notable flame retardancy, as it can self-extinguish within 3 s. This nanofiber membrane holds significant promise for applications in personal protection, indoor air filtration, oily wastewater treatment, and environmental protection.

Keywords: electrospinning; PVDF; nanofiber membrane; air filtration; oil–water separation

1. Introduction

With the rapid development of the economy and urbanization, issues related to urban pollution and protection are increasingly receiving attention. On the one hand, the main culprit for the serious impact of air pollutants on the brain is PMs with a diameter of less than 2.5 μm [1]. Especially, $PM_{0.3}$ has a greater impact on human health due to its small particle size, attachment of large amounts of harmful and toxic substances, wide dispersion range, and long residence time in the atmosphere [2]. On the other hand, water pollution can contaminate drinking water sources, causing a wide array of health issues from gastrointestinal disorders to long-term exposure-related cancers. As a result, the development of highly effective filtration technologies has become an urgent and crucial task in the field of environmental and health sciences [3]. In the existing filtration, membrane filtration technology has the advantages of low energy consumption and simple operation [4], such as hot pressing membrane forming technology, gel technology, wet technology, etc. Micropores formed during the hot pressing membrane process permeate

each other, and their affinity is insufficient. There are many problems in the gel membrane process, such as large loss and difficulty in preparing nanomembranes. The wet process can produce microporous membrane materials with high micropore curvature, poor environmental protection, and poor thermal stability. Electrospun nanofibers have characteristics of continuity, large aspect ratios, large specific surface area, high flexibility, mechanical properties, and adjustable fiber diameters [5]. Researchers have developed a variety of methods for fabricating structured nanofiber membranes, with the aim of improving the filtration and separation performance of fiber membranes [6]. For example, increasing the thickness of a fiber membrane [7], changing the network structure of fiber membranes [8], and adding a certain charge to a fiber membrane can make it. However, improvement in filtration efficiency often brings about drawback of increased pressure. Thus, the quest to obtain membranes featuring high filtration efficiency and low air resistance remains a significant challenge.

Fiber air filtration mechanisms include gravity effects, sieving, interception, inertial collision, Brownian motion, and electrostatic effects [9]. When PMs in the air pass through filters, electrostatic forces not only effectively attract charged particles but also capture PMs through electrostatic induction effects [10]. As a kind of self-polarizing electret material, PVDF is a highly nonlinear and structural organic polymer with certain piezoelectric properties. PVDF undergoes various mechanical, thermal, and electrical treatments, resulting in the formation of five polycrystalline structures: α, β, δ, ε, and γ, which can interconvert [11]. The β phase overall trans of phase molecular chain is combined with specific polarization in the crystal to produce the highest piezoelectric effect, accompanied by additional piezoelectricity [12]. More importantly, β-PVDF is formed under the stretching of the high-voltage electric field in the process of electrospinning. Polydopamine (PDA) contains a substantial number of catechol structures, endowing it with remarkable adhesion properties. Catechol structures can impart charges to nanoparticles. Owing to strong electrostatic repulsion force, nanoparticles encapsulated by PDA display extremely high stability. The strong adhesion enables PDA to adhere to the surface of inorganic and organic materials [13]. For example, Ma et al. [14,15] electrospun PVDF/PDA fiber membranes, presenting significant adsorption capacity for MB and Cu^{2+}. Tian et al. [15] designed a two-stage electrostatically assisted air filtration device by a thin coating of PDA on the polyethylene terephthalate coarse filter. This filter achieved a high filtration efficiency of 99.48% for $PM_{0.3}$. Therefore, PDA could be used to improve the adsorption capacity of membranes.

Herein, we prepared PVDF-based nanofiber membranes featuring high PM filtration performance and efficient oil–water separation capabilities using a simple one-step double-nozzle electrospinning strategy (Scheme 1). The high-voltage electric field in electrospinning polarizes and stretches the PVDF jet, promoting β-PVDF high crystallization. The rich surface groups of PDA further enhance the filtration and separation performance of PVDF-PVDF/PDA nanofiber membranes (NFMs). Notably, the higher electronegativity of fluorine (F) atoms in PVDF compared to nitrogen (N) atoms in PDA induces electrostatic attraction, boosting the air filtration performance. At a basis weight of 8.82 g/m^2, the PVDF-PVDF/PDA-3 NFMs achieved a $PM_{0.3}$ filtration efficiency of 99.967% with a pressure of 144 Pa. Additionally, the hydrophobicity of PVDF-PVDF/PDA NFMs endows them with outstanding oil–water separation capabilities. Modified hydrophobic PVDF-PVDF/PDA NFMs also demonstrate remarkable acid/alkali resistance and flame-retardant properties. These characteristics make the membrane an ideal option for applications in personal protection during fire and other emergency situations, as well as in household air purification and filtration systems.

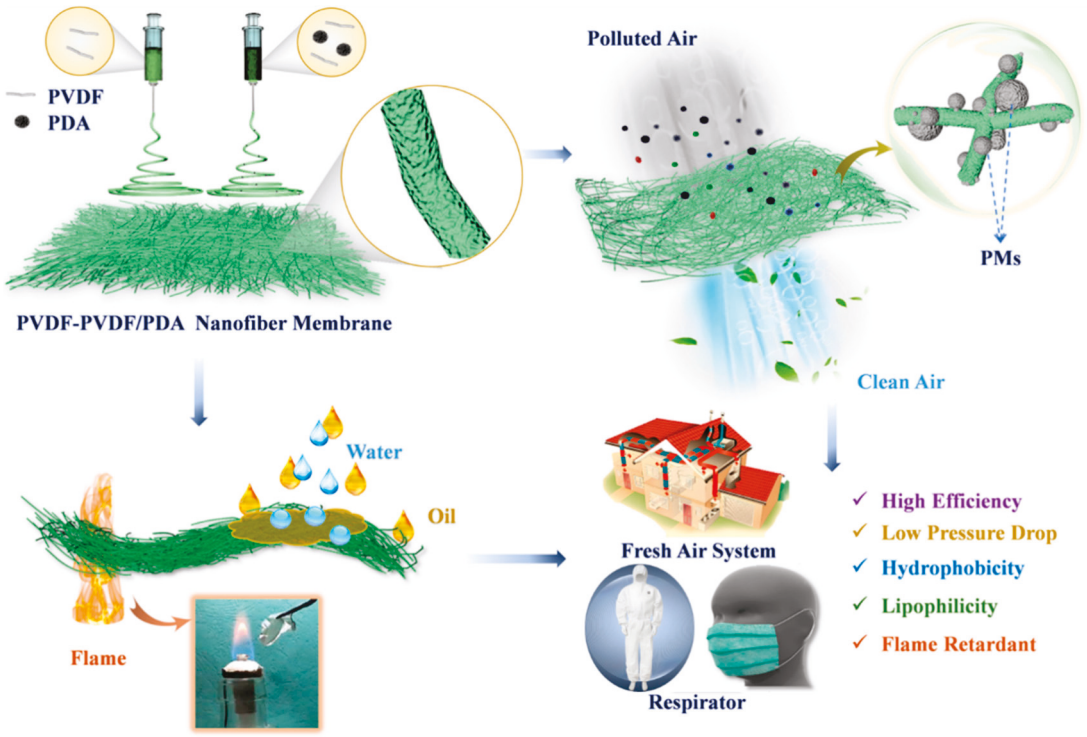

Scheme 1. Illustration of the fabrication and properties of PVDF-PVDF/PDA NFMs.

2. Material and Methods

2.1. Materials

N, *N*′-dimethylformamide (DMF, 99%, biotech grade), polyvinylidene difluoride (PVDF, M_w: 400,000 g/mol, powder), dopamine hydrochloride, potassium hydroxide (KOH, 85%), ethanol (99.7%), ammonia (25~28%), NaCl, NaOH, dichloromethane (AR), and HCl were purchased from Shanghai Macklin Biochemical Co., Ltd., Shanghai, China. Ultrapure water was made in the laboratory.

2.2. Fabrication of Electrospinning PVDF/PDA and PVDF-PVDF/PDA NFMs

Preparation of PVDF NFMs: A total of 1.0 g of PVDF was dissolved in DMF and stirred for 4 h at 25 °C, forming a 15 wt% PVDF spinning solution. A 20 wt% PVDF spinning solution was prepared in the same way. PVDF spinning solutions were electrospun to form PVDF NFMs. The spinneret was 18 G, and the spinning voltage was 20 kV. The ambient temperature and humidity were 25 °C and 80 ± 5 °C. Finally, the obtained PVDF NFMs were dried at 60 °C for 24 h to remove residual solvent.

Preparation of PVDF-PVDF/PDA NFMs: A total of 0.1 g of PDA was dispersed and sonicated for 2 h in DMF. PVDF was added to the above solution, obtaining a PVDF/PDA-1 spinning solution. The 20 wt% PVDF and PVDF/PDA-1 spinning solutions were transferred into two 5 mL syringes, respectively. The two syringes were placed in the main and secondary pumps. Spinning parameters were the same as those described above. After spinning, nanofiber membranes were dried at 60 °C for 24 h, obtaining PVDF-PVDF/PDA-1 (labeled S-1) NFMs, as shown in Scheme 1. In the same method, 0.2 g, 0.3 g, and 0.5 g of PDA were added to prepare the spinning solution, obtaining PVDF-PVDF/PDA-x (x = 2, 3, 5), labeled as S-2, S-3, and S-5, respectively. To better illustrate the filtration properties of PVDF-PVDF/PDA-x NFMs, single-nozzle electrospun PVDF/PDA-x NFMs were prepared as a control group. For double-nozzle electrospinning, one nozzle contained PVDF while the other contained PVDF/PDA. Then, contrast experiments were performed by electrospinning using a single-nozzle PVDF/PDA.

2.3. Measurement and Characterization

The characterization methods for the physical and chemical properties of materials were presented in the Supporting Information (SI). The air filtration performance of PVDF NFMs was evaluated by filtration efficiency (η), pressure drop (ΔP), and quality factor (QF). Filtration efficiency and pressure drop of nanofiber membranes were measured using an automatic filtration material tester. Specifically, sodium chloride particle matters from 0.3 to 10 μm were selected as particle models for PMs. The ambient temperature of the tested nanofiber membrane was 25 ± 5 °C. The airflow velocity was controlled between 10 and 85 L/min. All tests were conducted three times. QF was calculated to describe the comprehensive air filtration performance of the air filter using the following equation [16]:

$$QF = \frac{-\ln(1-\eta)}{\Delta P} \quad (1)$$

where η is the filtration efficiency and ΔP is the pressure drop.

3. Results and Discussion

3.1. Morphology, Structure, and Component of PVDF-Based NFMs

Figure 1a shows molecular structure models of the α and β phases of PVDF. During electrospinning, the static voltage could facilitate high crystallization of β-phase PVDF. Each unit cell of β-PVDF contains two molecular chains. Not only are dipole moments in the unit aligned parallel, but the dipole moments of the two molecular chains are also parallel, exhibiting TTTT transformation conformation, which enhances the polarity of the β phase. The average particle size of PDA was 55.3 nm (Figure S1a,b). The surface of PDA was rough with a rich sense of granularity (Figure S1c). PVDF nanofibers were randomly distributed and relatively straight, and the fiber surface had a large number of raised rough structures (Figure S2). All nanofibers from double-nozzle electrospun PVDF/PDA NFMs were randomly distributed but more curved, with a bumpy fiber surface, possibly due to PDA adhering to both the surface and interior of the fiber (Figures 1b,c and S3). PDA can improve the dispersion and uniformity of the material and may affect the internal structure and orientation of the fiber. Figure 1d clearly shows that PDA particles were dispersed on the surface and within the fibers. The average fiber diameter of PVDF-PVDF/PDA NFMs increased with increasing PDA doping levels (Figure S3). This may be because more PDA provides more abundant adsorption sites, increasing the surface area and enhancing the roughness of the surface, which strengthens the interaction with the polymer matrix (Table 1). With increasing PDA doping amount, the rich amino and polar role of PDA makes it adhere to the interior of the fiber, resulting in a reduced mean diameter of PVDF/PDA (Figure S4). When the PDA content was 0.1 g or 0.2 g, a large number of PDA particles attached to the fiber surface, and PDA agglomeration was observed on the fiber surface (Figure S4a,d). This may be due to double-nozzle electrospinning, where the jet is influenced by external electric field effects and Coulomb forces from other jets, resulting in a small fiber diameter. At the same PDA doping amount, the diameter of nanofibers prepared by double-nozzle electrospinning was smaller than that of single-nozzle electrospinning. This may be attributed to the interaction between abundant amino groups on the PDA surface and β-PVDF in double-nozzle electrospinning [17].

Table 1. Specific surface area, pore volume, and microspore volume of PVDF-PVDF/PDA NFMs with different PDA doping levels.

Samples	Surface Area (m^2/g)	Pore Volume (cm^3/g)	Microspore Volume (cm^3/g)
PVDF	7.337	0.032	0.002
S-1	2.824	0.009	0.001
S-2	8.654	0.050	0.002
S-3	11.484	0.043	0.003
S-5	9.176	0.049	0.002

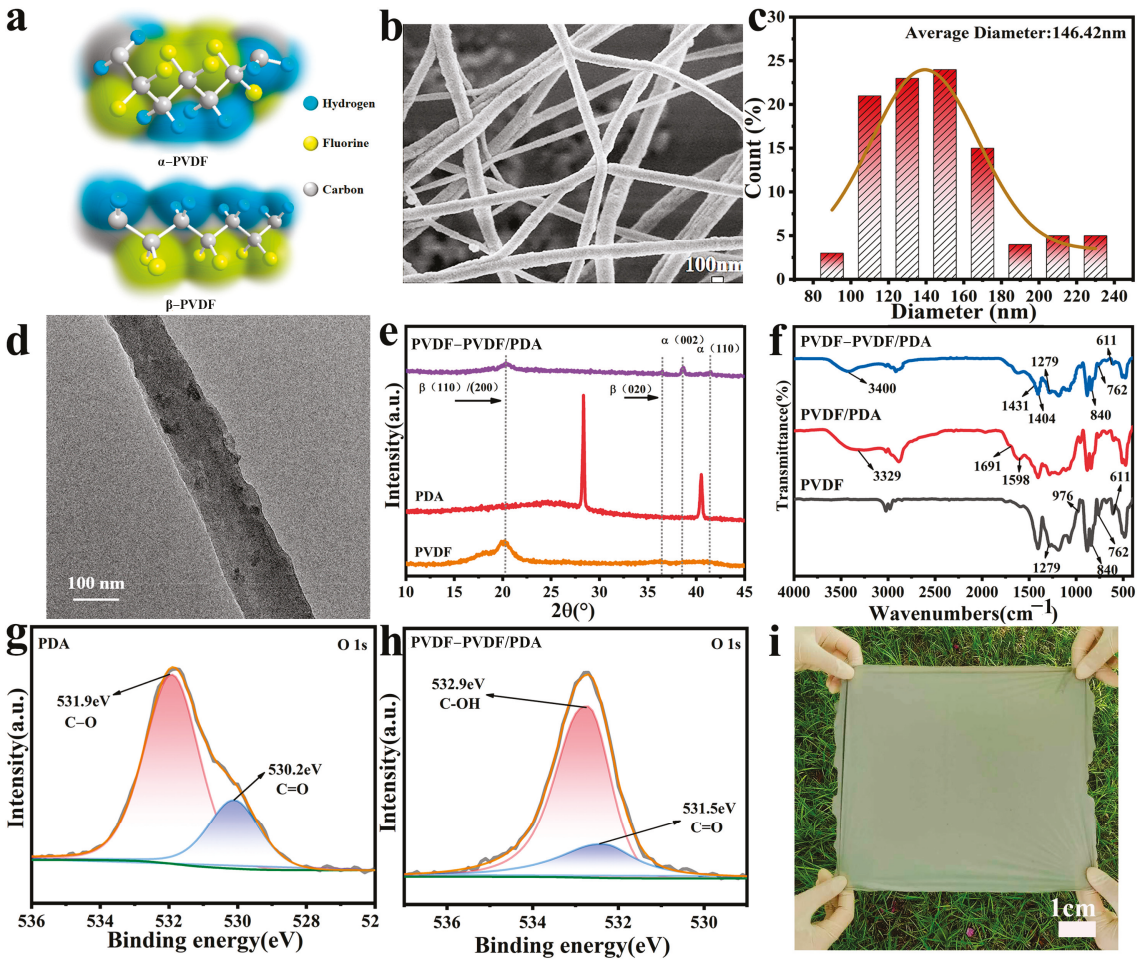

Figure 1. (**a**) Molecular structures of α-phase and β-phase PVDF. (**b**) SEM image and (**c**) nanofiber diameter distribution of S-3 NFMs. (**d**) TEM image of PVDF-PVDF/PDA NFMs. (**e**) XRD spectra and (**f**) FTIR spectra of PVDF, PVDF/PDA, and PVDF-PVDF/PDA NFMs. The O1s XPS spectra of (**g**) PDA and (**h**) PVDF-PVDF/PDA NFMs. (**i**) Photograph of PVDF-PVDF/PDA NFMs.

XRD spectra of PDA, PVDF NFMs, and PVDF-PVDF/PDA NFMs are shown in Figure 1e. It can be seen that both PVDF and PVDF-PVDF/PDA NFMs showed a strong diffraction peak at 20.4°, which is attributed to (110)/(200) crystal surface of β-PVDF [18]. This indicates that PDA does not affect the crystal structure and phase transformation of β-PVDF in electrospun PVDF-PVDF/PDA NFMs. In addition, PVDF-PVDF/PDA NFM had major peaks at 2θ of 38.6° and 41.5°, which correspond to the α crystalline phase with (002) and (110) reflective surfaces [19]. An additional new peak, 2θ of 36.5°, is attributed to the TTTT transformation of the β phase and the corresponding (020) reflection plane. This may be because the β phase is generated by in situ electric field polarization

and mechanical stretching assisted by electrospinning. Thus, the β phase was the main crystal form of PVDF-based NFMs. Therefore, the α to β phase transition was achieved during electrospinning, and it can be further verified by FTIR spectra (Figure 1f). Sharp absorption peaks of PVDF membranes at 611, 762, and 976 cm^{-1} can be attributed to vibrational absorption of α-PVDF, as well as at 840 and 1279 cm^{-1} for β-PVDF [20]. A weak band was visible in the PVDF/PDA membrane at 1691 cm^{-1}, which belonged to the stretching of PDA-derived aromatic ring [21]. There were two wide absorption bands at 1598 and 3329 cm^{-1}, which may be attributed to the stretching vibration of N-H and C=C groups of PDA. FTIR spectra of PVDF-PVDF/PDA NFMs were similar to PVDF and PVDF/PDA NFMs, indicating that the addition of PDA does not affect the structure of PVDF. However, the sharp absorption peak of PVDF-PVDF/PDA NFMs at 611 and 762 cm^{-1} can be attributed to the vibration absorption of α-PVDF, and at 840, 1279, 1404, and 1431 cm^{-1} to the vibration absorption of β-PVDF [22]. Moreover, the wide absorption band at 3400 cm^{-1} corresponds to the tensile vibration of PDA. The proportion of the β phase can be calculated by the following Formula (2) [23]:

$$F(\beta) = \frac{A_\beta}{A_\beta + 1.26A_\alpha} \quad (2)$$

where *F(β)* is the proportion of the β phase, and A_α and A_β are absorption peak intensities of α and β phases. According to A_α and A_β absorption peaks of PVDF-PVDF/PDA NFMs at 611 cm^{-1} and 1431 cm^{-1}, it has been calculated that the β-phase proportion was 65.02%. This is because electrospinning can promote the transition of the nonpolar α phase to the polar β phase. The reduction of the α-phase absorption peak and significant increase of the β phase in PVDF-PVDF/PDA NFMs once again verified that PDA addition and electrospinning can promote the transition of the nonpolar α phase to the polar β phase. This result is consistent with the XRD spectrum analysis shown in Figure 1e. The surface properties and chemical structure of the membrane were further analyzed by XPS. The signal of O1s PDA demonstrated the presence of C-O and C=O (Figure 1g). O1s of PVDF-PVDF/PDA NFMs had two major peaks, and spectral peaks at 531.5 and 532.9 eV were attributed to quinine C=O and catechol C-OH (Figure 1h), respectively [24]. PVDF-PVDF/PDA NFMs still have N and F elements (Figure S5a). The canonical N1s signal corresponded to species of N in PDA. In the N1s spectrum of PDA, -N= (397.9 eV) and -NH- (399 eV) correspond to cyclic nitrogen [25] (Figure S5b). In the F1s spectrum of PVDF-PVDF/PDA, there were 688.4 eV and 688.5 eV peaks at the high binding energy (Figure S5c). Both PDA and PVDF-PVDF/PDA had similar characteristic peaks, and the results confirmed the successful construction of PDA in composite nanomaterials. Figure 1i shows the prepared large-area PVDF-PVDF/PDA NFMs, which were gray.

3.2. Electrical Performance of PVDF-Based NFMs

Due to the high-voltage electric field and mechanical stretching in the electrospinning process, the PVDF jet is polarized and stretched. This promotes dipole moment-oriented transition of the PVDF molecular chain from α-PVDF to β-PVDF and enhances the crystallization of β-PVDF [26]. The charge can be stored in nanofibers when electrospinning [27]. PDA is an organic polymer with a large molecular weight and strong polarity. Based on this, PVDF-PVDF/PDA NFMs have good electrical properties, which can enable PVDF-PVDF/PDA NFMs to achieve active adsorption and stable adhesion to particles by their own electrostatic force [28].

Figure 2 shows changes in piezoelectric coefficient (d_{33}), surface potential, dielectric constant, and dielectric loss of PVDF-PVDF/PDA NFMs. D_{33} value of S-3 was 1.5 PC/N, and that of S-5 was 3.1 PC/N (Figure 2a), which indicated the piezo effect of S-5 can produce

a greater charge and higher sensitivity [29]. Surface Zeta potential was a representation of the number of charges on the surface of a material, and negative values indicated that PVDF-PVDF/PDA NFMs were negatively charged [30] (Figure 2b). It can be seen that the absolute value of S-5 was the largest, at 79.412 mV. The absolute value of the surface Zeta potential of S-3 NFMs was higher than that of PVDF/PDA-3 (Figure S6). This indicated that the higher the absolute value of S-3 was, the greater its electrostatic repulsion and the more stable the system would be. Importantly, the absolute value of the surface Zeta potential of all membranes was greater than 50 mV, indicating that all membranes we prepared had relatively good stability [31]. The dielectric constant and dielectric loss of PVDF-PVDF/PDA NFMs are shown in Figure 2c,d with the increase of PDA content. A study shows that the dielectric constant and dielectric loss values of ideal matter were small [32]. The dielectric constant of S-3 decreased from 2.55 to 1.77, and the minimum dielectric loss was 0.0407. This indicated that S-3 had a small polarization charge, small response capacity, and small loss. The electrical properties of composite nanofiber membranes are realized by the interaction between functional groups on PDA and specific groups in the PVDF segment. Specifically, there are a large number of -NH- groups in composite nanostructure, and -CF_2 in the PVDF segment forms hydrogen bonds, which can also promote the β phase transition. The charge of nanofiber membrane was mainly derived from β-PVDF. Therefore, polarized PVDF-PVDF/PDA NFMs could absorb and adhere by electrostatic effect, achieving efficient air filtration efficiency and oil–water separation [33]. It can be seen that membrane still maintains good or even higher electrical performance after filtration (Figure S6b,c). This is because the adsorption of PMs on the membrane increases surface roughness, which makes it easier to intensify friction and generate more static electricity.

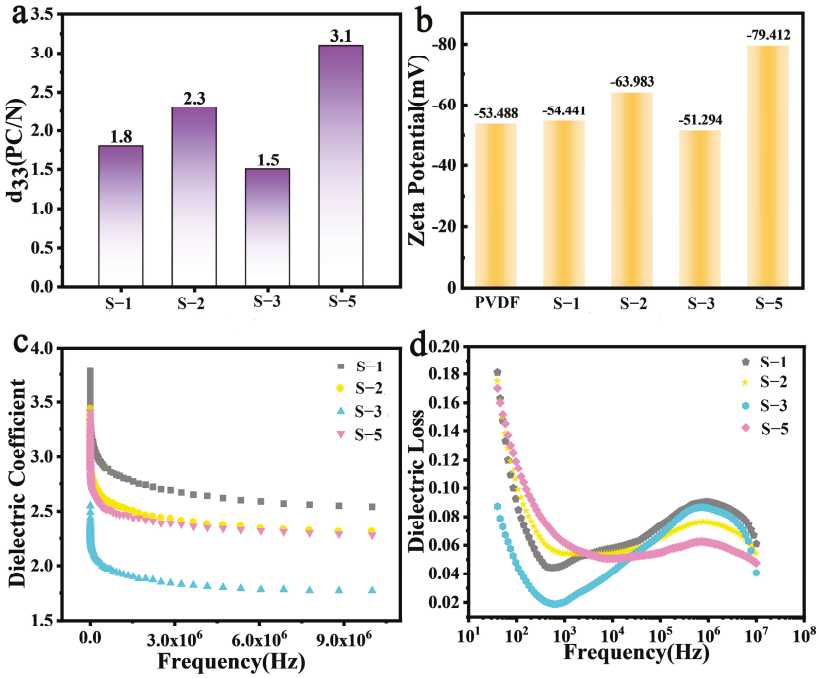

Figure 2. (**a**) d_{33}, (**b**) Zeta potential on the solid surface, (**c**) dielectric coefficient, and (**d**) dielectric loss of S-1, S-2, S-3, and S-5 NFMs.

3.3. Air Filtration Performance and Oil–Water Separation of PVDF-Based NFMs

Figure 3a,b shows the PM filtration properties of nanofiber membranes at the same base weight and airflow velocity. The filtration efficiency of $PM_{0.3}$ of PVDF NFMs reached 88.799%, but the filtration efficiency of the nanofiber membrane after the addition of PDA was greatly improved. $PM_{0.3}$ filtration efficiency of S-1 NFMs was 99.986%, but the pressure

drop was 343 Pa. In particular, the $PM_{0.3}$ filtration efficiency of S-3 NFM was as high as 99.998%, and the pressure drop was 255 Pa. The quality factor was 0.0424 Pa^{-1}. This may be due to the small pore size between fibers caused by a fine fiber diameter and a bumpy surface structure, which increased the probability of PM capture, enhanced filtration efficiency, and pressure drop. Furthermore, it can also be seen that the filtration performance of the double-nozzle electrospinning nanofiber membrane was better than that of the single-nozzle electrospinning nanofiber membrane (Figure S7a,b). $PM_{0.3}$ filtration efficiency of PVDF/PDA-3 NFMs was 99.987%, and pressure drop and quality factor were 296 Pa and 0.0351 Pa^{-1}, respectively. This may be because PDA contains abundant π electron clouds, which can produce π–π interactions with other molecules in a π-containing system, thus adsorbing small molecules [34]. To better demonstrate the excellent filtration performance of the nanofiber membrane, PMs filtration efficiency of PVDF-PVDF/PDA-3 NFM and PVDF/PDA-3 NFM at different base weights and different airflow velocities were characterized (Figure S7c–f). At a basis weight of 8.82 g/m^2 for S-3, $PM_{0.3}$ filtration efficiency was 99.967%, and pressure drop was 144 Pa. S-3 and PVDF/PDA-3 NFMs were characterized for 60 cycles at a basis weight of 29.39 g/m^2 and airflow velocity of 32 L/min (Figure 3c,d). The filter performance tester can emit 60,000 PM particles in one test. The nanofiber membrane was tested for filtration performance once, which means a cycle, followed by the next test without cleaning. S-3 and PVDF/PDA-3 NFMs had increasing filtration efficiency and pressure drop at 60 cycles. $PM_{0.3}$ filtration efficiency of S-3 was 100%, which was greater than that of PVDF/PDA-3 (99.971%), but the pressure drop of 401 Pa was less than that of PVDF/PDA-3 (648 Pa). Necessarily, the filtration efficiency of S-3 NFMs had reached 99.998% at 20 times (Figure 3c,d). In addition, PDA carbon material has good adhesion, which can enhance the adsorption capacity of PMs, while PVDF provides mechanical strength and chemical stability. Therefore, the composite nanofiber membrane can not only ensure a good adsorption effect of PMs but also maintain the structural stability of the membrane, so as to ensure that the cycle neutral energy of PM adsorption does not decrease after many times. Moreover, electrospinning can produce nanofiber membranes with continuous fibers and moderate porosity, which can improve the adsorption performance and stability of the membrane and make it able to withstand more adsorption cycles.

N_2 adsorption–desorption isotherms of PVDF, PVDF/PDA, and PVDF-PVDF/PDA NFMs all slowly increased with increasing relative pressure (Figure 3e,f), indicating that the adsorption capacity of membranes to N_2 was weak [35]. Specific surface area and pore volume of nanofiber membranes are shown in Tables 1 and S1. The distribution of PVDF and PVDF-PVDF/PDA NFMs was relatively consistent, with pores concentrated at 0–50 nm and belonging to mesoporous. However, the pore distribution of PVDF-PVDF/PDA NFMs was much greater than that of PVDF/PDA NFMs (Figure S8). Specific surface area (11.484 m^2/g), microspore volume (0.003 cm^3/g), and total pore volume (0.043 cm^3/g) of S-3 NFM were greatly increased (Table 1) and were worse than PVDF/PDA-3, which is conducive to the adsorption of small particles. Generally speaking, the smaller the pore volume of the membrane is, the higher the filtration efficiency is, as a smaller pore volume can capture more PMs. Therefore, S-3 has better capture capability.

To more clearly illustrate the excellent filtration performance of nanofiber membranes, we performed real simulation experiments as shown in Figure 3g. The inset shows a simulated experimental setup. The cuboid was divided into two parts, with the filtered photograph on the left and the one before filtering on the right [36]. We placed the membrane at the middle junction on the left and right sides, and the pollution source was a lit cigarette. From the SEM image in Figure 3g, it was also obvious that filtered fibers adhered to many PMs of different sizes. Figure 3h more clearly indicates the filtration

mechanism of nanofiber membranes. PVDF-PVDF/PDA NFM has five PM capture mechanisms, namely, the interception effect, diffusion effect, inertia effect, gravity effect, and electrostatic effect [37]. The nanofiber membranes with a bumpy structure not only had a larger specific surface area but also increased collision between fibers and PMs, leading to physical trapping, thus increasing filtration efficiency, especially for small particles. In detail, first, PVDF-PVDF/PDA NFMs have abundant adsorption sites and high specific surface area, increasing collision and adhesion between fibers and PMs and improving physical interception capability [38]. Next, strong polarity and abundant amino groups of PDA increase the active adsorption between fibers and PMs, thus producing a strong adhesion to the surface of the fiber [39]. Then, PDA has amino groups, and the hybridization mode of their N atoms is sp^3 hybridization, with a pair of lone pair electrons [40]. The electronegativity of the F atom in PVDF is stronger than that of N, which will attract electrons to the N atom and generate electrostatic attraction, thereby improving the electrostatic effect of the nanofiber membrane. Finally, high voltage electric field and mechanical stretching of electrospinning promote high crystallization of β-PVDF, and electrostatic action of surface charge generated by β-PVDF adsorbs PMs in the atmosphere [41]. Table S2 compares the comprehensive properties of various PVDF-based nanofiber membranes. It can be seen that compared with other PVDF-based nanofiber membranes, our work has finer nanofiber diameter, higher PM filtration efficiency, and good electrical performance, which can be used in high-efficiency PM capture.

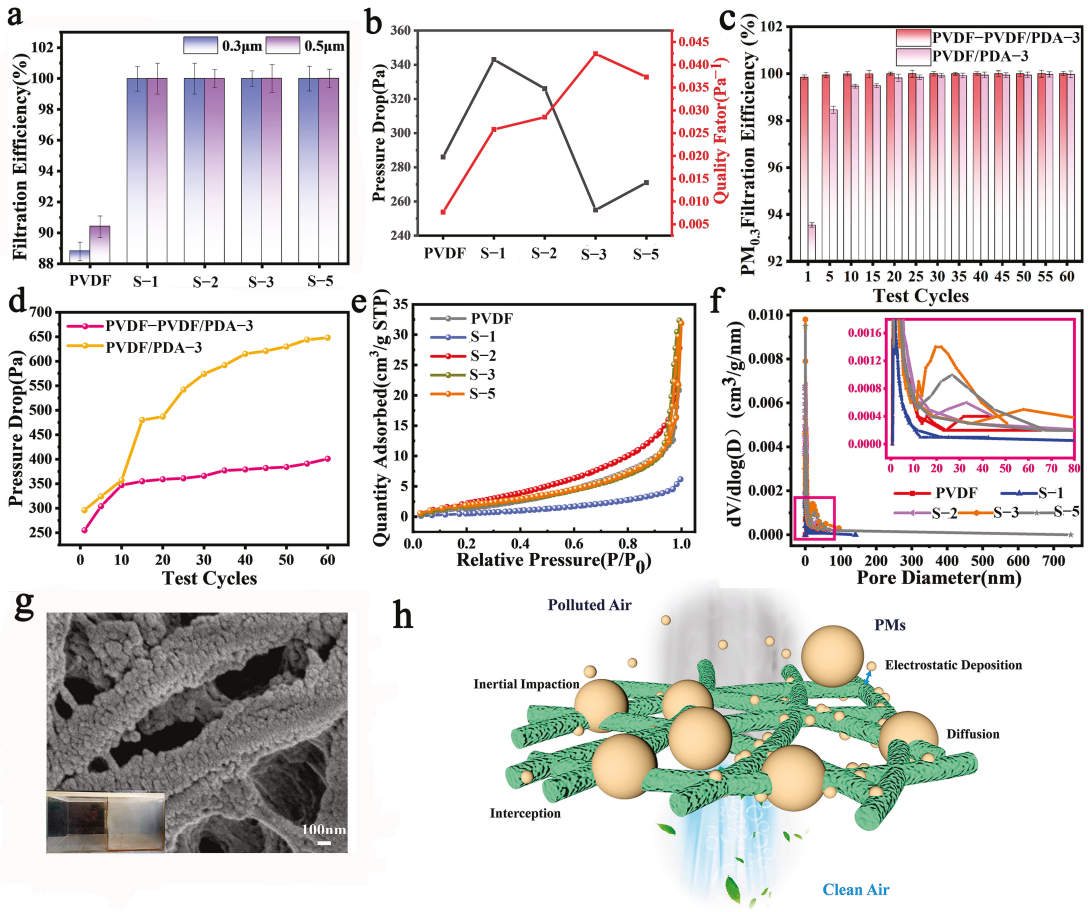

Figure 3. (**a**) Filtration efficiency, (**b**) pressure drop, and quality factor of PVDF, S-1, S-2, S-3, and S-5 NFMs. (**c**) Filtration efficiency and (**d**) pressure drop of S-3 and PVDF/PDA-3 under 60 cycles of filtration. (**e**) N_2 adsorption–desorption isotherms and (**f**) pore diameter distributions of PVDF, S-1, S-2, S-3, and S-5. (**g**) SEM image of PVDF-PVDF/PDA after filtration (inset showing the filter simulation device). (**h**) Schematic of the filtration mechanism of PVDF-PDF/PDA NFMs.

The wettability of the membrane plays an important role in its permeability and antifouling properties. WCA is an important method to characterize the wetting properties of the membrane surface, so we systematically studied the wetting behavior of the nanofiber membrane. Figure 4a, S9 shows the WCA of PVDF, PVDF-PVDF/PDA, and PVDF/PDA. PVDF membrane was a hydrophobic membrane (WCA was 144.217°). Hydrophobic PVDF nanofiber membrane shows that it has a certain repelling effect on water but has a relatively good affinity for oil substances, which provides a basic physical property difference for oil–water separation to a certain extent. After the addition of PDA, WCA decreased, which was due to the nanofiber membrane with many hydrophilic groups such as hydroxyl and amino groups [42]. At the same amount of PDA doping amounts, the water contact angle of PVDF/PDA (Figure S9a) was smaller than that of the double-nozzle electrospinning membrane, which also indicated that PVDF is hydrophobic, and WCA decreased under the influence of the hydrophilic group of PDA [43]. In addition, with an increase in PDA, the water contact angle showed a trend of decreasing first, and then rising. WCA of S-3 reached its minimum, which was 125.863°. This may be due to the effects of the morphological change and PVDF on the surface properties. More importantly, there were tiny protrusions on the surface of the nanofibers, which form an extremely thin layer of air between protrusions, preventing water droplets from infiltrating the fiber surface and automatically aggregating to form water droplets (as shown in the inset of Figure 4a), thus demonstrating hydrophobicity. To illustrate the possibility of prolonged use of the filter membrane, S-3 NFMs were characterized. As can be seen, the WCA of S-3 NFM showed a downward trend within 30 min (water contact angle was 91.429°) (Figure S9b), but it was still a hydrophobic membrane. This indicated that the nanofiber membrane was not easy to wet and could be used for a long time. Necessarily, the decrease in WCA contributes to the dispersion and adsorption process of membranes in water.

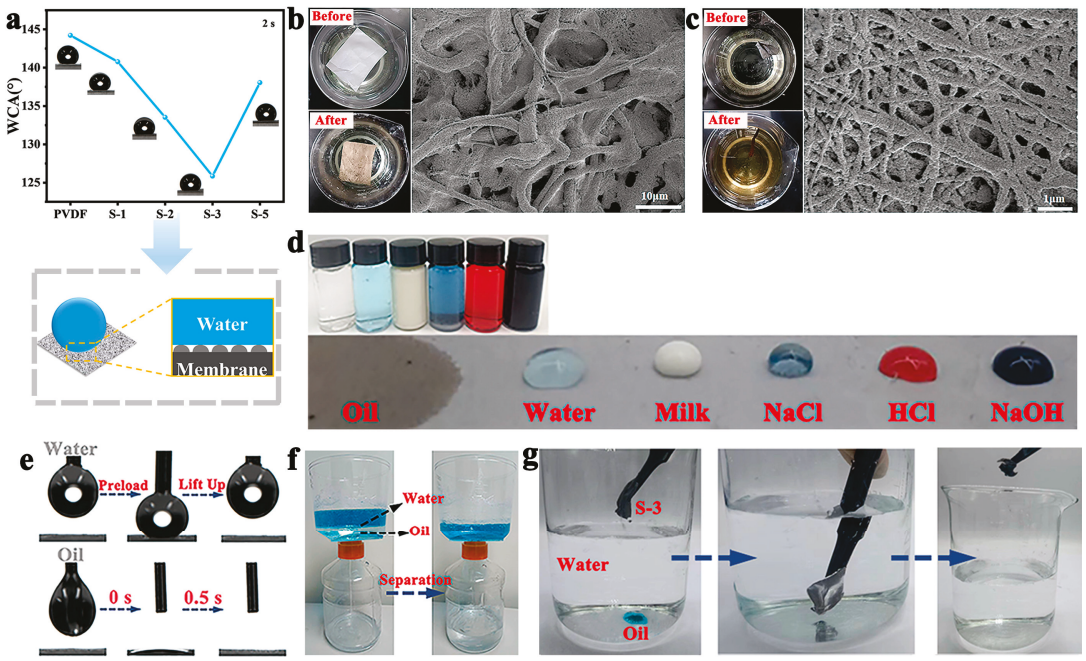

Figure 4. (**a**) WCA of PVDF and PVDF-PVDF/PDA NFMs. (**b**,**c**) Photos (top: before testing, bottom: after testing) and SEM images of PVDF and PVDF-PVDF/PDA-3 NFMs after testing in NaCl (0.5 mol/L) solution. (**d**) Photos of PVDF-PVDF/PDA NFMs surface with oil, water, milk, NaCl, HCl, and NaOH droplets. (**e**) Dynamic photos showing water and oil behavior on PVDF-PVDF/PDA membrane. (**f**) Separation process of oil–water mixture (blue liquid represents water). (**g**) Photo of PVDF-PVDF/PDA membrane with adsorbed oil in water (blue droplet represents oil).

PVDF and PVDF-PVDF/PDA NFMs were put into 0.5 mol/L NaCl solution for two weeks, as shown in Figure 4b,c. When PVDF NFMs were in solution, the structure of the fiber was destroyed. However, PVDF-PVDF/PDA NFMs can maintain good fiber structure, and a large number of particles were adsorbed on the surface of the fiber. This may be because the specific surface area and other microstructures of the composite nanofiber membrane provide a basis for its adsorption in water. Moreover, modification of hydrophilic groups of PDA was conducive to the adsorption of membranes in water. Therefore, the composite nanofiber membrane can maintain good adsorption properties and fiber structure in a wet environment for a long time. This can provide ideas for its application in masks, protective clothing, and other fields. PVDF-PVDF/PDA nanofiber membrane was extremely lipophilic and hydrophobic to water, milk, saturated salt water (NaCl), acid solution (HCl, PH = 1), and alkaline solution (NaOH, PH = 13) (Figure 4d). PVDF-PVDF/PDA membrane was very good for oil infiltration and has a high contact angle for saturated salt water, acid solution, and alkaline solution. These characteristics make oil substances easier to spread on the surface of the nanofiber membrane. We studied the infiltration of the fibrous membrane by oil and water using a water contact angle tester. We used dichloromethane as the oily material. It can be seen that the water droplets completely leave the membrane surface after contact with the membrane, and the oil quickly diffuses on the membrane surface, indicating the good hydrophobic and lipophilic of the fibrous membrane (Figure 4e). PVDF-PVDF/PDA nanofiber membranes were composed of nanofibers with small fiber diameters and interconnected pores. This microstructure makes membranes have high porosity, can provide a larger specific surface area, and increases the contact area with the oil–water mixture, which is conducive to oil–water separation. Then, the ability of the PVDF-PVDF/PDA membrane to separate the oil–water mixture was investigated. It can be seen that transparent oil can easily penetrate the fibrous membrane, which is collected in the bottle below, and the blue aqueous solution remains above the container (Figure 4f). PVDF-PVDF/PDA membrane adsorbs methylene chloride (blue) in the water (Figure 4g), also indicating the hydrophobic oil affinity of the membrane. Due to the hydrophilicity of PDA carbon material and the hydrophobicity of PVDF, adhesion between water and the membrane surface is strong, while adhesion between oil droplets and the membrane surface is weak. In this case, oil droplets are more likely to be pushed by the water phase or taken away by water flow at the interface. Therefore, the synergistic action of surface charge and hydrophobicity of composite nanofiber membranes causes small oily droplets to aggregate and separate from trapped miscibility. This indicates that the composite nanofiber membrane has great potential in the field of oil–water separation.

3.4. Acid and Alkali Resistance, Mechanical Property, Thermal Stability, and Flame Resistance of PVDF-Based NFMs

Resistance to chemical erosion is of great importance for medical workers and in the field of water and oil separation. After soaking PVDF-PVDF/PDA nanofiber membrane in an acidic solution (HCl, PH = 1) and alkaline solution (NaOH, PH = 15) for 5 h, fiber morphology was unchanged (Figure 5a,b). After 50 h of chemical erosion, the weight of the fiber film was slightly lost (Figure 5c), and filtration efficiency was also slightly reduced (Figure 5c) after 5 h treatment, but the filtration efficiency of $PM_{0.3}$ was still greater than 97.5%. This is because the molecular chain of PVDF contains a large number of fluorine atoms, and this structure gives the membrane excellent chemical stability and corrosion resistance to erosion of most acids, bases, and organic solvents. It thus indicates that composite nanofibrous membranes are resistant to acid and base erosion. Figure 5e is a characterization of the mechanical properties of PVDF-PVDF/PDA NFMs. PVDF NFM showed excellent mechanical properties with stress and strain of 2.052 MPa and 49.382%, but mechanical properties decreased due to the addition of PDA. The stress showed a

decreasing trend with increasing PDA content. PVDF/PDA NFMs showed the same trend. Moreover, at the same PDA content, PVDF-PVDF/PDA NFMs had less stress and strain than PVDF/PDA NFMs (Figure S10), which may be because two jets repel each other due to Coulomb repulsion in double-nozzle electrospinning [44].

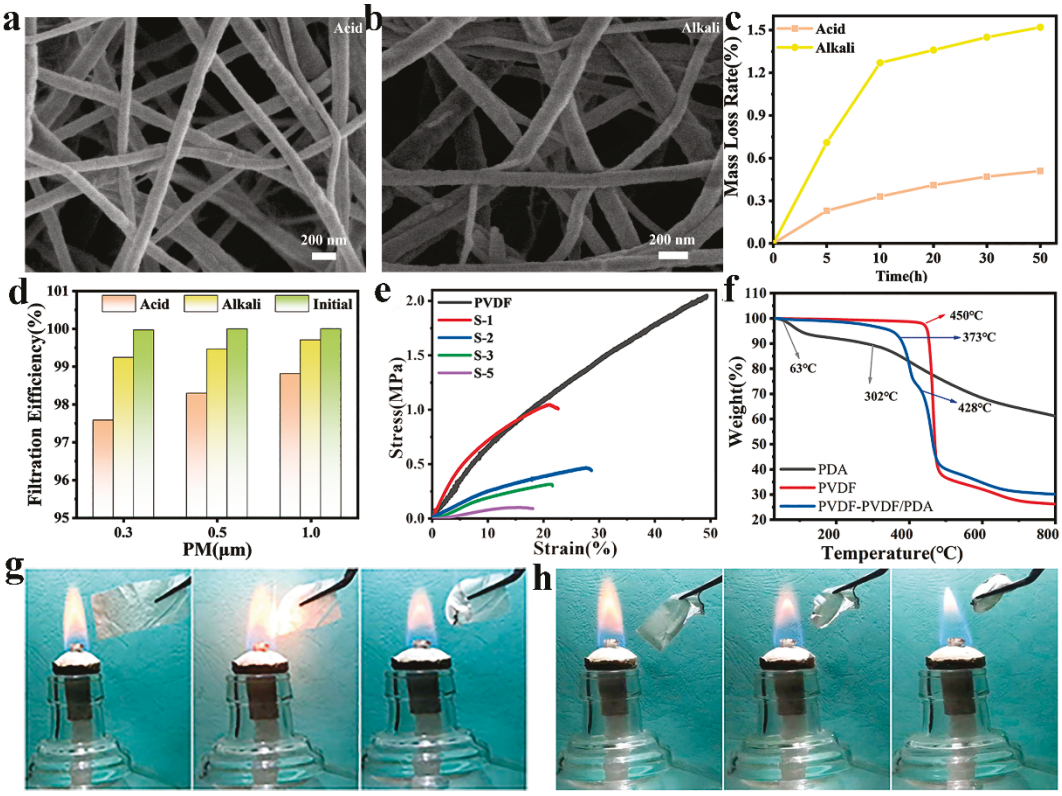

Figure 5. SEM images of PVDF-PVDF/PDA NFMs after a 5 h immersion in (**a**) HCl and (**b**) NaOH solution. (**c**,**d**) Mass loss after varying immersion time in HCl and NaOH solution and filtration efficiency after 5 h treatment. (**e**) Stress-strain curves of PVDF, S-1, S-2, S-3, and S-5. (**f**) TGA curves of PDA, PVDF, and PVDF-PVDF/PDA NFMs. Photographs showing (**g**) PVDF and (**h**) PVDF-PVDF/PDA NFMs under combustion.

The TGA curves of PDA, PVDF powder, and PVDF-PVDF/PDA NFMs are shown in Figure 5f. PDA degraded at 63 °C, probably due to evaporation of residual water in PDA. The maximum weight loss peak was observed at 302 °C. PVDF powder showed a maximum degradation rate of 450 °C. For PVDF-PVDF/PDA NFMs, there were two thermal degradation phases. Thermal degradation occurred at 373 °C, probably because of the degradation of PDA, While the 428 °C degradation occurred due to the thermal degradation of the PVDF matrix. The final residual rate of the nanofiber membrane was 30.103%. Results show that PDA can promote the thermal decomposition of nanofiber membranes. Figure 5g,h shows the flame resistance properties of PVDF and PVDF-PVDF/PDA-3 NFMs [45]. The membrane was tailored into a 2–3 cm rectangle. We used a lit alcohol lamp as a source of fire. The PVDF nanofiber membrane was extinguished and retained its original form immediately after leaving the fire source. PVDF-PVDF/PDA NFMs automatically curled up when approaching the fire source and were extinguished immediately after leaving the fire source in 3 s, but they still maintained the curled appearance. On the one hand, because F atoms release a large amount of fluorine gas during combustion, they help suppress flames. On the other hand, the inert gas released from the decomposition of the -NH group in PDA dilutes the flame flow in the gas phase. Therefore, the membrane had some self-quenching properties [46,47]. Table S2 compares the comprehensive properties of various PVDF-based

nanofiber membranes. By comparing diameter, η, ΔP, QF, electrical performance, and flame resistance with other filtration materials, our work has more outstanding efficiency in PM capture and oil–water separation, especially in the field of personal protection in fire and other emergencies and household purification.

4. Conclusions

In summary, our research focused on the successful fabrication of PVDF-PVDF/PDA NFMs via double-nozzle electrospinning. During the electrospinning process, a precisely controlled high-voltage electric field was applied, which not only facilitated the formation of nanofibers but also influenced their morphological and structural characteristics. The incorporation of PDA into the PVDF matrix was a key aspect of our study. PDA, with its rich surface groups, played a crucial role in enhancing the properties of nanofiber membranes. β-PVDF phase, induced by electrospinning conditions, further contributed to excellent filtration and separation capabilities of membranes. When examining the physical characteristics of membranes, we found that PVDF-PVDF/PDA-3 NFM, in particular, had a diameter of 146.42 nm. In terms of filtration performance, the membrane demonstrated an outstanding $PM_{0.3}$ filtration efficiency of 99.967%. This efficiency was measured using a customized air filtration test rig, where a controlled flow of air containing $PM_{0.3}$ particles was passed through the membrane. A low pressure drop of 144 Pa was simultaneously recorded, indicating the membrane's ability to maintain efficient filtration with minimal energy consumption. The filter membrane also demonstrated excellent hydrophobicity and lipophilicity. Oil–water separation experiments were also carried out, where the membrane effectively separated oil from water mixtures, highlighting its high-performance capabilities in this area. Additionally, the composite nanofiber membrane displayed strong acid and alkali resistance. Moreover, PVDF-PVDF/PDA NFMs had excellent flame retardancy, self-extinguishing within 3 s, ensuring suitability for protective clothing applications. In conclusion, our strategy of fabricating PVDF-PVDF/PDA NFMs provides valuable insights for the development of multifunctional fiber membrane materials. The detailed understanding of the relationship between the fabrication process, material composition, and resulting properties can serve as a foundation for further research and optimization of similar membrane materials.

Supplementary Materials: The following supporting information can be downloaded at: https://www.mdpi.com/article/10.3390/polym17050703/s1. Figure S1: (a,b) SEM images and diameter distribution of PDA carbon materials. (c) Pore diameter distribution of PDA carbon materials; Figure S2: (a,b) SEM image and diameter distribution of PVDF; Figure S3: SEM images and diameter distribution of (a-b) S-1, (c,d) S-2, (e,f) S-5; Figure S4: SEM images and diameter distribution of (a,b) PVDF/PDA-1, (c,d) PVDF/PDA-2, (e,f) PVDF/PDA-3, (g,h) PVDF/PDA-5.; Figure S5: (a) XPS full spectrum, and XPS spectra of (b) N1s for PDA and (c) F1s for PVDF-PVDF/PDA NFMs; Figure S6: (a) Zeta potential on the solid surface of PVDF/PDA NFMs. (b) Changes in d33 and zeta potential on the solid surface of PVDF-PVDF/PDA-3 NFMs after filtration. (c,d) Changes in dielectric coefficient and dielectric loss of PVDF-PVDF/PDA NFMs after filtration; Figure S7: (a,b) PMs filtration efficiency, pressure drop and quality factors of PVDF/PDA NFMs. PM0.3 filterability of PVDF-PVDF/PDA-3 and PVDF/PDA-3 NFMs with (c,d) different base weights and (e,f) different airflow velocities; Figure S8: Pore diameter distributions of PVDF/PDA NFMs; Figure S9: (a) Water contact angle of PVDF/PDA-x NFMs. (b) Water contact angle changes with time of S-3; Figure S10: Stress-strain curves of PVDF/PDA-x NFMs; Table S1: Specific surface area, total pore volume and microspore volume of PVDF/PDA NFMs with different PDA doping amounts; Table S2: Nanofiber membrane various performance comparison from the reported literature. References [1,23,31,48–58] are cited in the Supplementary Materials.

Author Contributions: Conceptualization, X.Z.; methodology, T.F. and W.W.; software, T.F. and Z.M.; validation, T.F. and X.Z.; formal analysis, T.F., L.F., W.L. and L.M.; investigation, X.L., Y.W. and X.W.; resources; T.W. and M.G.; data curation, T.F. and G.X.; writing—original draft preparation, T.F.; writing—review and editing, L.F., Z.M., X.L. and X.Z.; visualization, T.F. and X.Z.; supervision, G.X. and X.Z.; project administration, X.Z.; funding acquisition, X.Z. All authors have read and agreed to the published version of the manuscript.

Funding: This work was supported by the National Natural Science Foundation of China (51808328 and 62475128), the Natural Science Foundation of Shandong Province (ZR2023ME188), the Major Scientific and Technological Innovation Project of Shandong (2019JZZY020309 and 2020CXGC010309), the Youth Innovation Team Program of Shandong Higher Education Institution (2024KJN016), the Science, Production, Education, and Research projects of Qilu University of Technology (Shandong Academy of Sciences) (2023PY055 and 2020-CXY36), and the Technology Innovation Guidance Project of Shandong Province (YDZX2024143).

Data Availability Statement: The original contributions presented in the study are included in the article/Supplementary Material. Further inquiries can be directed to the corresponding author.

Conflicts of Interest: Author Lin Fu was employed by the company Sino Science and Technology Co., Ltd. Author Liang Ma was employed by the company Guochen Industrial Group Co., Ltd. The remaining authors declare that the research was conducted in the absence of any commercial or financial relationships that could be construed as a potential conflict of interest.

References

1. Sanyal, A.; Sinha-Ray, S. Ultrafine PVDF nanofibers for filtration of air-borne particulate matters: A comprehensive review. *Polymers* **2021**, *13*, 1864. [CrossRef] [PubMed]
2. Chen, J.; Guo, C.; Zhang, Q.; Wu, X.; Zhong, L.; Zheng, Y. Preparation of transparent, amphiphobic and recyclable electrospun window screen air filter for high-efficiency particulate matters capture. *J. Membr. Sci.* **2023**, *675*, 121545. [CrossRef]
3. Liang, G.; Zhang, W.; Zhang, X.; Yu, J.; Zhang, S.; Ding, B. Ultralight, superelastic, and antibacterial micro/nanofibrous sponges with dual-network interwoven structure for warmth retention. *Compos. Commun.* **2024**, *50*, 102006. [CrossRef]
4. Li, P.; Jiang, D.; Xu, C.; Su, Z. A scanning manometry method to image the atomization pressure field for pre-debugging the nanocomposite spraying system. *Compos. Commun.* **2025**, *53*, 102189. [CrossRef]
5. Zhou, N.; Gao, Y.; Huo, Y.; Zhang, K.; Zhu, J.; Chen, M.; Zhu, L.; Dong, Y.; Gao, H.; Soo Kim, I.; et al. Biodegradable micro-nanofiber medical tape with antibacterial and unidirectional moisture permeability. *Chem. Eng. J.* **2023**, *474*, 145793. [CrossRef]
6. Ren, X.; Liu, H.; Wang, J.; Yu, J. Electrospinning-Derived functional carbon-based materials for energy conversion and storage. *Chin. Chem. Lett.* **2024**, *35*, 109282. [CrossRef]
7. Liu, Y.; Wang, L.; Liu, Y.; Zhang, F.; Leng, J. Recent progress in shape memory polymer composites: Driving modes, forming technologies, and applications. *Compos. Commun.* **2024**, *51*, 102062. [CrossRef]
8. Fan, C.; Long, Z.; Zhang, Y.; Mensah, A.; He, H.; Wei, Q.; Lv, P. Robust integration of energy harvesting with daytime radiative cooling enables wearing thermal comfort self-powered electronic devices. *Nano Energy* **2023**, *116*, 108842. [CrossRef]
9. Wang, C.; He, X.; Zhu, G.; Li, X.; Zhu, X.; Chen, R.; Tian, S.; Li, X.; Zhu, J.; Shao, J.; et al. Extreme orientation of stereocomplexed poly (lactic acid) induced ultrafine electroactive nanofibers for respiratory healthcare and intelligent diagnosis. *ACS Sustain. Chem. Eng.* **2024**, *12*, 9290–9300. [CrossRef]
10. Li, Y.; Wang, D.; Xu, G.; Qiao, L.; Li, Y.; Gong, H.; Shi, L.; Li, D.; Gao, M.; Liu, G.; et al. ZIF-8/PI Nanofibrous Membranes With High-Temperature Resistance for Highly Efficient $PM_{0.3}$ Air Filtration and Oil-Water Separation. *Front. Chem.* **2021**, *9*, 810861. [CrossRef]
11. Singh, R.K.; Lye, S.W.; Miao, J. Holistic investigation of the electrospinning parameters for high percentage of β-phase in PVDF nanofibers. *Polymer* **2021**, *214*, 123366. [CrossRef]
12. Chen, J.; Ayranci, C.; Tang, T. Piezoelectric performance of electrospun PVDF and PVDF composite fibers: A review and machine learning-based analysis. *Mater. Today Chem.* **2023**, *30*, 101571. [CrossRef]
13. Dai, G.; Chu, J.C.H.; Chan, C.K.W.; Choi, C.H.J.; Ng, D.K.P. Reactive oxygen species-responsive polydopamine nanoparticles for targeted and synergistic chemo and photodynamic anticancer therapy. *Nanoscale* **2021**, *13*, 15899–15915. [CrossRef]

14. Zhang, Y.; Zeng, Z.; Ma, X.Y.D.; Zhao, C.; Ang, J.M.; Ng, B.F.; Wan, M.P.; Wong, S.-C.; Wang, Z.; Lu, X. Mussel-Inspired approach to cross-linked functional 3D nanofibrous aerogels for energy-efficient filtration of ultrafine airborne particles. *Appl. Surf. Sci.* **2019**, *479*, 700–708. [CrossRef]
15. Ma, F.; Zhang, N.; Wei, X.; Yang, J.; Wang, Y.; Zhou, Z. Blend-electrospun poly (vinylidene fluoride)/polydopamine membranes: Self-polymerization of dopamine and the excellent adsorption/separation abilities. *J. Mater. Chem. A* **2017**, *5*, 14430–14443. [CrossRef]
16. Li, Y.; Yuan, D.; Geng, Q.; Yang, X.; Wu, H.; Xie, Y.; Wang, L.; Ning, X.; Ming, J. MOF-Embedded bifunctional composite nanofiber membranes with a tunable hierarchical structure for high-efficiency $PM_{0.3}$ purification and oil/water separation. *ACS Appl. Mater. Interfaces* **2021**, *13*, 39831–39843. [CrossRef] [PubMed]
17. Liu, Y.; Liu, S.; Xie, X.; Li, Z.; Wang, P.; Lu, B.; Liang, S.; Tang, Y.; Zhou, J. A functionalized separator enables dendrite-free Zn anode via metal-polydopamine coordination chemistry. *InfoMat* **2022**, *5*, 12374. [CrossRef]
18. Wang, Z.; Sahadevan, R.; Crandall, C.; Menkhaus, T.J.; Fong, H. Hot-Pressed PAN/PVDF hybrid electrospun nanofiber membranes for ultrafiltration. *J. Membr. Sci.* **2020**, *611*, 118327. [CrossRef]
19. Yang, Y.; Huang, E.; Dansawad, P.; Li, Y.; Qing, Y.; Lv, C.; Cao, L.; You, S.; Li, Y.; Li, W. Superhydrophilic and underwater superoleophobic PVDF-PES nanofibrous membranes for highly efficient surfactant-stabilized oil-in-water emulsions separation. *J. Membr. Sci.* **2023**, *687*, 122044. [CrossRef]
20. Li, X.; Wang, C.; Huang, X.; Zhang, T.; Wang, X.; Min, M.; Wang, L.; Huang, H.; Hsiao, B.S. Anionic surfactant-triggered steiner geometrical poly (vinylidene fluoride) nanofiber/nanonet air filter for efficient particulate matter removal. *ACS Appl. Mater. Interfaces* **2018**, *10*, 42891–42904. [CrossRef]
21. Zhao, K.; Wei, S.; Cao, M.; Wang, M.; Li, P.; Li, H.; Zhang, X.; Zhang, Y.; Chen, Y. Dielectric polyimide composites with enhanced thermal conductivity and excellent electrical insulation properties by constructing 3D oriented heat transfer network. *Compos. Sci. Technol.* **2024**, *245*, 110323. [CrossRef]
22. Wu, X.; Wu, X.; Wang, T.; Zhao, L.; Truong, Y.B.; Ng, D.; Zheng, Y.; Xie, Z. Omniphobic surface modification of electrospun nanofiber membrane via vapor deposition for enhanced anti-wetting property in membrane distillation. *J. Membr. Sci.* **2020**, *606*, 118075. [CrossRef]
23. Su, C.; Zhang, L.; Zhang, Y.; Huang, X.; Ye, Y.; Xia, Y.; Gong, Z.; Qin, X.; Liu, Y.; Guo, S. P(VDF-TrFE)/$BaTiO_3$ nanofibrous membrane with enhanced piezoelectricity for high $PM_{0.3}$ filtration and reusable face masks. *ACS Appl. Mater. Interfaces* **2023**, *15*, 5845–5855. [CrossRef]
24. Wang, T.; Wang, P.; Pan, L.; He, Z.; Dai, L.; Wang, L.; Liu, S.; Jun, S.C.; Lu, B.; Liang, S.; et al. Stabling zinc metal anode with polydopamine regulation through dual effects of fast desolvation and ion confinement. *Adv. Energy Mater.* **2022**, *13*, 2203523. [CrossRef]
25. Wang, M.; Cheng, X.; Jiang, G.; Xie, J.; Cai, W.; Li, J.; Wang, Y. Preparation and pervaporation performance of PVA membrane with biomimetic modified silica nanoparticles as coating. *J. Membr. Sci.* **2022**, *653*, 120535. [CrossRef]
26. Zhang, M.; Tan, Z.; Zhang, Q.; Shen, Y.; Mao, X.; Wei, L.; Sun, R.; Zhou, F.; Liu, C. Flexible self-powered friction piezoelectric sensor based on structured PVDF-based composite nanofiber membranes. *ACS Appl. Mater. Interfaces* **2023**, *15*, 30849–30858. [CrossRef] [PubMed]
27. Wang, C.; Song, X.; Li, T.; Zhu, X.; Yang, S.; Zhu, J.; He, X.; Gao, J.; Xu, H. Biodegradable electroactive banofibrous air filters for long-term respiratory healthcare and self-powered monitoring. *ACS Appl. Mater. Interfaces* **2023**, *15*, 37580–37592. [CrossRef]
28. Deng, H.; Zhao, N.; You, J.; Pan, Z.; Xing, B.; Ye, Y.; Lai, B.; Wang, Y.; Lu, T.; Liu, X. Removal of bisphenol A through peroxymonosulfate activation with N-doped graphite carbon spheres coated cobalt nanoparticles catalyst: Synergy of nonradicals. *Chin. Chem. Lett.* **2024**, 110650, *in press*. [CrossRef]
29. Kim, S.; Lee, H. Piezoelectric ceramics with high d_{33} constants and their application to film speakers. *Materials* **2021**, *14*, 5795. [CrossRef]
30. Ding, S.; Cao, Y.; Huang, F.; Wang, Y.; Li, J.; Chen, S. Spontaneous polarization induced electrostatic charge in washable electret composite fabrics for reusable air-filtering application. *Compos. Sci. Technol.* **2022**, *217*, 109093. [CrossRef]
31. Chen, M.; Jiang, J.; Feng, S.; Low, Z.-X.; Zhong, Z.; Xing, W. Graphene oxide functionalized polyvinylidene fluoride nanofibrous membranes for efficient particulate matter removal. *J. Membr. Sci.* **2021**, *635*, 119463. [CrossRef]
32. Yang, T.; Zhu, X.; Zhang, Y.; Ke, L.; Zhu, J.; Huang, R.; Li, S.; Zhu, Y.; Zhang, S.; Zhong, G.-J.; et al. Nanopatterning of beaded poly (lactic acid) nanofibers for highly electroactive, breathable, UV-shielding and antibacterial protective membranes. *Int. J. Biol. Macromol.* **2024**, *260*, 129566. [CrossRef]
33. Wang, M.J.; Yang, J.; Peng, L.; Bai, Y.; Liu, Z.; Yang, X.; Lu, H.; Zhou, B.; Jiang, N.; He, G.; et al. Optimizing the size and electronic effects of core-shell heterostructures via well-constructed Ru clusters encapsulated in N-doped carbon layers. *Chin. Chem. Lett.* **2024**, 110573, *in press*. [CrossRef]

34. Liu, S.; Zhang, C.; Zhou, Y.; Zhang, F.; Duan, X.; Liu, Y.; Zhao, X.; Liu, J.; Shuai, X.; Wang, J.; et al. MRI-Visible mesoporous polydopamine nanoparticles with enhanced antioxidant capacity for osteoarthritis therapy. *Biomaterials* **2023**, *295*, 122030. [CrossRef]
35. Cheng, N.; Miao, D.; Wang, C.; Lin, Y.; Babar, A.A.; Wang, X.; Wang, Z.; Yu, J.; Ding, B. Nanosphere-Structured hierarchically porous PVDF-HFP fabric for passive daytime radiative cooling via one-step water vapor-induced phase separation. *Chem. Eng. J.* **2023**, *460*, 141581. [CrossRef]
36. Liu, H.; Zhang, S.; Liu, L.; Yu, J.; Ding, B. A fluffy dual-network structured nanofiber/net filter enables high-efficiency air fltration. *Adv. Funct. Mater.* **2019**, *29*, 1904108. [CrossRef]
37. Zhu, G.; Li, X.; Li, X.-P.; Wang, A.; Li, T.; Zhu, X.; Tang, D.; Zhu, J.; He, X.; Li, H.; et al. Nanopatterned electroactive polylactic acid nanofibrous MOFilters for efficient $PM_{0.3}$ filtration and bacterial inhibition. *ACS Appl. Mater. Interfaces* **2023**, *15*, 47145–47157. [CrossRef] [PubMed]
38. Zong, D.; Bai, W.; Geng, M.; Yin, X.; Wang, F.; Yu, J.; Zhang, S.; Ding, B. Direct synthesis of elastic and stretchable hierarchical structured fiber and graphene-based sponges for noise reduction. *ACS Nano* **2023**, *17*, 17576–17586. [CrossRef]
39. Peng, L.; Hung, C.-T.; Wang, S.; Zhang, X.; Zhu, X.; Zhao, Z.; Wang, C.; Tang, Y.; Li, W.; Zhao, D. Versatile nanoemulsion assembly approach to synthesize functional mesoporous carbon nanospheres with tunable pore sizes and architectures. *J. Am. Chem. Soc.* **2019**, *141*, 7073–7080. [CrossRef]
40. Liang, C.; Li, J.; Chen, Y.; Ke, L.; Zhu, J.; Zheng, L.; Li, X.-P.; Zhang, S.; Li, H.; Zhong, G.-J.; et al. Self-charging, breathable, and antibacterial poly (lactic acid) nanofibrous air filters by surface engineering of ultrasmall electroactive nanohybrids. *ACS Appl. Mater. Interfaces* **2023**, *15*, 57636–57648. [CrossRef]
41. Li, J.; Yin, J.; Wee, M.G.V.; Chinnappan, A.; Ramakrishna, S. A self-Powered piezoelectric nanofibrous membrane as wearable tactile sensor for human body motion monitoring and recognition. *Adv. Fiber Mater.* **2023**, *5*, 1417–1430. [CrossRef]
42. Zhu, Y.; Yan, J.; Liu, J.; Chen, H.; Gui, J.; Wu, C.; Zhu, X.; Yin, P.; Liu, M.; Zhang, Y.; et al. Multi-mimic activities of Co_3O_4 nanopolyhedrons and application in regulating the content of intracellular hydrogen peroxide/oxygen. *ACS Appl. Nano Mater.* **2022**, *5*, 15102–15114. [CrossRef]
43. Dong, W.; Zhao, Z.; Liu, F.; Li, P.; Wang, L.; Zhou, Y.; Shen, Y.; Lang, C.; Deng, B.; Li, H.; et al. PVDF nanofiber modified with ZnO nanowires/polydopamine for the treatment of sewage containing heavy metals, organic dyes, and bacteria. *ACS Appl. Mater. Interfaces* **2023**, *15*, 58994–59004. [CrossRef]
44. Zhi, Q.; Li, D.; Zhang, Z.; Fu, L.; Zhu, W. High-Content continuous carbon fiber reinforced multifunctional prepreg filaments suitable for direct 3D-printing. *Compos. Commun.* **2023**, *44*, 101726. [CrossRef]
45. Xue, M.; Qin, R.; Peng, C.; Xia, L.; Xu, Y.; Luo, W.; Chen, G.; Zeng, B.; Liu, X.; Dai, L. *o*-Vanillin based MOFs as phosphorus-free flame retardant for reinforced epoxy resin. *Compos. Commun.* **2024**, *46*, 101821. [CrossRef]
46. Si, Y.; Yang, J.; Wang, D.; Shi, S.; Zhi, C.; Huang, K.; Hu, J. Bioinspired hierarchical multi-protective membrane for extreme environments via co-electrospinning-electrospray strategy. *Small* **2023**, *20*, 2304705. [CrossRef]
47. Wang, H.; Wang, Z.; Shi, Y.; Liu, M.; Yao, A.; Feng, Y.; Fu, L.; Lv, Y.; Yang, F.; Yu, B. Supramolecular engineered ultrathin MXene towards fire safe polylactic acid composites. *Compos. Commun.* **2023**, *37*, 101405. [CrossRef]
48. Peng, Z.; Shi, J.; Xiao, X.; Hong, Y.; Li, X.; Zhang, W.; Cheng, Y.; Wang, Z.; Li, W.J.; Chen, J.; et al. Self-charging electrostatic face masks leveraging triboelectrification for prolonged air filtration. *Nat. Commun.* **2022**, *13*, 7835. [CrossRef]
49. Al-Attabi, R.; She, F.; Zhao, S.; Dumée, L.F.; Schütz, J.A.; Xing, W.; Zhong, Z.; Kong, L. Durable and comfortable electrospun nanofiber membranes for face mask applications. *Sep. Purif. Technol.* **2023**, *322*, 124370. [CrossRef]
50. Wang, H.; Bao, Y.; Yang, X.; Lan, X.; Guo, J.; Pan, Y.; Huang, W.; Tang, L.; Luo, Z.; Zhou, B.; et al. Study on filtration performance of PVDF/PUL composite air filtration membrane based on far-field electrospinning. *Polymers* **2022**, *14*, 3294. [CrossRef]
51. Bui, T.T.; Shin, M.K.; Jee, S.Y.; Long, D.X.; Hong, J.; Kim, M.-G. Ferroelectric PVDF nanofiber membrane for high-efficiency $PM_{0.3}$ air filtration with low air flow resistance. *Colloids Surf. A* **2022**, *640*, 128418. [CrossRef] [PubMed]
52. Zheng, J.; Zhou, X.; Wang, B.; Dai, F.; Liu, J. Modified PVDF/PMMA/SiO_2 composite nanofibrous membrane in airborne filtration: Transparency, mechanical properties and filtration performance. *J. Environ. Chem. Eng.* **2024**, *12*, 114109. [CrossRef]
53. Moon, J.; Bui, T.T.; Jang, S.; Ji, S.; Park, J.T.; Kim, M.-G. A highly efficient nanofibrous air filter membrane fabricated using electrospun amphiphilic PVDF-g-POEM double comb copolymer. *Sep. Purif. Technol.* **2021**, *279*, 119625. [CrossRef] [PubMed]
54. Gao, H.; Li, Z.-J.; Xu, X.-F.; Wang, N.; Yang, M.-Y.; Long, Y.-Z.; Zhang, H.-D. Electrospinning dual energy-saving design of PVDF-HFP nanofiber films for passive radiant cooling and air filtration. *AIP Adv.* **2024**, *14*, 015349. [CrossRef]
55. Wu, Y.; Li, X.; Zhong, Q.; Wang, F.; Yang, B. Preparation and filtration performance of antibacterial PVDF/SiO_2/Ag composite nanofiber membrane. *J. Build. Eng.* **2023**, *74*, 106864. [CrossRef]
56. Geng, Q.; Dong, S.; Li, Y.; Wu, H.; Yang, X.; Ning, X.; Yuan, D. High-performance photoinduced antimicrobial membrane toward efficient $PM_{2.5\text{-}0.3}$ capture and oil-water separation. *Sep. Purif. Technol.* **2022**, *284*, 120267. [CrossRef]

57. Toptaş, A.; Çalışır, M.D.; Kılıç, A. Production of ultrafine PVDF nanofiber/nanonet-based air filters via the electroblowing technique by employing PEG as a pore-forming agent. *ACS Omega* **2023**, *8*, 38557–38565. [CrossRef]
58. Liu, F.; Li, M.; Li, F.; Weng, K.; Qi, K.; Liu, C.; Ni, Q.; Tao, X.; Zhang, J.; Shao, W.; et al. Preparation and properties of PVDF/Fe_3O_4 nanofibers with magnetic and electret effects and their application in air filtration. *Macromol. Mater. Eng.* **2020**, *305*, 1900856. [CrossRef]

polymers

MDPI

Article

Smart Bacterial Cellulose–Methylacrylated Chitosan Composite Hydrogel: Multifunctional Characterization for Real-Time pH Monitoring

Zixian Bao [1], Jiezheng Liu [1,2], Yujia Bi [1] and Guang Zhao [1,*]

[1] State Key Laboratory of Microbial Technology, Institute of Microbial Technology, Shandong University, Qingdao 266237, China; baozixian@sdu.edu.cn (Z.B.)
[2] CAS Key Laboratory of Biobased Materials, Qingdao Institute of Bioenergy and Bioprocess Technology, Chinese Academy of Sciences, Qingdao 266101, China
* Correspondence: zhaoguang@sdu.edu.cn

Abstract: pH is a critical parameter that influences biochemical and environmental processes. Real-time and accurate pH detection is essential for monitoring health and the environment. Herein, a bacterial cellulose and methylacrylated chitosan (BC-MACS) composite hydrogel was prepared to achieve rapid pH detection. The integration of MACS reduced the crystallinity of pristine BC, with no adverse effects on thermal stability. SEM images validated the fibrous nature of the BC-MACS composite, indicating that MACS was successfully infiltrated into the pores of BC. By incorporating MACS into the BC matrix, the exceptional biocompatibility of BC was maintained, while simultaneously augmenting its mechanical properties. Due to the excellent swelling ability of MACS, the fabricated BC-MACS hydrogel exhibited superior swelling behavior compared to the BC hydrogel, which facilitated the absorption of the solution under test. A BC-MACS pH sensor was fabricated by introducing the pH indicator solution, and the color variation across the pH range (2–12) demonstrated a clear response to pH changes. Therefore, the BC-MACS pH sensor holds potential for use as a visual indicator in a diverse range of applications, especially for health and environmental monitoring.

Keywords: bacterial cellulose; methylacrylated chitosan; pH sensor

1. Introduction

Biochemical and environmental processes are greatly influenced by pH [1]. The measurement of pH has significant importance in industrial processes, including in chemistry, medicine, biology, and environmental monitoring [2]. To achieve real-time and accurate pH detection, various pH sensors have been developed and are used in a variety of fields, including health monitoring, water quality detection, food packaging, and other processes [1,3–7]. Normally, these pH sensors are composed of a solid support and a colorimetric indicator. The solid support is associated with the sensitivity, response time, reversibility, and reproducibility of the pH sensor [8]. Different natural and synthetic polymers have been used to immobilize a colorimetric indicator to fabricate pH sensors, such as polyethylene [9], chitosan [10,11], starch–polyvinyl alcohol [12], chitosan–polyvinyl alcohol [13], methylcellulose [14], and nanocellulose [8].

Bacterial cellulose (BC), a biopolymer obtained from Gram-negative acetic acid bacteria, possesses satisfactory properties, including high purity, non-toxicity, low immunogenicity, an ultrafine network architecture, high specific surface area, and excellent mechanical

strength [15,16]. Based on these properties, BC has been developed to fabricate pH sensors for fish freshness and sweat pH detection [8,17–19]. These sensors are prepared by immersing BC films in the colorimetric indicator solution and are subsequently air-dried. Despite the color of these sensors changing with pH, the fibrous structure of pristine BC is reported to collapse upon drying, which can influence the re-swelling ability and may cause the color change distortion [17,20]. Therefore, the re-swelling ability is crucial for the application of a BC-based pH sensor, especially in the fields of health or seawater monitoring. Carboxymethyl cellulose has been incorporated into BC to enhance the re-swelling ability using the undisturbed method, fabricating a colorimetric sensor for sweat pH detection [17]. However, other methods have rarely been reported.

Methylacrylated chitosan (MACS) represents a class of chitosan derivatives synthesized through methacrylate grafting to enhance aqueous solubility and confer the ultraviolet (UV)-initiated cross-linking capability [21]. This modification preserves the inherent biocompatibility of chitosan while introducing advantageous characteristics such as three-dimensional (3D) printability, tunable mechanical properties, and remarkable swelling behavior [21,22]. Therefore, MACS has been proposed to be applied as a drug delivery platform, skin substitute, and tissue-engineering scaffold [21,23–26]. MACS displays an intriguing swelling behavior, and can rapidly absorb an enormous amount of water (with a swelling ratio higher than 100%) [21,27], which is a gratifying property to incorporate with BC to enhance the water absorption ability.

Herein, MACS was incorporated into BC based on simple immersion and UV irradiation to prepare the BC-MACS hydrogel. The proposed method is straightforward, highly efficient, and necessitates neither special chemicals nor prior modification of the BC. The crystalline structure and surface morphology were characterized using X-ray diffraction (XRD) analysis and scanning electron microscopy (SEM), respectively. The thermal stability, swelling behavior, and mechanical properties were also evaluated. The colorimetric indicator was incorporated into the BC-MACS hydrogel to fabricate the BC-MACS pH sensor, and the color differentiation performance was determined.

2. Materials and Methods

2.1. Materials

Chitosan (viscosity 72 cps, degree of deacetylation, DD = 90%) was purchased from Laizhou Haili Biological Product Co., Ltd. (Laizhou, China). pH indicator solution was purchased from Beijing Gersion Bio-Technology Co., Ltd. (Beijing, China). Cetyltrimethyl ammonium bromide (CTAB) was purchased from Sigma-Aldrich (St. Louis, MO, USA). High-glucose Dulbecco's modified Eagle's medium (DMEM) was obtained from Hyclone (Logan, UT, USA). A CCK-8 kit was purchased from Macklin Biochemical Co., Ltd. (Shanghai, China). All other reagents were of analytical grade and used as received.

2.2. Synthesis of MACS and BC

2.2.1. Synthesis of MACS

MACS was synthesized by reacting chitosan with methacrylic anhydride (MA) [26]. In brief, chitosan (1.5 wt%) was dissolved overnight in acetic acid solution (4 wt%). Then, MA at a molar ratio of 100:1 (with respect to chitosan) was added slowly to the chitosan acetic acid solution, which was stirred at 40 °C, 60 rpm, for 12 h, under dark conditions. The resulting production was a milky suspension that was dialyzed (MWCO 8–14 kDa dialysis bag) using deionized water for one week and lyophilized.

2.2.2. Synthesis of BC Pellicles

The BC was produced by *Komagataeibacter sucrofermentans* (*K. sucrofermentans*) fermentation [16]. *K. sucrofermentans* was inoculated in 7% (*v*/*v*) H-S basic medium (containing 25 g L^{-1} of glucose, 5 g L^{-1} of yeast extract, 5 g L^{-1} of peptone, 1.2 g L^{-1} of citric acid monohydrate, and 2.7 g L^{-1} of Na_2HPO_4) and cultured at 30 °C for 5 days. The obtained BC pellicles were treated with NaOH solution overnight at 60 °C, and subsequently washed with deionized water. BC pellicles were stored at 4 °C until use.

2.3. Preparation of MACS and BC-MACS Hydrogels

MACS was dissolved in deionized water to obtain 20 mg mL^{-1} of homogeneous solution. Subsequently, Irgacure 2959 was added to MACS solution at a final concentration of 0.5 mg mL^{-1}. Afterward, the BC pellicles were soaked in the MACS solution for 15 min. The MACS and BC-MACS solutions were exposed to UV light (365 nm) with a light intensity of 5 W cm^{-2} for 15 min to prepare the MACS and the BC-MACS hydrogels [22,28].

2.4. Characterization of BC-MACS Hydrogel

2.4.1. FTIR Analysis

The chitosan, MACS (before cross-linking), and air-dried BC-MACS hydrogels (after cross-linking) were characterized using FTIR spectroscopy. The infrared spectra were recorded on an FTIR spectrometer (Nicolet 6700, Thermo Fisher, Waltham, MA, USA) with the frequency range from 4000 to 400 cm^{-1} at a data acquisition rate of 2 cm^{-1} per point [29].

2.4.2. XRD Analysis

The air-dried BC-MACS hydrogel was analyzed with an X-ray diffractometer (D8 Advance, Bruker, Berlin, Germany), operated at 20 kV (CuKα target) with a scanning range of 5–50° and a diffraction rate of 10° min^{-1}. The background noise was subtracted following the collection of XRD data [30].

2.4.3. Thermogravimetric Analysis (TGA)

TGA measurements were performed using a thermogravimetric analyzer (TGA2, Mettler Toledo, Greifensee, Switzerland) with a heating rate of 20 °C min^{-1}, over a range of 30–800 °C, and under a nitrogen atmosphere (20 mL min^{-1}) [26].

2.4.4. SEM

The pristine BC, MACS, and BC-MACS hydrogels were all air-dried and sputter-coated with gold. The surface and cross-section structures were examined using a field emission scanning electron microscope (Quanta 250 FEG, FEI, Hillsboro, OR, USA).

2.4.5. Cytocompatibility

The cytotoxicity of different hydrogels was assessed using a CCK-8 assay against L929 cells. In brief, the MACS, BC, and BC-MACS hydrogels were cultured in the DMEM medium supplemented with 10% (*v*/*v*) FBS (Gibco, Invitrogen, Carlsbad, CA, USA), 100 IU mL^{-1} of penicillin, and 100 μg mL^{-1} of streptomycin (Sigma-Aldrich, Gillingham, UK) at 37 °C for 24 h. The DMEM medium of the overnight cultured L929 cells was replaced with 100 μL of hydrogel extract medium. After 24 h of incubation, CCK-8 solution (10 μL) was added to each well and continuously incubated for 4 h. The absorbance at 450 nm was recorded using a microplate reader. The percentage of viability was calculated as a percentage of the untreated control cells.

2.5. Swelling Behavior

The prepared MACS, BC, and BC-MACS hydrogels were weighed (W_0) and then immersed in deionized water at room temperature for 24 h. The weight (W_t) of the swollen hydrogels was determined after removing the excess water. The swelling ratio of the hydrogels was calculated as follows:

$$\text{Swelling ratio } (\%) = \frac{W_t - W_0}{W_0} \times 100 \quad (1)$$

2.6. Mechanical Properties

The mechanical properties of BC-MACS hydrogels were performed using an Instron 5543 universal testing machine (Instron Corp., Canton, OH, USA). All the samples were air-dried and cut into strips (0.5 × 5 cm^2). The breaking strength of the samples was conducted with a speed of 30 mm min^{-1} at room temperature. Tensile strength refers to the average of the ultimate stress at failure [30].

2.7. Preparation of BC-MACS pH Sensor

CTAB (0.1 wt%) was added to the pH indicator solution (containing methyl red, methyl yellow, thymol blue, bromothymol blue, and phenolphthalein). Subsequently, the BC-MACS hydrogel was immersed in this pH indicator solution for 15 min, and rinsed with deionized water.

The performance of the BC-MACS pH sensor was evaluated by adding different pH buffers (pH 2~11) on the sensor, and the color change was measured in terms of hue angle value using a portable spectrophotometer (Datacolor Check3, Datacolor, Lawrenceville, NJ, USA) [17].

2.8. Statistical Analysis

Each experiment was performed independently in triplicate at least. Results were given as mean ± standard deviation (SD). A one-way analysis of variance with Dunnett's post hoc test was performed. Statistical significance was set as $p < 0.05$.

3. Results and Discussion

3.1. Preparation and Characterization of BC-MACS Hydrogel

In this study, MACS was incorporated into the BC network to fabricate the BC-MACS hydrogel based on UV cross-linking (Scheme 1). Chitosan has abundant amine groups that are available for modification by MA. The result of the FTIR analysis verified the successful synthesis of MACS (Figure 1a). The characterized peaks at 1701 cm^{-1} and 1652 cm^{-1} in the spectrum of MACS were associated with a C=O group and C=C group, respectively, belonging to MA [29]. After cross-linking, the disappearance of the C=C group peak centered at 845 cm^{-1} indicated that MACS still owned high reactivity when incorporated into the BC network (Figure S1) [27]. The result suggested that the BC-MACS semi-interpenetrating network was formed after UV cross-linking. XRD analysis was performed to investigate the crystalline structure of the BC-MACS. As shown in Figure 1b, pure air-dried MACS hydrogel shows an amorphous state, characterized by the presence of a broad peak in the 2θ scattering angle range from 17° to 25°. The pristine BC and BC-MACS hydrogel exhibits two characteristic absorption peaks at 14.5° and 22.6°, which were assigned to the (110) and (200) planes of the cellulose form I-β crystal [16,31,32]. However, the intensity of these two diffraction peaks in the BC-MACS group was slightly lower than that of the BC group, indicating that the crystallinity of BC was slightly decreased after the integration of MACS [33].

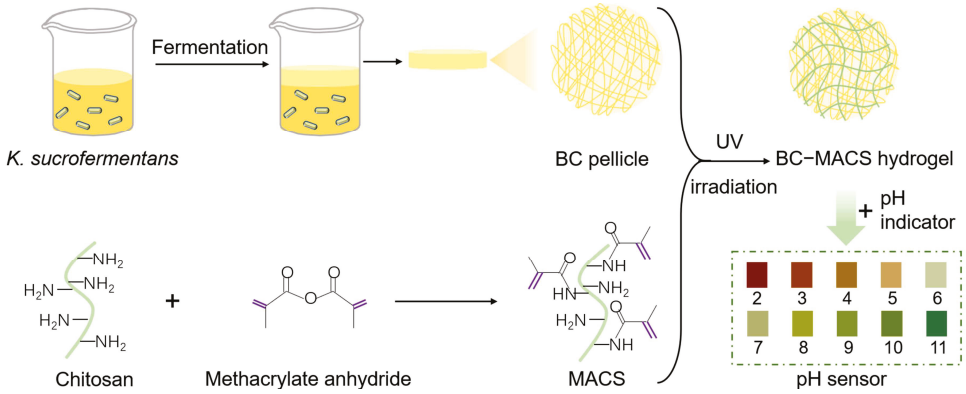

Scheme 1. Schematic representation of the preparation process of BC-MACS pH sensor and its application.

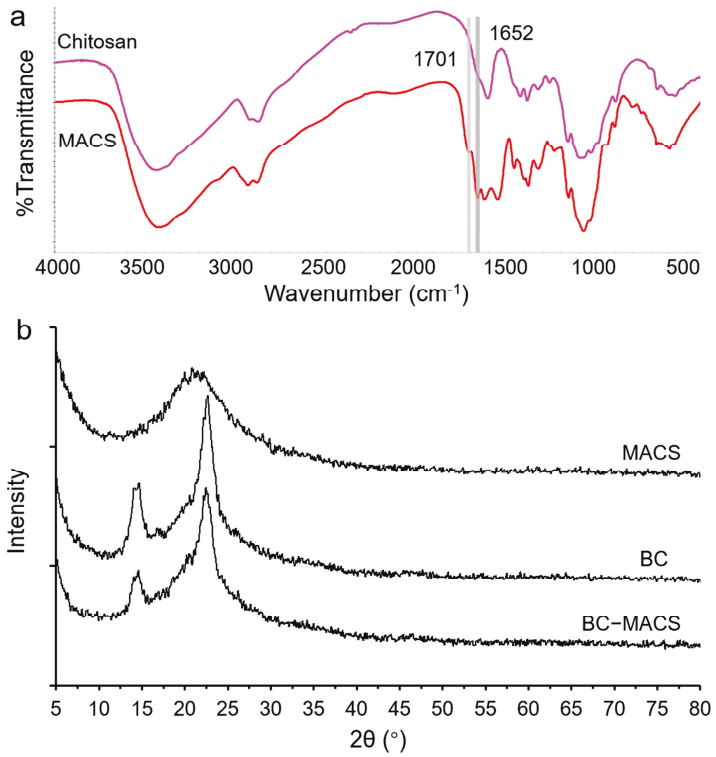

Figure 1. Characterization of MACS and BC-MACS hydrogels: (**a**) FTIR spectra of chitosan and MACS; (**b**) XRD patterns of MACS, BC, and BC-MACS.

The thermal stability of the BC-MACS hydrogel was evaluated by TGA (Figure 2). Pure MACS exhibited a weight loss of 47% in the temperature range of 244–408 °C. The pristine BC exhibited a more substantial decomposition profile, with a 66% mass loss occurring between 246 and 397 °C, indicative of significant thermal decomposition. This behavior is attributed to the breakdown of the cellulose backbone structure. For the BC-MACS, the degradation (62% weight loss) occurred in the temperature range of 214–412 °C, suggesting a broader decomposition temperature range compared to individual components. To further characterize thermal properties, differential thermogravimetry (DTG) curves were analyzed (Figure 2b). The maximum thermal decomposition temperature of pure MACS was 289 °C, while pristine BC exhibited a higher peak temperature of 341 °C. This enhanced thermal stability in BC is associated with its crystalline structure, as confirmed by the X-ray diffraction (XRD) patterns in Figure 1. Conversely, MACS forms an amorphous matrix, which correlates with its lower decomposition temperature. The thermal decomposition

temperature of BC-MACS was 335 °C, which had no significant difference from that of pristine BC. The result indicated that the crystalline BC component dominated the thermal behavior in the composite system.

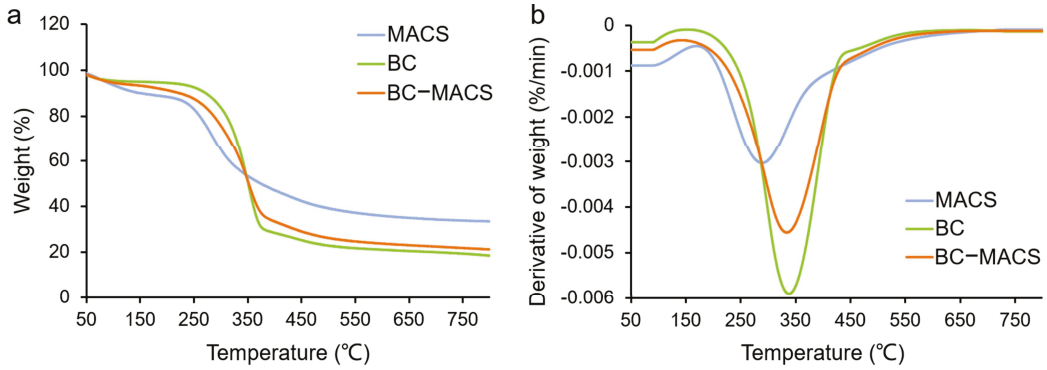

Figure 2. Thermal stability of MACS, BC, and BC-MACS: (**a**) TGA profiles; (**b**) DTG curves.

The surface and cross-section morphology of the BC-MACS were imaged by SEM (Figure 3). The pure MACS hydrogel (after UV cross-linking) shows a smooth surface structure (Figure 3a). Both BC and BC-MACS exhibit fibrous networks. For the BC samples, the fibers are packed and tiny pores can be observed in the margin of the stacked fibers (Figure 3b). For the BC-MACS samples, only a few tiny pores can be observed (Figure 3c), which might be due to the permeation of the incorporated MACS solution into these pores. MACS was subsequently cross-linked in situ by UV irradiation to form the hydrogel, leading to the disappearance of pores. However, compared to the BC samples, the stacked form of fibers, fiber size, and nanofibrous structure in BC-MACS were not influenced by the incorporation of MACS. Compared to the surface morphology, the internal morphology shows no significant difference between the BC and BC-MACS groups (Figure 3d,e), indicating that the incorporated MACS was mainly deposited on the surface and only a small proportion penetrated into the interior.

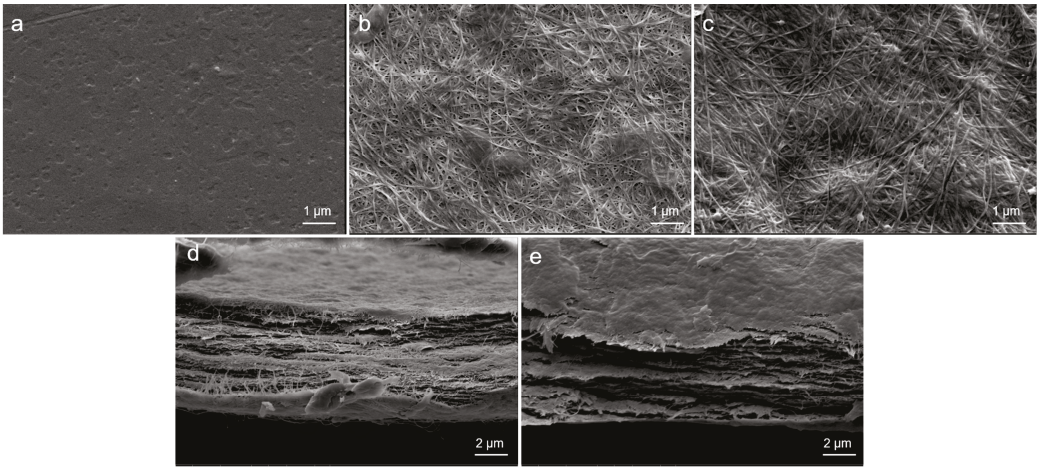

Figure 3. SEM images of different air-dried hydrogels. (**a**–**c**) Surface morphology of MACS (**a**), BC (**b**), and BC-MACS (**c**). The scale bar corresponds to 1 μm. (**d**,**e**) Cross-section morphology of BC (**d**) and BC-MACS (**e**). The scale bar corresponds to 2 μm.

A CCK-8 assay was used to evaluate the cytotoxicity of the BC and MACS hydrogels (Figure 4). The relative cell viability of the MACS, BC, and BC-MACS hydrogels was all higher than 90%, indicating their excellent biocompatibility. All of the groups showed no significant difference in their cell viability, demonstrating that the incorporation of MACS could not alter the biocompatibility of pristine BC.

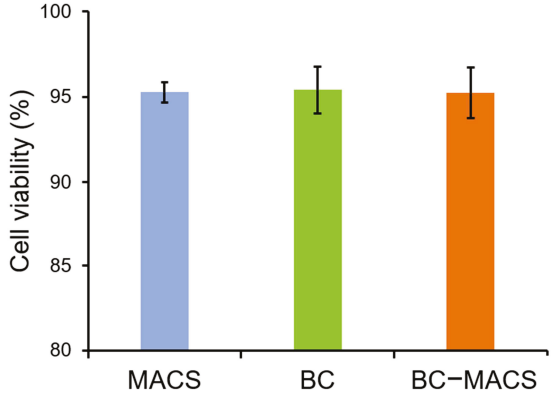

Figure 4. The cytotoxicity of MACS, BC, and BC-MACS hydrogels.

3.2. Swelling Behavior

In order to incorporate the pH indicator, the fabricated hydrogel should rapidly absorb large amounts of solution. The swelling behavior of the MACS hydrogel was rapid and achieved the swelling balance within 1 h (Figure 5a). The swelling ratio almost reached 216% for the MACS hydrogel. However, the swelling ratio of the BC hydrogel was much lower than that of the MACS hydrogel, and the maximum swelling ratio was 36.4 ± 4.0%. The swelling behavior of the BC-MACS hydrogel was intervening between the MACS and BC hydrogels, and the swelling ratio could reach around 64% within 1 h. Due to the incorporation of MACS, the swelling behavior was enhanced 2-fold, facilitating the absorption of the pH indicator into the BC-MACS hydrogels. For air-dried hydrogels, the change trend of the swelling ratio among different groups (MACS, BC, and BC-MACS) was similar to that of the corresponding wet hydrogels (Figure 5b). Air-dried MACS hydrogel could absorb more solution compared to the wet hydrogel, and the final swelling ratio was 601.9 ± 6.7%. In addition, the swelling behavior of MACS occurred rapidly, and the swelling balance was achieved within 0.5 h. However, the air-dried BC hydrogel exhibited a lower swelling ratio (1.3 ± 0.6%) in comparison to wet hydrogel within 0.5 h, although the final swelling ratio displayed no significant difference between the air-dried and wet BC hydrogels. For the air-dried BC-MACS hydrogel, swelling balance was also reached within 0.5 h, and the swelling ratio (42.9 ± 0.3%) was considerably higher than that of the air-dried BC hydrogel. Therefore, the incorporation of MACS enhanced the swelling property of the BC hydrogel. The rapid and massive absorption of solution was crucial for the BC-MACS hydrogel to realize its function, especially as a pH sensor.

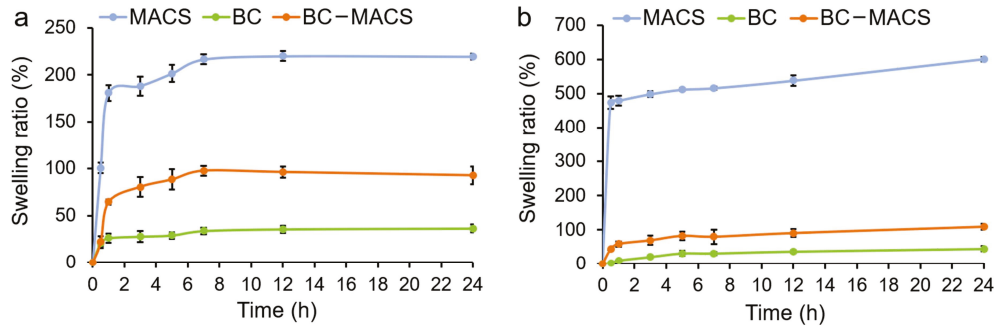

Figure 5. Swelling ratios of MACS, BC, and BC-MACS hydrogels: (**a**) wet hydrogels; (**b**) air-dried hydrogels.

3.3. Mechanical Properties

The tensile testing was performed to evaluate the mechanical performance of the air-dried BC-MACS (Figure 6a). The integration of MACS has no significant influence

on the mechanical properties of BC. The fracture stress was 18.40 ± 1.20 MPa for BC, consistent with previously reported values for BC [34]. In contrast, MACS demonstrated a lower fracture stress of 2.65 ± 0.15 MPa, which can be attributed to its amorphous structural configuration (as evidenced by the XRD analysis in Figure 1b) compared to the unique 3D nanofibrillar network of BC [34]. The integration of MACS with BC was fabricated by a facile matrix immersion methodology coupled with UV cross-linking. This approach preserved the mechanical integrity of BC, as evidenced by the comparable fracture stress between the BC hydrogel (18.40 ± 1.20 MPa) and BC-MACS hydrogel (16.71 ± 1.05 MPa). These findings corroborate previous research demonstrating that non-cross-linked collagen-BC blends exhibit negligible changes in mechanical performance [34]. The fracture strain of BC-MACS (1.07 ± 0.25%) was slightly enhanced compared to BC (0.87 ± 0.11%) (Figure 6b). The Young's modulus of BC (6.57 ± 1.19 MPa) was increased to 10.57 ± 2.07 MPa (BC-MACS) when incorporated with MACS, indicating an enhancement in stiffness in BC-MACS.

a

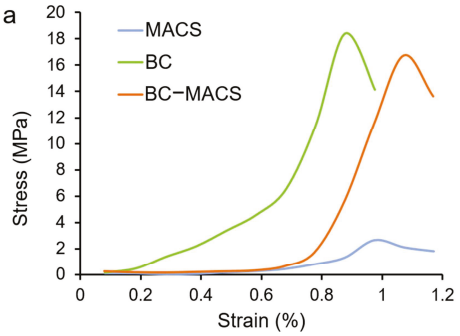

b

Sample	Stress (MPa)	Strain (%)	Young's modulus (MPa)
MACS	2.65±0.15	0.97±0.10	1.95±1.10
BC	18.40±1.20	0.87±0.11	6.57±1.19
BC−MACS	16.71±1.05	1.07±0.25	10.57±2.07

Figure 6. Mechanical properties of different hydrogels: (**a**) stress–strain curves; (**b**) profiles of fracture stress, strain, and Young's modulus of different hydrogels.

3.4. BC-MACS-Based Colorimetric pH Sensor

CTAB was introduced in the BC-MACS pH sensor to enhance the stability of the pH indicator inside the BC-MACS hydrogel via the electrostatic interactions between the positively charged CTAB and negatively charged indicator dyes [17,35,36]. The BC-MACS hydrogel exhibited a fast response to different pH buffers with the color change. The color change occurred immediately when adding the pH buffer (<3 s) and could be differentiated by the naked eye. The color of the pH indicator appeared red at a low pH (pH 2), then turned to orange and green when the pH was 3 to 11, and turned to blue at pH 12 (Figure 7). The hue angle of the calibration plot displayed a good correlation coefficient of the determination (R^2 = 0.9686) (Figure S2a).

BC membranes have been adapted into film or paper-based sticker sensors for food freshness detection [8,18,19], where high water absorptivity is not a critical requirement. The BC-MACS hydrogels developed in this study exhibit exceptional toughness and water adsorption capacity, rendering them highly stable in environments with substantial moisture (such as sweat, urine, and tears) and well-suited for use as wearable biosensors, outperforming traditional paper test strips in terms of conformability. Moreover, the BC-MACS hydrogel undergoes a noticeable color change with just a minute sample volume of 10 µL, significantly less than the 50 µL required by a previously reported textile-based pH sensor [36]. Additionally, the BC-MACS hydrogel boasts a broader range of detection accuracy (pH 2–11) compared to the BC/carboxymethyl cellulose pH sensor (pH 4–9) [17] or the fluorescent-probe-incorporated BC sensor (pH 3–7.5) [37], thereby expanding its potential applications across diverse fields.

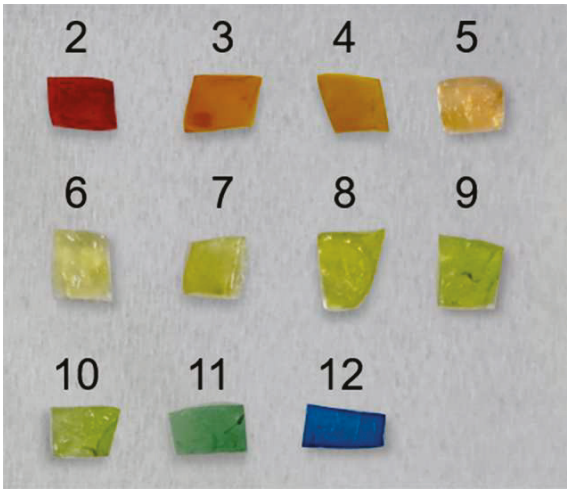

Figure 7. Color changes in BC-MACS pH sensor tested with different pH buffers.

A BC pH sensor was also prepared with the same method as the BC-MACS pH sensor, in which deionized water was used instead of MACS solution. However, the color difference in the BC pH sensor was not distinguishable. The color was similar in the pH range of 3–10 (Figure S2b) when observed by the naked eye. The reason might be due to the relatively poor swelling behavior of BC, in which the small amount of the fluid sample could not absolutely interact with the pH indicator to induce the color change [17]. A MACS pH sensor was also prepared. Although the color change in the MACS pH sensor was similar to the BC-MACS pH sensor, the poor mechanical strength led to it easily breaking. Based on the above results, BC-MACS could be used as an excellent pH sensor in a wide range of applications.

4. Conclusions

This study introduced a novel BC-MACS hydrogel created by integrating MACS into the BC network through UV cross-linking. XRD analysis revealed a minor crystallinity reduction upon MACS incorporation, with no adverse effects on thermal stability. SEM imaging confirmed the fibrous BC-MACS structure with MACS permeation into the BC pores. The integration of MACS into the BC matrix preserved the exceptional biocompatibility of BC while enhancing its swelling behavior and mechanical properties, especially stiffness. Notably, the BC-MACS hydrogel exhibited rapid swelling kinetics, making it essential for pH sensor applications. The fabricated BC-MACS pH sensor, stabilized by CTAB, demonstrated swift responsiveness to various pH buffers (ranging from pH 2 to 12) with distinct color changes. Therefore, the BC-MACS hydrogel holds promise as a versatile pH sensor for real-time monitoring in diverse applications such as biomedical devices (e.g., wound dressings) and environmental pollution detection systems. Its biocompatibility and mechanical durability further broaden its potential use in wearable biosensors or implantable diagnostic tools.

Supplementary Materials: The following supporting information can be downloaded at https://www.mdpi.com/article/10.3390/polym17070914/s1, Figure S1: FTIR spectra of BC, MACS, and BC-MACS hydrogels (after cross-linking); Figure S2: A calibration plot of the BC-MACS pH sensor over a pH range of 3–10 (a) and color changes in the BC pH sensor tested with different pH buffers (b).

Author Contributions: Conceptualization, Z.B. and G.Z.; methodology, Z.B., J.L. and Y.B.; writing—original draft preparation, Z.B.; writing—review and editing, Z.B. and G.Z. All authors have read and agreed to the published version of the manuscript.

Funding: This research was funded by the Natural Science Foundation of Qingdao (23-2-1-170-zyyd-jch), the Shandong Provincial Natural Science Foundation (ZR2024ME226), the Taishan Scholars Program (tstp20231208), the SKLMT Frontiers and Challenges Project (SKLMTFCP-2023-03), and the Young Scholars Program of Shandong University (Z.B.).

Institutional Review Board Statement: Not applicable.

Data Availability Statement: The original contributions presented in this study are included in the article/Supplementary Materials. Further inquiries can be directed to the corresponding author.

Conflicts of Interest: The authors declare no conflicts of interest.

References

1. Avolio, R.; Grozdanov, A.; Avella, M.; Barton, J.; Cocca, M.; De Falco, F.; Dimitrov, A.T.; Errico, M.E.; Fanjul-Bolado, P.; Gentile, G.; et al. Review of pH sensing materials from macro- to nano-scale: Recent developments and examples of seawater applications. *Crit. Rev. Environ. Sci. Technol.* **2022**, *52*, 979–1021.
2. Pan, X.; Li, J.; Ma, N.; Ma, X.; Gao, M. Bacterial cellulose hydrogel for sensors. *Chem. Eng. J.* **2023**, *461*, 142062.
3. Han, F.; Wang, T.; Liu, G.; Liu, H.; Xie, X.; Wei, Z.; Li, J.; Jiang, C.; He, Y.; Xu, F. Materials with tunable optical properties for wearable epidermal sensing in health monitoring. *Adv. Mater.* **2022**, *34*, 2109055.
4. Zhao, H.; Su, R.; Teng, L.; Tian, Q.; Han, F.; Li, H.; Cao, Z.; Xie, R.; Li, G.; Liu, X.; et al. Recent advances in flexible and wearable sensors for monitoring chemical molecules. *Nanoscale* **2022**, *14*, 1653–1669. [PubMed]
5. Vivaldi, F.; Santalucia, D.; Poma, N.; Bonini, A.; Salvo, P.; Del Noce, L.; Melai, B.; Kirchhain, A.; Kolivoška, V.; Sokolova, R.; et al. A voltammetric pH sensor for food and biological matrices. *Sens. Actuators B Chem.* **2020**, *322*, 128650.
6. Waimin, J.; Gopalakrishnan, S.; Heredia-Rivera, U.; Kerr, N.A.; Nejati, S.; Gallina, N.L.F.; Bhunia, A.K.; Rahimi, R. Low-Cost nonreversible electronic-free wireless pH sensor for spoilage detection in packaged meat products. *ACS Appl. Mater. Interfaces* **2022**, *14*, 45752–45764.
7. Briggs, E.M.; Sandoval, S.; Erten, A.; Takeshita, Y.; Kummel, A.C.; Martz, T.R. Solid state sensor for simultaneous measurement of total alkalinity and pH of seawater. *ACS Sens.* **2017**, *2*, 1302–1309. [PubMed]
8. Pourjavaher, S.; Almasi, H.; Meshkini, S.; Pirsa, S.; Parandi, E. Development of a colorimetric pH indicator based on bacterial cellulose nanofibers and red cabbage (*Brassica oleraceae*) extract. *Carbohydr. Polym.* **2017**, *156*, 193–201.
9. Wells, N.; Yusufu, D.; Mills, A. Colourimetric plastic film indicator for the detection of the volatile basic nitrogen compounds associated with fish spoilage. *Talanta* **2019**, *194*, 830–836.
10. Yoshida, C.M.; Maciel, V.B.V.; Mendonça, M.E.D.; Franco, T.T. Chitosan biobased and intelligent films: Monitoring pH variations. *LWT-Food Sci. Technol.* **2014**, *55*, 83–89.
11. Zhang, X.; Lu, S.; Chen, X.J.S.; Chemical, A.B. A visual pH sensing film using natural dyes from Bauhinia blakeana Dunn. *Sens. Actuators B Chem.* **2014**, *198*, 268–273.
12. Zhai, X.; Shi, J.; Zou, X.; Wang, S.; Jiang, C.; Zhang, J.; Huang, X.; Zhang, W.; Holmes, M. Novel colorimetric films based on starch/polyvinyl alcohol incorporated with roselle anthocyanins for fish freshness monitoring. *Food Hydrocoll.* **2017**, *69*, 308–317.
13. Pereira, V.A., Jr.; de Arruda, I.N.Q.; Stefani, R. Active chitosan/PVA films with anthocyanins from *Brassica oleraceae* (Red Cabbage) as Time–Temperature Indicators for application in intelligent food packaging. *Food Hydrocoll.* **2015**, *43*, 180–188.
14. Rukchon, C.; Nopwinyuwong, A.; Trevanich, S.; Jinkarn, T.; Suppakul, P. Development of a food spoilage indicator for monitoring freshness of skinless chicken breast. *Talanta* **2014**, *130*, 547–554. [PubMed]
15. Shah, N.; Ul-Islam, M.; Khattak, W.A.; Park, J.K. Overview of bacterial cellulose composites: A multipurpose advanced material. *Carbohydr. Polym.* **2013**, *98*, 1585–1598. [PubMed]
16. Gao, M.; Li, J.; Bao, Z.; Hu, M.; Nian, R.; Feng, D.; An, D.; Li, X.; Xian, M.; Zhang, H. A natural in situ fabrication method of functional bacterial cellulose using a microorganism. *Nat. Commun.* **2019**, *10*, 437.
17. Siripongpreda, T.; Somchob, B.; Rodthongkum, N.; Hoven, V.P. Bacterial cellulose-based re-swellable hydrogel: Facile preparation and its potential application as colorimetric sensor of sweat pH and glucose. *Carbohydr. Polym.* **2021**, *256*, 117506.
18. Moradi, M.; Tajik, H.; Almasi, H.; Forough, M.; Ezati, P.J. A novel pH-sensing indicator based on bacterial cellulose nanofibers and black carrot anthocyanins for monitoring fish freshness. *Carbohydr. Polym.* **2019**, *222*, 115030.
19. Shi, C.; Han, J.; Sun, X.; Guo, Y.; Yang, X.; Jia, Z. An intelligent colorimetric film based on complex anthocyanins and bacterial cellulose nanofibers for tilapia freshness detection in an actual cold chain. *Int. J. Biol. Macromol.* **2022**, *221*, 183–192.
20. Korhonen, J.T.; Hiekkataipale, P.; Malm, J.; Karppinen, M.; Ikkala, O.; Ras, R.H.A. Inorganic hollow nanotube aerogels by atomic layer deposition onto native nanocellulose templates. *ACS Nano* **2011**, *5*, 1967–1974.

21. Osi, A.R.; Zhang, H.; Chen, J.; Zhou, Y.; Wang, R.; Fu, J.; Müller-Buschbaum, P.; Zhong, Q. Three-Dimensional-printable thermo/photo-cross-linked methacrylated chitosan–gelatin hydrogel composites for tissue engineering. *ACS Appl. Mater. Interfaces* **2021**, *13*, 22902–22913. [CrossRef] [PubMed]
22. Zhu, L.; Bratlie, K.M. pH sensitive methacrylated chitosan hydrogels with tunable physical and chemical properties. *Biochem. Eng. J.* **2018**, *132*, 38–46. [CrossRef]
23. Zhou, Y.; Liang, K.; Zhang, C.; Li, J.; Yang, H.; Liu, X.; Yin, X.; Chen, D.; Xu, W.; Xiao, P. Photocrosslinked methacrylated chitosan-based nanofibrous scaffolds as potential skin substitute. *Cellulose* **2017**, *24*, 4253–4262. [CrossRef]
24. Han, J.; Wang, K.; Yang, D.; Nie, J. Photopolymerization of methacrylated chitosan/PNIPAAm hybrid dual-sensitive hydrogels as carrier for drug delivery. *Int. J. Biol. Macromol.* **2009**, *44*, 229–235. [CrossRef]
25. Kolawole, O.M.; Lau, W.M.; Khutoryanskiy, V. Methacrylated chitosan as a polymer with enhanced mucoadhesive properties for transmucosal drug delivery. *Int. J. Pharm.* **2018**, *550*, 123–129. [CrossRef] [PubMed]
26. Li, Y.; Liu, C.; Liu, W.; Cheng, X.; Zhang, A.; Zhang, S.; Liu, C.; Li, N.; Jian, X. Apatite formation induced by chitosan/gelatin hydrogel coating anchored on poly(aryl ether nitrile ketone) substrates to promote osteoblastic differentiation. *Macromol. Biosci.* **2021**, *21*, 2100262. [CrossRef]
27. Feng, Z.; Hakkarainen, M.; Grützmacher, H.; Chiappone, A.; Sangermano, M. Photocrosslinked chitosan hydrogels reinforced with chitosan-derived nano-graphene oxide. *Macromol. Chem. Phys.* **2019**, *220*, 1900174. [CrossRef]
28. Liu, Y.; Luo, X.; Wu, W.; Zhang, A.; Lu, B.; Zhang, T.; Kong, M. Dual cure (thermal/photo) composite hydrogel derived from chitosan/collagen for in situ 3D bioprinting. *Int. J. Biol. Macromol.* **2021**, *182*, 689–700. [CrossRef]
29. He, X.; Liu, X.; Yang, J.; Du, H.; Chai, N.; Sha, Z.; Geng, M.; Zhou, X.; He, C. Tannic acid-reinforced methacrylated chitosan/methacrylated silk fibroin hydrogels with multifunctionality for accelerating wound healing. *Carbohydr. Polym.* **2020**, *247*, 116689. [CrossRef]
30. Peng, X.; Cui, Y.; Chen, J.; Gao, C.; Yang, Y.; Yu, W.; Rai, K.; Zhang, M.; Nian, R.; Bao, Z.; et al. High-Strength collagen-based composite films regulated by water-soluble recombinant spider silk proteins and water annealing. *ACS Biomater. Sci. Eng.* **2022**, *8*, 3341–3353. [CrossRef]
31. Araújo, I.M.S.; Silva, R.R.; Pacheco, G.; Lustri, W.R.; Tercjak, A.; Gutierrez, J.; Júnior, J.R.S.; Azevedo, F.H.C.; Figuêredo, G.S.; Vega, M.L.; et al. Hydrothermal synthesis of bacterial cellulose–copper oxide nanocomposites and evaluation of their antimicrobial activity. *Carbohydr. Polym.* **2018**, *179*, 341–349. [CrossRef] [PubMed]
32. de Lima Fontes, M.; Meneguin, A.B.; Tercjak, A.; Gutierrez, J.; Cury, B.S.F.; dos Santos, A.M.; Ribeiro, S.J.L.; Barud, H.S. Effect of in situ modification of bacterial cellulose with carboxymethylcellulose on its nano/microstructure and methotrexate release properties. *Carbohydr. Polym.* **2018**, *179*, 126–134. [PubMed]
33. Shi, C.; Ji, Z.; Zhang, J.; Jia, Z.; Yang, X. Preparation and characterization of intelligent packaging film for visual inspection of tilapia fillets freshness using cyanidin and bacterial cellulose. *Int. J. Biol. Macromol.* **2022**, *205*, 357–365. [PubMed]
34. Yang, Q.; Ma, H.; Dai, Z.; Wang, J.; Dong, S.; Shen, J.; Dong, J. Improved thermal and mechanical properties of bacterial cellulose with the introduction of collagen. *Cellulose* **2017**, *24*, 3777–3787.
35. Lu, K.; Zhang, X.-L.; Zhao, Y.-L.; Wu, Z.-L. Removal of color from textile dyeing wastewater by foam separation. *J. Hazard. Mater.* **2010**, *182*, 928–932. [PubMed]
36. Promphet, N.; Rattanawaleedirojn, P.; Siralertmukul, K.; Soatthiyanon, N.; Potiyaraj, P.; Thanawattano, C.; Hinestroza, J.P.; Rodthongkum, N. Non-Invasive textile based colorimetric sensor for the simultaneous detection of sweat pH and lactate. *Talanta* **2019**, *192*, 424–430.
37. Zhang, X.; Yao, J.; Yan, Y.; Zhang, Y.; Tang, Y.; Yang, Y. Bacterial cellulose incorporating multicolor fluorescent probes for visual acidity detection in paper-based cultural relics. *ACS Appl. Mater. Interfaces* **2024**, *16*, 60902–60911.

polymers

MDPI

Article

Effect of Mechanical Interlocking Damage on Bond Durability of Ribbed and Sand-Coated GFRP Bars Embedded in Concrete Under Chloride Dry–Wet Exposure

Zhennan Yang, Chunhua Lu *, Siqi Yuan and Hao Ge

Faculty of Civil Engineering and Mechanics, Jiangsu University, Zhenjiang 212013, China;
yangzhennan2022@163.com (Z.Y.); 1000006440@ujs.edu.cn (S.Y.); 2212023025@stmail.ujs.edu.cn (H.G.)
* Correspondence: luch79@163.com

Abstract: The substitution conventional steel reinforcement with glass fiber-reinforced polymer (GFRP) bars is a widely adopted strategy used to improve the durability of concrete structures in chloride environments, offering benefits such as enhanced corrosion resistance, reduced maintenance needs, and increased service life. This study investigates the bond behavior between glass fiber-reinforced polymer (GFRP) bars and concrete under long-term chloride dry–wet cycling exposure. Pull-out tests were conducted on various specimens subjected to exposure durations of 0, 3, 6, 9, and 12 months. The experimental results indicate that, after 12 months of chloride dry–wet cycling, the bond strength retention rates of threaded ribbed GFRP with a bond length of 5d, sand-coated GFRP with a bond length of 5d, and threaded ribbed GFRP with a bond length of 7d were 57.9%, 62.2%, and 63.8%, respectively. To predict the GFRP–concrete bond performance after chloride exposure, a novel bond strength model for GFRP bars embedded in concrete, considering the mechanical interlocking effect of ribs, was proposed and validated by the test results. The overall prediction errors for RG-5d, SG-5d, and RG-7d specimens were 0.98, 0.81, and 0.93, respectively. Additionally, a sensitivity analysis was conducted on the main parameters in the model. Finally, the long-term GFRP–concrete bond performance deterioration was estimated using the proposed model. These findings are expected to provide valuable insights into the long-term bond performance and service life prediction of GFRP–concrete members in chloride environments.

Keywords: GFRP bars; bond-slip behavior; chlorine dry–wet exposure; pull-out tests; analytical model; long-term prediction

1. Introduction

Various fiber-reinforced composite materials have been widely used to enhance structural strength, including glass fiber, basalt fiber, carbon fiber, and certain bio-based fibers, all of which exhibit significant potential for further development [1–4]. Among these, glass fiber-reinforced polymer (GFRP) bars have emerged as a commonly used alternative to traditional steel rebars, particularly in concrete structures exposed to chloride-induced corrosion, due to their excellent corrosion resistance and mechanical properties [5,6].

In reinforced concrete structures, the bond strength between reinforcement and concrete is a critical factor that influences overall structural performance [7]. Unlike steel rebars, FRP bars exhibit anisotropic behavior, and their bond performance is affected by factors such as surface texture and chemical composition [8]. These differences highlight the need for targeted research on the bond behavior of FRP bars, as existing findings

on steel–concrete bond performance cannot be directly extrapolated. A comprehensive understanding of FRP–concrete bond properties is essential for the implementation of FRP bars in structural applications [9].

Previous research on the bond performance of FRP bars in concrete has identified several influential factors, including bar diameter, surface texture, and bond length [10,11]. However, as summarized in Table 1, most studies have focused on the bond performance of FRP bars under uncorroded conditions or short-term exposure scenarios, with insufficient attention given to the effects of prolonged chloride exposure [12]. This gap in the literature emphasizes the need for further research on the impact of long-term exposure to aggressive conditions, such as chloride-induced wet–dry cycles, on the bond performance of FRP bars. To evaluate the bond performance of FRP–concrete systems, researchers frequently utilize bond-slip curves derived from pull-out tests. As indicated in Table 1, most existing studies continue to employ traditional mathematical models, which are primarily derived from the development of steel–concrete bonding behavior. While these models provide valuable theoretical insights, they predominantly focus on fitting bond-slip curves rather than analytically describing slip behavior. As a result, the accuracy of these models heavily depends on the quantity and quality of the sample data used for calibration [13]. This reliance on empirical fitting means that deviations in the dataset, variations in material properties, or changes in environmental conditions can significantly impact prediction accuracy. Additionally, these models do not incorporate the long-term degradation effects caused by chloride exposure, which further limits their ability to provide reliable bond strength predictions over time. Therefore, the development of a more precise and physically relevant predictive model is necessary.

Table 1. Existing experimental research on GFRP bond performance.

Reference	Chloride Environment		FRP Bar		Prediction Model
	Environment	Duration (Day)	Bond Length	Surface Texture	
Zhang et al. (2024) [5]	Dry–wet cycles	360	5*d*	RB	
Lu et al. (2023) [6]	Emersion	180	5*d*	RB	Mathematical
Nelson et al. (2024) [7]	/	/	/	/	Mathematical
Shi et al. (2024) [8]	/	/	5*d*/10*d*/15*d*	SM	Mathematical
Zhou et al. (2024) [9]	/	/	5*d*	SC/RB	Mathematical
Chen et al. (2023) [10]	/	/	5*d*	RB	/
Hussain et al. (2022) [11]	Emersion	90	5*d*/10*d*/15*d*	RB	/
Yang et al. (2022) [12]	/	/	3*d*/5*d*	RB	Mechanical

Note: *d* denotes the diameter of the tested FRP bars. SM, SC, and RB refer to the surface textures of the FRP bars: smooth, sand-coated, and ribbed, respectively [5–12].

The primary objective of this study is to evaluate the bond performance between GFRP bars and concrete under chloride dry–wet cycling exposure and to develop an analytical model that could accurately predict this behavior. The research involved a series of pull-out tests conducted over one year using various GFRP–concrete specimens, which were evaluated at five different exposure intervals. The specimens were categorized based on bond length and surface texture to assess their impact on bond performance as chloride exposure increased. An analytical bond-slip prediction model was also developed, incorporating the damage characteristics of both GFRP bars and concrete. This study provides valuable insights into critical factors affecting bond strength, such as surface texture, bond length, and exposure duration, while proposing a new approach to predict bond-slip behavior under long-term exposure conditions.

2. Experimental Setup

Figure 1 shows the key testing steps in the experimental procedure. The testing process begins with mold preparation, followed by concrete mixing, and then casting to produce the test specimens. After casting, the specimens undergo 28-day curing to achieve the desired material properties. Once the curing phase is completed, the specimens are subjected to chloride salt wet–dry cycles, simulating aggressive environmental conditions to assess the long-term effects of chloride exposure. Following the exposure phase, prior to pull-out tests, the loading zone is reinforced using steel tubes to prevent damage to the GFRP bars by the loading grip. Finally, the specimens undergo the pull-out test, where the bond performance between the GFRP bar and concrete is evaluated under controlled loading conditions.

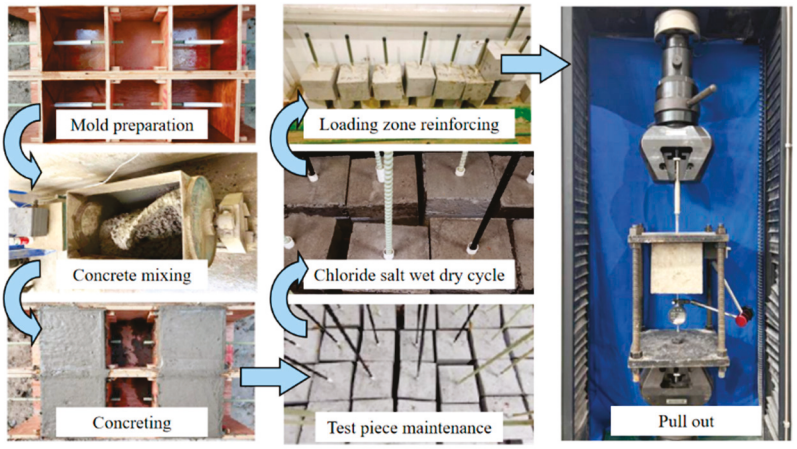

Figure 1. A flow diagram to illustrate the testing processes.

2.1. Design of Pull-Out Specimen

The experimental investigation utilized two types of 12 mm diameter GFRP bars: SG bars with a sand-coated surface and RG bars with a threaded ribbed surface. The key geometric parameters of the ribbed bars, including rib spacing, width, and height, are illustrated in Figure 2. Both GFRP bar types were manufactured by Jiangsu Feibo New Material Technology Co. (Yancheng, China, state for China), with a tensile strength of 874.1 MPa and an elastic modulus (E_f) of 36 GPa. The ribs were produced by winding a strand tightly around the smooth GFRP bundles during the manufacturing process, resulting in a helical groove pattern on the bar surface. As listed in Table 2, the conventional C40 concrete used for casting the specimens achieved a 28-day compressive strength of 47.1 MPa.

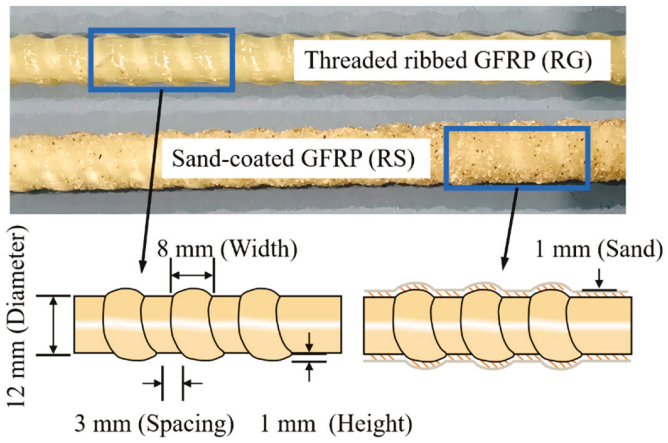

Figure 2. Geometric details of the GFRP bars.

Table 2. Concrete admixture design (unit: kg (for one m^3 of concrete)).

Strength Grade	Water–Cement Ratio	Water	Cement	Sand	Stones
C40	0.49	220	449	615	1116

A series of pull-out test specimens were fabricated to evaluate the bond behavior between GFRP bars and conventional concrete. As shown in Figure 3, GFRP bars were cut to a length of 580 mm and concentrically embedded in concrete cubes measuring 200 mm × 200 mm × 200 mm, following the guidelines of ACI 440.3R-12. A 16 mm diameter PVC pipe served as a bond breaker to control the bond length. To prevent GFRP bar rupture during testing, a steel tube, 200 mm long, was bonded to the loaded end of the bar using epoxy adhesive. During casting, the GFRP bars were oriented perpendicular to the specimen surface to minimize micro-void formation at the bar-concrete interface. The molds were removed 24 h after casting, and the specimens were cured under ambient conditions for 28 days. The embedded length of the bars in the pull-out specimens was set to five times the bar diameter (5*d*). To further investigate the effect of embedment length, an additional set of specimens was cast with an embedded length equivalent to seven times the bar diameter (7*d*). In addition, a certain number of 150 mm cubic blocks were also prepared to assess the compressive strength variation during the dry–wet cycling test.

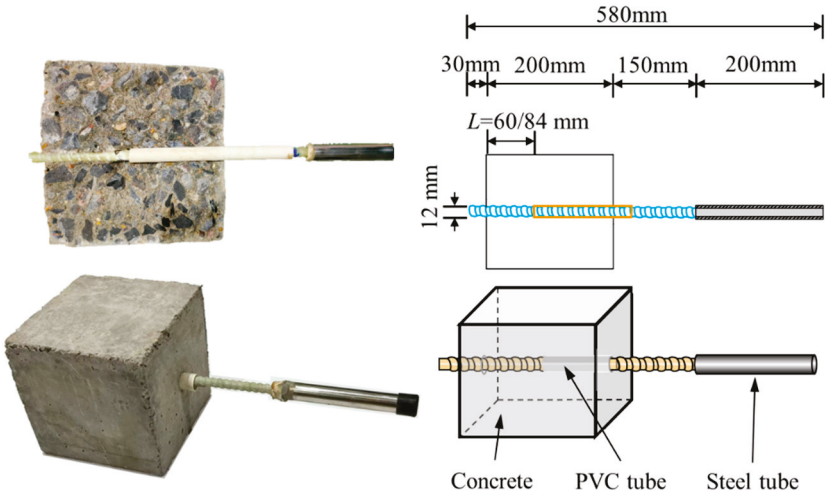

Figure 3. Pull-out test specimen diagram.

2.2. Chloride Dry–Wet Exposure Program

Following 28 days of natural curing, the pull-out specialties were subjected to wet–dry cycling in solution, and a 5% NaCl solution was chosen to approach the salinity of seawater more closely [14]. Each cycle comprised a 12 h wet phase followed by a 12 h dry phase, with an average temperature of 20 ± 2 °C and a relative humidity of 80% to simulate marine conditions [15]. During exposure, the specimens were positioned vertically on heel blocks, allowing for chloride diffusion in the concrete from the free end. As shown in Figure 4, the TR-ZXC artificial marine tidal salt spray environmental control system, manufactured by Shanghai Tongrui Instrument Equipment Co. (Shanghai, China, state for China), was used to regulate the cyclic exposure time and temperature of artificial seawater during chlorine exposure. Additionally, the HB-211ATC Optical Salinity Meter (Bestone Industrial Ltd., Shenzhen, China) was employed to monitor chloride ion concentration, ensuring the consistency and accuracy of the exposure conditions.

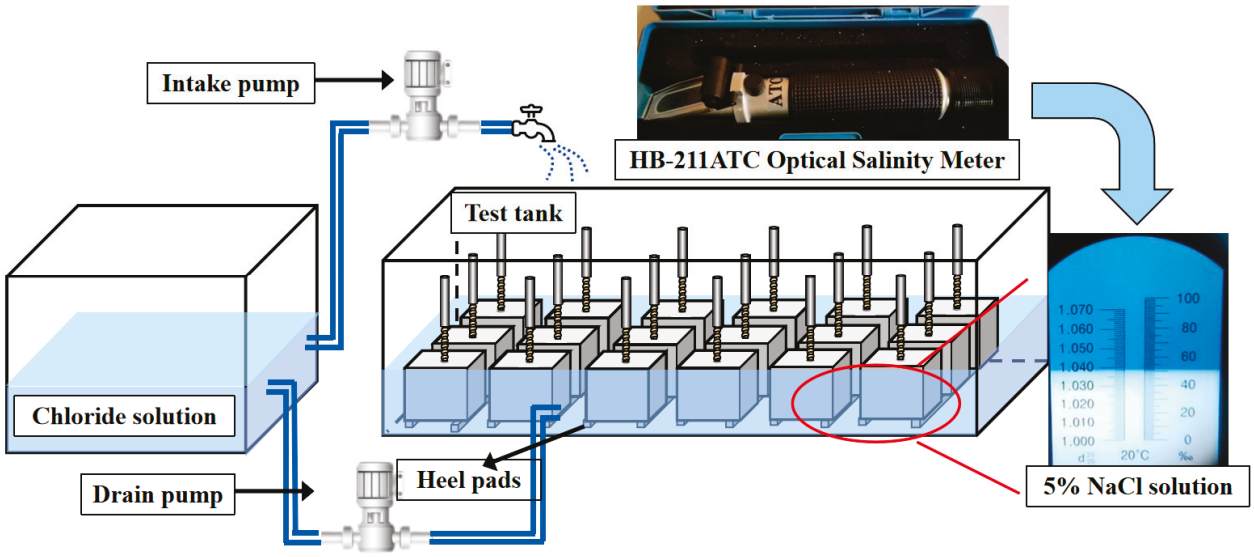

Figure 4. Automated chloride dry–wet cycle exposure device and chlorine concentration monitoring.

To assess the degradation of GFRP–concrete bond performance, due to chloride exposure, the pull-out tests were conducted at five intervals: immediately after curing (0 months), and at 3, 6, 9, and 12 months after chloride exposure. The three groups of pull-out specimens were fabricated and tested, as summarized in Table 3. As given in Table 3, the specimen identifier comprises three components: the initial letters denote the GFRP bar surface texture, the subsequent numeral indicates the effective bond length as a multiple of the bar diameter, and the final numeral specifies the duration of chloride exposure in months. For example, SG-5d-6 refers to a specimen with a sand-coated GFRP bar, an effective bond length of five times the bar diameter, and six months of chloride exposure.

Table 3. Design parameters for the tested pull-out specimens.

Group	Specimen	Surface Texture	Diameter	Bond Length	Chloride Duration
RG-5d	RG-5d-0	Threaded ribbed	12 mm	5*d*	0 months
	RG-5d-3	Threaded ribbed	12 mm	5*d*	3 months
	RG-5d-6	Threaded ribbed	12 mm	5*d*	6 months
	RG-5d-9	Threaded ribbed	12 mm	5*d*	9 months
	RG-5d-12	Threaded ribbed	12 mm	5*d*	12 months
SG-5d	SG-5d-0	Sand-coated	12 mm	5*d*	0 months
	SG-5d-3	Sand-coated	12 mm	5*d*	3 months
	SG-5d-6	Sand-coated	12 mm	5*d*	6 months
	SG-5d-9	Sand-coated	12 mm	5*d*	9 months
	SG-5d-12	Sand-coated	12 mm	5*d*	12 months
RG-7d	RG-7d-0	Threaded ribbed	12 mm	7*d*	0 months
	RG-7d-3	Threaded ribbed	12 mm	7*d*	3 months
	RG-7d-6	Threaded ribbed	12 mm	7*d*	6 months
	RG-7d-9	Threaded ribbed	12 mm	7*d*	9 months
	RG-7d-12	Threaded ribbed	12 mm	7*d*	12 months

2.3. Pull-Out Loading Scheme

This study followed the guidelines established by ACI 440.3R-12 and CSA S806-12 for the design of test specimens and the experimental setup. As illustrated in Figure 5, pull-out tests were performed using a 600 kN capacity servo-hydraulic testing machine manufactured by Shenzhen SUNS Technology Stock Co. (Shenzhen, China, state for China). The force measurement accuracy of the testing machine is ±1%, ensuring reliable data

acquisition. Additionally, a hydraulic pressure sensor was utilized for force measurement and control during the tests. The specimens were securely positioned on a steel frame connected to the top grip system. To minimize misalignment and reduce friction between the concrete cube and the steel plate, a soft rubber pad and a low-friction film were employed. A displacement-controlled loading scheme was utilized to capture the complete post-peak behavior of the specimens. The load was applied to the GFRP bar at a rate of 1 mm/min until failure occurred (ACI 440.3R-12). The machine system could precisely record the applied load and displacement during the test, while an extra LVDT was utilized to measure the displacement at the free end of the tested GFRP bar. The LVDT has a measurement accuracy of 0.01 mm and an error margin of 1%, providing precise and consistent displacement data throughout the experiment.

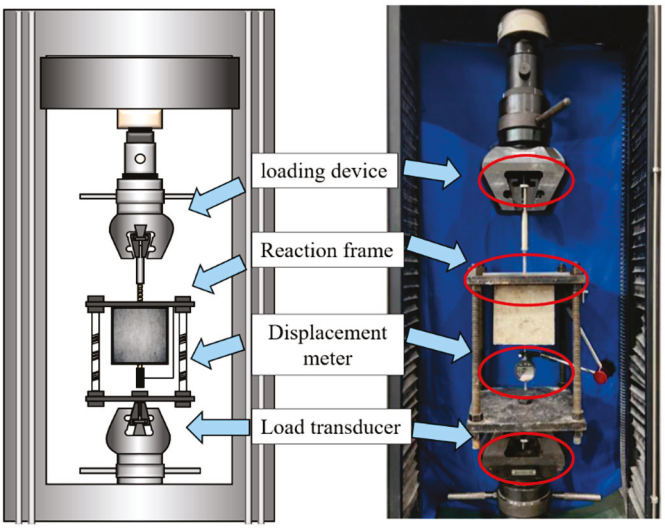

Figure 5. Loading device for the uniaxial pull-out test.

The bond behavior discussed in this paper is characterized by nominal bond stress (τ) calculated using the following equation:

$$\tau = \frac{F_{\text{test}}}{\pi d L} \tag{1}$$

where F_{test} is the applied load during the test; d is the nominal bar diameter; L is the bond length, which is $5d$ or $7d$ in this test.

3. Experimental Results and Discussions

3.1. Failure Patterns and Test Results

Two distinct failure patterns were observed in the pull-out tests: Type A (pull-out failure) and Type B (peeling-off failure). In Type A failure (Figure 6a), residual concrete remained between the ribs of the extracted GFRP bar, indicating that the bond strength was primarily maintained by mechanical interlock. As the applied load increased, stress transferred through the ribs, and when the bond strength was exceeded, the GFRP bar was extracted along with residual concrete. In contrast, Type B failure (Figure 6b) exhibited extensive rib wear, with no concrete residue left on the bar surface, suggesting that damage was concentrated on the ribs, leading to progressive material loss and eventual peeling-off failure.

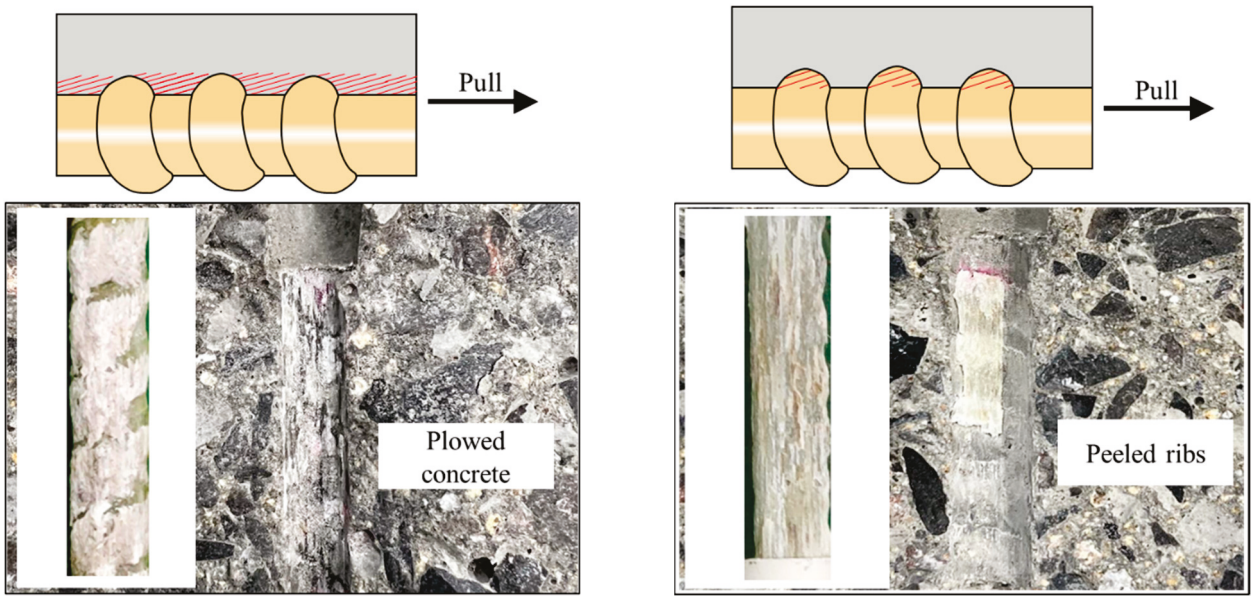

Figure 6. Typical failure patterns of tested pull-out specimens: (**a**) Failure A pattern; (**b**) Failure B pattern.

The red area in Figure 6 marks the weak zone that experienced the most damage, where bond failure initiated and propagated. The occurrence of these failure modes was influenced by the relative strengths of the GFRP bar and concrete. Type A failure was more likely when the concrete strength was higher, ensuring strong mechanical interlock, while Type B failure tended to occur when the GFRP rib strength was lower, leading to excessive wear and peeling. Additionally, environmental factors such as chloride ingress can alter the failure mechanism over time, potentially causing a transition from Type A to Type B.

The bond-slip performance and corresponding failure patterns are summarized in Table 4. With the exception of the RG-5d-0 specimen (which underwent no chloride exposure) and some RG-7d specimens (which were subjected to shorter exposure durations), all other specimens exhibited a Type B failure. This finding suggests that the ribs of the GFRP bars deteriorated significantly after chloride dry–wet exposure. Furthermore, the tested peak bond strength (τ_t) displayed a general decreasing trend with the increasing duration of chloride exposure. However, variations in slip corresponding to the peak point (s_t) differed significantly among test specimens.

Significant differences in bond strength were observed between the two rebar types under identical bond lengths and chloride exposure durations. Initially, the RG-5d-0 specimen exhibited a peak bond strength of 36.8 MPa, while the SG-5d-0 specimen recorded a lower value of 21.7 MPa. After 12 months of chloride exposure, the bond strength decreased to 21.3 MPa for the RG-5d-12 specimen and to 13.5 MPa for the SG-5d-12 specimen. Conversely, the corresponding slip displacement was slightly higher in the RG-type GFRP specimens. For instance, RG-5d-0 exhibited a slip of 5.8 mm compared to 4.7 mm for SG-5d-0. The SG-5d specimens displayed minimal changes in slip with chloride exposure, with slip values of 4.7 mm for SG-5d-0 and 4.9 mm for SG-5d-12. Additionally, an increase in bond length generally resulted in a decrease in peak bond strength. For example, the RG-5d-0 specimen had a peak bond strength of 36.8 MPa, whereas the RG-7d-0 specimen exhibited a lower value of 29.0 MPa. Longer bond lengths were also associated with greater slip displacements; RG-7d-0 exhibited a slip of 10.7 mm compared to 5.8 mm for RG-5d-0.

Table 4. Failure modes and peak characteristics of tested pull-out specimens.

Specimen	Failure Patterns	τ_t		s_t	
		Value/MPa	Rate/%	Value/mm	Rate/%
RG-5d-0	A	36.8	100.0	5.8	100.0
RG-5d-3	B	31.9	86.7	8.1	139.7
RG-5d-6	B	28.1	76.4	6.2	106.9
RG-5d-9	B	25.4	69.0	5.1	87.9
RG-5d-12	B	21.3	57.9	8.6	148.3
SG-5d-0	B	21.7	100.0	4.7	100.0
SG-5d-3	B	19.8	91.2	4.2	89.4
SG-5d-6	B	18.6	85.7	6.6	140.4
SG-5d-9	B	14.3	65.9	4.0	85.1
SG-5d-12	B	13.5	62.2	4.9	104.3
RG-7d-0	A	29.0	100.0	10.7	100.0
RG-7d-3	A	25.6	88.3	11.9	111.2
RG-7d-6	A	22.2	76.6	10.4	97.2
RG-7d-9	B	21.4	73.8	7.6	71.0
RG-7d-12	B	18.5	63.8	6.8	63.6

In summary, peak bond strength was affected by chloride exposure duration, surface texture, and effective bond length. While the corresponding slip displacement did not follow a consistent pattern across all specimens, it was generally higher in those with increased bond lengths and RG-type GFRP bars. These results highlight the complex interactions governing bond–slip behavior under different exposure conditions, which is further examined in subsequent sections.

3.2. Effects of Surface Textures

Figure 7 provides a detailed comparison of the bond–slip behavior of threaded ribbed GFRP (RG) bars and sandblasted GFRP (SG) bars. The bonding behavior of each group was similar, and one representative curve was selected for discussion. Under initial conditions without chloride exposure, specimen RG-5d-0 exhibited a significantly steeper ascending slope, reaching a peak bond strength of 36.8 MPa. In contrast, the SG-5d-0 bars displayed lower bond strength during this phase, with a more gradual increase in bond stress. As the duration of chloride exposure increased from 0 to 12 months, both RG-5d and SG-5d specimens showed a decline in bond strength. However, RG-5d specimens consistently exhibited a steeper ascending slope and higher peak values compared to SG-5d specimens throughout the chloride exposure period.

Figure 8 illustrates the peak bond strength and corresponding slip values. For RG-5d series specimens, the bond stress decreased from 36.8 MPa at 0 month to 21.3 MPa at 12 months, resulting in a retention ratio of 0.58. In comparison, the sand-coated GFRP bars (SG-5d) showed a reduction from 21.7 MPa to 13.5 MPa over the same period, corresponding to a retention ratio of 0.62. The peak strength of the RG-5d specimens was approximately 1.4 times higher than that of the SG-5d specimens during all exposures, indicating that both types experienced a comparable rate of deterioration. However, no consistent pattern of change was observed in the slip values at peak points. In general, the RG-5d specimens exhibited greater slip compared to the SG-5d specimens, suggesting that sand-coated GFRP bars demonstrate lower stiffness.

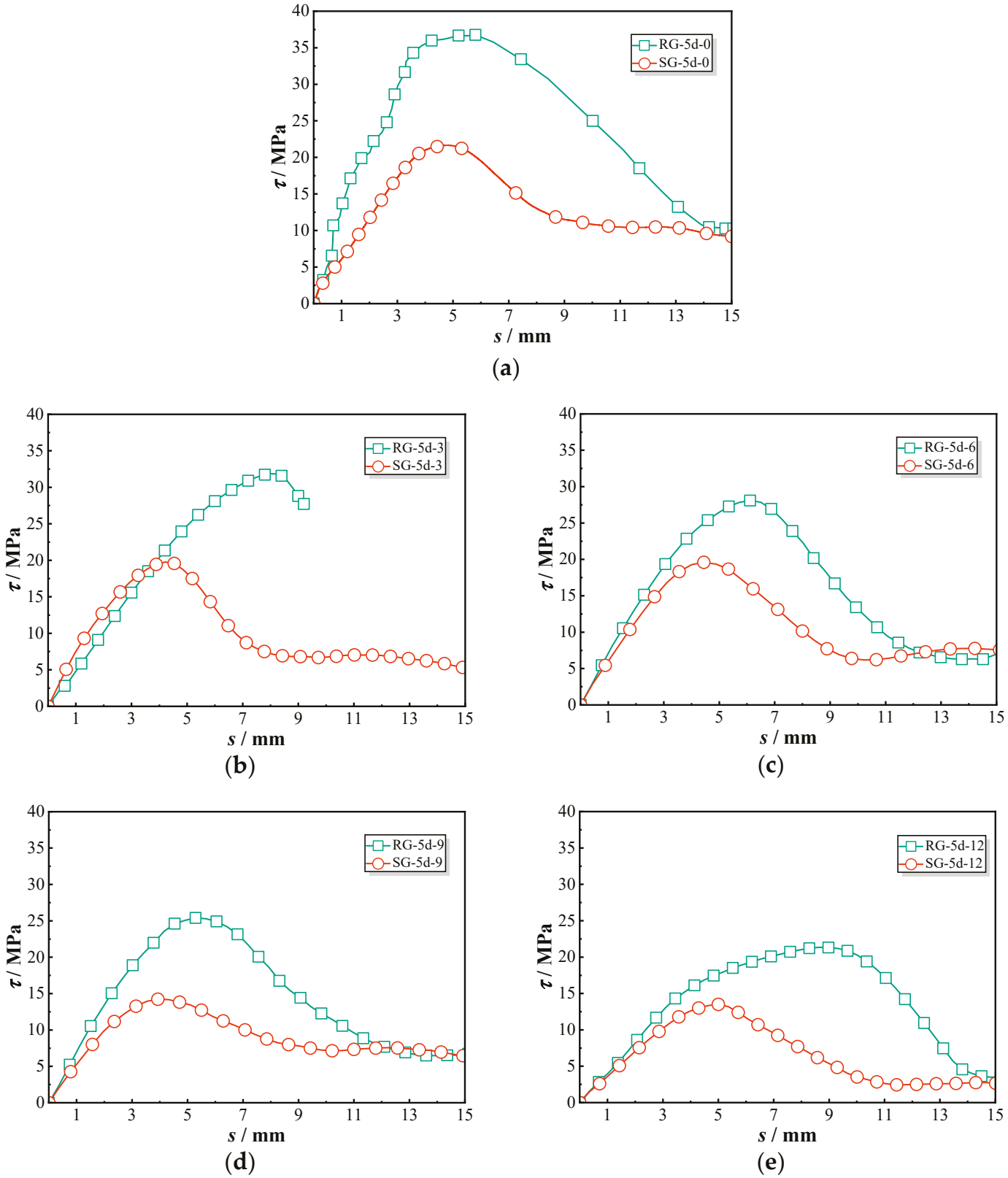

Figure 7. Bond–slip curves of tested RG-5d and SG-5d specimens: (**a**) RG-5d-0 and SG-5d-0; (**b**) RG-5d-3 and SG-5d-3; (**c**) RG-5d-6 and SG-5d-6; (**d**) RG-5d-9 and SG-5d-9; (**e**) RG-5d-12 and SG-5d-12.

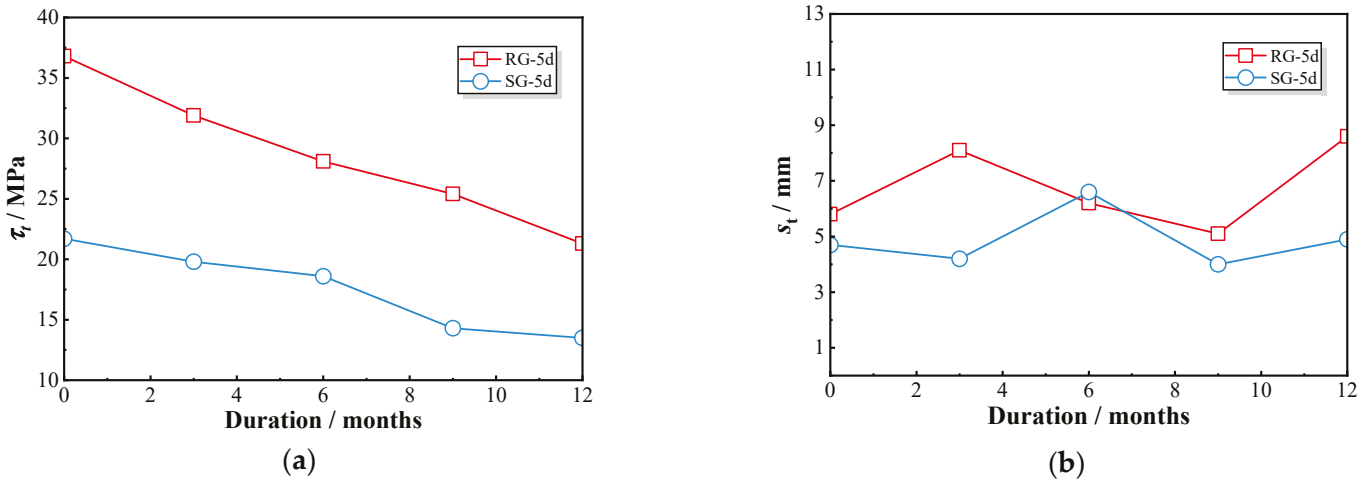

Figure 8. Variations in peak bond strength and the corresponding slip of RG-5d and SG-5d specimens: (**a**) peak bond strength; (**b**) corresponding slip.

The bond performance differences between threaded ribbed GFRP (RG) bars and sand-coated GFRP (SG) bars stem from their distinct bonding mechanisms with the surrounding concrete matrix. RG bars, with their continuous helical ribs, create a strong mechanical interlock, allowing for more efficient stress transfer and improved shear resistance along the bond interface [16]. The ribbed surface also enhances confinement in the surrounding concrete, reducing slip and improving pull-out resistance. Additionally, as chloride exposure progresses, the rougher profile of RG bars helps maintain bond integrity, providing better bond durability compared to SG bars [17].

In contrast, SG bars rely primarily on friction and adhesion, with the sand-coated layer reducing mechanical interlocking efficiency. While the roughened sand surface initially provides high frictional resistance during the early slip stage, the peak bond strength of SG bars is lower than that of RG bars. Studies have shown that the sand layer can detach under cyclic loading or sustained exposure to aggressive environments, decreasing the effective contact area at the bar–concrete interface [18]. This leads to a more rapid decline in bond strength, particularly in chloride-rich conditions where aggressive ion ingress weakens interfacial adhesion. Based on the results of this study, SG specimens consistently exhibited lower bond performance than RG specimens, regardless of chloride exposure duration. This finding indicates that, under the specific conditions of this experiment, the ribbed structure significantly enhances the bond behavior of GFRP bars in chloride-exposed environments.

3.3. Effects of Bond Length

Figure 9 presents a detailed comparison of the bond–slip behavior for GFRP bars with different bond lengths (5*d* and 7*d*). For specimens without chloride exposure, RG-5d-0 exhibited a steeper increase in average bond stress, resulting in higher average bond strength, while RG-7d-0 demonstrated greater slip displacement. These results suggest that shorter bond lengths enhance average bond strength.

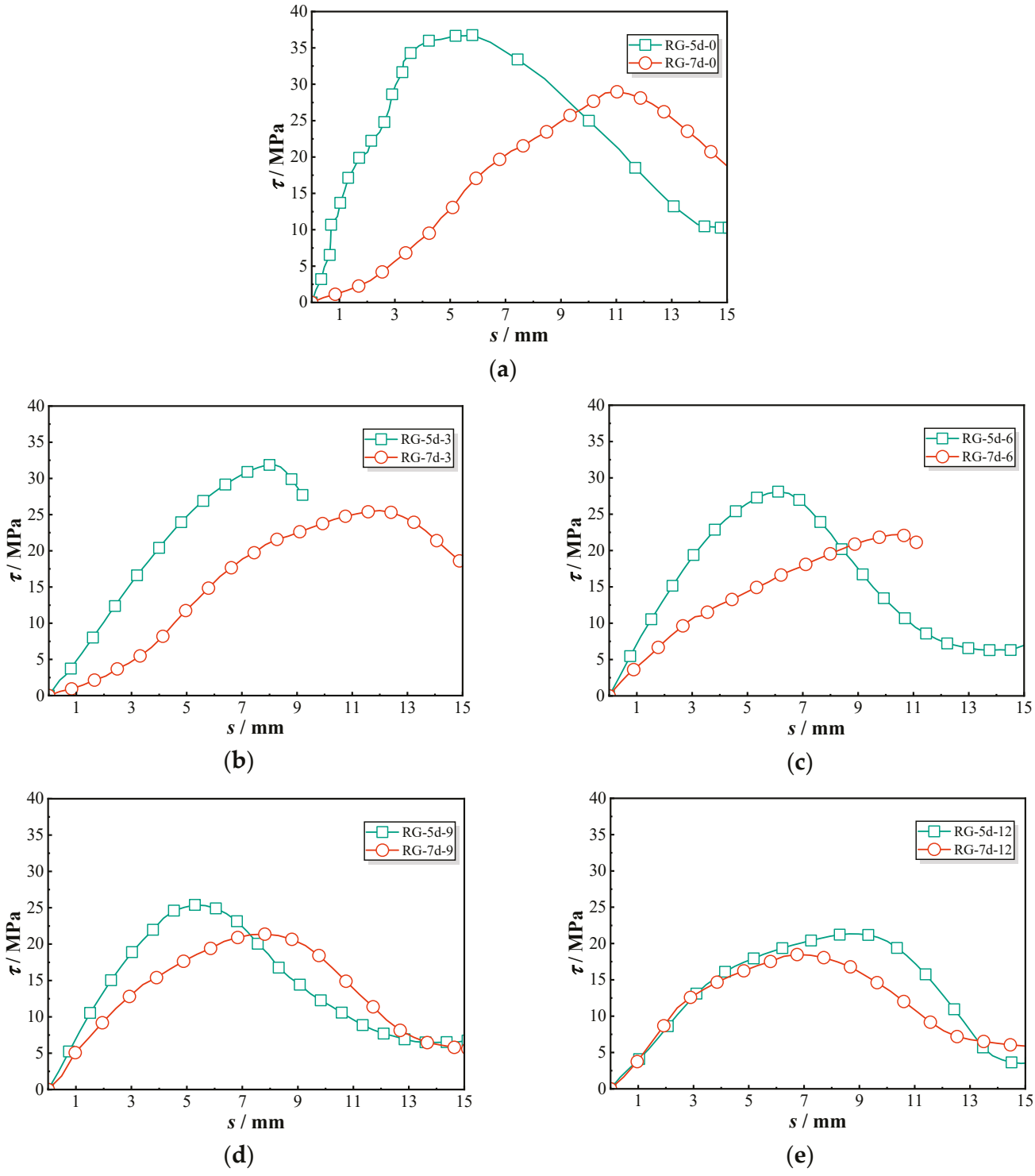

Figure 9. Bond–slip curves of tested RG-5d and RG-7d specimens: (**a**) RG-5d-0 and RG-7d-0; (**b**) RG-5d-3 and RG-7d-3; (**c**) RG-5d-6 and RG-7d-6; (**d**) RG-5d-9 and RG-7d-9; (**e**) RG-5d-12 and RG-7d-12.

With increased chloride exposure duration, both RG-5d and RG-7d specimens showed significant reductions in bond strength. Over time, the bond–slip curves for the two bond lengths converged, indicating that the influence of bond length diminished under prolonged chloride exposure.

The analysis of peak bond strength and the corresponding slip is presented in Figure 10. A distinct difference in peak bond stress was observed between the RG-5d-0 and RG-7d-0 specimens, with RG-5d-0 exhibiting a higher peak bond stress of 36.8 MPa, compared to

29.0 MPa for RG-7d-0—a 21% reduction. Additionally, the slip displacement for RG-7d-0 was approximately 80% greater than that of RG-5d-0. After 12 months of chloride exposure, RG-5d-12 showed only a 15% higher peak bond stress than RG-7d-12; however, their slip displacements were more comparable, with RG-5d-12 being 26% greater than RG-7d-12.

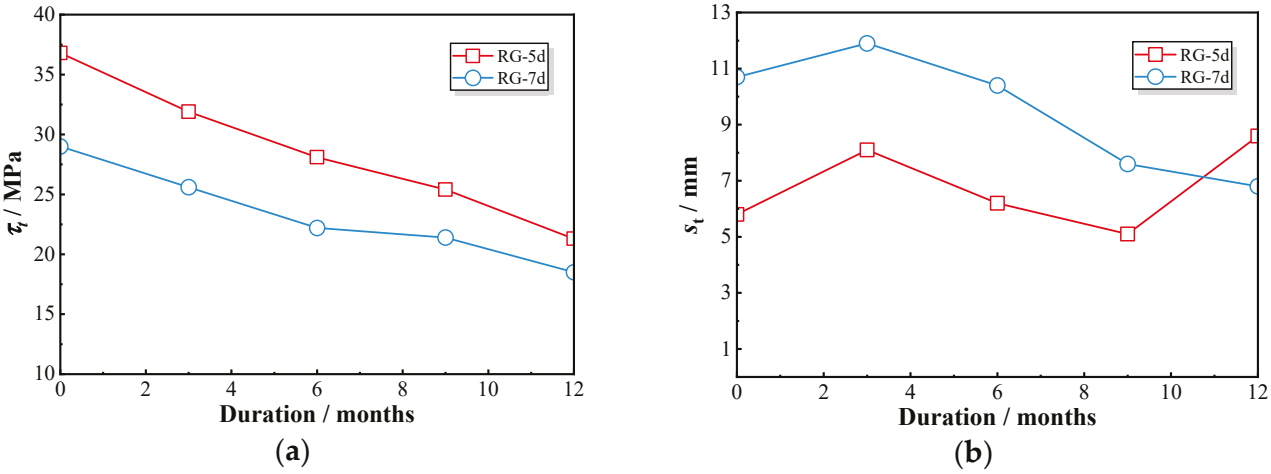

Figure 10. Variations in peak bond strength and the corresponding slip of RG-5d and RG-7d specimens: (**a**) peak bond strength; (**b**) corresponding slip.

This difference can be primarily attributed to the uneven stress distribution along the GFRP bar in the pull-out specimens. Under direct tensile loading, asynchronous deformation may occur between the core and outer layers of the ribbed GFRP bar, leading to uneven stress distribution across the cross-section and shear lag [19]. During the pullout test, the bond stress along the rebar was not uniformly distributed, and the ultimate bond stress gradually migrated from the loaded end to the free end. When the bond length is short, the high-stress zone expands proportionally, causing the stress curve to bulge more prominently along the anchorage length. This results in a higher average bond stress. Conversely, when the bond length increases, the bond stress distribution becomes more uniform, leading to a lower average bond stress [20].

3.4. Effects of Chlorine Salt Erosion

Figure 11a illustrates the bond–slip variations of RG-5d specimens under different chloride exposure durations. The RG-5d-0 specimen initially exhibited a steep ascending slope, reflecting strong bond strength. However, as chloride exposure duration increased, the slope became less pronounced. Figure 11b demonstrates the bond–slip behaviors of SG-5d specimens, which experienced little changes in bond performance during the first six months of exposure, followed by a reduction in curve convexity after nine months. In Figure 11c, the bond–slip behaviors of RG-7d specimens reveal two distinct trends. Before nine months of exposure, the bond–slip curve exhibits an S-shaped trajectory characterized by a gradual increase during the initial slip phase, a sharper rise around the 3 mm slip, peaking at approximately 6.5 mm. This pattern results in a higher peak slip displacement. After nine months, the curve adopts a different shape, with a steep initial slope followed by a pronounced reduction at the inflection point, resulting in lower peak slip displacement and bond strength. Overall, chloride exposure significantly impacts the pull-out behaviors of GFRP–concrete bond specimens. As exposure time increases, the bond–slip curves shift from a convex shape to a more flattened profile, reflecting the gradual deterioration in bond strength.

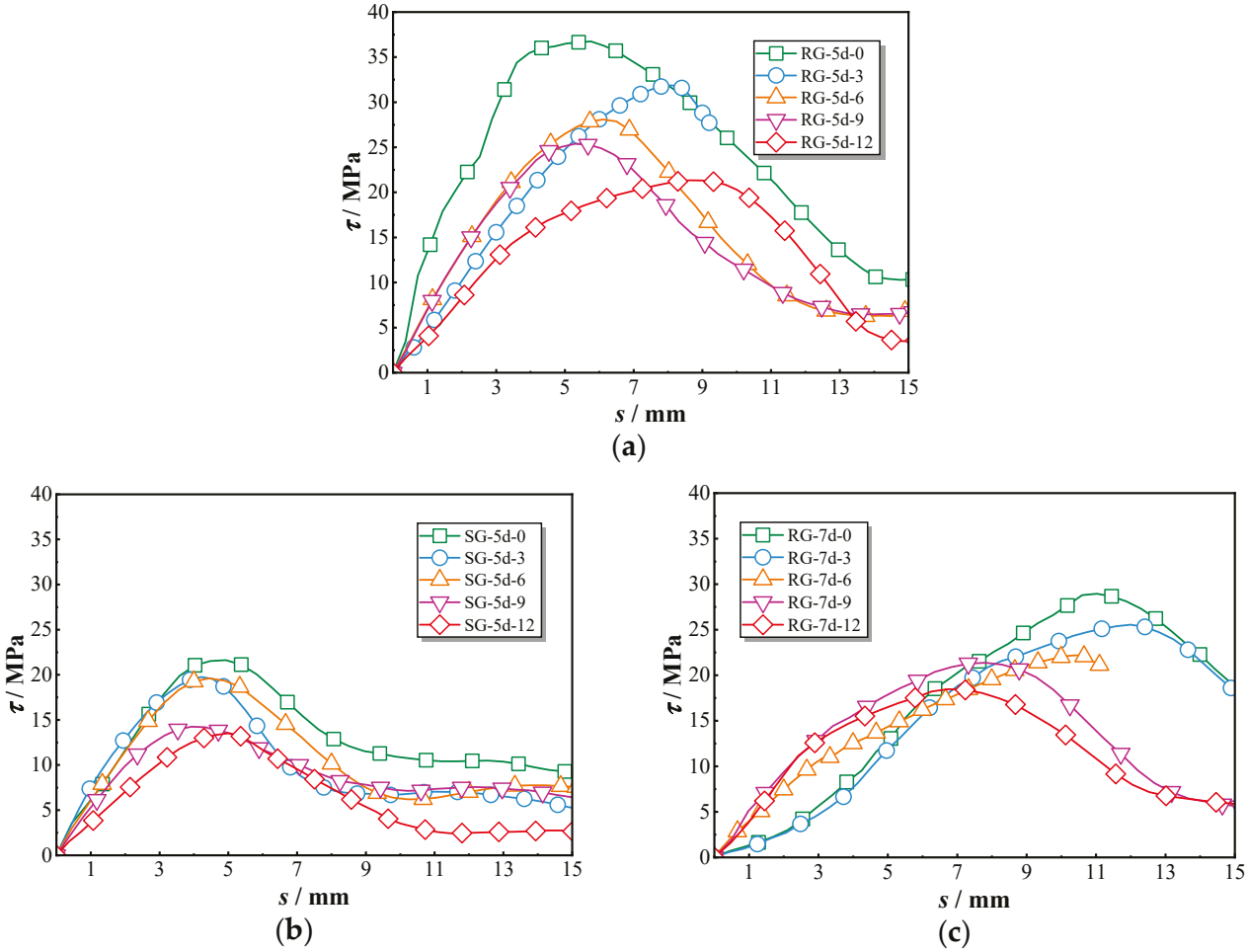

Figure 11. Bond–slip curves of all tested specimens: (**a**) RG-5d group; (**b**) SG-5d group; (**c**) RG-7d group.

Figure 12a illustrates the progressive decline in peak bond strength for each group of specimens subjected to chloride exposure. Specifically, the peak bond strength of the RG-5d series decreased from 36.8 MPa (RG-5d-0) to 21.3 MPa (RG-5d-12), the SG-5d series decreased from 21.7 MPa (SG-5d-0) to 13.5 MPa (SG-5d-12), and the RG-7d series decreased from 29.0 MPa (RG-7d-0) to 18.5 MPa (RG-7d-12). This consistent decline across all groups indicates that chloride exposure induces a comparable rate of bond strength deterioration in GFRP–concrete pull-out specimens, irrespective of the specimen type. Figure 12b presents the slip values corresponding to the peak point under chloride exposure. While the RG-5d and SG-5d groups display a fluctuating pattern without a clear trend, the RG-7d group shows a significant variation in peak slip around the 9-month exposure period. For example, the peak slip of the RG-7d-6 specimen reached 10.4 mm but then decreased to 7.6 mm for the RG-7d-9 specimen, representing a reduction of 26.9%. Prolonged exposure thus results in a noticeable reduction in peak slip values for the RG-7d specimens.

As previously discussed, the pull-out behavior of GFRP–concrete bond specimens undergoes considerable changes with the increasing duration of chloride dry–wet cycles. Chloride ingress weakens the bond between the GFRP bars and the concrete, resulting in a shift in the bond–slip curves from a convex shape to a flattened trend [21]. All specimen groups exhibited a gradual decline in peak bond strength at a similar rate over the exposure period. However, the slip values of the RG-5d and SG-5d groups showed a wave-like pattern, whereas the RG-7d group displayed significant changes around the 9-month exposure mark, likely due to alterations in the failure mode of the specimens.

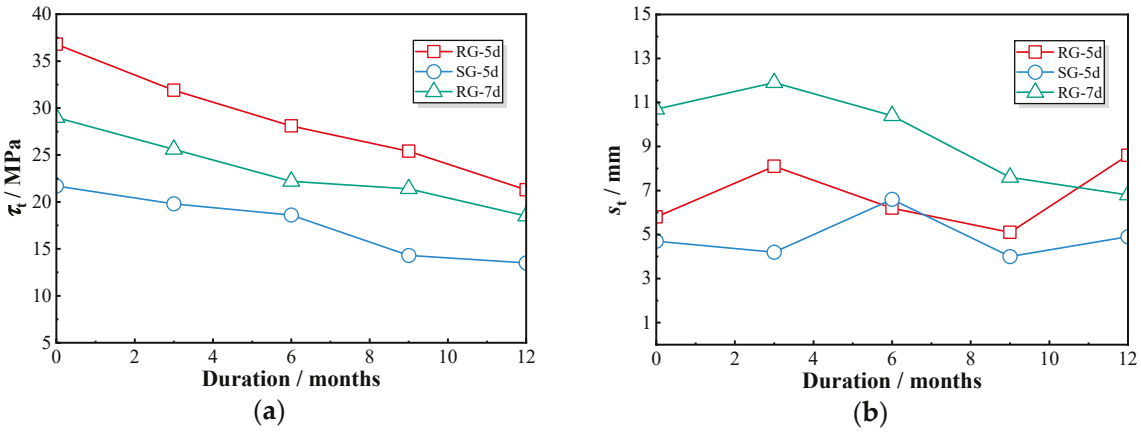

Figure 12. Variations in peak bond strength and the corresponding slip of all tested specimens: (**a**) peak bond strength; (**b**) corresponding slip.

To assess the impact of concrete strength on bond–slip behavior under chloride exposure, the compressive strength of concrete exposed to the same environment was tested. Figure 13 compares the retention rates of concrete compressive strength and bond strength over time. The data revealed that the reduction in concrete compressive strength does not directly correlate with the degradation of bond strength in GFRP bars. While the concrete retained over 90% of its initial strength during the first four months, it dropped sharply to 76.6% after 12 months of exposure. In contrast, the bond strength of the RG-5d specimens steadily declined by 42.1% over the same period. This suggests that the reduction in concrete strength alone does not account for the observed decrease in bond strength [22,23]. The degradation of ribbed FRP bars in chloride environments appears to play a decisive role in bond strength deterioration [24].

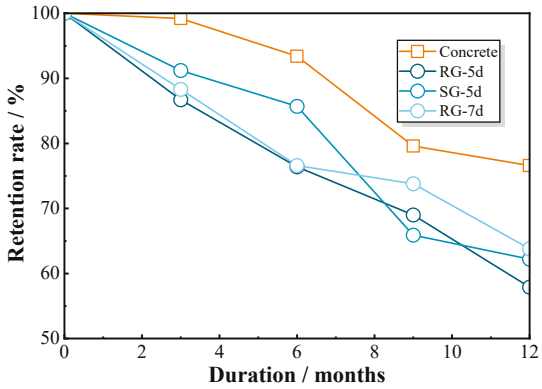

Figure 13. Comparison of bond strength with concrete compressive strength in retention rate.

The experimental results of this study were compared with previous research on the bond behavior of GFRP bars under seawater exposure. Mai et al. conducted a 9-month seawater exposure test using artificial seawater with a salinity of 3% and observed a bond strength reduction of 17.5%, which aligns with the findings of this study, as both indicate a decline in bond strength after exposure. Similarly, Pan et al. reported a 39.68% reduction in bond strength after 6 months of seawater exposure, demonstrating a more significant degradation. However, their study also included mechanical loading during exposure, which may have contributed to the greater bond strength reduction compared to this study [25].

In contrast, Nepomuceno et al. reported an increase of 39% in bond strength after one year of seawater exposure, which contradicts the findings of this study. However, separate

strength tests on GFRP bars alone in their study indicated that the GFRP material itself experienced degradation, suggesting that the bond strength increase could be attributed to enhanced cement hydration in the presence of seawater, rather than an improvement in the GFRP–concrete interface [26].

The results of studies that reported bond strength reduction are consistent with the findings of this study and can be attributed to seawater-induced damage to both GFRP bars and concrete. On the other hand, studies reporting bond strength improvement suggest that the chemical interaction between seawater and cementitious materials may enhance hydration, leading to a temporary increase in bond strength. These comparisons highlight the complex influence of seawater exposure on GFRP–concrete bonding and the need for further investigation to fully understand the long-term degradation mechanisms [27].

4. Theoretical Modeling

4.1. Analytical Model for Bond Stress and Slip Behavior

According to the test descriptions in Section 3, chloride exposure significantly influenced the failure pattern and bond strength of GFRP–concrete pull-out specimens. Therefore, it is essential to develop a mechanical model for the bond–slip behavior of GFRP bars in concrete that accounts for chloride-induced damage. After considering that practical applications often prioritize the peak strength, this paper emphasized the characteristics of the ascending segment of the bond–slip curve. As illustrated in Figure 14, the ascending segment can be typically divided into three distinct stages based on their contributions to bond stress [28]. In Stage I, bond stress is primarily attributed to adhesion (F_a), friction (F_f), and mechanical interlock (F_m). In Stage II, the bond–slip behavior causes a transition from static to dynamic friction, rendering the adhesive effect negligible. In Stage III, the mechanical interlock behavior enters an inelastic phase due to the plastic deformation of the ribs.

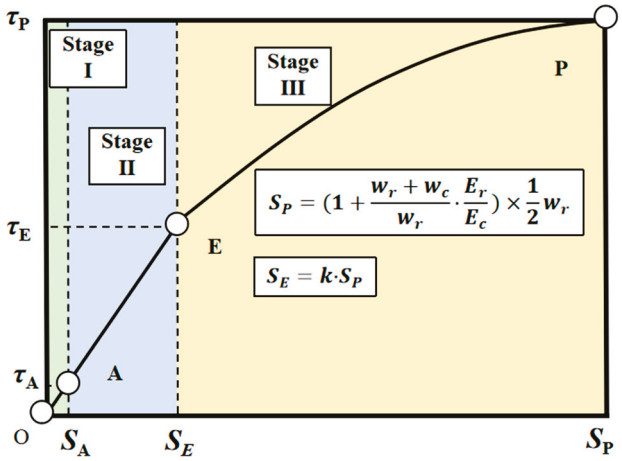

Figure 14. Three stages for the ascending portion in the bond–slip curve.

Since Stage I constitutes a relatively small portion of the entire slip process, the bond–slip model can be effectively calculated and analyzed from Stage II onward. In Stages II and III, the slip behavior of the bars is attributed to a combination of deformations in both the concrete and the GFRP ribs. Given that the rib width (w_r) is typically much larger than the rib height (h_r), the ribs can be approximated as triangular shapes on the bar [29]. As illustrated in Figure 15a, the overall slip of the GFRP bar (s) can be determined as follows:

$$\delta_c = \frac{w_r + w_c}{w_r} \cdot \frac{E_r}{E_c} \delta_r \quad (2)$$

$$s = \left(1 + \frac{w_r + w_c}{w_r} \cdot \frac{E_r}{E_c}\right)\delta_r \tag{3}$$

where δ_c and δ_r are the axial deformation in concrete and GFRP ribs in Figure 15a, respectively; w_r is the width of the GFRP rib; and w_c is the width between the ribs.

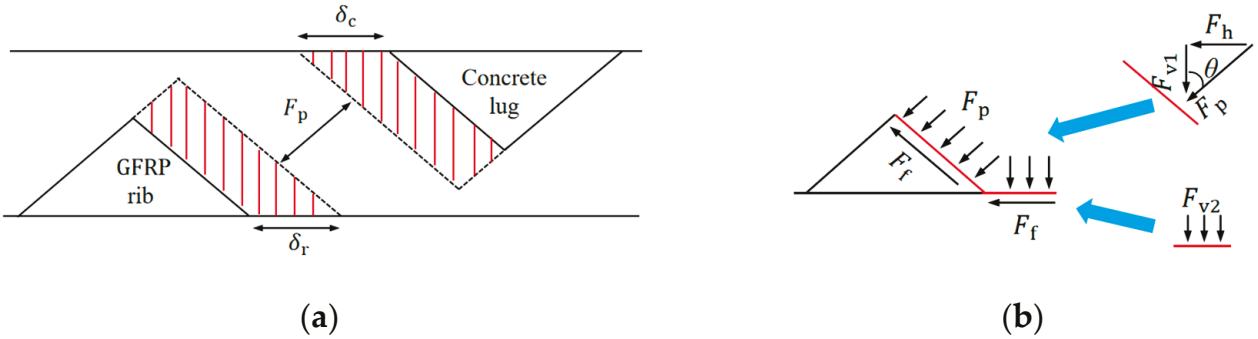

Figure 15. Schematic diagram illustrating slip generation and force generation on a single rib: (**a**) slip generation; (**b**) force generation.

Since GFRP bars are anisotropic materials, their transverse elastic modulus is typically lower than their longitudinal elastic modulus [30]. Therefore, in this study, the transverse modulus of elasticity for GFRP ribs is denoted as E_r, with γ representing the discount factor applied to the longitudinal modulus of elasticity E_f.

In Type B failure, the ribs of the GFRP bar are nearly completely worn away, while the concrete remains largely intact. Consequently, the concrete can be considered a rigid body during the pull-out test to analyze the elastic deformation of the rib, but in fact, concrete also undergoes deformation simultaneously. At the peak of Type B failure, it is assumed that the rib width is compressed by the concrete lug to half of its original value, a hypothesis widely applied in bond–slip analysis at this scale [29,31]. Therefore, the slip corresponding to the peak bond strength (s_P) can be calculated as follows:

$$s_P = \left(1 + \frac{w_r + w_c}{w_r} \cdot \frac{E_r}{E_c}\right) \times \frac{1}{2} w_r \tag{4}$$

A parameter k is introduced to determine point E for the limit state of Stage II:

$$s_E = k \cdot s_P = \left(1 + \frac{w_r + w_c}{w_r} \cdot \frac{E_r}{E_c}\right) \times \frac{k}{2} w_r \tag{5}$$

During these stages, bond stress is primarily influenced by the mechanical interlock between the FRP ribs and the concrete lugs. A simplified model is proposed in Figure 16 to illustrate the compressive deformation behavior of FRP ribs, suggesting that damage to ribbed FRP bars is primarily caused by the compressive crushing of ribs rather than direct slip failure at the bar surface. Figure 16a illustrates the initial state of a GFRP bar under pull-out loading, where the original blue semicircular rib is compressed by the concrete lugs, with specific geometric characteristics marked. Figure 16b shows the state of the FRP bars after experiencing rib deformation by δ_r. The deformed contact profile is divided into two components: the deformed rib (blue) and the extruded horizontal Section (green). For simplification, the blue curve is approximated as the red dotted line. Figure 16c depicts the stress distribution following rib deformation, where the red area represents compressive stress on the deformed rib, and the green area indicates radial stress exerted on the GFRP bar. Among these two regions, only the red area generates a longitudinal component force that contributes to pull-out resistance, while the green area induces radial force, enhancing the frictional effect along the GFRP bar surface.

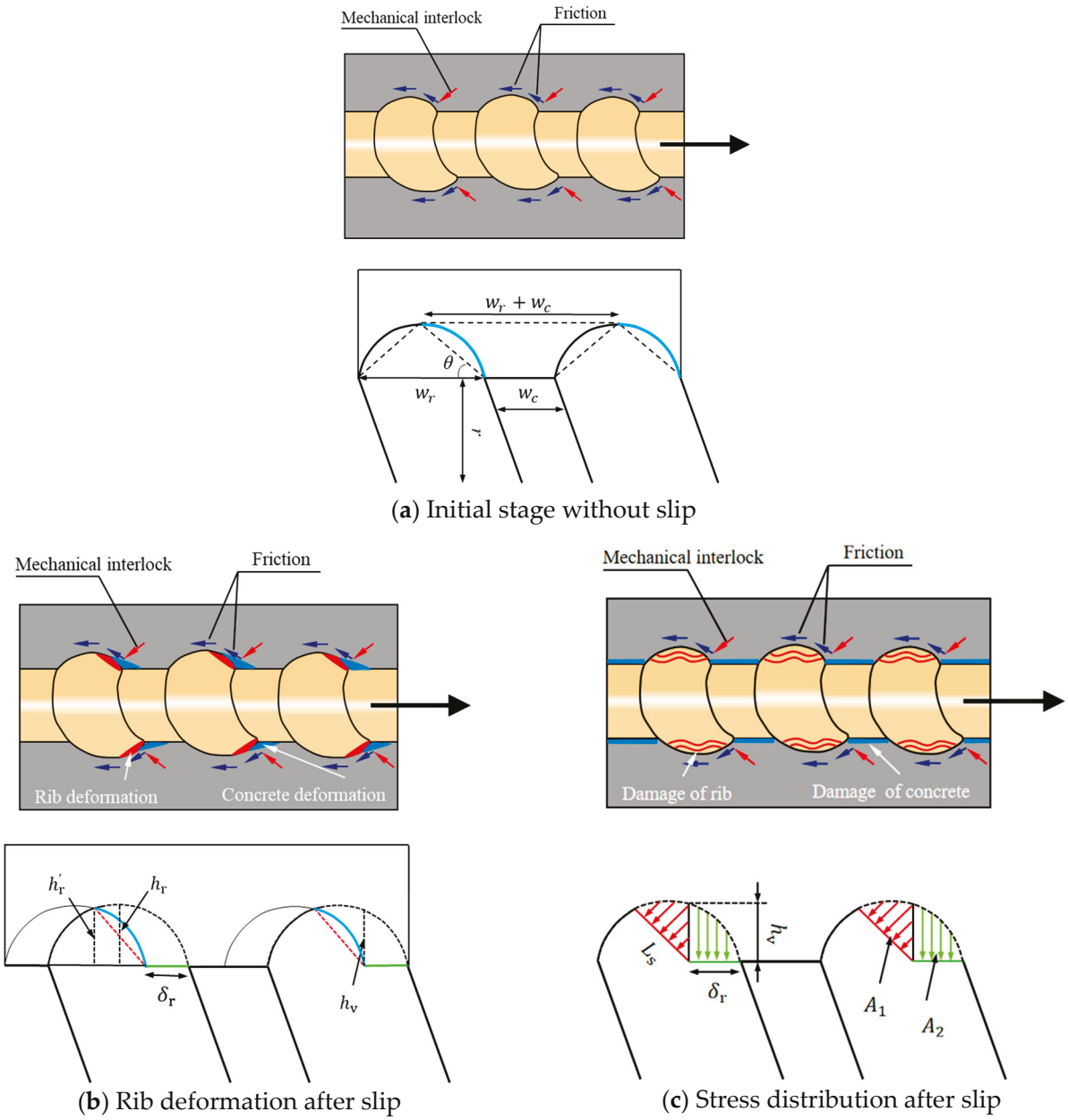

Figure 16. Force diagram of deformed GFRP bars: (**a**): Initial stage without slip; (**b**): Rib deformation after slip; (**c**) Stress distribution after slip.

As depicted in Figure 16c, the length of the contact surface of the FRP rod after rib compression deformation is represented by L_s, while the maximum radial compression deformation is denoted as h_v. Both parameters can be determined using the following equations:

$$L_s = \frac{w_r - \delta_r}{2\cos\theta} \tag{6}$$

$$h_v = h_r - h_r' \tag{7}$$

The radial deformation on the contact surface changes linearly along the longitudinal direction of the FRP bar. Given that the vertical radius of the GFRP bar (r) is typically much greater than the rib height (h_r), the average vertical strain (ε_v) on the contact surface can be determined as follows:

$$\varepsilon_v = \frac{h_v/2}{r} \tag{8}$$

The average radial stress on the contact surface can be derived through Equation (9):

$$\sigma_{\mathrm{v}} = E_{\mathrm{r}}\varepsilon_{\mathrm{v}} \tag{9}$$

Then, the vertical forces in Figure 15b (F_{v1} and F_{v2}) generated by a single rib can be calculated as:

$$F_{\mathrm{v1}} = 2\pi r L_s \sigma_v \tag{10}$$

$$F_{\mathrm{v2}} = 2\pi r \delta_{\mathrm{r}} \sigma_v \tag{11}$$

The horizontal force generated at the contact surface is:

$$F_{\mathrm{h}} = F_{\mathrm{v1}}\tan\theta \tag{12}$$

The friction force F_{f} caused by rib compression deformation can be obtained as:

$$F_{\mathrm{f}} = u_{\mathrm{s}}F_{\mathrm{v1}}\tan\theta + u_{\mathrm{s}}F_{\mathrm{v2}} = u_{\mathrm{s}}F_{\mathrm{h}} + u_{\mathrm{s}}F_{\mathrm{v2}} \tag{13}$$

where u_{s} denotes the friction coefficient of the GFRP rib.

Then, the bond stress along the GFRP bars at unit length ($w_{\mathrm{r}} + w_{\mathrm{c}}$) can be obtained:

$$\tau = \frac{F_{\mathrm{h}} + F_{\mathrm{f}}}{2\pi r(w_{\mathrm{r}} + w_{\mathrm{c}})} \tag{14}$$

Hence, the bond stress for stages I and II (from point O to point E) can be collated as:

$$\tau_{\mathrm{OE}} = (1 + u_{\mathrm{s}})E_{\mathrm{r}}\frac{h_{\mathrm{r}}}{rw_{\mathrm{r}}(w_{\mathrm{r}} + w_{\mathrm{c}})}\frac{\sin\theta}{2\cos^2\theta}\delta_{\mathrm{r}}(w_{\mathrm{r}} - \delta_{\mathrm{r}}) + u_{\mathrm{s}}E_{\mathrm{r}}\frac{h_{\mathrm{r}}}{rw_{\mathrm{r}}s_{\mathrm{r}}}{\delta_{\mathrm{r}}}^2 \tag{15}$$

In stage III, the friction remains constant at the maximum friction force observed in stage II. Another way of saying this is that the friction force of stage E~P is constant as the friction force at point E, denoted as τ_{Ef}:

$$\tau_{Ef} = \tau_{\mathrm{E}} - \gamma E_{\mathrm{r}}\frac{h_{\mathrm{r}}}{rw_{\mathrm{r}}(w_{\mathrm{r}} + w_{\mathrm{c}})}\frac{\sin\theta}{2\cos^2\theta}\delta_{\mathrm{A}}(w_{\mathrm{r}} - \delta_{\mathrm{E}}) \tag{16}$$

Based on this, the bond strength for stage III (from point E to point P) can be collated as:

$$\tau_{EB} = E_{\mathrm{r}}\frac{h_{\mathrm{r}}}{rw_{\mathrm{r}}(w_{\mathrm{r}} + w_{\mathrm{c}})}\frac{\sin\theta}{2\cos^2\theta}\left[\delta_{\mathrm{r}}(w_{\mathrm{r}} - \delta_{\mathrm{r}}) - \frac{k}{2}w_{\mathrm{r}}\left(w_{\mathrm{r}} - \frac{k}{2}w_{\mathrm{r}}\right)\right] + \tau_{\mathrm{Ef}} \tag{17}$$

This section presents an analytical model for predicting bond–slip behavior in FRP-concrete pull-out interactions. In the model, the slip is presented in Equation (3), while the bond stresses for the OE segment and the EB segment are shown in Equations (15) and (17), respectively.

$$\begin{cases} s = \left(1 + \frac{w_{\mathrm{r}} + w_{\mathrm{c}}}{w_{\mathrm{r}}} \cdot \frac{E_{\mathrm{r}}}{E_{\mathrm{c}}}\right)\delta_{\mathrm{r}} \\ \tau = \begin{cases} (1 + u_{\mathrm{s}})E_{\mathrm{r}}\frac{h_{\mathrm{r}}}{rw_{\mathrm{r}}(w_{\mathrm{r}} + w_{\mathrm{c}})}\frac{\sin\theta}{2\cos^2\theta}\delta_{\mathrm{r}}(w_{\mathrm{r}} - \delta_{\mathrm{r}}) + u_{\mathrm{s}}E_{\mathrm{r}}\frac{h_{\mathrm{r}}}{rw_{\mathrm{r}}s_{\mathrm{r}}}{\delta_{\mathrm{r}}}^2 & s < s_{\mathrm{E}} \\ E_{\mathrm{r}}\frac{h_{\mathrm{r}}}{rw_{\mathrm{r}}(w_{\mathrm{r}} + w_{\mathrm{c}})}\frac{\sin\theta}{2\cos^2\theta}\left[\delta_{\mathrm{r}}(w_{\mathrm{r}} - \delta_{\mathrm{r}}) - \frac{k}{2}w_{\mathrm{r}}\left(w_{\mathrm{r}} - \frac{k}{2}w_{\mathrm{r}}\right)\right] + \tau_{\mathrm{Ef}} & s_{\mathrm{E}} \le s \end{cases} \end{cases}$$

The resulting bond stress is uniformly distributed across the effective bond zone, while the calculated slip represents the cumulative displacement of the FRP bars. Furthermore, the model is applicable to specimens with a failure mode of peeling off, and this model does not account for the effects of chloride exposure.

4.2. Model Modification Under Chloride Exposure

Previously, Section 4.1 presented an analytical model for bond–slip behavior without considering the effects of chloride exposure. However, as demonstrated in Section 3, the experimental results show that chloride wet–dry cycles significantly impact the bond performance of GFRP–concrete specimens. Both GFRP bars and concrete can deteriorate under these conditions, indicating the need to revise the analytical model for more accurate long-term performance predictions. To address this, two damage indicators denoted as d_r and d_c are introduced to quantify the deterioration in the elastic modulus of GFRP bars and the compressive strength of concrete, respectively. In this study, d_r and d_c account solely for the effects of chloride wet–dry cycles. Assuming uniform damage progression, the two indicators can be calculated as follows:

$$d_r = \frac{E_r - E_r'}{E_r} \tag{18}$$

$$d_c = \frac{f_c - f_c'}{f_c} \tag{19}$$

The compressive strength of the concrete was measured concurrently with the pull-out test. Since the first exposure period was 3 months, the concrete had already undergone the strengthening phase. Thus, the measurements showed that the compressive strength of concrete continuously decreased with the increase in exposure time, as indicated in Figure 13. The relationship between concrete damage and erosion time can be described using the Boltzmann equation [32], as shown in Equation (20). The Boltzmann equation is characterized by stability in the early stage, rapid changes in the medium term, and stability again in the later stage. Additionally, it is capable of representing any changes induced by parameters, as the system will return to a new equilibrium state following any disturbance applied to it [33,34]. Here, the damage indicator d_c can be derived from the fitted test data with the following Equation (20):

$$d_c = a_1 - \frac{a_1 - a_2}{1 + \exp\left(\frac{t - a_t}{d_x}\right)} \tag{20}$$

where t is the duration of chloride exposure in months; a_1, a_2, d_x, and a_t are fitting parameters between damage and erosion time. In this experiment, these parameters were fitted as $a_1 = 0.25$, $a_2 = 0$, $d_x = 1.26$, and $a_t = 7.86$, utilizing the measurements of concrete compressive strength displayed in Figure 17a.

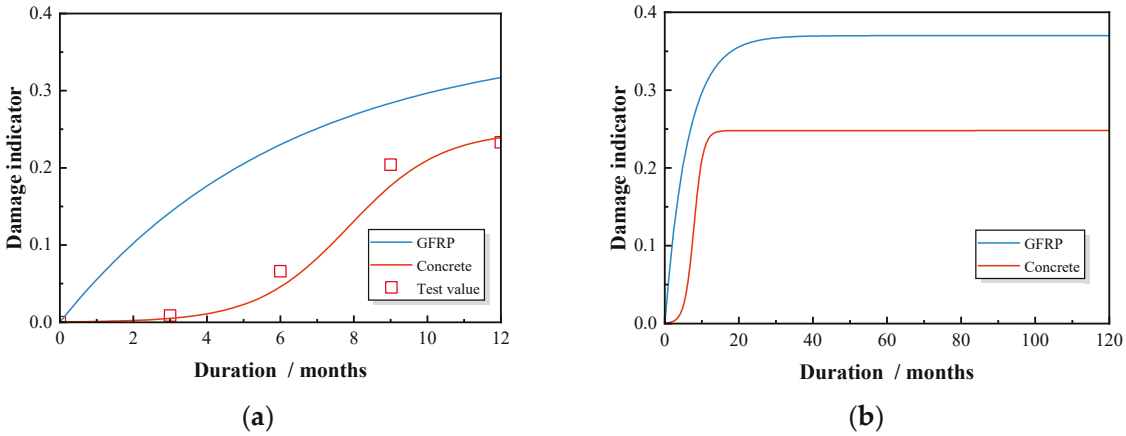

Figure 17. Damage indicator evolution for GFRP and concrete: (**a**) short-term damage evolution; (**b**) long-term damage evolution.

For the GFRP bars, for ease of calculation, a constant degradation mechanism is assumed, unaffected by variations in time and temperature [35]. The damage factor of the elastic modulus for the GFRP bar (d_{r}) can be determined using the established Arrhenius model [36], expressed as:

$$d_r = \frac{\alpha}{\beta} \cdot \frac{1 - \exp(-\beta \mathrm{t})}{100} \tag{21}$$

$$\beta = \frac{(14.0 - pH)/pH}{\frac{T_{\mathrm{c}}}{T_{\mathrm{r}}} \cdot \phi_{\mathrm{F}} \cdot \left(\frac{2r}{D_r}\right)^2} \tag{22}$$

where α is a calculation constant, set to 0.2 in this paper; β is reduction factor for GFRP degradation; pH is the pH value within the concrete, fixed at 13.6 for normal concrete; T_{c} denotes the current temperature of the GFRP bars in Kelvin; T_{r} is the reference temperature, set to 293 K; D_{r} is the reference value, established at 2.0 mm; ϕ_{F} is the surface coefficient quantifying the contact area of GFRP bars with the surrounding solution (for a GFRP bar placed in pure solution, this value is 1.0, while for GFRP bars in concrete, this value is defined as the porosity of cement paste surrounding GFRP bars).

The evolution of the damage indicators d_r and d_c is illustrated in Figure 17, highlighting the deterioration characteristics under chloride wet–dry cycles. The d_r curve exhibits a steep slope during the first three months, indicating rapid damage accumulation in the GFRP bar. After this period, the slope decreases, suggesting a transition to a slower damage phase, likely due to the saturation of chloride ion penetration, which reduces the overall diffusion rate and stabilizes surface damage [36]. In the subsequent months, the damage rate remains relatively stable with minimal fluctuations. In contrast, the d_c curve for concrete damage follows an S-shaped pattern. Initially, the damage rate is low, with a gentle slope during the first three months. Between months three and eight, the damage accumulation accelerates significantly, as reflected by the increased slope. After the ninth month, the damage rate slows down, and the curve flattens, indicating that the concrete has entered a more stable phase of damage accumulation.

These two damage indicators, d_{r} and d_{c}, can be utilized to refine the analytical model presented in Section 4.1. The long-term elastic modulus of GFRP, E'_r, and the concrete compressive strength, f'_{c}, under chloride exposure can be expressed as follows:

$$\mathrm{E}'_r = (1 - d_r) E_{\mathrm{r}} \tag{23}$$

$$f'_c = (1 - d_c) f_c \tag{24}$$

This modification allows for the prediction of bond–slip curves across various chloride exposure durations. However, it is important to note that the relatively short exposure duration in the experiments may limit the predictive model's accuracy regarding long-term performance. Additional experimental data are necessary to further refine and enhance the calculation model.

4.3. Model Validation

Based on the analysis derived in Sections 4.1 and 4.2, a predictive method was developed to estimate the bond–slip behavior between GFRP bars and concrete under the influence of chloride wet–dry cycles. The variable, u_s, representing the friction coefficient at the interface between GFRP bars and concrete was set to 0.5 for the RG series and 0.55 for the SG series [37,38]. The ratio of the transverse elastic modulus of GFRP to its longitudinal elastic modulus (γ) was selected as 0.25 for RG series and 0.125 for SG series in this paper [30]. The coefficient k, obtained through the regression of experimental results, was determined to be 0.85, as shown in Figure 18.

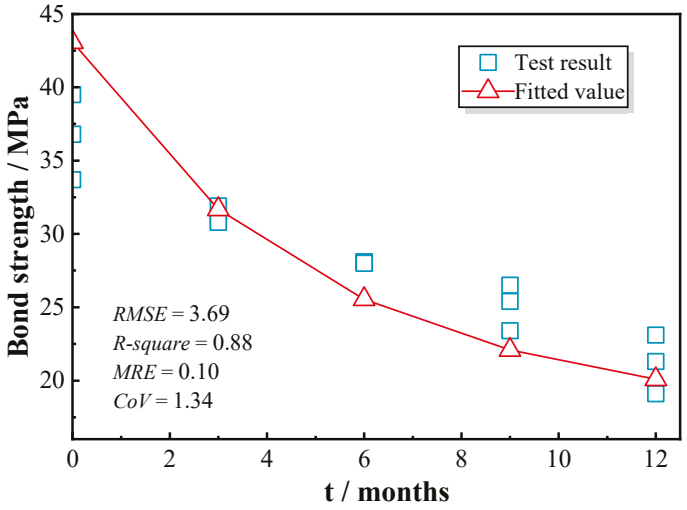

Figure 18. Relationship between coefficient k and test results.

According to ACI 318 (2012) [39], the shear modulus of concrete can be calculated as:

$$E_c = \frac{57,000\sqrt{(145 \times f_c)}}{290 \times (1 + 0.2)} \tag{25}$$

where f_c is cylinder compressive strength, which can be assumed to be 0.8 times the prism compressive strength in this test.

The predicted bond–slip curves and the statistical evaluations were compared with the experimental results and are presented in Figures 19–21. This study used *RMSE*, *R-square*, *MRE*, and *CoV* to quantify the feasibility of the model. Specifically, a smaller *RMSE* indicates better model performance; an *R-square* above 0.8 typically suggests that the model fits the data well; an *MRE* less than 0.2 is considered a good level; and a *CoV* below 0.3 indicates superior predictive performance. As indicated in Figures 19–21, the proposed model showed good agreement for test specimens exhibiting failure pattern B. In contrast, specimens with failure pattern A (specimens RG-7d-0, RG-7d-3, and RG-7d-6) demonstrated greater variability in the correlation metrics. This discrepancy is primarily due to the assumption in the proposed analytical model, which does not account for concrete crushing damage.

Table 5 presents a comparison of the predicted and tested peak values for the GFRP bar pull-out tests in concrete. The ratio of predicted bond strength (τ_p) to the tested strength (τ_t) was close to 1 and exceeded 0.7 for all tested specimens, indicating a strong predictive capacity of the proposed analytical model for assessing the ascending portion of the bond–slip performance. For the RG-5d group, the ratio of predicted to experimental peak strength (τ_p/τ_t) ranged from 0.87 to 1.17, with an average error of 2%. The ratio of predicted to experimental peak slip (s_p/s_t) varied between 0.69 and 1.32, with an average error of 1%. Notably, the highest prediction errors for both peak strength and peak slip in the RG-5d group occurred in the RG-5d-0 test, and they were attributed to a different failure mode. It was possible for local concrete crushing in specimen RG-5d-0 to result in a lower measured peak strength than that predicted for GFRP rib failure.

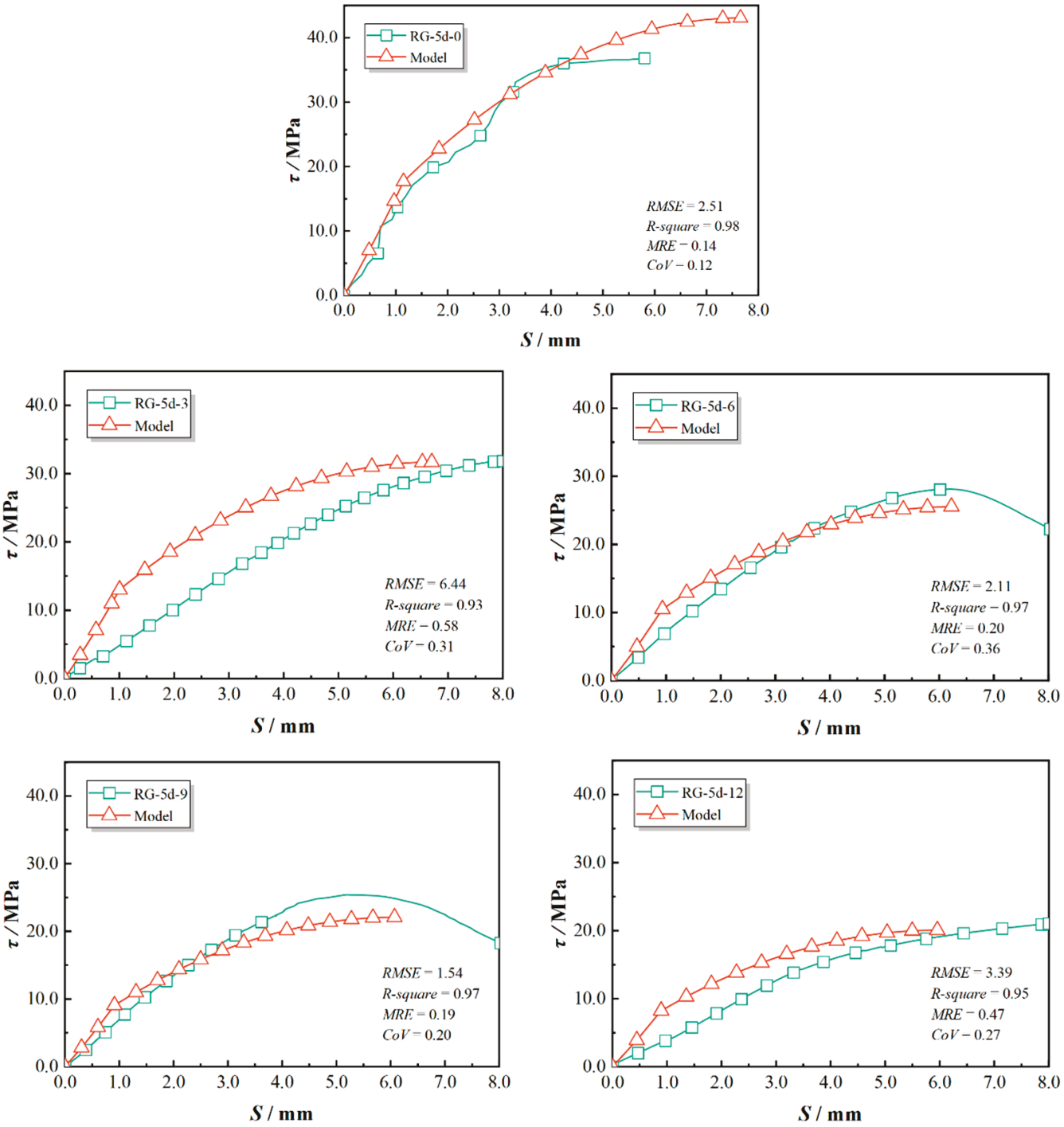

Figure 19. Prediction accuracy for RG-5d series specimens.

In the SG-5d group, the τ_p/τ_t ratio ranged from 0.70 to 1.01, with an average error of 19%. The s_p/s_t ratio spanned from 0.77 to 1.26, with an average error of 11%. It is evident that the predicted peak strengths for the SG-5d group were generally lower than the experimental values, which may be due to the conservative selection of the γ value. Additionally, the proposed GFRP damage indicator d_r in Equations (22) and (23) did not account for the effects of the sand-blasted surface. Previous studies have indicated that sand-blasted surfaces are more susceptible to damage and stripping from the GFRP bar.

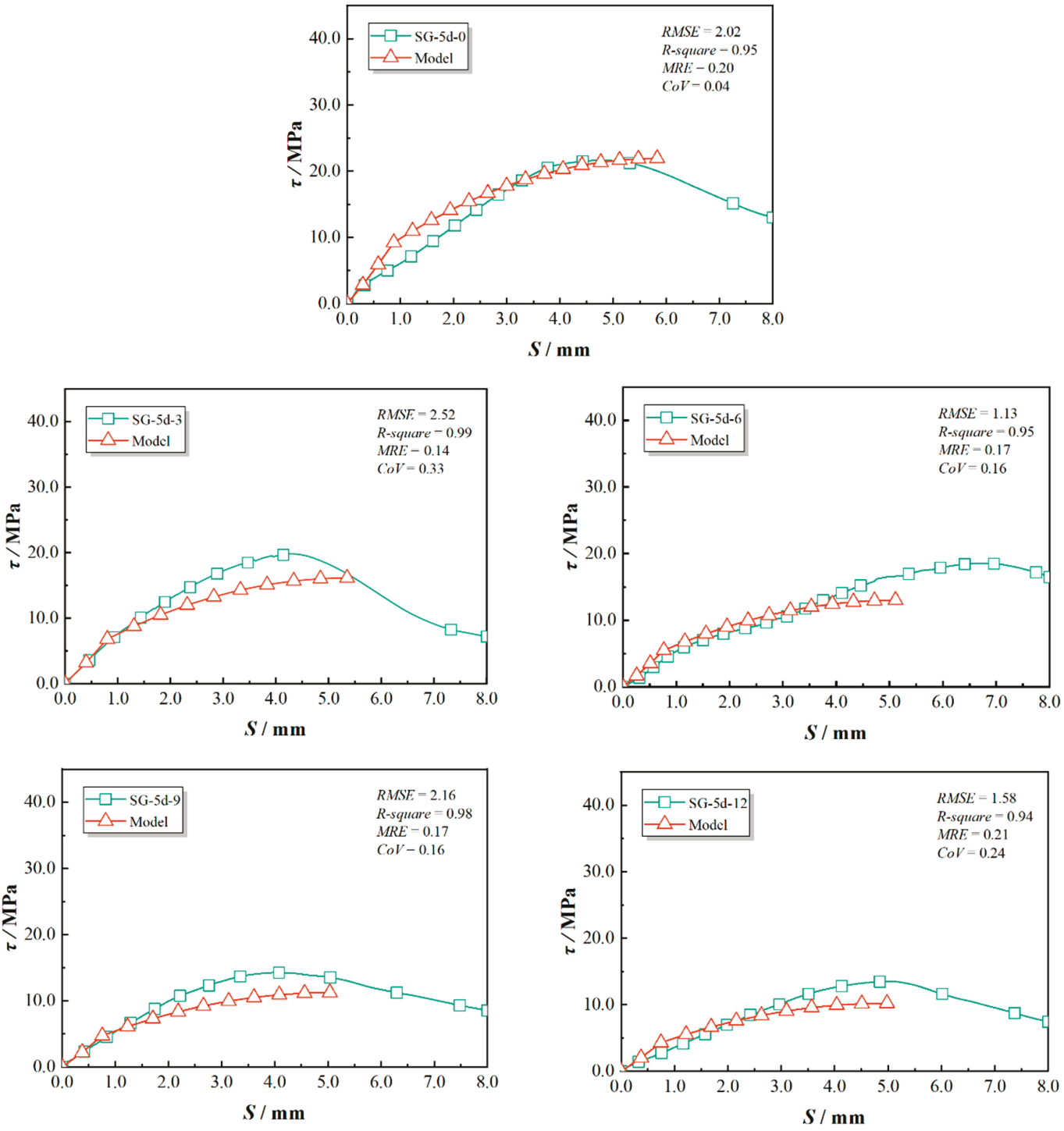

Figure 20. Prediction accuracy for SG-5d series specimens.

For the RG-7d group, the τ_p/τ_t ratio lay between 0.74 and 1.15, with an average error of 7%, while the s_p/s_t ratio ranged from 0.56 to 0.95, with an average error of 27%. The predicted peak bond strength for the RG-7d group was calculated using a reduction factor based on the RG-5d group. However, the longer bond length led to a deeper chloride erosion pathway when exposed in the chloride solution tank, potentially enhancing chloride resistance for the RG-7d series pull-out specimens [11]. Furthermore, the τ_p for the RG-7d group was derived under the assumption of a uniform bond stress distribution along the GFRP, similar to that of the RG-5d group. This assumption overlooked the non-uniform distribution of the bond stress, resulting in an overestimation of bond strength [8].

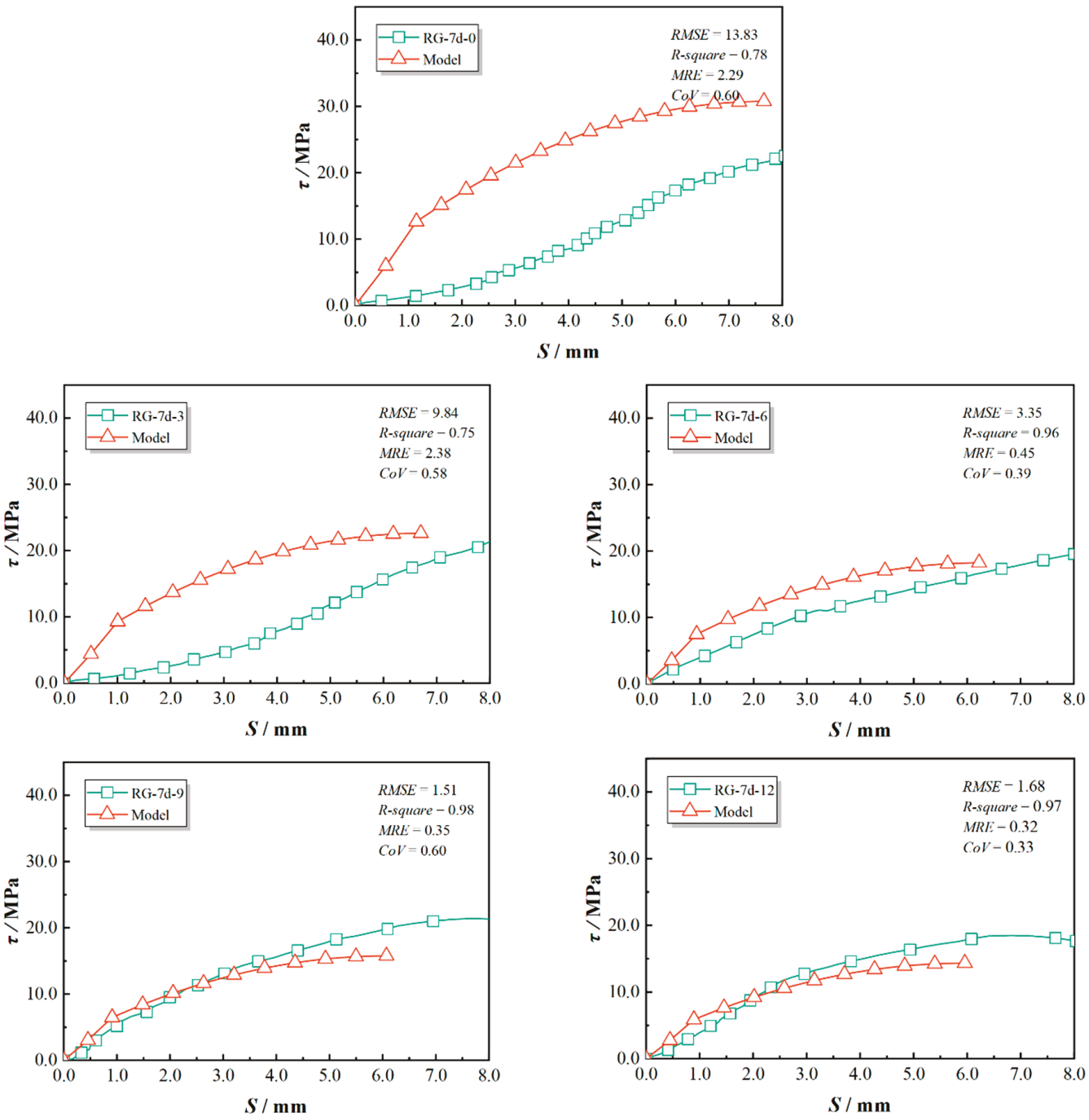

Figure 21. Prediction accuracy for RG-7d series specimens.

Furthermore, Figure 22 presents a comparison between the bond strength test results from various studies and the predicted values from the model developed in this study [25,29,40]. It can be observed that the predicted bond strengths align well with the experimental results across multiple datasets, demonstrating the reliability of the proposed model. The model provides a highly accurate estimation of bond strength, effectively capturing the influence of key parameters. While some variations exist due to differences in experimental conditions and material properties, the overall trend indicates that the proposed model can robustly predict bond performance in chloride-exposed environments. Therefore, the validation results confirm that the model developed in this study exhibits sufficient accuracy and applicability for predicting the bond behavior of FRP bars in concrete.

Table 5. Comparison of the predicted and tested peak points.

Specimen	Failure Patterns	τ_P	τ_P/τ_t		s_P	s_P/s_t	
			Rate	Average		Rate	Average
RG-5d-0	A	43.08	1.17		7.66	1.32	
RG-5d-3	B	31.68	0.99		6.70	0.83	
RG-5d-6	B	25.54	0.91	0.98	6.22	1.00	1.01
RG-5d-9	B	22.09	0.87		6.07	1.19	
RG-5d-12	B	20.09	0.94		5.96	0.69	
SG-5d-0	B	21.94	1.01		5.83	1.24	
SG-5d-3	B	16.13	0.81		5.35	1.27	
SG-5d-6	B	13.01	0.70	0.81	5.11	0.77	1.11
SG-5d-9	B	11.25	0.79		5.04	1.26	
SG-5d-12	B	10.23	0.76		4.98	1.02	
RG-7d-0	A	30.77	1.06		7.66	0.72	
RG-7d-3	A	22.63	0.88		6.70	0.56	
RG-7d-6	A	18.24	0.82	0.93	6.22	0.60	0.73
RG-7d-9	B	15.78	0.74		6.07	0.80	
RG-7d-12	B	21.2	1.15		6.43	0.95	

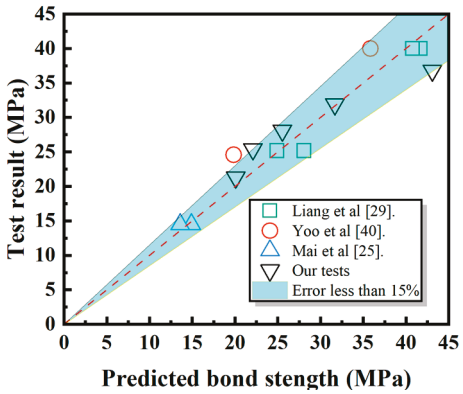

Figure 22. A comparison of bond strengths and predicted results from various sources.

5. Model's Application

5.1. Analysis of Parametric Sensitivity

The parameters u_s, k, and γ are essential for the proposed bond–slip model. This section analyzes the sensitivity of the predicted bond–slip curves to variations in u_s, k, and γ. Initially, Figure 23a illustrates the effect of different u_s values (0.4, 0.3, 0.2, and 0.1) on the bond–slip curves. The parameter u_s represents the contribution of friction to the bond performance between GFRP bars and concrete during pull-out testing, where a higher u_s value indicates a rougher contact surface and increased frictional resistance. The results show that decreasing u_s slightly reduces the convexity of the predicted curve. Although the peak strength is only moderately reduced by approximately 11%, the strength at the end of the elastic stage exhibits a more significant decrease of around 27%. This is because friction plays a dominant role in the initial stages of the pull-out test. As the GFRP bar slip increases, the bond stress at the interface is primarily governed by mechanical interlock rather than friction [7]. Consequently, the friction coefficient u_s primarily affects the elastic stage characteristics of the bond–slip curve, demonstrating minimal sensitivity in the subsequent phases.

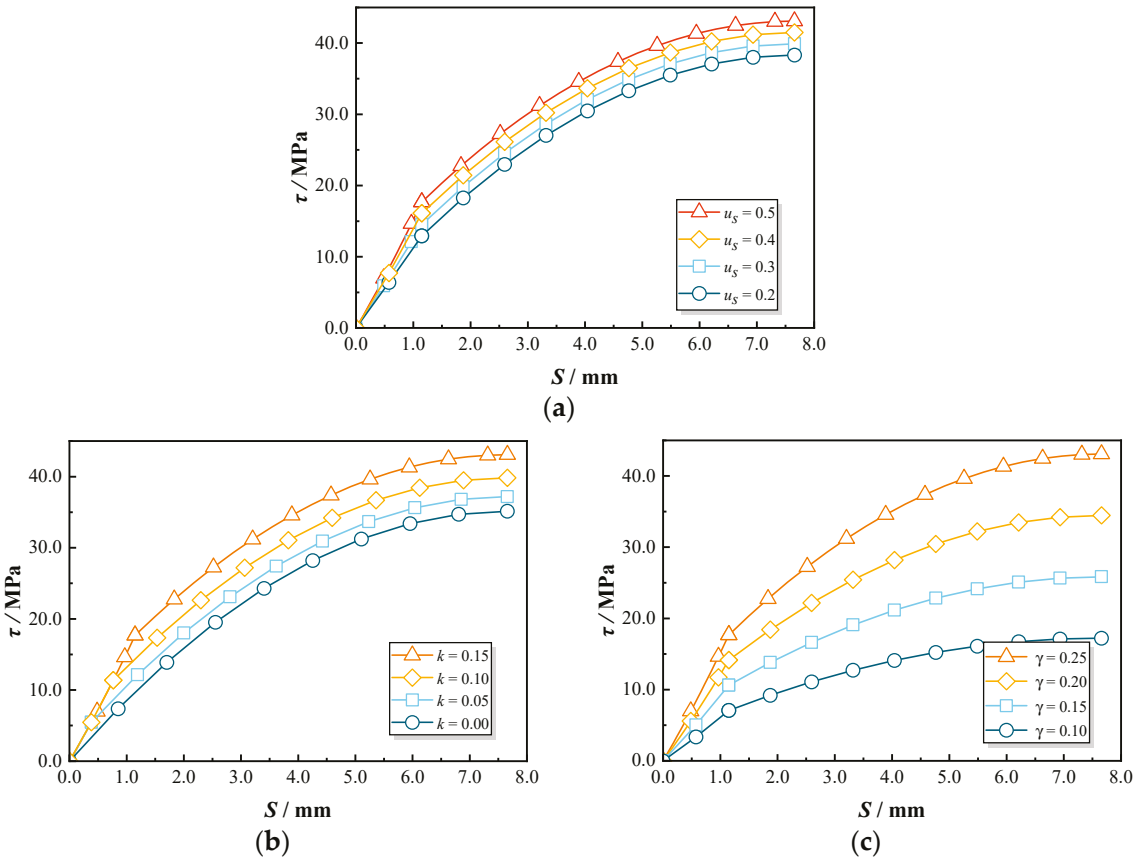

Figure 23. Parametric sensitivity in the predicted bond–slip curve: (**a**) effect of u_s; (**b**) effect of k; (**c**) effect of γ.

In this study, the coefficient k influences the elastic stage of the pull-out test, as detailed in Equation (6). To assess the impact of k on the predicted curves, different values of k (1.0, 0.95, 0.90, 0.85) were incorporated into the proposed model for comparison, as illustrated in Figure 23b. As the coefficient k increases, the slip for the elastic stage shortens. It clearly demonstrates that the predicted curve exhibits a diminishing "convex" trend with increasing k. When k changes from 0.85 to 1.00, the peak strength gradually decreases by 19%. These results indicate that the predicted curve shows a certain degree of sensitivity to variations in k.

To investigate the impact of γ on the predicted curve, various γ values were introduced into the proposed model for comparison. Figure 23c illustrates the comparison among γ values of 0.25, 0.20, 0.15, and 0.10. The parameter γ represents the discount factor for the transverse elastic modulus of the GFRP. As γ decreases, the overall trend of the curve flattens, and the peak strength correspondingly reduces. The predictive model employed in this study as based on the elastic deformation of GFRP ribs. For specimens with other identical parameters, a smaller γ value indicates that the same deformation will generate a reduced elastic force. Consequently, the predicted curve declines with the decrease in γ.

5.2. Long-Term Bond Performance Prediction

The validated bond–slip prediction model was applied to evaluate the long-term bond performance between GFRP bars and concrete under prolonged chloride exposure. This section examines the progressive changes in the bond–slip behavior of GFRP–concrete pull-out specimens over a 10-year period. It is assumed that concrete degradation follows the trends outlined in Section 4, while GFRP bars are exposed to stable chloride conditions,

with similar environmental factors in terms of concentration, temperature, and so on. All parameters used in this analysis are consistent with those defined in Section 4.3.

Figure 24a illustrates the evolution of the bond–slip curve for GFRP–concrete (RG-5d) specimens over one year. Significant changes in the bond–slip curves are observed at different intervals, although the rate of strength degradation decreases over time. The peak bond strength declines by approximately 26.5% within the first three months, while the reduction from months 9 to 12 is only around 9%. This indicates that damage accumulation in GFRP–concrete bond specimens is more severe in the early stages under chloride dry–wet cycles.

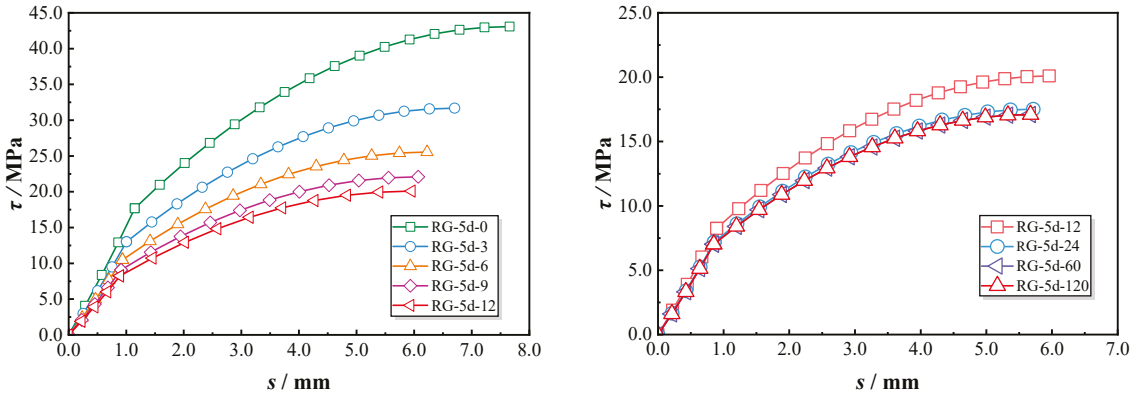

Figure 24. The predicted bond–slip curves for RG-5d specimens. (**a**) Short-term prediction; (**b**) Long-term prediction.

Figure 24b extends this analysis to a 10-year exposure period. The most pronounced changes in the bond–slip curve occur within the first 24 months, after which minimal alterations are observed beyond 36 months, with peak bond strength stabilizing at 17.1 MPa. These results suggest that the bond performance degradation rate of GFRP–concrete (RG-5d) pull-out specimens diminishes with increased exposure time.

In summary, this study offers theoretical insights into predicting the long-term bond–slip behavior between GFRP bars and concrete under chloride wet–dry cycles. However, the predictive outcomes are based on a mechanical model that may not fully capture complex real-world conditions. Specifically, the model assumes uniform damage distribution within the material, while in practice, damage could be localized and heterogeneous, potentially affecting the accuracy of the bond–slip behavior predictions. Therefore, future research should incorporate additional experimental data to refine and validate the model, thereby enhancing its precision and applicability. It should be noted that this study employs an indoor dry–wet cycle accelerated test, in which the experimental duration is relatively short. While discrepancies between this accelerated testing method and real-world conditions remain, it has been widely adopted by many researchers and has been proven to be a scientifically feasible approach for studying the degradation of the bond performance between GFRP bars and concrete.

6. Conclusions

This study systematically investigated the bond behaviors between GFRP bars and concrete under chloride wet–dry cycles, focusing on the effects of bond length and surface texture. The experimental results demonstrate that both bond length and surface texture significantly influence bond performance and degradation patterns during chloride expo-

sure. An analytical bond–slip relation model with high applicability and accuracy was proposed. The main conclusions are summarized as follows:

(1) The application of a sand-coated surface on GFRP bars resulted in significantly lower bond strength and stiffness compared to threaded ribbed GFRP bars. However, the sand-coated GFRP bars exhibited better resistance to deterioration under chloride exposure, with a reduction of approximately 37.7% after 12 months, compared to a 42.1% reduction in threaded ribbed GFRP bars.

(2) Bond length significantly influenced the failure pattern and bond–slip behaviors between GFRP and concrete. Pull-out specimens with shorter bond lengths were more prone to peeling-off failure after exposure, and the failure mode in RG-7d group changed from pull-out failure to peeling-off failure as the exposure duration exceeded 9 months. GFRP bars with a shorter bond length (5d) consistently exhibited higher bond strength across all exposure durations, while increasing the bond length to 7d resulted in a more gradual decrease in bond strength.

(3) The test results revealed a clear relationship between chloride exposure duration and the degradation of GFRP–concrete bond performance. A comparison of the retentions in concrete compressive strength and bond strength indicated that the deterioration of GFRP bars is a critical factor contributing to bond deterioration.

(4) An analytical model was developed that incorporated GFRP bar geometry, surface texture, and bond length, and it was validated against experimental data. The model successfully predicted bond behavior under varying conditions, demonstrating its effectiveness in capturing the key factors influencing bond performance. This model can also predict bond behavior over a ten-year period under continuous chloride exposure.

(5) Future research will focus on optimizing the predictive model to improve its applicability and accuracy in engineering practice. Additionally, extended experimental studies will be conducted to obtain more comprehensive long-term degradation data, as the current study was limited to 12 months of exposure. These findings will help validate and refine the model, ensuring its reliability in assessing the durability of GFRP-reinforced concrete structures.

Author Contributions: Methodology, C.L.; formal analysis, Z.Y., H.G. and S.Y.; data curation, H.G.; writing—original draft preparation, Z.Y. and H.G.; writing—review and editing, S.Y. and S.Y.; supervision, S.Y. and C.L. All authors have read and agreed to the published version of the manuscript.

Funding: This research received no external funding.

Data Availability Statement: Data are contained within the article.

Acknowledgments: This research was financially supported by the National Natural Science Foundation of China (No. 52478177) and Natural Science Foundation for Young Scientists of Jiangsu Province (BK20240876).

Conflicts of Interest: The authors declare no conflict of interest.

References

1. Maganti, T.R.; Boddepalli, K.R. Optimization of mechanical and impact resistance of high strength glass fiber reinforced alkali activated concrete containing silica fume: An experimental and response surface methodology approach. *Case Stud. Constr. Mater.* **2025**, *22*, e04343. [CrossRef]
2. Wei, Y.; Chen, Z.; Sun, Y. Unraveling the atomic-scale mechanism of interfacial alkali ion close packing in nano glassy fibers driven by CO_2-mediated attraction. *Nanoscale* **2024**, *16*, 17338–17344. [CrossRef] [PubMed]
3. Ahmad, K.; Din, Z.; Ullah, H. Preparation and characterization of bio-based nanocomposites packaging films reinforced with cellulose nanofibers from unripe banana peels. *Starch-Starke* **2022**, *74*, 2100283. [CrossRef]
4. Ji, Q.; Zhou, C.; Li, Z. Is nanocellulose a good substitute for non-renewable raw materials? A comprehensive review of the state of the art, preparations, and industrial applications. *Ind. Ind. Crop Prod.* **2023**, *202*, 117093. [CrossRef]

5. Zhang, B.; Xu, F.; Zhu, H. Deterioration of bond performance between BFRP bars and coral aggregate concrete incorporating slag-based geopolymers under seawater corrosion environments. *Constr. Build. Mater.* **2024**, *411*, 134518. [CrossRef]
6. Lu, Z.; Zhao, C.; Zhao, J. Bond durability of FRP bars and seawater–sea sand–geopolymer concrete: Coupled effects of seawater immersion and sustained load. *Constr. Build. Mater.* **2023**, *400*, 132667. [CrossRef]
7. Nelson, L.A.; Weekes, L.; Milani, G. Generalised analytical solutions for linear and non-linear bond–slip models for externally bonded FRP to a concrete substrate. *Eng. Struct.* **2024**, *298*, 117025.
8. Shi, M.; Xu, G.; Zhao, J. The study on bond-slip constitutive model of shape memory alloy fiber-reinforced concrete. *Constr. Build. Mater.* **2024**, *418*, 135395. [CrossRef]
9. Zhou, C.; Yang, B.; Zhang, Z. Bond-slip behavior of the FRP bar-sea sand concrete interface and its effect on the finite element analysis of RC beam. *Constr. Build. Mater.* **2024**, *436*, 136917. [CrossRef]
10. Chen, L.; Liang, K.; Shan, Z. Experimental and theoretical studies on bond behavior between concrete and FRP bars with different surface conditions. *Compos. Struct.* **2023**, *309*, 116721. [CrossRef]
11. Hussain, S.; Khan, M.Z.N.; Khan, H.A. Bond performance of basalt FRP bar against aggressive environment in high-strength concrete with varying bar diameter and bond length. *Constr. Build. Mater.* **2022**, *349*, 128779. [CrossRef]
12. Yang, S.; Yang, T.; Sun, Z. A predictive model for determining shear strength and shear fracture energy of FRP bars in alkali-activated slag seawater coral aggregate concrete. *J. Build. Eng.* **2022**, *59*, 105085. [CrossRef]
13. Zhou, Q.; Xue, X.; Chen, C. Canopy deposition characteristics of different orchard pesticide dose models. *Int. J. Agric. Biol. Eng.* **2023**, *16*, 1–6. [CrossRef]
14. Solangi, K.; Siyal, A.A.; Wu, Y. An assessment of the spatial and temporal distribution of soil salinity in combination with field and satellite data: A case study in Sujawal District. *Agronomy* **2019**, *9*, 869. [CrossRef]
15. Zhang, T.; Luo, X.S.; Xu, J. Dry–wet cycle changes the influence of microplastics (MPs) on the antioxidant activity of lettuce and the rhizospheric bacterial community. *J. Soil. Sediment.* **2023**, *23*, 2189–2201. [CrossRef]
16. Wu, S.; Wei, X. Mechanical interaction between a canopy opener and rice stalks based on the transient dynamic analysis. *Biosyst. Eng.* **2019**, *178*, 256–263. [CrossRef]
17. Wang, Y.; Wang, M.; Zhang, X. Bond of steel-FRP composite bar embedded in FRP-confined concrete: Behavior, mechanism, and strength model. *Eng. Struct.* **2024**, *318*, 118693. [CrossRef]
18. Peng, K.; Zeng, J.; Huang, B. Bond performance of FRP bars in plain and fiber-reinforced geopolymer under pull-out loading. *J. Build. Eng.* **2022**, *57*, 104893. [CrossRef]
19. Ke, L.; Ai, Z.; Feng, Z. Interfacial bond behavior between ribbed CFRP bars and UHPFRC: Effects of anchorage length and cover thickness. *Eng. Struct.* **2023**, *286*, 116140. [CrossRef]
20. Ding, Y.; Mao, W.; Wei, W. Bond behavior and anchorage length of deformed bars in steel-polyethylene hybrid fiber engineered cementitious composites. *Eng. Struct.* **2022**, *252*, 113675. [CrossRef]
21. Machello, C.; Bazli, M.; Rajabipour, A. FRP bar and concrete bond durability in seawater: A meta-analysis review on degradation process, effective parameters, and predictive models. *Structures* **2024**, *62*, 106231. [CrossRef]
22. El-Nemr, A.; Ahmed, E.A.; Barris, C. Bond performance of fiber reinforced polymer bars in normal-and high-strength concrete. *Constr. Build. Mater.* **2023**, *393*, 131957. [CrossRef]
23. Nepomuceno, E.; Sena-Cruz, J.; Correia, L. Review on the bond behavior and durability of FRP bars to concrete. *Constr. Build. Mater.* **2021**, *287*, 123042. [CrossRef]
24. Li, J.; Gravina, R.J.; Smith, S.T. Bond strength and bond stress-slip analysis of FRP bar to concrete incorporating environmental durability. *Constr. Build. Mater.* **2020**, *261*, 119860. [CrossRef]
25. Mai, G.; Xiong, Z.; Zhou, H. Bond durability between GFRP bars and seawater sea sand concrete in marine environments. *Eng. Struct.* **2025**, *330*, 119808. [CrossRef]
26. Pan, Y.; Yu, Y.; Yu, J. Effects of simulated seawater on static and fatigue performance of GFRP bar–concrete bond. *J. Build. Eng.* **2023**, *68*, 105985. [CrossRef]
27. Nepomuceno, E.; Sena-Cruz, J.; Lourenço, L. Assessment of bond durability between GFRP bars and concrete produced with seawater under seawater exposure at different temperatures. *Constr. Build. Mater.* **2025**, *469*, 140479. [CrossRef]
28. Corres, E.; Muttoni, A. Local bond-slip model based on mechanical considerations. *Eng. Struct.* **2024**, *314*, 118190. [CrossRef]
29. Liang, K.; Chen, L.; Shan, Z. Experimental and theoretical study on bond behavior of helically wound FRP bars with different rib geometry embedded in ultra-high-performance concrete. *Eng. Struct.* **2023**, *281*, 115769. [CrossRef]
30. Yu, H.; Cox, J.V. Radial Elastic Modulus for the Interface between FRP Reinforcing Bars and Concrete. *J. Reinf. Plastl. Comp.* **2002**, *21*, 14. [CrossRef]
31. He, S.; Li, L.; Lin, J. Bond performance between ribbed BFRP bar and seawater sea-sand concrete: Influences of rib geometry. *Structures* **2024**, *65*, 106660. [CrossRef]
32. Karagöl, F.; Yegin, Y.; Polat, R. The influence of lightweight aggregate, freezing–thawing procedure and air entraining agent on freezing–thawing damage. *Struct. Concr.* **2018**, *19*, 1328–1340. [CrossRef]

33. Arora, S.; Singh, B.; Bhardwaj, B. Strength performance of recycled aggregate concretes containing mineral admixtures and their performance prediction through various modeling techniques. *J. Build. Eng.* **2019**, *24*, 100741. [CrossRef]
34. Choi, P.; Yeon, J.H.; Yun, K.K. Air-void structure, strength, and permeability of wet-mix shotcrete before and after shotcreting operation: The influences of silica fume and air-entraining agent. *Cem. Concr. Comp.* **2016**, *70*, 69–77. [CrossRef]
35. Wang, Z.; Zhao, X.; Xian, G. Long-term durability of basalt-and glass-fibre reinforced polymer (BFRP/GFRP) bars in seawater and sea sand concrete environment. *Constr. Build. Mater.* **2017**, *139*, 467–489. [CrossRef]
36. Iwama, K.; Kai, M.; Dai, J. Physicochemical-mechanical simulation of the short-and long-term performance of FRP reinforced concrete beams under marine environments. *Eng. Struct.* **2024**, *308*, 118051. [CrossRef]
37. Yuan, J.; Hadi, M.N.S. Friction coefficient between FRP pultruded profiles and concrete. *Mater. Struct.* **2018**, *51*, 120. [CrossRef]
38. Xu, L.Z.; Ma, M.Z.; Li, Y.M. Test and analyses of the reciprocal friction properties between the rapeseeds threshing mixture and non-smooth bionic surface. *AMA Agric. Mech. Asia Afr. Lat. Am.* **2016**, *47*, 17–23.
39. *ACI 318-12*; Building Code Requirements for Structural Concrete. American Concrete Institute: Farmington Hills, MI, USA, 2012.
40. Yoo, S.J.; Kim, Y.H.; Yuan, T.F. Evaluation of residual bond behavior of CFRP and steel bars embedded in UHPC after exposure to elevated temperature. *J. Build. Eng.* **2022**, *56*, 104768. [CrossRef]

MDPI AG
Grosspeteranlage 5
4052 Basel
Switzerland
Tel.: +41 61 683 77 34

Polymers Editorial Office
E-mail: polymers@mdpi.com
www.mdpi.com/journal/polymers

Academic Open
Access Publishing

mdpi.com

ISBN 978-3-7258-7678-5